Electron Diffraction using a Cold Atom Source

Rory William Speirs

ORCID: 0000-0002-1432-0887

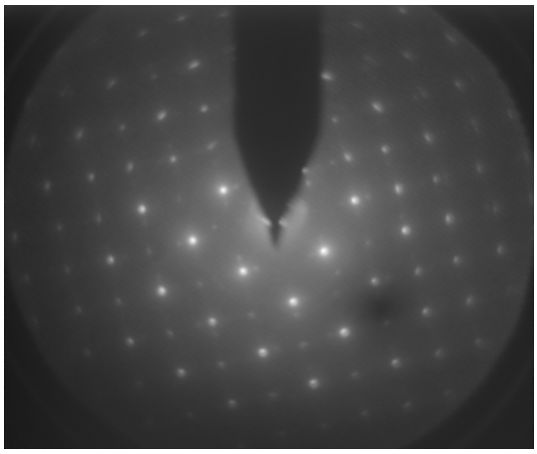

Submitted in total fulfilment of the requirements
of the degree of Doctor of Philosophy

School of Physics
The University of Melbourne

December 7, 2017

Supervised by Professor Robert E. Scholten
and Doctor Benjamin M. Sparkes

Cover image: Electron diffraction from gold. The image shows the average of 2000 electron bunches after scattering off a single crystal of gold. The pulses were 5 ns in duration, and contained 100,000 electrons each. The images were individually aligned before being added to the average in order to remove the blurring effect of beam drift. Further explanation is given in the text adjoining Figure 6.11.

Abstract

Observing matter on atomic length and time scales simultaneously is now routinely achieved in ultrafast electron and X-ray imaging techniques, but continued advances in both approaches promise to deliver huge leaps in our understanding of all kinds of atomic structures and processes. Both technologies rely on the generation of ultrabright, ultrashort duration electron bunches, with these bunches being used directly to probe the sample in electron diffraction, or to generate ultrabright X-ray pulses in X-ray free electron lasers.

The Cold Atom Electron and Ion Source (CAEIS) was conceived as a possible way to generate ultrafast electron bunches that are brighter than can currently be produced, with the aim of enabling next-generation structural determination techniques, particularly those based on electron diffraction. The CAEIS generates electrons by near-threshold photoionisation of an atomic gas, which has been shown to produce electron bunches with temperature as low as 10 K. Such cold electron bunches have the potential to be much brighter than those generated from solid photocathode sources, which typically have temperatures in the thousands of Kelvin range. Extremely cold ions are also generated in the CAEIS, which show great potential for use in ion microscopy and milling.

This thesis presents work on a number of different aspects of the continued development of the cold atom electron and ion source, with a particular emphasis on progress towards ultrafast single-shot electron diffraction based experiments.

The brightness degrading effects of space-charge repulsion are investigated using nanosecond duration ion bunches as analogues of ultrafast, picosecond duration electron bunches. Ion bunch shaping was achieved through tailoring of the spatial profile of lasers used in ionisation of the atomic gas. It was found that atomic fluorescence could substantially reduce the fidelity with which the ion bunch profile could be controlled, but methods were developed to circumvent the fluorescence problem.

The improved shaping procedures allowed generation of uniformly filled ellipsoidal bunches, which theoretically will not suffer emittance degradation under space-charge expansion. Emittance measurements following space-charge driven expansion showed that these uniformly filled ellipsoids did indeed have reduced emittance growth compared to other profiles.

Photoexcitation and field-ionisation processes involved in generation of cold electrons on ultrafast timescales were investigated, with the aim of determining the mechanisms that affect the ultimate electron bunch duration. Bunch duration was measured for a range of excitation conditions, with the finding that previously assumed ultrafast excitation pathways in fact generated fairly slow nanosecond long bunches. Ionisation time could also be a million times slower than assumed if atoms were excited below the classical ionisation threshold. Identification of the conditions required for ultrafast excitation and ionisation ultimately allowed generation of ultrafast cold electron bunches with duration of tens of picoseconds.

Electron diffraction using nanosecond long electron bunches was achieved in both transmission and reflection modes for a variety of large samples of inorganic crystals. Bunches were of sufficiently high charge to allow identification

of features of a crystal structure using only a single shot. Bragg peaks could also be identified by averaging together many images formed using ultrafast, but low-charge bunches.

Simulations were performed to determine the feasibility of using electrons generated in the CAEIS for electron coherent diffractive imaging of nanoscale apertures. It was found that it should be possible to successfully reconstruct the object plane wavefield, even taking into account realistic experimental parameters for partial coherence and noise.

Declaration

I declare that:

i. the thesis comprises only my original work towards the PhD except where indicated in the preface;

ii. due acknowledgement has been made in the text to all other material used;

iii. the thesis is fewer than 100,000 words in length, exclusive of tables, maps, bibliographies and appendices.

Rory W. Speirs

Acknowledgements

Firstly, a big thank you to Rob. You assembled a group that was a pleasure to work with, and a project that gave me the freedom to do the things which I enjoy. Few PhD students get work in such well resourced labs, which is a direct result of your seemingly unending ability to find funding - even though I know you'd rather be playing in the lab too. I appreciated the sacrifice.

Thanks to the guys in the office. We had more fun - and midweek beers - than we probably ought to have had, but I had a blast. Specifically, thanks to Dan for the stories, Dene for the high fives, Josh for geeking out, Dick for the sick beats, and the guys who visited on exchange for adding some spice to the mix.

Thanks to the postdocs. Corey and Dave, you taught me a bunch about atoms, lasers, and crystals... and style. Alex, those afternoon coffees wrote a large part of this document. Ben, you are a consummate professional, thanks for the help and supervision. Andy, it was always a total pleasure working with you in the lab: you got absolutely perfect tips.

More broadly, thanks to all the members of the School of Physics, you made me feel very welcome, and I'm glad I got to know so many of you.

Of course, thanks to Mum and Dad. What separates us from amoeba is genetics and the environment in which we develop, and you are largely responsible for both.

And finally to my Sara, this would have been no fun without you. We do indeed have fun here.

Contributions

This thesis presents work I was involved with as part of the atom optics group at The University of Melbourne. All work contained within can be considered as having been conducted by me, except where indicated below:

- Experimental apparatus: The Cold Atom Electron and Ion Source (CAEIS) was originally designed and constructed by members of the atom optics group before I arrived. Constant experimental maintenance and changes were made by all other members of the group who were present at some point during my candidature, including Andrew J. McCulloch (AJM), Dene Murphy (DM), Corey T. Putkunz (CTP), Robert E. Scholten (RES), David V. Sheludko (DVS), Ben M. Sparkes (BMS), Richard J. Taylor (RJT), Joshua S. J. Torrance (JSJT) and Daniel J. Thompson (DJT).

- Chapter 4: The body of work presented in section 4.1 was primarily driven by DM. All simulation work in the section was conducted by DM, as were the experimental results in figures 4.1 and 4.2, with assistance from AJM, CTP and DVS. Figures 4.3 and 4.4 were retouched by RES. My contribution was based around experimental design and execution, and analysis of experimental and simulated data.

  Work presented in section 4.2 was primarily driven by DJT. Figures 4.5 and 4.6 were largely produced by DJT and BMS. Experimental results were taken by DJT, BMS, DM, AJM, and myself, and simulations were performed by DJT and BMS. Rick van Bijnen provided software to generate phase masks for the SLM. My contribution was centred around experimental design and execution, and analysis of experimental and simulated data.

- Chapter 5: Many experimental results throughout were taken with the assistance of AJM. Figures 5.2 and 5.4 were retouched by RES. The specific data shown in figure 5.10 was taken by AJM, using a system that was jointly developed by AJM and myself.

- Chapter 6: The specific data shown in figure 6.20 was taken by JSJT. The change to the sample mount that allowed electrical biasing of the sample was designed by AJM.

- Appendix A: The degree of contribution to publications is approximately indicated by the order of the author list.

Table of contents

List of acronyms

2D Two-Dimensional

3D Three-Dimensional

AOM Acousto-Optic Modulator

BNC Bayonet Neill-Concelman

CAEIS Cold Atom Electron and Ion Source

CAES Cold Atom Electron Source

CDI Coherent Diffractive Imaging

CN Conical

CW Continuous-Wave

DC Direct Current

eCDI Electron Coherent Diffractive Imaging

ECDL External Cavity Diode Laser

FFT Fast Fourier Transform

FOLZ First Order Laue Zone

FT Flat-Topped

FWHM Full Width At Half Maximum

GPT General Particle Tracer

GS Gaussian

HIO Hybrid Input-Output

HS Half-Spherical

HV High Voltage

MCP Micro-Channel Plate

MOT Magneto-Optical Trap

MPE Multiphoton Excitation

OBE Optical Bloch Equation

PCI Peripheral Component Interconnect

PSF Point Spread Function

REMPE Resonance-Enhanced Multiphoton Excitation

RF Radio Frequency

RHEED Reflection High-Energy Electron Diffraction

RMS Root Mean Square

RNA Ribonucleic Acid

SE Sequential Excitation

SLM Spatial Light Modulator

TA Tapered Amplifier

TCMPE Two-Colour Multiphoton Excitation

TDG Timing Delay Generator

TEM Transmission Electron Microscope

UED Ultrafast Electron Diffraction

UHV Ultra-High Vacuum

USB Universal Serial Bus

VCO Voltage Controlled Oscillator

XFEL X-ray Free Electron Laser

ZOLZ Zeroth Order Laue Zone

List of figures

List of publications

The following is a list of peer reviewed journal articles that I contributed to over the course of my PhD candidature that are relevant to this thesis. Articles appear in order of degree of my contribution to them, or in order of published date if the level of contribution is equal.

- R. W. Speirs, C. T. Putkunz, A. J. McCulloch, K. A. Nugent, B. M. Sparkes & R. E. Scholten, 'Single-shot electron diffraction using a cold atom electron source', *Journal of Physics B: Atomic, Molecular and Optical Physics* **48**, 214002 (2015). Included in *Highlights of 2015* collection. [Ref. [141], discussed in Ch. 6 and included as Appx. A.1]

- R. W. Speirs, A. J. McCulloch, B. M. Sparkes & R. E. Scholten, 'Identification of competing ionization processes in the generation of ultrafast electron bunches from cold-atom electron sources', *Physical Review A* **95**, 053408 (2017). [Ref. [106], discussed in Ch. 5 and included as Appx. A.2]

- D. Murphy, R. W. Speirs, D. V. Sheludko, C. T. Putkunz, A. J. McCulloch, B. M. Sparkes & R. E. Scholten, 'Detailed observation of space-charge dynamics using ultracold ion bunches', *Nature Communications* **5**, 4489 (2014). [Ref. [59], discussed in Ch. 4 and included as Appx. A.3]

- A. J. McCulloch, R. W. Speirs, J. Grimmel, B. M. Sparkes, D. Comparat, & R. E. Scholten, 'Field ionization of Rydberg atoms for high brightness electron and ion beams', *Physical Review A* **95**, 063845 (2017). [Ref. [131], discussed in Ch. 5 and included as Appx. A.4]

- D. J. Thompson, D. Murphy, R. W. Speirs, R. M. W. van Bijnen, A. J. McCulloch, R. E. Scholten & B. M. Sparkes, 'Suppression of emittance growth using a shaped cold atom electron and ion source', *Physical Review Letters* **117**, 193202 (2016). [Ref. [94], discussed in Ch. 4 and included as Appx. A.5]

- B. M. Sparkes, D. Murphy, R. J. Taylor, R. W. Speirs, A. J. McCulloch & R. E. Scholten, 'Stimulated Raman adiabatic passage for improved performance of a cold-atom electron and ion source', *Physical Review A* **94**, 023404 (2016). [Ref. [180], included as Appx. A.6]

- B. M. Sparkes, D. J. Thompson, A. J. McCulloch, D. Murphy, R. W. Speirs, J. S. J. Torrance & R. E. Scholten, 'High-coherence electron and ion bunches from laser-cooled atoms', *Microscopy and Microanalysis* **20**, 1008 (2014). [Ref. [57], included as Appx. A.7]

Chapter 1

Introduction

Electron diffraction has been a staple technique in structural determination of crystals ever since it was first demonstrated by Davisson and Germer in 1927 [1]. Together with X-ray and neutron based methods [2, 3], electron diffraction has elucidated the structure of many types of materials with atomic resolution. Continued development of real space and diffraction based imaging techniques using electrons and X-rays has resulted in a literal quantum leap in our understanding of all types of materials, both by increasing the range of samples that can be investigated, but also the types information that can be extracted.

One recent advance of particular interest is the development of ultrafast imaging techniques, which promise to illuminate the dynamics of electronic and atomic motion. Ultrafast techniques also offer a route forward for imaging structures that still cannot be determined to atomic resolution, most notably a large fraction of all known biological proteins [4, 5], though cryogenic electron microscopy is making significant headway in this area [6, 7]. Both electron and X-ray based techniques show promise in dynamical imaging, and in macromolecular structural determination, often giving complementary information, with each having advantages and disadvantages for any given problem. The ultimate limit of what can be achieved with ultrafast X-ray and electron imaging is contingent on the outcomes of continued development of X-ray and electron sources, which pose problems both of engineering and of fundamental physics.

This thesis investigates uses and properties of a source of electrons and ions based on photoionisation of a laser cooled atomic gas. The original motivation for developing such a source was to create ultrafast coherent electron bunches that could be used in similar diffractive imaging modalities as ultrafast X-ray pulses. It was also realised that such electron bunches could be ideally suited for injection into the particle accelerators that are currently used to create these

X-ray pulses. In addition to these applications, it has become increasingly clear that ions extracted from cold atom sources may also be applicable in the ever expanding fields of ion microscopy and nano-fabrication, however such continuous ion beams are only briefly touched upon in this thesis.

1.1 Ultrafast X-ray Diffraction

The development of X-ray diffraction techniques first allowed the probing of the structure of matter at the sub-nanometer atomic length scale, and the plethora of techniques now available can be used to determine structures ranging from geological minerals [8] to the complex quaternary structure of biologically produced proteins [9]. However not all materials can be imaged with current X-ray diffraction techniques, which usually require many identical units of the structure being imaged to be combined in a crystal in order to enhance the diffracted signal strength and reduce the radiation damage acquired per unit [10]. The need to crystallise materials is the main impediment to obtaining the structure of biological macromolecules, and in particular membrane proteins, since attempts to crystallise most such molecules either completely fail [11] or result in only micrometer or nanometer sized crystals [12].

Knowing the structure of a material or molecule to atomic resolution by no means implies that the system is fully understood, since it is the dynamical motion of these systems that often results in their most interesting properties. The timescales of these dynamics vary greatly depending on what system is being investigated, with internal motion of proteins happening on the nanosecond to picosecond scale, atomic vibrational motion on the picosecond to femtosecond scale, and motion of electrons being on the femtosecond to attosecond scale [13]. The sub-picosecond *ultrafast* domain has until recently been only accessible by ultrafast pulsed lasers, which when employed in pump-probe type experiments can be used to infer electronic or atomic motion through spectroscopic type measurements [14].

The greatly reduced wavelength of X-rays compared to visible light means that ultrafast X-ray pulses can more directly image the desired system on atomic timescales, making the technique potentially much more flexible than ultrafast optical measurments. While it has been possible to create ultrafast X-ray pulses for some time using laser initiated plasmas [15] or Thompson scattering [16], the more recent development of X-ray Free Electron Lasers (XFELs) enables new types of experiments due to the extreme pulse brightnesses that can be generated

in these devices.

For example, XFEL pulses have been used to simultaneously induce and observe electron dynamics on single femtosecond timescales in Buckminsterfullerenes [17]. They have illuminated intermediate structural changes that occur to photosystem II during optical laser induced photosynthesis [18], and real time switching of Ribonucleic Acid (RNA) structure in response to chemical mixing using serial crystallography [19].

Observing dynamical processes is not the only use for XFEL pulses. The extreme brightness also allows classical diffraction studies to be performed on crystals much smaller than would normally be possible [20]. Diffraction from very small crystals is possible because the high X-ray flux and short pulse length results in sufficient numbers of X-rays scattering elastically from the sample before it is so damaged that the constituent units no longer accurately represent the original structure. The logical limit of solving molecular structures using smaller and smaller crystals is requiring only a single isolated molecule, and performing such experiments is an ambitious goal that requires a different approach to classical crystallography.

1.1.1 Ultrafast Coherent Diffractive Imaging

One proposed solution to solving the structure of uncrystallisable molecules is to illuminate individual molecules one at a time as illustrated in Figure 1.1, and combine the resulting diffraction information. Such a scheme is only possible under two conditions: that sufficient signal is scattered from each molecule so that alignment and averaging can be performed, and that this signal is obtained before the molecule is overly degraded by the beam [21]. In order to fulfil these requirements a single pulse must be both extremely intense, and extremely short [22].

A critical requirement in the proposed single molecule technique is that the beam be *coherent* across the length of the molecule so that the wave diffracted from different parts of the molecule interferes coherently. The coherent diffraction patten then represents the squared modulus of the complex Fourier coefficients representing the original object or molecule. Direct inversion using the detected diffraction pattern is not possible because the relative phase of these Fourier coefficients is lost; the well known phase problem [24]. The technique of CDI uses a variety of methods (often iterative computational refinement) to retrieve the lost phase and so allows reconstruction of the object [25]. Transverse coherence is also

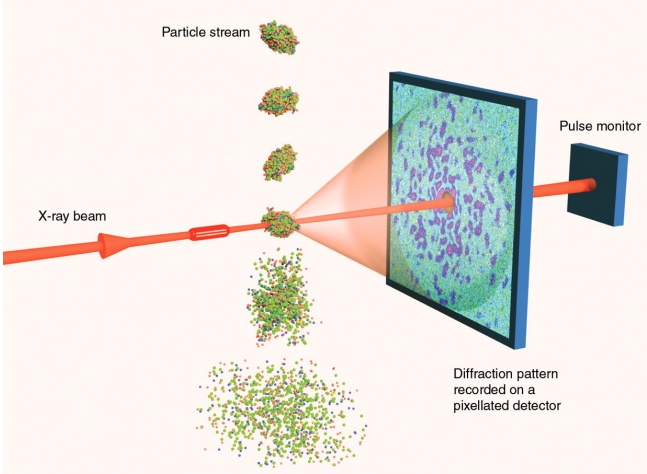

Figure 1.1: Single molecule CDI concept: With sufficiently bright and short X-ray pulses, it may be possible to image a single molecule before it is destroyed. Electrons could also possibly be used as the probing beam. Image adapted from reference [23].

required to some extent for Bragg diffraction obtained in traditional crystallography, and the resulting diffraction pattern also contains no phase information, but the techniques for reconstructing the original object vary considerably between CDI and crystallography.

Femtosecond diffract-before-destroy CDI of micron-scale binary objects has been successfully demonstrated using a single pulse from an XFEL [22], indicating feasibility of ultrafast CDI in general. While a plethora of technical challenges must be overcome before such single-shot, single molecule CDI can be performed, one of the basic problems is that X-rays simply do not interact strongly with atoms - particularly for the light atoms that constitute biological proteins. This problem may be overcome by building ever brighter X-ray sources that can squeeze more and more photons into ever shorter pulses, though it is an open question as to whether or not it is truly possible to outrun the electronic damage that the X-rays impart to the constituent atoms [26].

A proposed alternative approach for such single-molecule CDI is to use electrons rather than X-rays [27]. Electrons interact much more strongly with atoms than X-rays do, in principle allowing much less intense pulses to perform the same task. Electrons also typically deposit less energy in the sample per elastic scattering event than X-rays, potentially reducing the severity of problems associated with sample damage. However electron CDI is still an emerging field, and much work remains to be done before it can be combined with ultrafast electron diffraction techniques.

1.2 Ultrafast Electron Diffraction

Ultrafast Electron Diffraction (UED) is almost exclusively employed in pump-probe type experiments to elucidate electronic or atomic dynamics. The vast majority of these experiments use an optical pulse as the pump, with probe pulses consisting of only a small number of electrons - often less than one on average. Where only a single electron is used, such experiments are able to reveal the dynamics of systems with temporal resolution that is limited only by the timing jitter between the arrival of the optical pulse and the incident electron. Experiments of this nature are applicable only to systems with extremely repeatable responses to the optical pulses, as images for each desired delay time must be built up over millions (or billions) of cycles. Examples of such experiments performed on gas phase samples include observing atomic vibrations in diatomic gases aligned by an optical pulse [28], and identification of short-lived intermediate structures in photo-induced decomposition of organohalides [29]. Dynamic phenomena on the surface and in the bulk of solids have also been observed such as energy transfer from heated electrons to bulk lattice deformation [30], and ultrafast transitions from ordered to amorphous phases of polymer folded-chain crystals registered to free standing graphene [31].

A limitation of using single or few electron pulses in ultrafast diffraction experiments is that the system under investigation must be highly reproducible or insensitive to the pumping and probing beams. Single-shot experiments using high-charge electron bunches are not constrained by the requirement of exact reproducibility, since a single probing pulse delivers all the required flux. The generation of sub-picosecond single-shot diffraction patterns has been demonstrated several times from simple metal foils [32–34], though these are simply proof-of-concept experiments, since no time dependent information is extracted. Observation of ultrafast lattice expansion using multiple single-shots at variable delay times between the pump laser pulse and probing electron pulse has also been demonstrated [35]. While this type of experiment requires far fewer shots than one that uses single electron pulses, it is not fundamentally different since it is assumed that the sample behaves identically for each pump-probe cycle. The potential to extract dynamical information in a true single shot has been investigated through the addition of a post-sample streaking deflector, which can be used to deflect features in a diffraction pattern across the detector as a function of time [36, 37]. The same effect has been achieved using several spatially offset photocathodes which create multiple diffraction patterns that are transversely

translated when imaged at the detector [38].

Whether or not it will be possible to use electrons in single-shot ultrafast coherent diffractive imaging of single molecules or nanocrystals is much more uncertain than for X-rays. As with X-rays, it is not certain that molecular damage can be outrun, though the relative cross-sections of elastic and inelastic scattering are in favour of electrons in that regard [27]. It may also be fundamentally impossible to produce an electron bunch of sufficient brightness because the required density and momentum spread of the electrons within a bunch may exceed that of the quantum degeneracy limit [39]. No source of high-bunch-charge electron pulses approach that limit, so efforts towards achieving single-shot imaging of nanoscale objects are focused on obtaining increases in obtainable bunch brightness, charge, and speed. Significant improvements in these beam properties could drastically change the possible uses for electron bunches even if single-shot, single-molecule imaging is not possible.

1.3 Ultrafast Electron Sources

The first ultrafast electron sources were standard thermionic continuous sources which utilised deflectors supplied with a Radio Frequency (RF) voltage to sweep the beam transversely past a slit. The time of zero deflection occasionally coincided with the presence of an electron at the deflectors, and so electron pulses could be created that contained an average of less than one electron per pulse, where the 'duration' of the pulse was determined by the RF stability and geometrical factors [40].

Modern ultrafast electron sources are almost exclusively based on some form of ultrafast photoemission, leveraging the great advances made in ultrafast laser technology to generate electron bunches with durations on the sub-picosecond timescale. Generally speaking, electrons are generated by illuminating a photocathode material with a short pulse of light with photon energy larger than the material work function or band gap. Photocathodes can be either flat, or tipped in configuration [41], and may be composed of a variety of metallic or semiconducting materials depending on the requirements of average and peak current, photocathode lifetime, pulse duration, and constraints of the illuminating laser. Additionally, spin-polarised electrons can be generated by illuminating strained crystals of gallium arsenide with circularly polarised light [42].

Ultrafast photoelectron sources can be either Direct Current (DC), where electrons ejected by the cathode are accelerated by a static electric field, or RF where

the accelerating field is oscillating at a radio frequency which is synchronised with the arrival time of the optical pulse. Further acceleration can be added to either type of source by downstream RF accelerators, and both have been used for electron diffraction experiments and for injection into particle accelerators [43].

The brightness of solid photocathode sources is limited by the high initial temperature of the electrons produced, typically 10^3 K to 10^4 K [44]. This high initial temperature is a result of the tradeoff between electron temperature and quantum efficiency [45, 46]. If a photon energy very close to that of the work function (or bandgap) is used, the emitted electrons have low excess energy, and so are cold. However using a photon energy that creates electrons with low excess energy also results in an extremely low quantum efficiency, so to generate the desired number of electrons the intensity of the laser pulse must be increased to an extent where it rapidly degrades the cathode.

In addition to the direct brightness reduction caused by high electron thermal energy, a high electron temperature may also hamper attempts to manage the other significant contributor to brightness reduction in ultrashort electron pulses, that of space-charge repulsion.

1.3.1 Space-Charge

The internal electrostatic repulsion of bunches containing more than one electron acts to spread the bunch out in space. An ideal lens performs a linear transformation on the phase space of electrons within a bunch, conserving the emittance, a measure of beam quality. Generally the expansion caused by space-charge repulsion is not that of an ideal lens, and leads to a warping of the electron bunch phase space, increasing the effective emittance, and reducing the brightness. However one class of charge distribution, the hard-edged uniform density ellipsoid, has internal electric field strength that increases linearly with radial position, and thus creates an ideal linear lensing effect which conserves effective emittance [47].

The internal space-charge forces are not the only process working to change the distribution of charge in the bunch. The initial thermal motion of the electrons also affects the distribution of charge as it propagates, which will tend to change an initially hard-edged uniform density ellipsoid into a more diffuse bunch [48]. As the bunch evolves away from the ideal uniform ellipsoidal shape, nonlinear space-charge forces will degrade emittance once again, negating the benefit of the original shaping [49].

There have been many suggestions of how to generate uniform density ellip-

soidal electron bunches with photocathode sources, some of which have been demonstrated experimentally [50]. However achieving an actual reduction in emittance growth using shaped electron bunches generated from photocathodes is problematic, because a high initial temperature of the electrons leads to rapid electron diffusion, destroying the desired shape.

A high initial temperature of generated electrons creates problems with space-charge expansion even if bunch shaping is not employed. To create a low emittance bunch with initially hot electrons requires that the transverse size of the bunch initially be small [51]. But for a given total bunch charge, the smaller the bunch, the larger the space-charge forces that degrade the emittance, so a balance must be struck to minimise the emittance for a particular application.

To decrease the emittance at the time of creation, and to allow for the possibility of gaining a greater advantage by bunch shaping, the initial temperature of the generated electrons needs to be reduced over what is currently possible with photocathode sources. Achieving these goals was precisely the motivation for the development of cold atom electron sources.

1.4 Cold Atom Electron Sources

Cold Atom Electron Sources (CAESs) are effectively photocathode sources that have replaced a solid cathode material with a gas phase target [52,53]. A gaseous cathode has several advantages, the first being that it is possible to get an extremely high quantum efficiency even using photons tuned to liberate electrons with very little excess energy. Such near-threshold photoionisation necessarily creates colder electrons than is possible if the light is tuned to generate electrons with high excess energy [54], ultimately resulting in a lower emittance bunch for a given bunch size and charge. The high quantum efficiency is achieved because of the simplicity of the system absorbing the photon. In metals or semiconductors, an electron may be excited by a photon but fail to be liberated from the surface because of scattering or other interactions with the surrounding atoms. The simple structure of an isolated atom limits the possible outcomes following absorption of a photon to either ionisation or radiative decay, where the probability of the former can be made very close to unity by appropriate laser tuning [55].

Optically induced damage of gas cathodes is not a problem as it is for solid cathodes, so high intensities can be used to ensure large electron yields. While it is true that a gas atom is consumed for every electron that is generated, rapid

and reliable replacement of the gas is implicitly designed into cold atom electron sources, whereas degradation of solid cathode materials gradually reduces the performance of the cathode until it must be replaced [56], which is often a time consuming operation.

The name *cold atom electron source* does not really describe the key features of the source, rather it describes the particular implementation used in experiments in this thesis. The University of Melbourne CAES uses lasers to cool and trap a cloud of rubidium atoms, from which electrons are extracted by near-threshold photoionisation [57]. While cooling and trapping in this way can increase the gas density, improving total electron yield, the fact that the atoms are cold before photoionisation has a negligible effect on the temperature of the liberated electrons. Temperature is a measure of the spread of kinetic energy of the particles, and the kinetic energy of electrons traveling at velocities typical of atoms in a gas at room temperature is very low because of the small electron mass. The main contributor to electron thermal energy is the ionisation process itself [58], which is largely unaffected by the atom cloud temperature, and which is discussed in detail later in this thesis.

The creation of electrons by photoionisation simultaneously creates ions, which are accelerated in the opposite direction to the electrons in the static electric field. Unlike the electrons, the initial temperature of the generated ions is almost completely determined by temperature of the original neutral gas, and is largely unaffected by the details of the ionisation process [59]. Photoionisation of a laser cooled gas therefore results in extraordinarily cold ions, with applications that are potentially as far reaching as the corresponding electron source [60]. Throughout this thesis the system is alternately referred to as either the CAES, or the *CAEIS* (Cold Atom Electron and *Ion* Source), depending on whether it is the electrons or ions that are the relevant subject of investigation. Irrespective of the name used, the system provided a versatile platform from which to investigate a range of atomic, diffraction, and classical beam physics, and all three topics are covered to a varying extent in this thesis.

1.5 Thesis Outline

This thesis covers a range of topics that are relevant to the possible uses of the CAEIS. Chapter 2 describes the experimental implementation of the CAEIS in order to give some context to experiments discussed in later chapters. The level of detail presented varies considerably between different components of the

system, since some elements have been described previously in the theses of former students, while other elements were developed during the course of this project.

Since improved beam quality is the main potential advantage of the CAEIS over other sources of electrons and ions, chapter 3 delves into precisely how beam quality is defined. Section 3.1 summarises the quantities of brightness and emittance, which are commonly used figures of merit when discussing beams of particles, and which are heavily referenced in chapter 4 where intra-beam forces are discussed. Section 3.2 on the other hand introduces quantities taken from the language of statistical optics, such as coherence length. Wave coherence is the natural formalism to use when discussing beam quality in the context of diffraction physics, which is explored experimentally chapter 6.

Chapter 4 covers the affect that intra-beam Coulomb interactions have on the properties of charged particle bunches. Experiments were conducted with ions rather than electrons due to the favourable ion temperature, and the relative ease of creating space-charge dominated ion bunches. Section 4.1 demonstrates some basic effects of space-charge interactions, and also raises some complications that are specific to cold atom electron and ion sources. Section 4.2 covers the successful experimental demonstration of bunch shaping to reduce space-charge induced emittance growth.

In chapter 5, the processes involved in electron generation in a CAES are described, with a particular emphasis on the factors that affect electron bunch duration. A key proposed feature of the CAES is that it should be capable of producing ultrafast electron bunches. Direct measurements of bunch duration were made for a variety of ionisation pathways to determine under what circumstances ultrafast bunch generation is possible. The processes of photoexcitation and field ionisation were investigated independently, and the affect that each process has on both electron bunch duration and temperature is considered. Section 5.3 describes some high resolution Rydberg spectroscopy measurements made on rubidium. These measurements complement the data displayed elsewhere in the chapter, though they are more relevant to the potential use of a CAEIS as a bright continuous ion source rather than a source of ultrafast electrons.

Chapter 6 covers both experimental and theoretical aspects of electron diffraction using the CAES. Section 6.1 describes the first successful experimental electron diffraction experiments performed with our system. Traditional Bragg diffraction was demonstrated both in transmission and reflection modes for a variety of samples. Importantly, single-shot diffraction patterns were demonstrated which required only a single high-charge electron bunch to create a useful

diffraction image. Diffraction patterns were also generated using ultrafast electron bunches, with the duration of the electron bunches validated in the previous chapter. Section 6.2 covers simulations of proposed electron coherent diffractive imaging experiments that should be possible using electrons generated in the CAES. The simulations attempt to be as realistic as possible, using experimentally measured parameters for determining factors like partial coherence, detector noise, and electron intensity. While ultrafast CDI was not achieved experimentally in this project, successful demonstration of Bragg diffraction combined with simulations showing the feasibility of CDI mean that experimental demonstration of such imaging is the next logical step for CAES diffraction experiments.

Chapter 2

The Cold Atom Electron and Ion Source

The core of The University of Melbourne Cold Atom Electron and Ion Source (CAEIS) consists of a Magneto-Optical Trap (MOT) with integrated accelerator electrodes, and a Zeeman slower which loads the MOT. This system core has not changed significantly since it was initially constructed, and is described in detail in the theses of former students from the lab [39, 61–63]. This chapter will therefore not describe the whole system in great detail, but will focus on system modifications and additions that have been made during the course of my PhD project which have allowed the completion of the work described in later chapters. An overview of the whole system is still given to provide context for the detailed modifications and the experiments described later.

2.1 Description of the Source

To generate electron or ion bunches from the CAEIS, the MOT is first rapidly loaded with rubidium atoms using the Zeeman slower (Figure 2.1), then the magnetic fields and laser beams of the MOT and Zeeman slower are switched off. Ionisation of the ground-state cold atoms is achieved using some combination of red 'excitation' and blue 'ionisation' laser pulses, and the electrons or ions are accelerated toward the detector by a static electric field produced by the accelerator electrodes.

When generating electrons, the magnetic fields of the MOT and Zeeman slower must be switched off before ionisation because of the severe deflection that is otherwise caused to the electron trajectories. There is no feasible way to correct this deflection because the non-axial orientation of the MOT causes a large astigmatism in the beam. When ions are desired, the magnetic fields can be left on

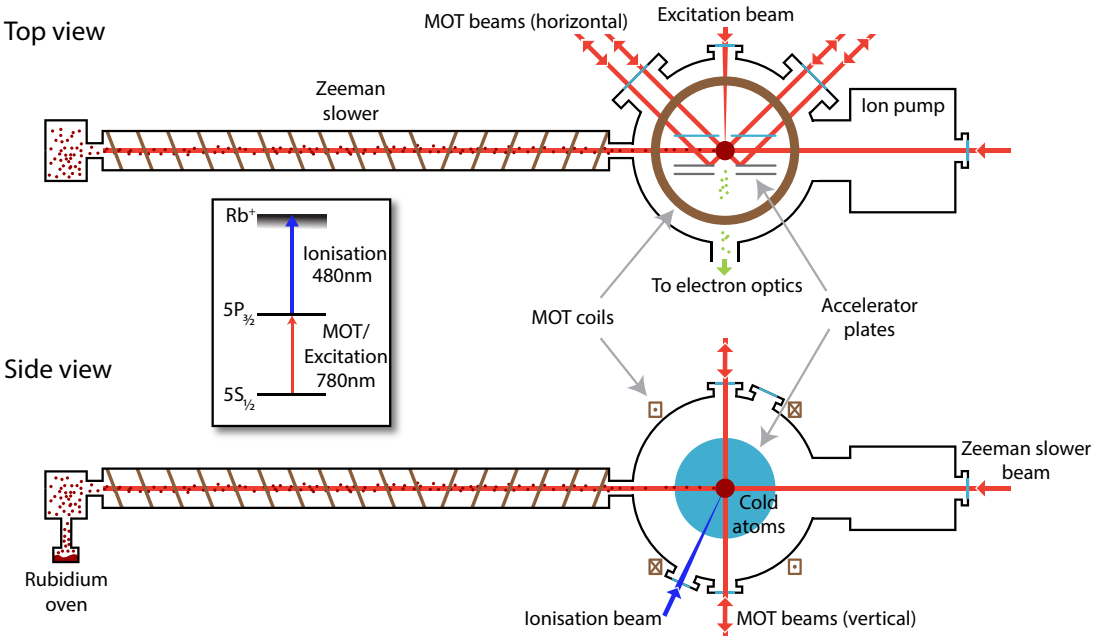

Figure 2.1: The core of the CAES. A rubidium MOT is positioned between accelerating electrodes, and is loaded with a Zeeman slower. Atoms can be ionised in a two stage process (inset), and electrons or ions are accelerated towards additional electron optics (not shown). Only minor modifications to the basic hardware of the cold atom system have been made since its initial construction.

without causing significant deflection due to the much higher ion mass.

2.1.1 Cooling and Trapping Lasers

An array of new experiments required greater reliability and control of the lasers used for the cooling, trapping, excitation, and imaging than was previously achievable. The laser system designed to address specific transitions in rubidium was completely overhauled, enabled in part by the availability of relatively low cost Tapered Amplifiers (TAs) in the 780 nm wavelength range, with output powers of up to 2 W.

One of the main problems with the previous laser set-up was the lack of reliability of the system, which consisted of up to six External Cavity Diode Lasers (ECDLs) independently locked to their own rubidium vapour cells. The loss of lock on any one ECDL would force the experiment to be stopped until the offending laser could be identified and relocked, a situation that substantially affected the rate of progress.

Both the stability and flexibility of the system were addressed in the rebuilt setup. The new design consisted of only two independently locked ECDLs: one

addressing the $5S_{1/2}(F = 3) \rightarrow 5P_{3/2}(F' = 4)$ cycling transition, and the other the $5S_{1/2}(F = 2) \rightarrow 5P_{3/2}(F' = 3)$ repumping transition shown in Figure 2.2.

For the cycling transition, a fraction of the beam was split off and frequency shifted with a single-pass AOM before being used in saturated absorption spectroscopy to lock the laser to a specific frequency [64]. The laser was locked using the $F' = 2/4$ crossover resonance at a detuning of $\Delta = -92\,\text{MHz}$ from the desired cycling transition frequency.

The majority of the laser output beam was passed into a TA, boosting the power from around 50 mW to around 1.5 W. The output of this TA was then split off into separate beams for the MOT, Zeeman slower, excitation (as part of the ionisation system), and absorption imaging. The Zeeman beam was then shifted with a single-pass Acousto-Optic Modulator (AOM) at a fixed frequency before being fibre coupled, but all other beams were shifted using double-pass AOMs so their frequencies could be changed dynamically during an experiment while maintaining beam alignment. AOMs were supplied with an amplified Radio Frequency (RF) signal generated by Voltage Controlled Oscillators (VCOs), which were controlled with an amplified analog voltage originating at a Peripheral Component Interconnect (PCI) based data acquisition and control card in one of the lab computers. Beam power could also be adjusted using voltage controlled variable attenuators positioned between the VCO and the RF amplifier, with the attenuator voltage being controlled by the same PCI card as the VCOs.

The repump transition laser configuration was similar to that of the cycling transition, but with a few small differences. The portion of the beam that was split off for saturated absorption spectroscopy was shifted with a double-pass AOM, and the frequency was locked to the $F' = 1/2$ crossover resonance at a detuning of $\Delta = -78\,\text{MHz}$ from the repumping transition frequency.

The portion of the beam not used for laser locking was amplified with a TA, then a fraction of this amplified beam was coupled directly to the Zeeman slower fibre. The remainder of the beam was first frequency shifted with a double-pass AOM, before being shifted again by one of two single-pass AOMs and coupled into either the excitation beam fibre, or a fibre directed at the MOT. The output of the MOT repump fibre was formed into a hollow beam by first expanding and collimating the beam, and then passing it through a glass window with a small ball of opaque adhesive putty in the centre. The hollow repump beam was used to create a 'dark spot MOT' which can increase peak atomic density [65].

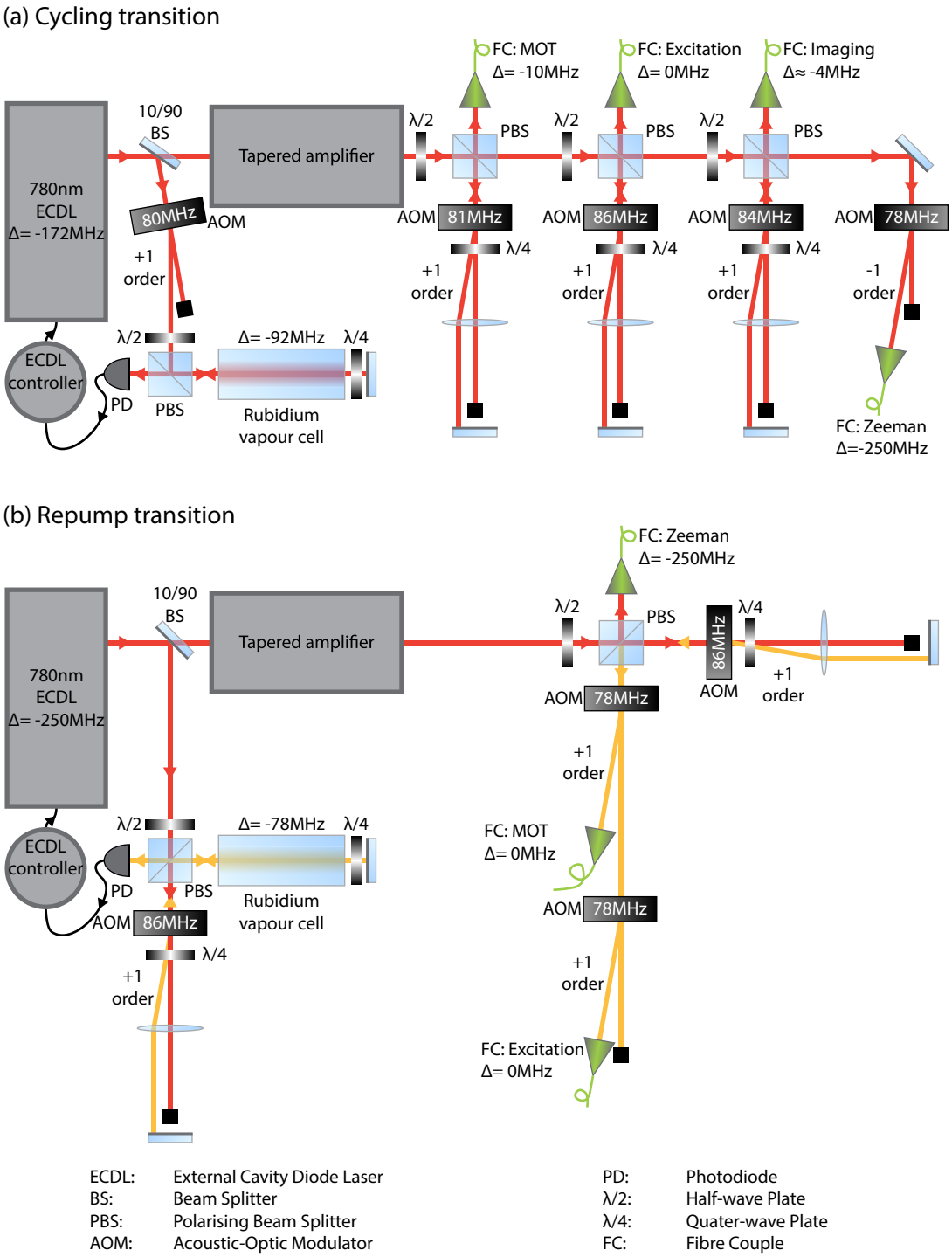

Figure 2.2: Cooling and Trapping lasers. ECDLs frequency locked using saturated absorption spectroscopy are used to generate light addressing the (a) cycling, and (b) repumping transitions. Different beam colour in (b) is used to remove ambiguity about beam route. Not all elements are shown: steering mirrors, optical isolators etc. removed for clarity.

2.1.2 Lasers for Atom Ionisation

The precise modes of ionisation are discussed in detail in chapter 5, but ionisation of rubidium generally required one red photon (wavelength ∼780 nm) and one blue photon (wavelength ∼480 nm), as shown in the inset of Figure 2.1 . For pulsed mode ionisation, blue laser pulses of 5 ns Full Width At Half Maximum (FWHM) duration were generated by a tunable dye laser pumped with a frequency tripled 1064 nm Nd:YAG pulsed laser, at a 10 Hz repetition rate. The energy of the blue laser pulse was up to 10 mJ at the atom cloud, and was focused in either one or both transverse directions, depending on the required intensity and spatial profile.

Continuous electron (or ion) beams could be created using illumination from a continuous blue laser beam. To create the blue light, a beam from a diode laser operating around 960 nm was amplified with a TA, and then frequency doubled. Peak optical power at the atom cloud could be up to 500 mW, and the wavelength was electronically scannable over 0.3 nm without manual adjustment, and was monitored with a wavemeter.

The output port of the fibre-coupled excitation laser beam was directed onto a phase modulating Spatial Light Modulator (SLM) [66]. The SLM imprinted an adjustable phase on the Gaussian beam, which resulted in a desired intensity profile when the laser was focused onto the atomic cloud. The transversely shaped atomic excited state profile could then be ionised with the blue laser, creating an electron (or ion) bunch with arbitrary transverse shape.

Ultrafast Laser

The creation of ultrashort pulses of electrons was achieved using an ionisation scheme that involved photoexcitation with an ultrashort laser pulse instead of illumination with the beam sourced from the cycling transition diode laser. Ultrashort laser pulses were produced using a mode-locked Ti:sapphire amplified pulsed laser, with wavelength range from 770 nm to 830 nm and minimum pulse duration of 35 fs. Such a broad bandwidth is unsuitable for atomic excitation to precise energies, and so a pulse shaper was constructed to select a desired bandwidth and central wavelength.

The temporal profile of an optical pulse depends on the amplitude and phase relationship of its constituent frequency components. Pulse shapers are optical setups that spatially separate the different spectral components of a broadband pulse, alter the relative phase and/or amplitude of each component, and then

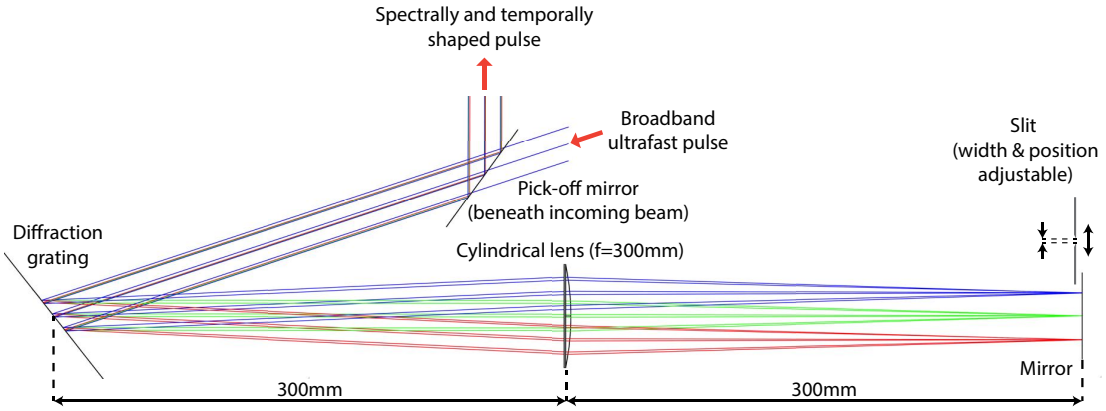

Figure 2.3: The folded 4f pulse shaper. The diffraction grating diffracts different spectral components to different angles, which the lens focuses to separated points in the focal plane. The slit translates to select the central wavelength, and the slit width sets the bandwidth. The spacing between the grating, lens and mirror ensure the outgoing pulse has the same spatial profile as the incoming pulse. A slight tilt of the incoming beam (into the page) means the outgoing beam is spatially offset, and so can be separated with a regular mirror.

reassemble the pulse. The pulse shaper constructed was a folded 4f design [67], with an adjustable slit in the Fourier plane as shown in Figure 2.3. A slit selected the central wavelength and bandwidth of the pulse, but could not alter the relative phase of different spectral components like liquid crystal based retarders [68], limiting the ability to control the temporal shape of a pulse.

For a given minimum slit width, the spectral resolution of the 4f design increases as the focal length of the lens is increased. The maximum usable focal length is set by the horizontal size of the lens, which must be wide enough to transmit the now horizontally spread beam. Using a wide cylindrical lens with focal length of 300 mm, and a precision slit on a translation stage allowed selection the central wavelength and bandwidth of the pulse with 0.2 nm resolution. A slit selects a wavelength range with a sharp cut-off, and if the bandwidth selected is much less than the original 26 nm FWHM, then the spectral density is approximately flat over the selected range.

Assuming a bandwidth-limited pulse, the time domain optical signal can be calculated from the known frequency cutoff values by performing an inverse Fourier transform. In the frequency domain, a rectangular spectral density function is given by a rectangular function of Fourier coefficients at both positive and negative frequencies. The relative phase of each frequency component is set by the relative values of the real and imaginary numbers that make up each coefficient. Assuming that all coefficients are purely real as in Figure 2.4(a) amounts to assuming the carrier electric field is in phase with the intensity envelope at the

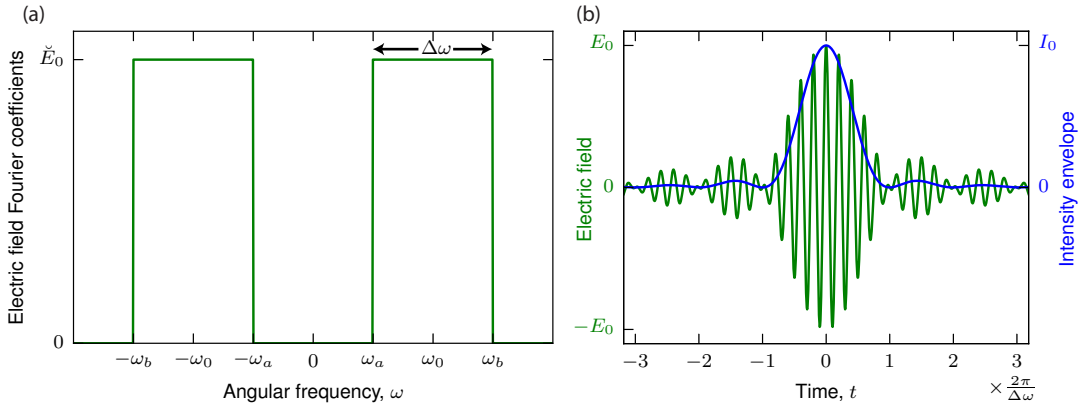

Figure 2.4: Pulse shaping with a slit. (a) A rectangular spectral density as selected by a single slit is represented by rectangular function of both positive and negative Fourier coefficients. (b) The temporal duration of the reconstructed pulse depends on the selected bandwidth.

pulse centre, which is not necessarily the case experimentally, but which simplifies the calculation. This Fourier signal is represented functionally by:

$$\breve{E}(\omega) = \begin{cases} \breve{E}_0, & \text{for } -\omega_b \leq \omega \leq -\omega_a \text{ and } \omega_a \leq \omega \leq \omega_b \\ 0, & \text{otherwise,} \end{cases} \tag{2.1}$$

where $\breve{E}$ has units of $\mathrm{Vm}^{-1}\mathrm{s}$. The resulting time domain electric field is given by:

$$E(t) = \frac{2\breve{E}_0\Delta\omega}{\sqrt{2\pi}} \operatorname{sinc}\left(\frac{\Delta\omega}{2}t\right)\cos\left(\omega_0 t\right), \tag{2.2}$$

where the bandwidth is given by $\Delta\omega \equiv \omega_b - \omega_a$, the central frequency is $\omega_0 \equiv (\omega_a + \omega_b)/2$, and the Fourier transform convention adopted is given in equation 3.24.

For a monochromatic electromagnetic wave, the intensity is given by $I = \frac{c\epsilon_0}{2}E_0^2$ [69], where c is the speed of light, and ϵ_0 is the permittivity of free space. So for small bandwidth pulses, the time-varying intensity is approximately:

$$I(t) \approx \frac{c\epsilon_0}{\pi}\left(\breve{E}_0\Delta\omega\right)^2 \operatorname{sinc}^2\left(\frac{\Delta\omega}{2}t\right), \quad \Delta\omega \ll \omega_0. \tag{2.3}$$

The resulting electric field and intensity envelope is visualised in Figure 2.4(b). The FWHM time-bandwidth product for the intensity of such a pulse is given by $\Delta\omega\Delta t = 5.57$, which can be compared to the much lower product given for a pulse with a Gaussian spectral density of $\Delta\omega\Delta t = 0.44$. The large difference in time-bandwidth product is to be expected because the FWHM measure of a rectangular spectral density encompass *all* the component frequencies, whereas a

Gaussian has a significant fraction of its total spectral energy beyond the FWHM boundaries, which help to localise the time-domain signal. In fact, using the standard deviation of bandwidth and time rather than FWHM, a Gaussian has the smallest time-bandwidth product possible, whereas the product becomes infinite for a rectangular spectral density because the standard deviation of the sinc^2 function is infinite, just like that of a Lorentzian function.

A calibration between slit position and wavelength was achieved by measuring which positions corresponded to the known wavelengths for the $5S_{1/2} \rightarrow 5P_{3/2}$ and $5S_{1/2} \rightarrow 5P_{1/2}$ transitions in rubidium. The positions corresponding to these transitions was found by observing the electron signal produced when the output of the pulse shaper illuminated the atomic cloud together with a pulse of blue light of appropriate wavelength.

The pulse shaper was modelled in a simple ray-tracing program, *Beam4* [70], which allowed the effects of certain misalignments to be identified and corrected in the real setup. Only the first order diffracted beam of both the incoming and outgoing beams were used, such that the output pulse contained only around one third the energy of the input pulse, even without the slit inserted in the system. Energy losses could have been significantly reduced using a blazed grating rather than a holographic one, but there was never a problem with insufficient energy: neutral density filters were still needed to further attenuate the beam.

A significant problem with the folded setup as opposed to the straight version (which uses a second lens and grating rather than a mirror), is the tendency of diffuse scatter off the slit to be refocused into the beam. This occurs because the lens and mirror are in a cateye configuration [71], which correctly refocuses the light into the beam irrespective of its reflected angle. Even a tiny amount of light at a wavelength that isn't deliberately selected can be a problem in ionisation experiments, because the transition probability of the atoms can be non-negligible when exposed to very small intensities of on-resonance light. To remedy the problem of back scattered light, black fabric with a small slit cut in it was stuck to the front of the slit assembly. While this did reduce light scattered back into the beam, resonant excitation could still be observed even when the slit was completely closed. Finally, the black cloth and slit assembly were coated in a layer of black soot by holding them above burning tissue paper soaked in lubrication oil. The low sheen, highly absorptive finish removed all observable trace of back-scattered light, though occasional re-coating was necessary if the surface became dirty, or the high power laser pulses damaged the coating.

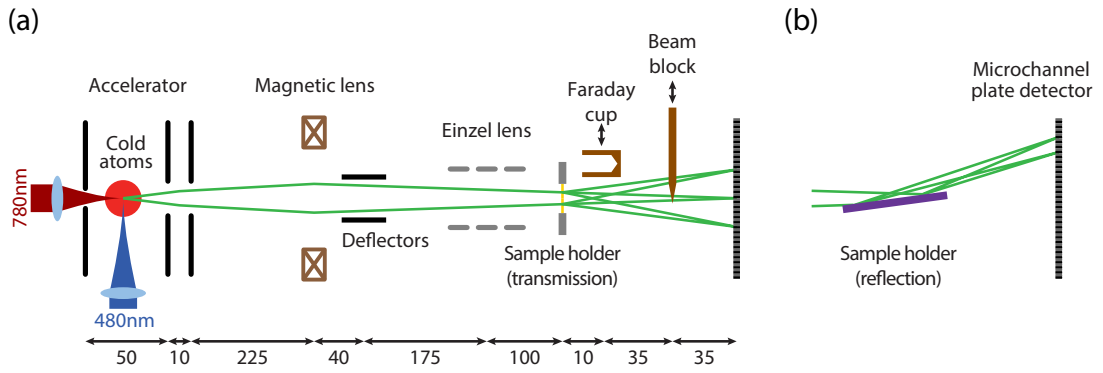

Figure 2.5: Electron optics in the CAEIS. (a) Shows most components along the column, with the sample holder being used for transmission electron diffraction. The sample holder could also be translated and rotated as shown in (b), enabling reflection electron diffraction. Distances are in millimetres.

2.2 Description of Electron Optics and Measurement Tools

The layout of electron optics along the electron/ion beamline is shown in Figure 2.5. Initially the optics consisted of the accelerator, deflectors, sample holder, and Micro-Channel Plate (MCP), which are described in earlier theses. Additional components were added over the course of the project, and some existing components were significantly modified to improve performance. The new or modified components are described below.

Magnetic lens

While the original electrostatic Einzel lens could successfully focus both electrons and ions, the close proximity to the sample holder and large distance from the source, made it unsuitable for the simple electron diffraction geometry shown in Figure 2.5, which is discussed in more detail in chapter 6. An additional problem when using the Einzel lens with the electron beam was that the electron bunches never travelled exactly down the central axis of the column. The deflection away from the axis was caused by the decaying MOT magnetic field, which had a characteristic decay time of a few milliseconds after the coils were switched off. The non-axial propagation of the electron beam resulted in the Einzel lens forming a poor focus due to the increased effect of lens aberrations away from the central axis. To remedy the problems of both diffraction geometry, and non-axial propagation, a solenoid magnetic lens was designed and constructed.

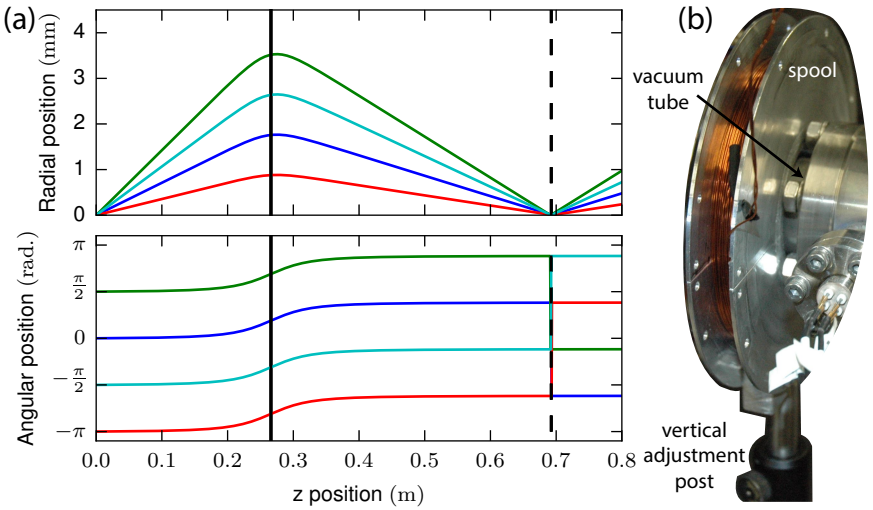

Figure 2.6: Magnetic lens development. Particle tracking simulations were used to determine the required solenoid parameters. The trajectory of four test electrons is shown in (a). The solid vertical line indicates the position of the lens, and the dashed line indicates the position of the MCP. (b) Shows the installed lens, including the mount that allowed vertical adjustment. Horizontal alignment was provided by a translation stage (not shown).

The solenoid was positioned as close to the accelerator as practically possible, resulting in a smaller more collimated beam at the sample as required for diffraction experiments. The lens was also external to the vacuum system, and was designed to be transversely translatable, so that it could be centred around the beam even if the beam was not centrally positioned inside the vacuum tubes. To enable translation, as well as initial winding of the solenoid, a spool was designed in Solidworks, which would fit around a narrow section of the vacuum tube in the desired position in the column.

The electric current and number of turns required to achieve focusing of electrons was determined by simulation with classical particle tracking code. In this simulation, the solenoid was made up of a set of circular current loops with radii and position reflecting the realistically achievable packing for 0.8 mm diameter wire. It was found that using 540 loops, at a current of 1.08 A, the electrons would come to a focus at the detector as shown in Figure 2.6(a). Given the known resistance of the wire, this was calculated to require a power supply of 13.3 V, and would generate 15.3 W of heat, which was estimated to be low enough not to require any active cooling.

The particle tracking code was self-written, and used the fifth-order Dormand-Prince adaptive step Runge-Kutta method [72] to integrate the non-relativistic equations of motion which incorporated the Lorentz force. At every timestep

the magnetic field components at the position of each simulated electron were calculated for all of the current loops individually. At a given position, the field from each loop was calculated using an analytic expression [73], providing confidence that the particle trajectories were correct even far away from the central axis, where approximations of magnetic field from a solenoid can become less accurate.

When the lens was installed and wound as shown in Figure 2.6(b), the focusing performed as expected taking into account the uncertainty in the actual number of wire turns used, which was estimated from the cross sectional area of the windings. It was not necessary to know the exact number of turns, and counting them during the winding process would also produce only an approximation of the resulting magnetic field, because the radius of each turn could not be measured accurately during winding. When experimentally producing non-circularly symmetric electron bunches, rotation of the electron bunch about its propagation axis was observed, as predicted by the simulated trajectories shown in Figure 2.6(a). The desired radial focusing of the electrons by a solenoid is a secondary effect, induced by the Lorentz force as a result of this rotational movement.

Sample holder

The original sample holder shown in Figure 2.7(a) was a small paddle on which three 3.05 mm Transmission Electron Microscope (TEM) samples could be mounted. This paddle was attached to a rod that could be translated several centimetres in one direction transverse to the beam axis, and around two centimetres in the other two dimensions. The rod (and attached sample holder) could be also be rotated around one axis.

Having access to only three samples at a time was less than optimal, because changing them meant exposing the sample chamber to atmosphere, which would then take two days to pump back down to an acceptably low pressure. However the most significant problem with the holder was that the dimensions of the surface facing the beam were smaller than the MCP, and allowed charged particles that were not part of the primary beam to strike the MCP, resulting in a significant background signal which can be seen in Figure 2.7(b).

A new sample holder was created both to hold more samples, and to block all charged particles coming from the accelerator that were not part of the primary beam. The holder was again a paddle design as can be seen in Figure 2.7(c), but it incorporated two commercially produced elements designed to mount four

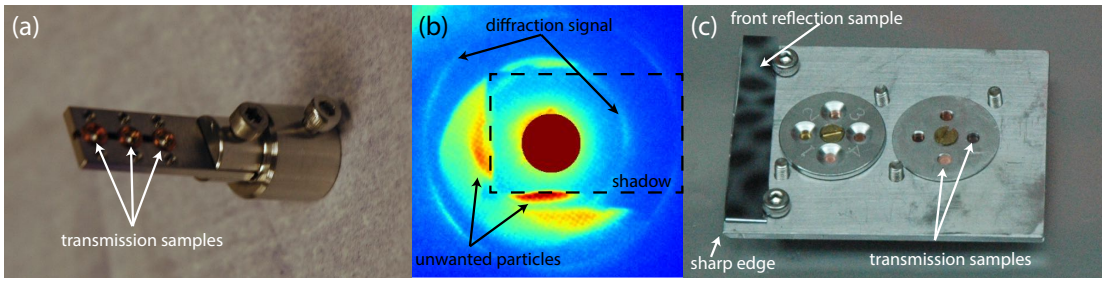

Figure 2.7: Sample holder upgrade. (a) Original sample holder: only three samples at a time could be mounted. (b) Diffraction image using the original sample holder: Unwanted charged particles that were not part of the primary beam were only partially blocked, casting a rectangular shadow. (c) The new sample holder: Eight transmission samples could be mounted, along with two reflection samples - one front (shown on left) and one back. The left edge was sharpened for use in scanning knife edge experiments.

3.05 mm TEM samples inside scanning electron microscopes. The paddle size was significantly increased to block unwanted components of the beam, and the leftmost edge (in the image) was sharpened so it could be used in knife edge measurements. This edge had small alignment notches filed into it to allow individual samples to be easily located. Sections of crystal wafer could also be mounted flat on the paddle, which is also visible in Figure 2.7(c), to act as grazing incidence reflection electron diffraction targets when the paddle was rotated to a horizontal orientation.

Faraday cup and beam block

To measure the absolute charge of the electron and ion bunches, a Faraday cup was constructed and installed in the system. The cup itself was a piece of copper rod with a 5 mm diameter hole in it, drilled 18 mm deep, and can be seen in Figure 2.8. The deep and narrow design ment that any secondary charges ejected from the inner surface of the cup due to the impact of the primary electron or ion beam would be recollected, thus ensuring that the measured output current represented the true beam current. The cup was coated in graphite using a colloidal suspension (*Aquadag*) to prevent any insulating oxidised regions from becoming electrically charged and repelling primary or secondary charges which could also affect the measured current. The cup was mounted in a holder using thin polyimide film (*Kapton*) to insulate the two, and electrically connected to an Ultra-High Vacuum (UHV) safe coaxial cable. The shielding of the cable was connected directly to the cup mounting assembly.

The beam block was a simple rod designed to block the intense zeroth order beam in diffraction experiments so as not to overly saturate the MCP (Fig-

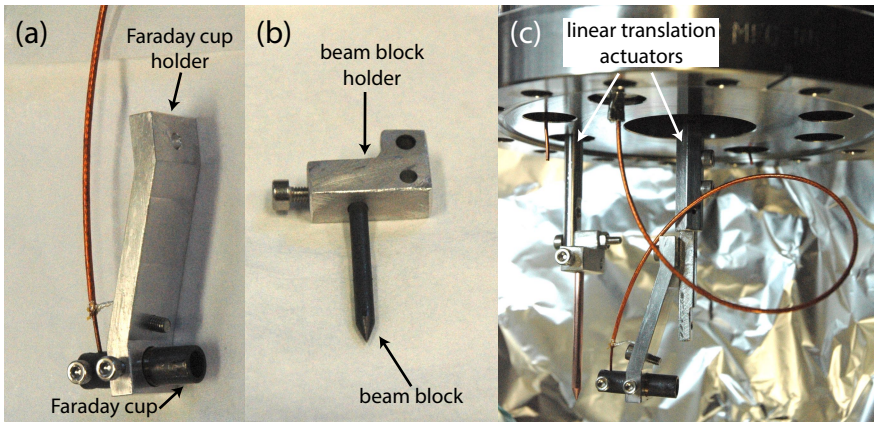

Figure 2.8: Faraday cup and beam block. (a) The Faraday cup is insulated from its holder with Kapton film, and electrically connected with small gauge coaxial cable. (b) The beam block is a copper rod with a holder that transversely positions it over the centre of the beam. (c) The Faraday cup and beam block are connected to linear translation actuators so they can be lowered in front of the beam.

ure 2.8(b). The rod shown in that image was coated in *Aquadag*, though it was replaced with a bare copper rod when it was found to be too short. The mount was designed to horizontally centre the rod over the beam, since the linear translation mount was offset slightly.

Both the Faraday cup and the beam block were mounted on linear translation manipulators so they could be moved in and out of the beam as shown in Figure 2.8(c). The Faraday cup holder offset the cup slightly along the beam direction to make room for the sample holder. The coaxial cable from the Faraday cup was connected to a Bayonet Neill-Concelman (BNC) feedthrough, and then connected to a *Femto - DDPCA-300* low-noise transimpedance amplifier with an adjustable gain up to 10^{13} V/A. To measure the charge of an electron or ion bunch, the time constant of the amplifier was set to 5 s, and the per pulse charge determined from the average current.

Microchannel plate

Transverse spatial profiles of the electron and ion beams were detected using a phosphor-screen-coupled MCP assembly, which was imaged with a camera. The original camera had a slow mechanical shutter and very slow readout time, so averaging over many electron pulses required single exposures long enough to encompass several electron bunch impacts, which repeated at 10 Hz. Averaging in this manner increased the background signal since it was being integrated during the time between the desired electron pulses, and also prevented observation of any shot-to-shot variation of the bunches.

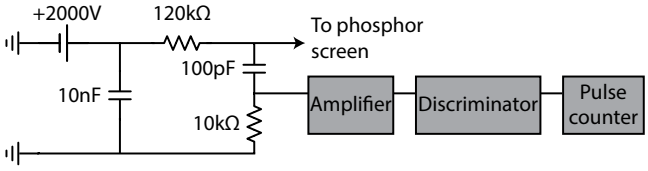

Figure 2.9: Capacitive coupling circuit for electron/ion counting at the MCP/Phosphor assembly. High voltage capable capacitors transmit the short voltage spikes initiated by single electron or ion impacts on the MCP. The spikes are amplified, filtered, and counted.

This slow camera was replaced with a *Point Grey - Grasshopper* CCD camera with electronic shutter, able to take complete images at frame rates in excess of 10 Hz, so averaging could be achieved by a post processing addition of successive images. The exposure duration was set to 4 ms: equal to the duration of optical output from the phosphor in response to a nanosecond duration incident electron bunch. An electronic signal triggered the exposure just before electron or ion impact at the MCP.

The MCP could also be used to electronically detect individual electron or ion impacts if the impact rate was sufficiently low, such as when the CAEIS was used to produce a continuous or quasi-continuous electron or ion beam. The phosphor screen acted as the anode to the cascade of electrons produced by each electron or ion impact on the MCP, so every impact resulted in a small voltage spike at the phosphor electrical input. This signal was separated from the high voltage phosphor supply using a custom capacitive coupling circuit (Figure 2.9), before being amplified with an *Ortec - 474 Timing Filter Amplifier* and fed into a discriminator (*Ortec - 436 100* MHz *discriminator*). The output of the discriminator was then passed to a counter on a *National Instruments - 6229* PCI interfaced data acquisition card.

Using the MCP in electronic counting mode sacrificed the spatial information about the electron/ion beam available when using the camera, but allowed versatile and robust measurement of relative current in continuous beams. This was particularly useful in the spectroscopy experiments presented in section 5.3, where spatial information was not required, but the reduced data volume and acquisition time of the counting system allowed higher resolution scans to be achieved.

Timing and synchronisation

When operating the system in 'regular excitation' mode, the cold atoms were ionised by first exciting them to the $5P_{3/2}$ state with light from the cycling tran-

sition diode laser. This beam was switched with an AOM, and illuminated the atoms continuously for a few hundred nanoseconds before the 5 ns pulse of blue light ionised the excited atoms. Timing stability in this mode was non-critical because the excitation beam continuously illuminated the atoms for hundreds of nanoseconds before and after the blue pulse passed through, so variable arrival time of the blue pulse of up to a hundred nanoseconds did not noticeably affect the results of the experiment. System timing was handled solely by a single *SpinCore - PulseBlasterPlus!* Universal Serial Bus (USB) interfaced pulse generator, which had an instruction timing resolution of 10 ns and sub-nanosecond timing jitter between instructions.

System timing became more complicated and less resistant to jitter when the ultrafast laser was used in the ionisation process. In this mode, it was critical that the ultrafast laser pulse (which was usually subpicosecond in duration) intersected the 5 ns blue pulse as it passed through the atomic cloud. The timing jitter of this intersection had to be significantly shorter than the duration of the blue pulse itself to avoid shot-to-shot variations in relative intensity of the ultrafast and blue pulses.

In the 'ultrafast excitation' mode, the timing critical elements were handled by the Timing Delay Generator (TDG) of the femtosecond laser system. The electronics in the TDG are clocked using the signal from a photodiode inside the laser oscillator itself, so electronic outputs are synchronised to the optical output of the laser, allowing for very low jitter. One of the electrical outputs of the TDG directly triggered the Q-switch on the blue laser pump, ensuring that the blue laser pulse and ultrafast laser pulse always arrived at the same time. Coarse timing adjustments in increments of 10 ns could be made via the TDG software, but finer adjustments were made by introducing or removing lengths of BNC cable to the triggering lines. The same TDG electrical output also triggered the *PulseBlaser* (which controlled all other timed system hardware), but the signal traveled via a separate delay generator in order to get the timings correct. The delay generator and the *PulseBlaster* introduce a jitter of around 10 ns each since they use digital processors with their own internal oscillators running at 100 MHz, and so are not synchronised to each other or the master laser oscillator. As such, no timing critical devices could be triggered from the *PulseBlaster*.

Aside from the Q-switch trigger, the only other timing critical components utilised were the electrical switches controlling the voltage on the deflector plates used in electron streaking experiments (discussed in chapter 5). In these experiments, two high-voltage switches swept the potential on deflector electrodes such

that the electron beam obtained a time-dependent transverse momentum kick, creating a streak on the imaging detector with length dependent on electron pulse duration.

The sweep time of the switches was about 10 ns, with an acceptable jitter of less than 1 ns between switching start time and electron bunch arrival. Both switches were triggered by a signal originating from a single TDG output, however signal conditioning circuits were designed and constructed to interface the low voltage TDG signal to the higher voltage required by the solid-state High Voltage (HV) switches. The circuits (shown in Figure 2.10) included physical delay lines to adjust relative switch-on time, a gating signal to reduce the switching frequency because the TDG output had a non-adjustable repetition rate of 1 kHz, and an inverting circuit so the switches could be made to ramp in opposite directions. The input to the HV switches was set high using a 50 Ω pull-up resistor, and was pulled low when the transistor was activated. Another 50 Ω resistor was placed in parallel to the transistor to ensure rapid, interference-proof switching. The supply voltages were connected to the HV switches via series resistors, with different values for the positive and negative sides. The asymmetry in the series resistor values allowed for faster, smoother ramping in one direction, so the electron bunches were always streaked using this transition direction.

The spectroscopy experiments discussed in chapter 5 were controlled in 'software time', rather than preloading instructions into devices which were then triggered, as was the case for all other experiments. The spectroscopy experiments involved measurements of a continuous, rather than pulsed beam, making timing constraints significantly more relaxed. Software timing allowed for flexible interfacing with an array of hardware over heterogeneous protocols, and simplified the process of automating experimental scans over large parameter spaces.

2.3 Summary

This chapter presented a general description of the core hardware components of the CAEIS, along with a summary of some of the procedures involved in generating, measuring, and manipulating the cold electrons and ions. While there are innumerable peripheral devices and procedures required to perform experiments involving the CAEIS, the level of detail provided here should be sufficient provide context for work described in later chapters.

Chapter 1 gave a general motivation for *why* cold electrons and ions are desirable in a number of applications, and the present chapter has described *how*

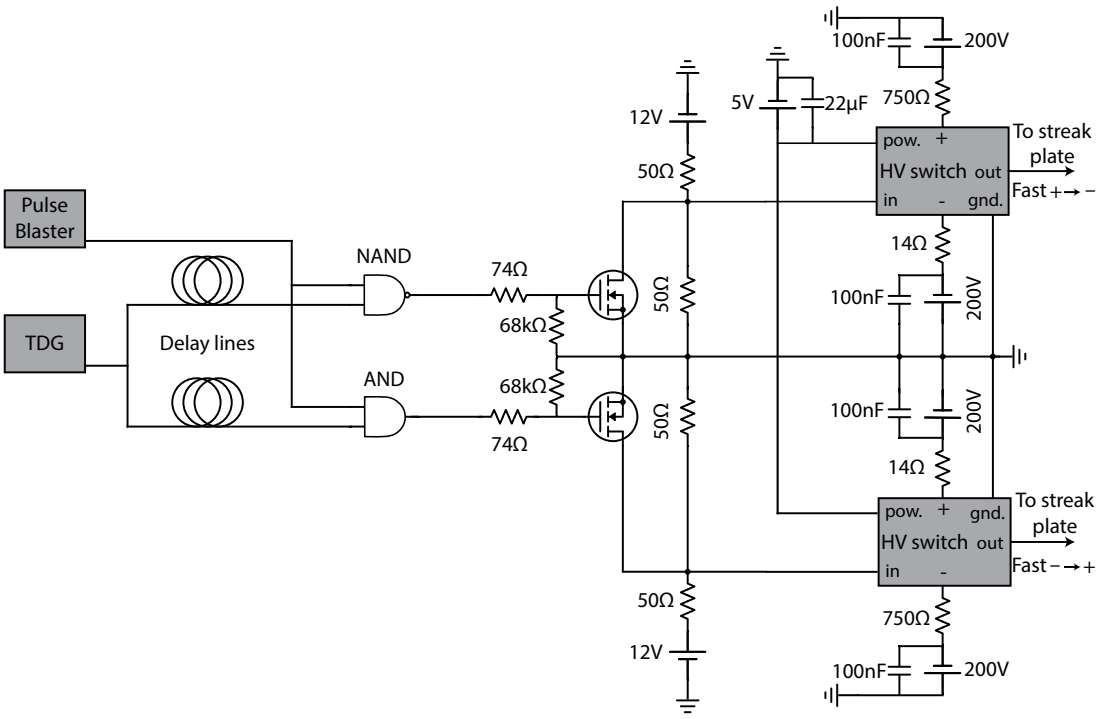

Figure 2.10: Electron streaking electronics. The voltage on the streaking deflectors is swept in response to a trigger signal originating at the TDG. The signal is delayed appropriately, gated (and inverted for one of the two switches), and then activates transistors which pull down or release the HV switch signalling line. The pair of HV switches then rapidly sweep the voltage on the deflectors in opposite directions.

these cold charged particles can be generated using the CAEIS. The next chapter describes more precisely *what* it means for charged particle beams to be cold, and presents the formalism used to describe and measure the quality of these beams.

Chapter 3

Beam Theory

The main motivation behind development of the Cold Atom Electron and Ion Source (CAEIS) is that, all other beam properties being equal, it can potentially generate both ultrafast electron pulses and continuous ion beams with better transverse properties than can be achieved with the current generation of sources. This chapter presents an overview of the tools used to describe transverse beam quality, including brightness, emittance, and coherence.

Section 3.1 presents typical measures used to characterise beams of particles, such as brightness and emittance. Unfortunately, a multitude of different definitions exist for such quantities, so definitions presented here will serve to define the meaning of values quoted in later chapters. Section 3.2 presents a summary of coherence theory from the perspective of statistical optics, and section 3.3 briefly describes how this coherence theory can be combined with Fourier optics to calculate the diffraction patterns expected when using partially coherent beams, which is referenced extensively in the context of Coherent Diffractive Imaging (CDI) in chapter 6.

Unless otherwise stated, the beam quality metrics discussed in this chapter refer to the transverse properties of the beam. While the longitudinal beam properties are no less important, the electron diffraction experiments performed with a Cold Atom Electron Source (CAES) are less critically dependent of the longitudinal metrics, so a discussion of these properties is kept to a minimum.

3.1 Measures of Beam Quality

One of the most informative metrics of a source of radiation (be it particles or waves), is the brightness $\mathscr{B}$, because it combines information about the beam

current, size, and angular spread [74]:

$$\mathscr{B} = \lim_{\mathrm{d}\Omega\to 0}\lim_{\mathrm{d}S\to 0}\frac{\mathrm{d}I}{\mathrm{d}S\mathrm{d}\Omega}. \tag{3.1}$$

This equation states that brightness is found from the current I, which passes thorough an area element perpendicular to the source $\mathrm{d}S$, with incident angles encompassed by the solid angle $\mathrm{d}\Omega$. The quantity $\mathrm{dI}/\mathrm{d}S$ is proportional to the intensity at any point, and $\mathrm{d}\Omega$ is related to the divergence σ_θ, of the beam at that point. Brightness of a beam is fixed by the brightness of the source (under linear transformations, which are discussed later), so does not change, irrespective of how far from the source it is measured.

There are two angular measures needed in the description of a beam as it propagates through an optical system which are referenced heavily in later chapters. Beam semiangle describes the focusing angle of the beam, which is changed by optical elements like lenses or space-charge repulsion. It is measured from the beam axis to some characteristic angle representing the angular spread of all particle trajectories about this axis. Beam divergence however, is a measure of the angular spread of particle trajectories passing through a single point. Divergence angle changes depending on where in a beam it is measured, but beam semiangle does not (so long as there are no optical elements affecting the beam), and the difference between the two measures is illustrated in Figure 3.1. The particular characteristic angle used to define semiangle and divergence can vary, and does not give full information about the shape of the distribution of particle trajectory angles, as is also shown in Figure 3.1.

A frequently used measure of beam quality that doesn't take into account particle current, is beam emittance, ϵ. Emittance determines the focal spot size for a non-self-interacting beam passing through an ideal achromatic lens. The emittance can be defined in both the x and y directions (where the beam is assumed to be heading in the z direction) as the product of beam divergence and diameter, $\sigma_{x,y}$, at a given point:

$$\epsilon_x = \sigma_x\sigma_{\theta_x}, \qquad \epsilon_y = \sigma_y\sigma_{\theta_y}. \tag{3.2}$$

Because both the angular and spatial distribution of particles in the beam is often non-uniform, the Root Mean Square (RMS) values of the quantities in equations 3.2 are usually used in order to get some characteristic value for the beam. However if more detail about the beam is required, it is necessary to describe the beam's phase space profile.

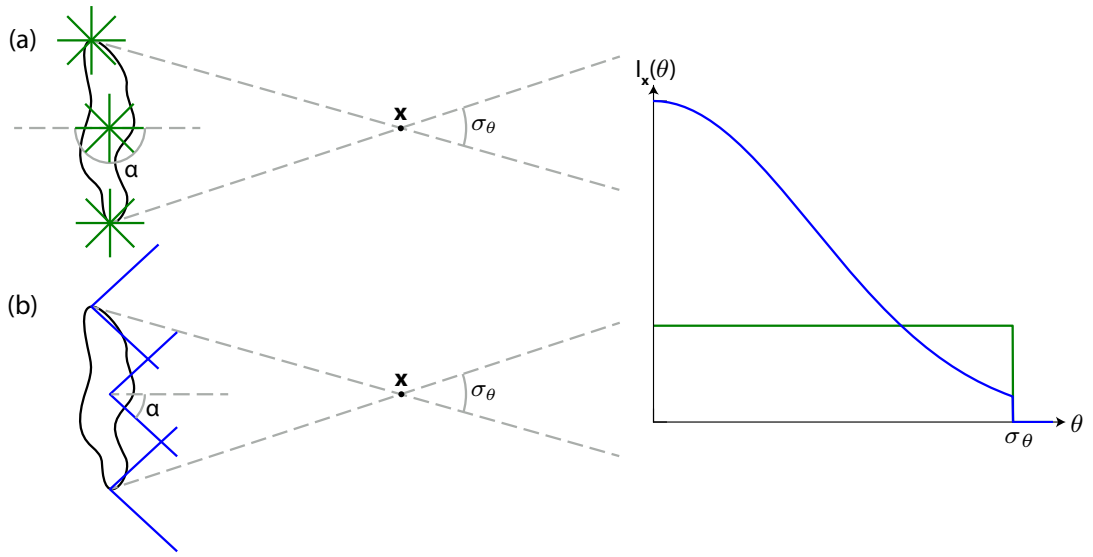

Figure 3.1: Beam semiangle and divergence description. Semiangle, α, is a measure of angular spread of all particles in the beam and determines the rate at which the beam changes diameter. Divergence, σ_θ, is a measure of angular spread of particles that pass through any given point (eg. point $\mathbf{x}$), and so can change depending on where it is measured. (a) shows the source of a beam with much higher semiangle than in (b), but the divergence at $\mathbf{x}$ is the same if the maximum particle angle is used. However the flux of particles I, passing through point $\mathbf{x}$, at a given angle θ, is very different for the two sources, as can be seen from the graph at the right.

Each particle in a beam has some momentum and position which occupies a place in a six dimensional phase space. For reasons of clarity each direction is usually plotted separately, and for circularly symmetric beams, information about transverse beam quality can be conveyed by plotting only one direction (eg. x, p_x). A typical phase space profile for a beam propagating through a lens can be seen in Figure 3.2. In a well-behaved beam, all particles will lie in an ellipse in phase space, where the area of the ellipse is equal to the emittance. The thinner this ellipse is, the more the phase space profile approximates a single straight line, and the lower the emittance.

If the phase space of a beam could be changed arbitrarily, it would make little sense to talk about beam quality since any beam could be made into any other. However most practical optical elements such as lenses or free propagation are limited to performing linear transformations of the phase space, examples of which are shown in Figure 3.2.

Effects like Coulomb repulsion and lens aberrations can cause non-linear transformations, warping the phase space profile to a non-ellipsoidal shape. Even if this warping does not increase the area of the bunch phase space, it can adversely affect experimental parameters such as minimum focal spot size when a regular

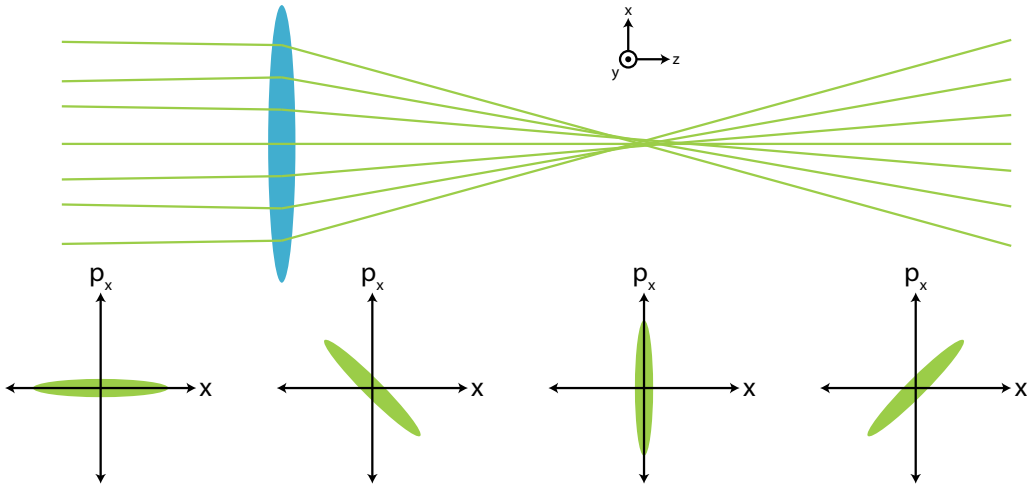

Figure 3.2: Phase space description of a beam of particles. Particles propagating through an ideal lens (top) undergo a series of linear transformations of the phase space profile (bottom). The beam emittance is constant under these transformations.

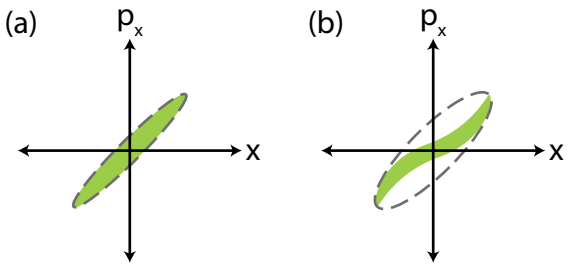

Figure 3.3: Difference between true and effective emittance. The beam in (a) has an elliptical phase space distribution, so characteristics like focal spot size are determined by its true emittance. In (b) the phase space profile is warped, so focal spot size is determined by its effective emittance (area of ellipse with grey dashed outline).

linear lens is used.

Where the beam has a warped phase space profile, a measure that better characterises immediately accessible beam properties is effective emittance, which is given by the area of an ellipse of best fit of the profile. The best-fit ellipse will necessarily have a larger area, and so realistically reflects the degradation in beam quality caused by non-linear transformations. The difference between true emittance and effective emittance is illustrated in Figure 3.3.

A multitude of different definitions exist for brightness and emittance, however they generally have a similar form to the following definitions, which are used throughout this thesis. For a non-relativistic beam of particles, where $p_x \ll p_z$, RMS emittance can be calculated from:

$$\epsilon_x = \frac{1}{\langle p_z \rangle} \sqrt{\langle x^2 \rangle \langle p_x^2 \rangle - \langle x p_x \rangle^2}, \tag{3.3}$$

where the angled brackets denote an average over the entire ensemble of particles. RMS brightness can then be calculated from the emittance using:

$$\mathscr{B} = \frac{I}{4\pi^2 \epsilon_x \epsilon_y}. \tag{3.4}$$

Many definitions of brightness also count only the current of particles with energy within some threshold range, or explicitly include energy spread in the denominator of equation 3.4.

The final quantity presented in this section is the transverse coherence length, ℓ_c, which can be defined in terms of the beam divergence [75] as:

$$\ell_c = \frac{\lambda}{2\pi\sigma_\theta}, \tag{3.5}$$

where λ is the de Broglie wavelength of the particle. However since coherence implicitly relates to the way wavefields interfere with each other, it will be discussed in more detail in the next section using the language of statistical optics.

3.2 Partial Coherence

Coherence is the measure of the degree of correlation that a wavefield has with itself over time and/or space. Field correlations are important when considering how the field adds together, as correlated fields can interfere to produce static regions of high and low amplitude, whereas uncorrelated fields will always 'average out'. Interference of correlated waves is the phenomenon responsible for electron diffraction, so understanding the degree of this correlation is necessary for analysis of electron diffraction experiments.

While field correlations between any number of points in space and time can be quantified, all effects of partial coherence needed in this thesis can be described by two-point correlations. The level of correlation between two points of a field can be found by taking the inner product of the field at each point, which effectively determines their level of similarity between the limits of the integral.

The most familiar two-point correlation function for a field Ψ of position $\mathbf{x}$ and time t, is the intensity $I(\mathbf{x})$:

$$I(\mathbf{x}) = \frac{1}{T} \int_{-T/2}^{T/2} \Psi^*(\mathbf{x}, t)\, \Psi(\mathbf{x}, t)\, \mathrm{d}t, \tag{3.6}$$

where T is the period over which the intensity is averaged. The average intensity

is taken to mean where T approaches infinity, and can be written compactly using the notation:

$$\langle A\, B\rangle \equiv \lim_{T\to\infty} \frac{1}{T} \int_{-T/2}^{T/2} A^*\, B \,\mathrm{d}t, \tag{3.7}$$

where A and B are arbitrary functions. Using this notation, the average intensity is given by:

$$I(\mathbf{x}) \equiv \langle \Psi(\mathbf{x}, t)\, \Psi(\mathbf{x}, t)\rangle. \tag{3.8}$$

For intensity, the two points in the correlation function are one and the same, so the degree of correlation is total, and the intensity gives information only about average field amplitude at $\mathbf{x}$. It is worth noting that the integrand of equation 3.8 is the probability density for quantum fields, so intensity here corresponds to time averaged probability density for a particle at position $\mathbf{x}$.

A simple generalisation of intensity can be made by correlating the field at one position $\mathbf{x_1}$, with the field at another position $\mathbf{x_2}$, instead of correlating the field with itself at a single position $\mathbf{x}$. The resulting quantity is the mutual intensity [76], $J(\mathbf{x_1}, \mathbf{x_2})$:

$$J(\mathbf{x_1}, \mathbf{x_2}) \equiv \langle \Psi(\mathbf{x_1}, t)\, \Psi(\mathbf{x_2}, t)\rangle. \tag{3.9}$$

Mutual intensity carries information both about the magnitude of the field at the two points, and the amount of correlation between them. It is often convenient to quantify the level of coherence in a way that is invariant to scale factors of the field. Normalising mutual intensity using the intensity of the field at the two points gives the complex coherence factor, μ:

$$\mu(\mathbf{x_1}, \mathbf{x_2}) \equiv \frac{J(\mathbf{x_1}, \mathbf{x_2})}{\sqrt{J(\mathbf{x_1}, \mathbf{x_1})\, J(\mathbf{x_2}, \mathbf{x_2})}} = \frac{J(\mathbf{x_1}, \mathbf{x_2})}{\sqrt{I(\mathbf{x_1})\, I(\mathbf{x_2})}}. \tag{3.10}$$

Both the mutual intensity, and the complex coherence factor can in general be complex. The complex coherence factor may have any complex value such that $0 \leq |\mu(\mathbf{x_1}, \mathbf{x_2})| \leq 1$, where the phase factor literally corresponds to the phase difference in the coherent components of the field at positions $\mathbf{x_1}$ and $\mathbf{x_2}$.

A further small generalisation to the original definition of intensity provides the core tools needed for the discussion of partial coherence in this thesis. Instead of correlating the field with itself at different locations at a particular time, as for mutual intensity, the time at which the fields are compared is now also allowed to vary by an amount τ. The resulting quantity is called the mutual coherence function Γ:

$$\Gamma(\mathbf{x_1}, \mathbf{x_2}, \tau) \equiv \langle \Psi(\mathbf{x_1}, t)\, \Psi(\mathbf{x_2}, t+\tau)\rangle. \tag{3.11}$$

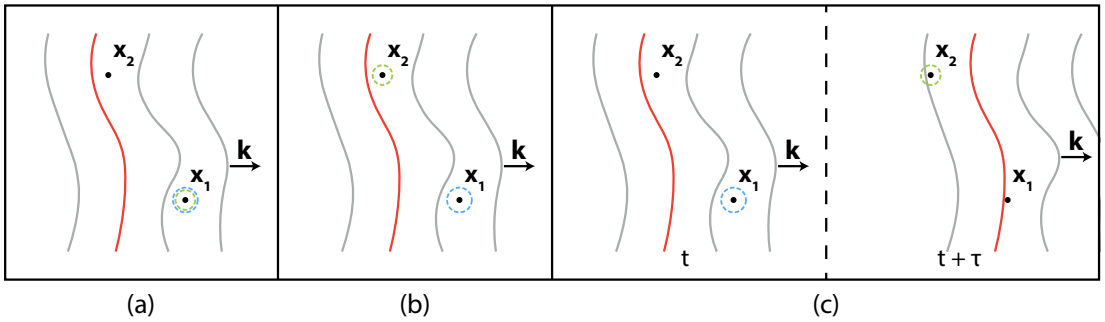

Figure 3.4: Field correlations at different points are encapsulated by different quantities. (a) Intensity, $I(\mathbf{x})$: same position, same time. (b) Mutual intensity, $J(\mathbf{x_1}, \mathbf{x_2})$: varying position, same time. (c) Mutual coherence function, $\Gamma(\mathbf{x_1}, \mathbf{x_2}, \tau)$: varying position, varying time. The dashed circles indicate the points being used in the correlation functions. One wavefront has been coloured red for ease of identification and $\mathbf{k}$ indicates the wavevector.

In the same way as mutual intensity was normalised to generate the complex coherence factor, the mutual coherence function also has a normalised companion function which gives a quantity related only to the degree of correlation. This quantity is called the complex degree of coherence γ:

$$\gamma(\mathbf{x_1}, \mathbf{x_2}, \tau) \equiv \frac{\Gamma(\mathbf{x_1}, \mathbf{x_2}, \tau)}{\sqrt{\Gamma(\mathbf{x_1}, \mathbf{x_1}, \tau = 0)\,\Gamma(\mathbf{x_2}, \mathbf{x_2}, \tau = 0)}} = \frac{\Gamma(\mathbf{x_1}, \mathbf{x_2}, \tau)}{\sqrt{I(\mathbf{x_1})\,I(\mathbf{x_2})}}, \tag{3.12}$$

and it can take the same values as the complex coherence factor ($0 \leq |\gamma(\mathbf{x_1}, \mathbf{x_2}, \tau)| \leq 1$). A graphical summary showing the positions of the field correlations used in intensity, mutual intensity, and the mutual coherence function is shown in Figure 3.4.

The level of coherence of a wavefield, as measured by the value of these correlation functions, affects the results of interference experiments. For example, consider a Young's two pinhole experiment, where the pinholes are at positions $\mathbf{x}_1$ and $\mathbf{x}_2$. The intensity that would be found at position $\mathbf{x}$ due to only pinhole 1 or 2 is denoted by $I_{1,2}$. Due to interference between the field coming from the two pinholes, the actual intensity at $\mathbf{x}$ is given by [77]:

$$I(\mathbf{x}) = I_1(\mathbf{x}) + I_2(\mathbf{x}) + 2\sqrt{I_1(\mathbf{x})I_2(\mathbf{x})}\mathrm{Re}[\gamma(\mathbf{x_1}, \mathbf{x_2}, \tau)], \tag{3.13}$$

where τ is the difference in travel time for the field to get from $\mathbf{x}_1$ to $\mathbf{x}$, and $\mathbf{x}_2$ to $\mathbf{x}$. The complex degree of coherence plays the role of the interference term here, which links it directly to experimentally important and measurable quantities. The magnitude of the interference term determines the visibility, $\mathscr{V}$

of the interference fringes, which can be defined by:

$$\mathscr{V} \equiv \frac{I_{\max} - I_{\min}}{I_{\max} + I_{\min}}, \tag{3.14}$$

where $I_{\max,\,\min}$ are the maximum and minimum intensities over a set of interference fringes. The interference term in equation 3.13 is related to the visibility by

$$\mathscr{V} = \frac{2\sqrt{I_1(\mathbf{x})\, I_2(\mathbf{x})}}{I_1(\mathbf{x}) + I_2(\mathbf{x})} |\gamma(\mathbf{x_1}, \mathbf{x_2}, \tau)|, \tag{3.15}$$

and in the case that the intensity at both pinholes is equal, the relationship between visibility and the complex degree of coherence becomes very simple:

$$\mathscr{V} = |\gamma(\mathbf{x_1}, \mathbf{x_2}, \tau)|. \tag{3.16}$$

In the case where a wavefield only has a small spread of frequencies $\Delta\omega$, the mutual intensity and the mutual coherence function are different only by a phase factor, in what is called the quasi-monochromatic approximation:

$$\Gamma(\mathbf{x_1}, \mathbf{x_2}, \tau) \approx J(\mathbf{x_1}, \mathbf{x_2})\, \exp(i\overline{\omega}\tau), \qquad \tau \ll 2\pi/\Delta\omega \tag{3.17}$$

where $\overline{\omega}$ is the average frequency. Under this approximation, the effect of temporal coherence can largely be ignored, so the simpler quantity of mutual intensity can be used instead of the mutual coherence function. The relationship in equation 3.17 is also true for the normalised versions of these two functions: the complex degree of coherence γ, and the complex coherence factor μ.

The visibility is a measure of the quality of the interference pattern, and fundamentally limits the amount of information that can be extracted from such a pattern. To link the visibility to a figure of merit for the coherence of a beam, we can assume a form for the appropriate correlation function, which is usually the mutual intensity if the beam is quasi-monochromatic.

The mutual intensity can in general be any arbitrary function, but for most beams of practical interest they will have some basic features. Firstly, the level of correlation between two points depends only on their separation so $\mu(\mathbf{x_1}, \mathbf{x_2})$ becomes $\mu(\mathbf{x_1} - \mathbf{x_2})$. Also, the correlations will decrease with increasing distance. This is a consequence of the Van Cittert-Zernike theorem [76], which describes how coherence is obtained as the waves from point sources propagate and overlap.

The quasi-homogeneous model for the mutual intensity uses an intensity component given by the intensity at the average position of two points, and a coher-

ence component which is a function of their separation:

$$J(\mathbf{x_1}, \mathbf{x_2}) = I\left(\frac{\mathbf{x_1} + \mathbf{x_2}}{2}\right) \mu(\mathbf{x_1} - \mathbf{x_2}). \tag{3.18}$$

The form of the complex coherence factor is then often approximated as a Gaussian function of this separation:

$$\mu(\mathbf{x_1} - \mathbf{x_2}) = \exp\left(\frac{-(\mathbf{x_1} - \mathbf{x_2})^2}{{\ell_c}^2}\right). \tag{3.19}$$

This yields a solid definition of coherence length based on wavefield interference, and also illustrates that the definition is only really valid when the form of the coherence function is Gaussian. In practice this is usually the case, again as a result of the way coherence is obtained by the overlap of originally uncorrelated fields as they propagate.

If the intensity in equation 3.18 is also a Gaussian function (but of position rather than separation), then the beam is known as Gaussian quasi-homogeneous. For these beams, with standard deviation in width given by σ_x, the ratio of coherence length to beam width is conserved as they propagate[78]:

$$\frac{\ell_c(z_1)}{\sigma_x(z_1)} = \frac{\ell_c(z_2)}{\sigma_x(z_2)}, \tag{3.20}$$

where the beam is assumed to be aligned along the z axis. The quantity $\sigma_x(z_2)/\sigma_x(z_1)$ is identified as magnification M, and can be arbitrarily changed by optical elements. Therefore, the coherence length at any point downstream of a Gaussian quasi-homogeneous source can easily be calculated from the coherence length at the source, and the magnification:

$$\ell_c(z) = M\ell_c(z_0). \tag{3.21}$$

Coherence in an optical beam can be Before finishing this section, it is worth discussing the how 'coherence' described above from the statistical optics point of view, compares to the 'coherence' as it is

The material presented in this section summarised what coherence is, how it affects interference patterns, and how it relates to experimentally producible beams. The next section summarises how electron diffraction patterns can be simulated, including how to incorporate the effects of partial coherence.

3.3 Fourier Optics and Simulation of Diffraction Patterns

Fourier optics is built on the solutions to the homogenous Helmholtz equation, which governs the propagation of monochromatic electromagnetic waves. The time-independent Schrödinger equation which governs electron wave stationary states, $\psi(\mathbf{x})$ can be written as:

$$\nabla^2\psi(\mathbf{x}) + \frac{2mE}{\hbar^2}\psi(\mathbf{x}) = \frac{2mV(\mathbf{x})}{\hbar^2}\psi(\mathbf{x}) \tag{3.22}$$

where m is mass, E is total energy, and V is potential energy. In free space, the potential energy can be set to zero, so equation 3.22 reduces to the homogeneous Helmholtz equation with the constant $\frac{2mE}{\hbar^2} = k^2$, noting that $E = p^2/2m$ with momentum p, and wavevector k, related by: $p = \hbar k$. All the tools of Fourier optics can therefore be directly applied to electron wavefields in order to study effects of electron diffraction.

The convention for the Fourier transform of a field Ψ, used throughout this thesis is:

$$\mathscr{F}\{\Psi(\mathbf{x})\} \equiv \breve{\Psi}(\mathbf{k}) = \frac{1}{\sqrt{2\pi}^N}\int \Psi(\mathbf{x})e^{-i\mathbf{k}\cdot\mathbf{x}}\,\mathrm{d}^N\mathbf{x}, \tag{3.23}$$

where $\mathbf{x}$ and $\mathbf{k}$ are the real and reciprocal space variables respectively, N is the dimensionality, and the integral is assumed to be over all space. The corresponding inverse transform is

$$\mathscr{F}^{-1}\{\breve{\Psi}(\mathbf{k})\} \equiv \Psi(\mathbf{x}) = \frac{1}{\sqrt{2\pi}^N}\int \breve{\Psi}(\mathbf{k})e^{i\mathbf{k}\cdot\mathbf{x}}\,\mathrm{d}^N\mathbf{k}. \tag{3.24}$$

Fields can be propagated from one plane to another using the angular spectrum formalism. A monochromatic field with wavevector $\mathbf{k}$ which has a positive z component, can be propagated from the plane $z = z_0$ to the plane $z = z_1$ using the operator equation:

$$\psi(x, y, z = z_1) = \mathscr{D}_{\Delta z}\psi(x, y, z = z_0), \qquad z_1 > z_0 \tag{3.25}$$

where $\Delta z = z_1 - z_0$, and the diffraction operator is:

$$\mathscr{D}_{\Delta z} = \mathscr{F}^{-1}\exp\left[i\Delta z\sqrt{k^2 - k_x^2 - k_y^2}\right]\mathscr{F}, \tag{3.26}$$

and operators are understood to act from right to left. The wavevector relates to the wavelength by

$$k = |\mathbf{k}| = \frac{2\pi}{\lambda} = \sqrt{k_x^2 + k_y^2 + k_z^2}. \tag{3.27}$$

If the field is approximately paraxial, such that $|k_x|, |k_y| \ll k_z$ the Fresnel approximation is often made to simplify the calculation. The diffraction operator in this regime can be modified to:

$$\mathscr{D}_{\Delta z} = \exp(ik\Delta z)\mathscr{F}^{-1} \exp\left[\frac{-i\Delta z(k_x^2 + k_y^2)}{2k}\right]\mathscr{F}. \tag{3.28}$$

If the field is allowed to propagate for a long distance compared to the region over which it is originally localised, then it is said to be in the far field, and can be calculated using the Fraunhofer diffraction integral, which turns out to be a scaled Fourier transform. The condition of being in the far field can be written as:

$$\frac{kb^2}{2\pi\Delta z} \ll 1, \tag{3.29}$$

where b is the diameter of the region over which the field was originally localised.

Under the Fraunhofer approximation, the field over a plane at some distance downstream can be calculated by the following:

$$\psi(x, y, z = z_1) = -\frac{ik\exp(ik\Delta z)}{\Delta z} \exp\left[\frac{ik}{2\Delta z}(x^2 + y^2)\right] \mathscr{F}\{\psi(x, y, z = z_0)\}, \underset{k_y = \frac{kx}{\Delta z}}{k_x = \frac{kx}{\Delta z}} \tag{3.30}$$

where this is subject to the same condition of paraxial fields as in the Fresnel approximation.

In most electron diffraction experiments the fields are scattered from a small target area and then detected in the far field. Eqn. 3.30 offers an easy and computationally efficient way to calculate this field given the field directly after the scatterer:

- Fast Fourier Transform (FFT) the field over the original plane, with real space grid spacing $\Delta x_0, \Delta y_0$.
- The axes of the transformed grid are now in wavenumbers, with grid spacing $\Delta k_{x_0} = \frac{2\pi}{n_x \Delta x_0}$, $\Delta k_{y_0} = \frac{2\pi}{n_y \Delta y_0}$, where $n_{x,y}$ are the number of elements per side of the array.
- Rescale the axes back to real space according to the Fraunhofer scaling factor in Eqn. 3.30.

To summarise, scaling between the original grid spacing $\Delta x_0, \Delta y_0$ and the far field grid spacing $\Delta x_1, \Delta y_1$ is finally given by:

$$\Delta x_1 = \frac{2\pi\Delta z}{k n_x \Delta x_0}, \qquad \Delta y_1 = \frac{2\pi\Delta z}{k n_y \Delta y_0} \tag{3.31}$$

Partial Coherence in Calculated Diffraction Patterns

The above methods of propagating fields from one plane to another only lead to realistic intensities where the incident field is fully coherent. There are many ways to include the effect of partial coherence on the propagated intensity profile, but one of the simplest is to make use of Schell's theorem [76, 79, 80]. Shell's theorem states that the far field intensity produced by a partially coherent beam is a convolution between the intensity produced by the Fraunhofer diffraction pattern, and the Fourier transform of the complex coherence factor with appropriate scaling:

$$I(x_1, y_1) = \frac{2\pi k^2}{\Delta z^2} \left| \mathscr{F}\{\psi(x_0, y_0)\} \right|^2_{\substack{k_{x_0}=\frac{kx_1}{\Delta z} \\ k_{y_0}=\frac{ky_1}{\Delta z}}} * \mathscr{F}\{\mu(\Delta x_0, \Delta y_0)\}._{\substack{k_{\Delta x_0}=\frac{kx_1}{\Delta z} \\ k_{\Delta y_0}=\frac{ky_1}{\Delta z}}} \tag{3.32}$$

The Fourier transform of the complex coherence factor is not guaranteed to be real, so the magnitude must be taken to ensure the calculated intensity is real. Additionally, the integral of this term over the whole plane will not in general be unity, so to preserve flux from one plane to another, Eqn. 3.32 should be divided by the magnitude of this integral.

Combining equations 3.19 & 3.32, gives a concise method for simulating the diffraction pattern from an aperture given a wavefield with a known coherence length. It also provides a way to determine the coherence length of a beam experimentally, by looking at the far field intensity pattern produced by diffraction from a known aperture.

3.4 Summary

Natively high transverse beam quality is a central motivation for development of the CAEIS. This chapter summarised the quantities used to measure transverse beam quality, and defined the specific conventions used throughout this thesis. Section 3.1 presented quantities of brightness, emittance, beam divergence, and

beam semiangle. These quantities are used extensively in the examination of the way space-charge affects beam quality, presented in chapter 4, and are also used in chapter 6, in the discussion of how beam quality and geometry affect electron diffraction experiments. Section 3.2 summarised the way beam quality can be quantified using a wave formalism, and in section 3.3 this formalism was combined with Fourier optics to demonstrate how partially coherent electron diffraction patterns can be simulated, which is drawn upon in chapter 6.

The high transverse beam quality generated from the CAEIS was used in ion bunch experiments presented in the next chapter to show, in detail, the way space-charge interactions can affect the beam.

Chapter 4

Space-Charge Effects in Charged Particle Beams

Both single-shot ultrafast electron diffraction, and the generation of X-rays in free electron lasers require very bright, ultrashort electron bunches with high bunch charge. High charge electron bunches produce significant repulsive Coulomb forces on the constituent particles that work to expand the bunch. In general this expansion induces a non-linear transformation of the particle phase space distribution which results in an increase in bunch emittance and corresponding reduction in brightness.

A particular electron bunch distribution, the uniform density three-dimensional (3D) ellipsoid, is known to conserve emittance under Coulomb expansion [81, 82], and so offers a route to overcoming space-charge induced brightness degradation. The Cold Atom Electron and Ion Source (CAEIS) is potentially an ideal candidate with which to generate uniform ellipsoid bunches, as the bunch can be initiated with a desired shape by selecting the appropriate spatial profile of the photoionisation lasers [52], and the low temperature of the generated electrons reduces thermal diffusion which would otherwise alter the distribution during propagation.

This chapter presents the results of space-charge experiments using cold ions generated in the CAEIS. The reasons for using ions instead of electrons are presented in section 4.1, as are the results of initial space-charge experiments which help to refine the procedures required for precise bunch shaping. Section 4.2 details how uniformly filled ellipsoidal bunches are generated, and presents results comparing the space-charge induced emittance degradation suffered by ellipsoidal bunches with that experienced by other distributions.

4.1 Ion Based Space-Charge Experiments in the Cold Atom Electron Source

One benefit of using ion bunches in investigations of space-charge effects is their significantly reduced creation temperature when compared to electrons. While the minimum achievable electron temperature in a CAEIS is of order 10 K, the temperature of the ions is around the millikelvin level [83]. The extremely low initial ion temperature allows for the almost total separation of thermal and Coulombic effects, making it easier to identify the mechanisms that produce a particular experimental result.

However, the main reason that ions were used in our experimental investigation of space-charge effects was the inability, using the current implementation of the CAEIS, to produce electron bunches with sufficiently high charge and short duration to induce significant and repeatable space-charge expansion.

4.1.1 Electron-Ion Equivalence

For a given ionisation duration of atoms in a static electric field, the space-charge expansion experienced by a resulting electron bunch will be significantly less than that of an ion bunch. The lighter electrons are spread over a larger distance in the direction of the static external electric field, and so experience less space-charge repulsion because of the $1/r^2$ nature of the Coulomb force.

For ionisation time $t_{\mathrm{i,e}}$ (where i and e refer to ions and electrons respectively), the longitudinal distance $d_{\mathrm{i,e}}$, over which the bunch is spread when accelerated in a uniform electric field $\mathbf{E}$, is given by:

$$d_{\mathrm{i,e}} = \frac{1}{2}\frac{q\,|\mathbf{E}|}{m_{\mathrm{i,e}}}t_{\mathrm{i,e}}^2, \tag{4.1}$$

where $q_{\mathrm{i,e}}$ is the charge on the particle and $m_{\mathrm{i,e}}$ is its mass. For equal length ion and electron bunches, which undergo identical amounts of space-charge expansion, the required ionisation time scales as:

$$t_{\mathrm{e}} = t_{\mathrm{i}}\sqrt{\frac{m_{\mathrm{e}}}{m_{\mathrm{i}}}}. \tag{4.2}$$

Thus, the spatial trajectories of particles in a 5 ns ion bunch (which is easy to generate with high charge in the CAEIS) should be exactly the same as those

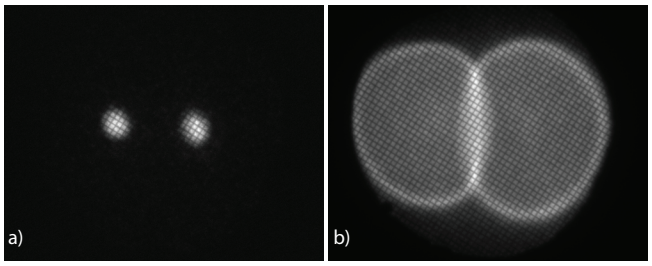

Figure 4.1: The detected projection of two point-like ion bunches. (a) shows the propagated bunches which contain very low charge. (b) shows high-charge bunches which expand due to space-charge effects, and form discs with high density rings, producing a collisional boundary as they interact. The grid structure that can be seen in both images is due to the shadow cast on the MCP by the grounding mesh that is directly in front of the MCP surface.

of a 12 ps electron bunch of the same charge. In the current implementation of the CAEIS, high-charge, short-duration electron bunches cannot be created for reasons that are explored in chapter 5. However, the simple time scaling between electron and ion trajectories implies that ions can be used as a convenient test platform for space-charge experiments, with results immediately transferable to electron bunches of shorter duration.

4.1.2 Unexpected Rings

The simplest experiment to perform with ions when investigating space-charge was to observe a propagated ion bunch. It was expected that the Coulomb repulsion of the charges would simply expand the bunch, resulting in an expanded and blurred version of the initial distribution. However, the first experiments performed in the CAEIS revealed unexpected features in the propagated ion bunches. When a single bunch was produced, it formed a high density ring around its perimeter, rather than the expected monotonic decrease in charge density with increasing radius. When two bunches were created in close proximity, the rings from the individual bunches formed a collisional boundary, rather than passing through each other. Both these effects can be seen from the detected profiles shown in Figure 4.1.

The ion rings were first noticed in experiments conducted by Dene Murphy, and the explanation given for their existence, and simulation supporting this explanation were also produced by him [84]. My contribution to this work was in design of subsequent experiments, execution of these experiments, and analysis of results. I collected all experimental data presented except that in Figure 4.2, and I analysed and plotted all data (simulated and experimental) in Figures 4.3

and 4.4.

Charged particle tracking simulations were performed using General Particle Tracer (GPT) [85] to try to reproduce the rings, where the initial distribution was set to be small, sharply defined ion bunches. These failed to show the kinds of features that had been observed experimentally, leading to the conclusion that the initial distribution of ions produced in the experiment must have been different in some way to that simulated. The discrepancy between simulation and theory was resolved by taking into account the finite illumination time of the excitation laser.

In the experiments, the excitation laser beam was turned on up to 50 μs before the ionisation laser pulse. Since the lifetime of the $5P_{3/2}$ state is $\tau = 26$ ns, this allowed the atoms that were being directly illuminated by the excitation laser to fluoresce for many cycles, scattering light into the surrounding atom cloud. The surrounding atoms then absorbed the scattered light, which ultimately led to a spatial broadening of the profile of the excited atoms at the time of ionisation. The intensity of the scattered light $I_{\mathrm{scat}}(\mathbf{x})$ can be calculated from the steady-state excited profile ρ_{e} by:

$$I_{\mathrm{scat}}(\mathbf{x}) = \frac{\hbar\omega}{\tau} \int \frac{N(\mathbf{x}')\,\rho_{\mathrm{e}}(\mathbf{x}')}{4\pi|\mathbf{x}-\mathbf{x}'|^2}\,\mathrm{d}V, \tag{4.3}$$

where $\hbar\omega$ is the energy of the scattered photon, and $N(\mathbf{x}')$ is the atomic number density at position $\mathbf{x}'$. This calculated scattered intensity assumes isotropic emission, and single scattering of the photons only. It also neglects the attenuation of the scattered light at larger distances from the central excited region due to absorption by the intervening atoms. The approximate initial excited-state profile could then be calculated by adding the original excitation intensity profile to the scattered intensity, and finding the steady state solutions of the Optical Bloch Equations (OBEs) using the updated illumination intensity [59].

By including in the GPT simulations a diffuse background of ions, which smoothly decreases in density at increasing distance from the directly illuminated region, the simulated propagated ion distributions matched those observed in the experiments. An experiment using an array of nine beamlets was tested, and the corresponding simulation showed the same basic features as can be seen in Figure 4.2. The experiment was repeated for several different incident laser intensities, which varied the total bunch charge.

The high density rings that form around individual bunches occur when the high charge core expands through a region of diffusely spaced ions. The sur-

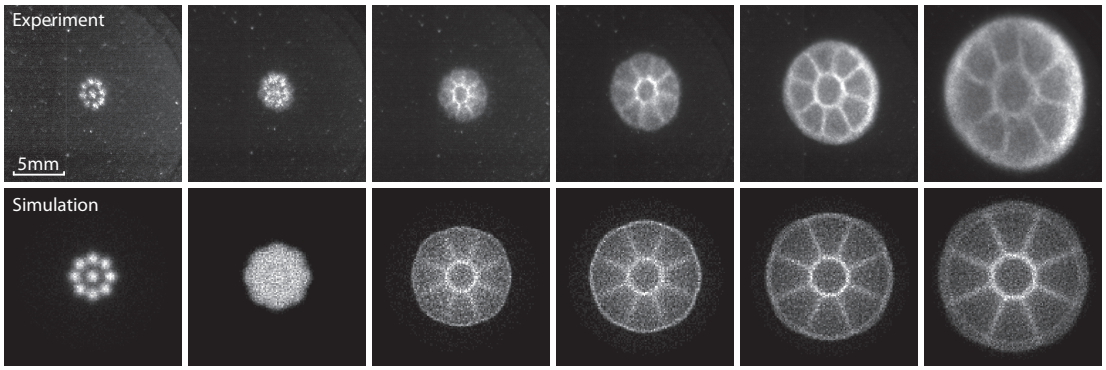

Figure 4.2: Simulation and experiment of a propagated array of nine ion bunches, where the simulation includes the surrounding low density ions produced from fluorescence. Charge per beamlet increases in the trials from left to right.

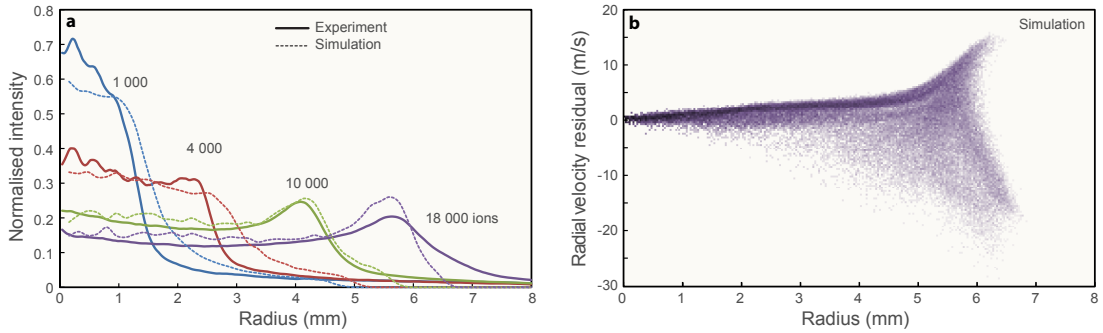

Figure 4.3: (a) The simulated and experimental radial profiles of a propagated ion bunch for increasing ion number, where the simulation takes into account a diffuse background of ions. (b) The simulated radial phase space profile for the largest simulated bunch shown in (a), which shows a large velocity spread at the position of the ring.

rounding ions which initially had very low transverse velocity, are then swept up by the expanding bunch, and so accumulate around its perimeter, leading to the observed rings. This can be seen in Figure 4.3(a), which shows the radial distribution of a propagated single ion bunch. As the total charge increases the bunch expands to a greater degree, which sweeps up more of the surrounding ions, resulting in the higher density ring around the perimeter. Figure 4.3(b) shows the radial phase-space profile for the largest simulated bunch shown in Figure 4.3(a). The phase-space profile clearly shows the increased spread of velocities in the region corresponding to the ring, and is reminiscent of shock wave phenomena in strongly interacting media [86,87]. The plot shows the velocity residuals after the line of best fit (representing an ideal linear bunch) has been subtracted. At the time this experiment was performed, there was no way to directly measure the number of ions in each bunch in order to input this number into the simulations. Instead, ion number was treated as a free parameter in the simulations, and was

varied so the simulation best matched experiment. After subsequent installation of the Faraday cup, it was found that the inferred number of ions matched the measured number within 20% for bunches of 10,000 ions or more, though the uncertainty increased to around 100% at ion numbers of 1000 because of noise on the amplifier.

4.1.3 Overcoming Ion Ring Generation

The diffuse halo of excited atoms outside the directly illuminated core, and the high density charge ring that can result, is undesirable where the goal is to generate very specific ion distributions, such as uniformly charged ellipsoids. The model of fluorescence and reabsorption that produces the diffuse ion background also suggests a method to avoid production of this halo. By reducing the time between excitation and ionisation of the atoms, less light is scattered out of the directly illuminated core since each atom can only scatter one photon every 26 ns on average.

To show that ring generation could be avoided by reducing the excitation-ionisation delay time, an experiment was conducted in which single ion bunches were generated using a variety of different delay times. The power of the excitation beam was adjusted so that the resulting bunch always expanded under space-charge to be approximately the same diameter at the detector, which was known from simulation to be a good indication that the bunches contained approximately the same number of ions in the directly illuminated core. The results of this experiment can be seen in Figure 4.4, which show the time between excitation and ionisation in (a), and the radial profile of the corresponding detected ion bunch in (b). The radial profiles show the expected behaviour of the high density ring becoming more prominent the longer the atoms are exposed to the excitation laser beam prior to ionisation.

The exact circumstances under which collisional boundaries form between two expanding ion bunches are somewhat less clear than those which lead to ring formation. A plausible explanation is that high density rings at the edge of expanding bunches form strong Coulomb barriers, which are sufficient to arrest the transverse momentum of some fraction of ions present within these rings. The greater transverse velocity spread in the rings as indicated in Figure 4.3(b) would support this production mechanism of collisional boundaries. While further modelling may clarify how collisional boundaries are formed, they do not pose a problem for the production of single uniformly filled ellipsoid bunches, as they

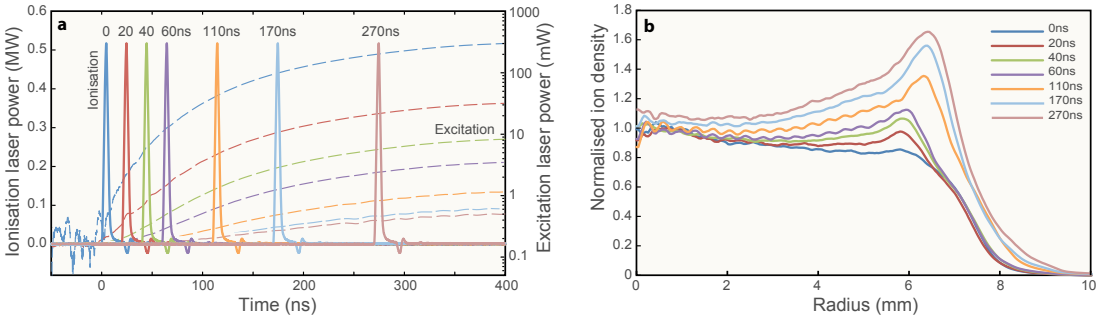

Figure 4.4: (a) The relative turn on times of the excitation and ionisation lasers corresponding to the propagated ion bunch radial profiles in (b). The rings don't occur when ionisation immediately follows excitation, but become increasingly prominent as the delay increases.

are only present where multiple bunches are generated simultaneously.

4.1.4 Summary of Initial Space-Charge Experiments

This section presented initial experiments investigating space-charge effects in ion bunches generated in the CAEIS. The use of ion bunches as an analogue for electron bunches was justified, and a relationship for the required scaling of bunch duration such that they both exhibit identical dynamics under space-charge expansion was presented. Initially, ion bunches were found to form high density rings around their edge, but this was shown to be caused by atomic fluorescence creating a diffuse halo of excited atoms which were subsequently ionised. Bunches could be created which did not form rings by limiting the time between atomic excitation and ionisation to less than the excited state lifetime of the atoms. This ionisation procedure is needed where very precise control of the initial bunch distribution is required, such as the generation of uniformly filled ellipsoids presented in the next section.

4.2 Bunch Shaping to Reduce Emittance Growth

Uniformly filled 3D ellipsoidal bunches can be generated through the creation of lower dimensional shapes that evolve into the desired distribution under their own space-charge forces [49, 88]. The 'pancake' bunch is an example, which is a circular distribution in the x and y directions, and is very thin in the z dimension. The initial two-dimensional (2D) charge density ρ, is the integral in the z direction

through a uniform density 3D ellipsoid of radius A in the x and y directions:

$$\rho(r) = \rho_0 \sqrt{1 - (r/A)^2}, \tag{4.4}$$

where r is the radial coordinate in the x, y plane and ρ_0 is the peak 2D charge density [88].

Creating bunches with this semi-circular distribution is possible since solid photocathodes illuminated by femtosecond lasers naturally create very thin initial electron bunches, and the transverse intensity of the laser beam can be shaped to achieve the required charge distribution. The expansion and propagation of such shaped bunches has been studied in photocathode sources [50, 89–93], however a reduction in emittance degradation as a result of this shaping has been challenging to demonstrate, in part because the high thermal energy of the electrons quickly degrades the ellipsoidal shape. A similar method can be used in the CAEIS to generate shaped ion bunches, except the thin ribbon ionisation laser beam takes the place of the flat solid cathode in order to create the initial pancake distribution.

Production of uniformly filled ellipsoid bunches which experience reduced space-charge induced emittance degradation represents a long standing goal for the entire CAEIS group. The following work was driven primarily by Daniel Thompson, with significant contributions from several others. My contribution to this work included assistance in experimental and simulated data analysis through creation of specially written analysis scripts, creation of the knife edge apparatus used to generate data presented in Figure 4.6, taking data in precursor experiments to that shown in Figure 4.6, and generally contributing to experimental design.

4.2.1 Bunch shaping

While perfect uniform ellipsoidal bunches are known to conserve emittance under space-charge expansion, any experimentally realised bunch will not be perfect, so the goal of these experiments was to minimise the increase in emittance due to space-charge forces. The method used to evaluate the extent to which the generation of near-ellipsoidal bunches were alleviating emittance growth was to compare the increase in emittance to that experienced by a set of explicitly non-ellipsoidal distributions. Creation of the different initial distributions was achieved by shaping the transverse profile of the red excitation beam, which couples the $5S_{1/2}$ to the $5P_{3/2}$ states, as shown in Figure 4.5(a) [94]. The required intensity profile

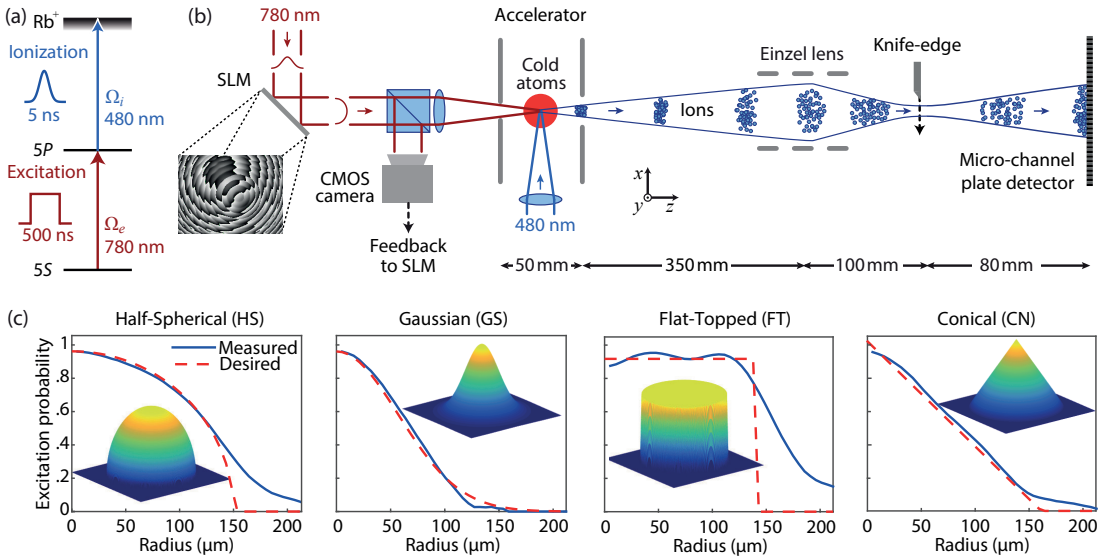

Figure 4.5: (a) Photoionisation is achieved in a two step process: excitation to an intermediate state, which shapes the transverse bunch profile, and ionisation from this state, which shapes the longitudinal profile. (b) The excitation laser beam is shaped with an SLM using feedback to optimise imprinted phase. The generated ions are accelerated in a static electric field and focused with an electrostatic Einzel lens so a movable knife edge can determine beam waist size. (c) The radially measured optical intensity achieved using the SLM is close to the desired intensity, however sharp edges are significantly smoothed out. The vertical scale takes into account the relationship between optical intensity of the excitation beam, and ionisation probability, where each image has been individually normalised.

was determined by working backwards from the desired final ion distribution, ρ_{ion}. Ionisation was achieved using an intense pulse of blue light with 5 ns duration, which ionised a high fraction of the atoms in the excited state ρ_e. Importantly this fraction was uniform in the transverse directions, so the ion bunch charge density was directly proportional to the spatially dependent excited state fraction: $\rho_{ion} \propto \rho_e$.

From the steady state solutions of the OBEs for a two level system, where intensity is well below the saturation parameter the fraction of atoms in the excited state is proportional to the intensity I_e of the coupling field [95]. Therefore, so long as the peak intensity is kept well below the saturation parameter, the ion density depends linearly on optical intensity, and the 2D ion distribution can be set by adjusting the transverse intensity profile of the excitation beam:

$$\rho_{ion}(r) \propto I_e(r). \tag{4.5}$$

Shaping the intensity of the focused excitation beam was achieved using the SLM. For a given desired intensity profile, the phase mask was calculated using

an iterative algorithm that included a feedback mechanism to achieve the closest possible fit between the desired intensity and that actually achieved [96, 97]. The feedback to the algorithm was provided by a camera that captured the intensity profile after each iteration, which the algorithm then used to modify the phase mask of the next iteration, as indicated in Figure 4.5(b).

The atoms were illuminated with the linearly polarised excitation laser (with polarisation axis the same as for the blue pulsed laser) for 500 ns prior to ionisation to allow them to achieve the steady state distribution. In section 4.1 it was shown that illumination of the atoms for even a few tens of nanoseconds could result in an excited state halo due to fluorescence of the directly illuminated core. However the intensity of the scattered light that causes the halo was significantly reduced for experiments presented in this section. The reduced scattering was a consequence of the laser intensity being significantly lower, with a corresponding reduction in the density of excited state atoms in the illuminated core.

Four 2D ion distributions were selected for comparison of space-charge induced emittance growth: Half-Spherical (HS), Gaussian (GS), Flat-Topped (FT), and Conical (CN). The HS distribution is described by equation 4.4 and was expected to evolve into a uniform ellipsoid. The GS distribution represents the shape which is naturally generated in photocathodes because Gaussian beams are the most common spatial mode generated in ultrafast lasers. The FT and CN distributions were chosen as distinct counter examples to the HS, that is, as shapes with non-linear internal fields that would increase in emittance more rapidly than the HS.

The desired and measured excitation intensity profiles are shown in Figure 4.5(c). The measured profiles generally conform well to the desired shape, but sharp edges were less well replicated, as might be expected given the limited numerical aperture of the optics, and limited spatial resolution of the SLM. An indication of the magnitude of the error in the measured distribution was obtained by finding the integral of the difference between the desired and measured radial profiles, and dividing by the integral of the desired profile. Doing this for the distributions in Figure 4.5(c) gives errors for the HS, GS, FT, and CN respectively of 7.3%, 1.5%, 23%, and 5%.

4.2.2 Relative Emittance Measurements

The relative emittance of the bunches after space-charge expansion was measured by focusing them using an electrostatic Einzel lens with fixed focal length, and measuring the beam diameter at the waist. Emittance is the product of Root

Mean Square (RMS) beam width, σ_x and RMS beam divergence, σ_{θ_x} as defined in equation 3.2. At a beam waist, the beam divergence is equal to the geometric beam angle (twice the beam semiangle, α), which is set by the width of the beam in the lens plane, and the focal length of the lens. For constant bunch diameter at the lens, the relative emittance is determined from the ratios of the focused beam waists. Bunches with different ion number expand to different diameters, so direct comparison of emittance can only be made between bunches with the same ion number. This direct comparison is possible because all bunches with the same initial size and ion number were found to expand the same extent in the lens plane, irrespective of exact initial profile.

The bunch width at the waist was determined by scanning a knife edge transversely across the beam and recording the total transmitted flux as a function of lateral position. This transmission function was fit with an error function (Figure 4.6(a)), dependent on the RMS waist size. The beam width was measured at several positions in the z direction, and then a parabolic fit determined the minimum RMS focal width, σ_f (Figure 4.6(b)). The waist width was measured for each of the four shapes for several values of total bunch charge, keeping the initial RMS width constant; $\sigma_x = \sigma_y = 67\,\mu$m. The results can be seen in Figure 4.6(c).

As the ion number increases, the beam waist increases in size for all shapes for two reasons. Firstly, space-charge induced emittance growth increases as space-charge forces become stronger, which should increase beam waist for a lens with fixed focal length. Secondly, the increased beam diameter at the lens plane can increase the effect of lens aberrations, thereby increasing emittance and leading to the same effect.

Figure 4.6(c) shows that for low bunch charges, the beam waist is the same for all shapes, because there is minimal space-charge induced emittance growth. As the bunch charge is increased, the different shapes develop different relative emittance values. The increase in relative emittance is a direct result of space-charge induced emittance growth, since the effect of lens aberrations is the same for all bunches of equal charge. At high bunch charge, the distribution with the lowest relative emittance is the half-spherical, as expected if the bunch it results in approximates the desired uniform ellipsoid bunch. Compared to the Gaussian bunch, the HS has a 50% reduction in the emittance at an ion number of $N = 8 \times 10^4$. The FT and CN distributions have relative emittance at intermediate values, between the minimum provided by the HS and the maximum experienced by the GS.

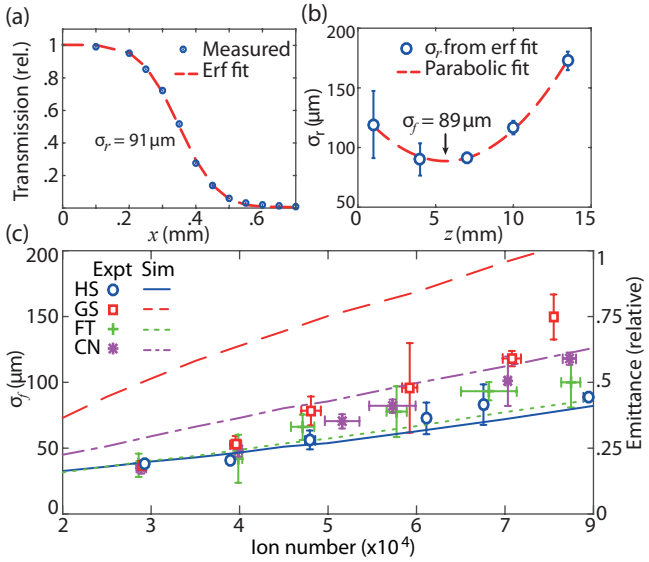

Figure 4.6: (a) The beam width is measured by detecting the transmitted beam fraction as a knife edge is inserted in the transverse direction. (b) The minimum beam width is found by measuring the width at several z positions, and then inferring the waist width from a parabolic fit. (c) For a given bunch charge, beam waist diameter is proportional to emittance. At low bunch charges, where there is little space-charge expansion, all initial distributions have the same emittance after propagation and focusing. In the space-charge dominated regime, the half-spherical initial distribution suffers significantly less emittance increase than the Gaussian, with the other shapes being affected to an intermediate extent. Simulations show similar trends, though absolute values differ by up to 150% because of the effect of accelerator aberrations as discussed in the text.

Figure 4.6(c) also shows the results of particle tracking simulations measuring the expected beam waist width as the bunch charge is varied. While the simulations do not quantitatively match the experimental measurements for all distributions, the behaviour of increased emittance with increasing ion number is consistent. The mismatch between simulation and experiment is largest at low ion number, where space-chage forces have minimal effect, and emittance increase is mostly determined by aberrations in the accelerator structure. Accelerator aberrations affect the GS or CN more strongly, because these distributions contain ions further from the central axis than the HS or FT for a given initial RMS size. In simulation, the initial distributions are set to exactly match the desired distribution, and so the more spread out bunches are affected by this aberration. In experiment however, all the profiles result in some ions being generated far from the central axis because of imperfections in the profile of the excitation beam, so all profiles are affected to a similar extent by accelerator aberrations in the absence of strong space-charge forces.

At higher bunch charges where the emittance becomes space-charge dominated, the experimental results tend toward simulations. Emittance measurements could not be made for bunches containing more than $N = 8 \times 10^4$ ions because they expanded to a size that was larger than the aperture through which they had to propagate.

4.2.3 Summary of Emittance Reduction by Bunch Shaping

The demonstrated reduction in emittance growth using bunch shaping is an important milestone in the development of cold atom electron and ion sources. Halving the emittance in both transverse directions for the half-spherical bunch compared to the regular Gaussian bunch implies an increase in transverse brightness by a factor of 4 (equation 3.4). The reduction in emittance growth appears to only become more prominent as the bunch charge is increased, potentially creating truly significant gains at charges relevant to ultrafast electron diffraction and high energy particle acceleration experiments. Even greater reduction in emittance growth could be expected by more stringently shaping the initial pancake distribution, which could be achieved using a higher resolution SLM and higher numerical aperture lenses for the excitation and ionisation beams.

4.3 Conclusion

The very low temperature of ions produced in the CAEIS has allowed the effects of space-charge expansion to be studied in a detail that has not previously been possible. The separation of thermal and Coulomb effects allowed high precision characterisation of the generated charge distributions in section 4.1, allowing the source of unpredicted charge rings to be identified as atomic fluorescence. Characterisation of such issues which are unique to the CAEIS proved useful in later experiments, which achieved the goal of producing uniformly filled 3D ellipsoidal charged bunches that have reduced emittance growth under Coulomb expansion.

While creating shaped electron bunches that display the same favourable expansion behaviour remains a goal for the CAEIS, the demonstration with ions is an excellent proof of principle, and the key results should be directly transferable to electron bunches. The creation of electron bunches that perform in a similar manner will require an ultrafast ionisation scheme that maintains the favourably low temperature and high bunch charge which is possible when using ions. The results of investigations into such ionisation schemes are presented in the following chapter.

Chapter 5

Electron Generation

A significant omission in the characterisation of Cold Atom Electron Sources (CAESs) up to this point has been measurement of the electron bunch pulse length. Photocathode response time is a critical parameter for producing ultrafast bunches with solid cathode materials [98], but with a CAES it has generally been assumed that electron liberation takes at most a few picoseconds. This assumption has been based on a combination of classical particle tracking simulations of electrons in Stark-shifted Coulomb potentials [99,100] and time resolved measurements of wave packet dynamics using single photon transitions from the ground state to above the classical field-ionisation threshold [101–103]. While such analyses offer insight into some factors affecting electron liberation time, neither accurately models the methods of electron generation hitherto employed for a CAES, involving excitation via intermediate states to a final energy very close to the ionisation threshold [57, 104, 105]. Photoexcitation with broadband ultrafast lasers can also result in simultaneous excitations to both above and below the threshold, which will affect the dynamics of the exiting electron wave packet.

This chapter describes direct measurements of the temporal profile of cold electron bunches produced from a CAES [106]. Electron liberation from the parent ion results from the distinct processes of photoexcitation, and field-ionisation, discussed separately in sections 5.1 and 5.2 respectively. It was found that photoexcitation to an ionising state and field-ionisation of that state can both take significantly longer than the ultrafast excitation laser pulse duration. Experiments show that excitation and ionisation are both highly sensitive to small changes in ultrafast laser wavelength and bandwidth, resulting in a variation of electron pulse duration by up to six orders of magnitude. With detailed consideration of these processes, the production of ultrafast cold electron bunches with

duration less than 130 ps was demonstrated, which was the resolution limit of the temporal measurement. The estimated true pulse length was a few tens of picoseconds: short enough for compression to 100 fs [34], which is sufficiently fast to observe dynamic diffraction on atomically relevant timescales [107].

Aside from the generation of ultrafast cold electron bunches, ionisation of cold atomic gases in a continuous mode has shown enormous promise as a source of ions for use in ion milling and microscopy [108–110]. Cold atom ion sources have two potential advantages over traditional gas field ion sources and liquid metal ion sources. The first advantage is that cold atom ion sources have the potential to be much brighter, which can allow images to be captured or structures to be milled more quickly, or at higher resolution. Cold atom sources can also potentially use any of the dozens of atomic species that have been successfully laser cooled, far more than can be produced from traditional sources. In microscopy, a large selection of ion species can allow different contrast forming mechanisms to be explored, while in milling, a large choice of ion species allows selection of one that will least affect the desired properties of the sample due to ion contamination. The large coherence length at generation of the very cold ions (of order 1 nm) could also make them ideal for use in ion interferometry experiments [111].

A proposal for further improving cold atom ion sources is to reduce the energy spread of ions produced in these systems by exciting the cold atoms to Stark states that ionise only at very specific values of electric field strength [112]. In an attempt to find such states, high resolution spectroscopy of high lying Stark states was carried out, the results of which are presented in section 5.3.

5.1 Photoexcitation

The ionisation threshold for ground state rubidium is 4.1771 eV, which can be generated using one blue and one red photon. In our experiments the tunable dye laser was used to produce blue pulses with Full Width At Half Maximum (FWHM) duration of 5 ns in the wavelength range from 460 nm (2.7 eV) to 490 nm (2.5 eV). Red light could be provided by the Continuous-Wave (CW) diode laser tuned to the 780.2 nm $5S_{1/2} \rightarrow 5P_{3/2}$ transition (1.5890 eV), pulsed using an acousto-optic modulator with a rise time of a few hundred nanoseconds. Alternatively, the mode-locked Ti:sapphire amplified pulsed laser could be used, with wavelength range 770 nm (1.6 eV) to 830 nm (1.5 eV), and minimum pulse width of 35 fs. The pulse shaper selected the central wavelength and bandwidth of the 35 fs pulse with 0.2 nm resolution, with commensurate increase in pulse dura-

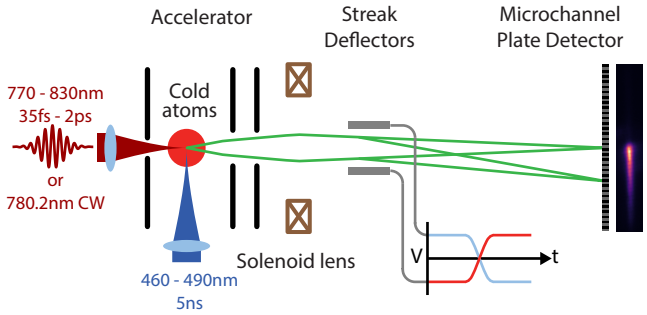

Figure 5.1: Electron streaking setup. Electron bunches are produced by photoionisation of laser-cooled rubidium gas. The temporal bunch length is determined by applying a time-varying deflection to the bunch while it is drifting, and measuring the length of the resulting streak on the detector.

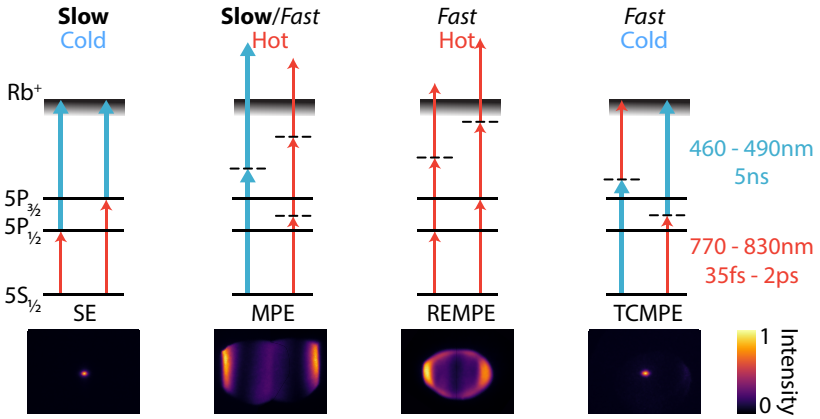

Figure 5.2: Photoexcitation pathways. Simultaneous illumination with two laser pulses can result in several excitation pathways: Sequential Excitation (SE), Multiphoton Excitation (MPE), Resonance-Enhanced Multiphoton Excitation (REMPE), and Two-Colour Multiphoton Excitation (TCMPE). Both SE and TCMPE produce cold electron bunches, but only TCMPE produces electron bunches that are both cold and ultrashort. The false-colour images show transverse momentum distributions of the detected bunches for the associated excitation pathways.

tion. All laser beams were focused to overlapping waists of approximately 100 μm FWHM within the atomic cloud, with the CW and pulsed red beams illuminating collinearly to electron propagation, and the blue beam incident transversely as shown in Figure 5.1.

5.1.1 Excitation Pathways

Atoms can be excited by several different pathways (Figure 5.2), with each pathway resulting in different electron bunch temperature and duration.

Sequential Excitation (SE) uses a single photon transition from the ground state to an intermediate state, and another single photon transition from the

intermediate state to a field-ionising state. The duration of the excitation process is determined by the duration of the laser pulse driving the transition to the ionising state, the lifetime of the intermediate state, or the depletion time of the intermediate state, whichever is shortest.

Focused laser pulses can easily produce sufficiently high intensities to cause nonlinear optical transitions. Multiphoton Excitation (MPE) occurs when two or more photons are absorbed without the atom transitioning via a real intermediate state. The transition rate is proportional to the nth power of optical intensity, where n is the number of photons absorbed before the atom reaches its final ionising state [113]. The lifetimes of intermediate virtual states are very short [114, 115], so the excitation period can only be determined by the duration of the laser pulse.

Resonance-Enhanced Multiphoton Excitation (REMPE) is a combination of sequential excitation and multiphoton excitation, where m photons are absorbed to excite the atom to a real intermediate state, and then a further p photons are absorbed in the transition to the final state. The reduction in the required number of photons for each transition can significantly increase the overall transition rate relative to an n-photon transition. The excitation duration is limited by the same factors as for sequential excitation and multiphoton excitation, with the precise set of intermediate states determining which factor ultimately limits the duration.

Two-Colour Multiphoton Excitation (TCMPE) is an MPE process where one photon is absorbed from each of two different laser fields. The excitation duration must then be determined by the shorter of the two pulses.

The temperature of electrons produced from any these excitation processes ultimately depends on the total energy imparted to the atom by any absorbed photons. The relationship between imparted energy and final electron temperature is not straight-forward because of the complex orbits possible for the electron at high-lying energies [105]. However it is generally true that the more energy imparted to the atom, the hotter the liberated electrons. The classical ionisation threshold energy for a hydrogenic atom is lowered if it is placed in an external electric field, with the Stark-shifted Coulomb potential V given by:

$$V = \frac{ke}{r} + Fz, \tag{5.1}$$

where r is the distance to the ion core, z is the position in the direction of the external electric field of strength F, k is the Coulomb constant, and e is the elementary charge [116]. The energy of an electron relative to the classical

ionisation threshold energy is given by

$$\Delta E(F) = -E_I + \sum_{i=1}^{n} \frac{hc}{\lambda_i} + 2\sqrt{ke^3F}, \tag{5.2}$$

where E_I is the field-free ionisation energy of the ground-state atom, the middle term is the total energy of the n photons involved in excitation with wavelengths λ_i, and the third term is the Stark shift of the classical ionisation threshold, corresponding to the saddle point energy, h is the Planck constant, and c is the speed of light [116]. The assumption that rubidium is hydrogen-like is a good approximation on the condition that $E_I \gg 2\sqrt{ke^3F}$.

Using the lasers described above, any process that uses one blue and one red photon will produce cold electrons so long as the lasers are appropriately tuned. So excitation using our lasers means that only SE and TCMPE can produce cold electrons, since all single colour processes result in a large excess energy. The large excess energy resulting from single colour processes is demonstrated in Figure 5.2, which show the detected transverse profiles of electron bunches generated be each process. These profiles correspond to the transverse momentum distribution for each bunch (with some blurring due to finite source size), so electron intensity further from the origin indicates hotter electrons. The profile corresponding to MPE was generated by atoms absorbing two photons from the blue laser. Ionisation was induced along the length of the vertically directed beam, so the initial electron bunch was a line rather than a point. The profile for the REMPE process shows the result of three red photons being absorbed, and looks similar irrespective of the particular intermediate state that is resonant. The profile looks similar even if no state is resonant, and the process is purely that of MPE, though there is a difference in the electron yield. The laser is directed into the page in this case, with the linear polarisation directed to the sides of the page.

5.1.2 Excitation Duration

Of the two processes that can create cold electrons, only for TCMPE is the expected excitation duration determined by the ultrafast laser pulse duration, since SE populates the $5P$ intermediate states, which have lifetimes in the tens of nanoseconds. To confirm that the electron pulse duration behaved as expected for the different excitation pathways, the temporal profile for electron bunches generated under a variety of conditions was determined using a streaking method.

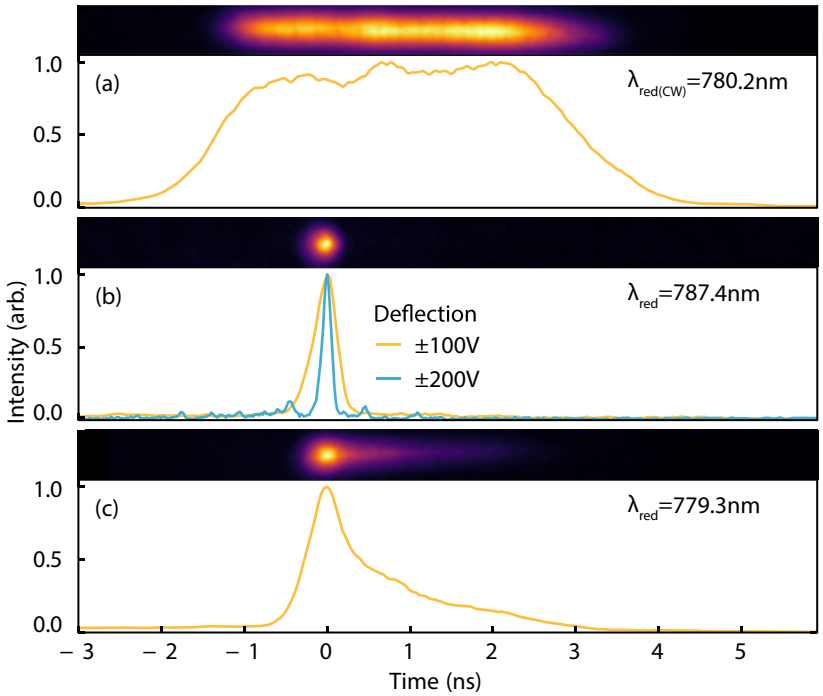

Figure 5.3: Electron streak profiles showing pulse broadening by intermediate state population. (a) Resonant CW excitation. Electron pulse profile mirrors the 5 ns blue laser pulse profile. (b) Far from resonance with intermediate states. TCMPE results in ultrafast bunches (profile in blue produced using higher streaking voltages). (c) Red photons from the ultrafast laser addressing an intermediate state leads to a slow sequential excitation component. The images show false-colour detected streaks.

In the streaking method, parallel plate electrodes deflect the beam with a time-varying potential to create a streak on the detector (Figure 5.1). The spatial profile of the streak corresponds to the temporal profile of the electron bunches. The potential of the streaking electrodes was ramped using a pair of bipolar push-pull solid-state switches with a fixed transition time of 10 ns as described in chapter 2.

Figure 5.3(a) shows the temporal profile of an electron bunch produced by sequential excitation, using the CW laser to excite atoms to the $5P_{3/2}$ intermediate state, and the pulsed blue laser for excitation to the ionising state. The bunch duration is 5 ns, mirroring the profile of the blue laser pulse as expected.

Ultrafast TCMPE was achieved by increasing the intensity of the blue laser pulse, and replacing the CW laser beam with a pulse from the ultrafast red laser tuned to 787.4 nm, well away from resonance with real intermediate states. To achieve a sufficiently high intensity for the blue laser light, it had to be focused in both transverse dimensions, rather than just being focused to a 'ribbon' as for sequential excitation. The ultrafast laser bandwidth was set to 1 nm, and the blue laser tuned to 482.1 nm, resulting in a ΔE with a small positive value, and

a spread of 2 meV due to the bandwidth of the ultrafast laser. The exact value of ΔE was not known because of the uncertainty in the strength of the electric field at the position of overlapping lasers. From tunnelling ionisation experiments discussed in the next section, it was estimated that the uncertainty in electric field strength corresponded to an uncertainty in excess energy of about 1 meV, so the central excess energy was calculated to be 5 ± 1 meV.

The duration for the resulting electron bunch was measured at 320 ps FWHM (Figure 5.3(b)), which is much shorter than the blue laser pulse, indicating the excitation process was TCMPE as expected. Shifting the central wavelength of the ultrafast laser close to the $5S_{1/2} \rightarrow 5P_{3/2}$ resonance at 780.2 nm results in the generation of electrons by both SE and TCMPE processes. The contribution from both processes is clearly seen from the profile in Figure 5.3(c), where there is a fast initial peak, but a slow tail of electrons excited from the populated $5P_{3/2}$ state.

The actual pulse length of our TCMPE bunches is expected to be much shorter than the 320 ps measured, but the temporal resolution of the electron streak is limited by the transverse focal spot size of the detected electron bunch. By increasing the maximum potential on the deflectors, the bunch is streaked more quickly, decreasing the apparent duration to 130 ps FWHM (Figure 5.3(b), blue curve), though temporal resolution was still limited by the focal spot size. The deflector potential could not be increased further without inducing electrical breakdown.

The true bunch length is expected to be the sum of the ultrafast laser pulse time (around 2 ps at 1 nm bandwidth), the electron extraction time, and the pulse lengthening that occurs during the drift phase due to position-dependent energy imparted by the accelerator, calculated to broaden the pulse by 1.8 ps by the time it reaches the deflectors. Electron extraction time is discussed in more detail in section 5.2, but is expected to take a few tens of picoseconds for the positive ΔE used here, meaning the actual electron pulse duration at the deflectors is expected to be less than 50 ps.

The pulse broadening observed in Figure 5.3(c) is strongly influenced by the wavelength of the ultrafast red laser. Figure 5.4 shows the pulse duration of electron bunches as the central wavelength of the ultrafast red laser was scanned over both $5P$ resonances. The ultrafast laser bandwidth was set to 0.5 nm, and the blue laser wavelength was adjusted such that the total combined photon energy was kept constant, with minimum combined photon energy still resulting in a positive ΔE. Pulse widths of less than 350 ps correspond to resolution-limited

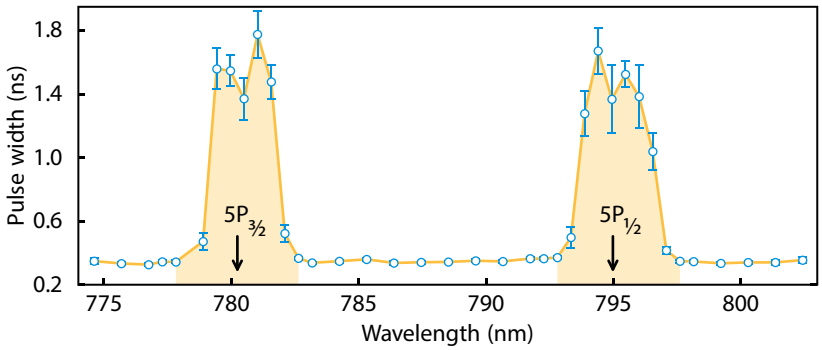

Figure 5.4: The measured $1/e$ pulse durations of electron bunches as the ultrafast red laser is scanned over $5P_{3/2}$ and $5P_{1/2}$ resonances. The ultrafast laser bandwidth was 0.5 nm. Shaded area indicates regions where there was detectable broadening.

durations, and the electrons generated in these regions are almost exclusively produced from two-colour multiphoton excitation. Pulse widths larger than 350 ps indicate that electrons are being generated via sequential excitation, after the ultrafast red pulse has passed through.

It can be seen that the laser wavelength must be a few nanometers from resonance before broadening by sequential excitation drops below detectable levels, which corresponds to a detuning of around 10^4 natural line widths. That such a large detuning can still result in an appreciable excited state population is unsurprising given the extreme power broadening that results from the high intensities of focused ultrafast pulses [95]. The decrease in bunch duration as the predominant excitation process changes from SE to TCMPE, is accompanied by a reduction in total electron yield. Around 10^5 electrons per bunch are created when the ultrafast laser directly overlaps with a resonance, but only around 100 are produced when exclusively TCMPE electrons are generated.

5.1.3 Hot Electrons from Multiphoton Processes

A major problem associated with generating ultrafast cold electron bunches using TCMPE is that the very high laser powers required tend also to generate electrons via competing MPE processes. This can become particularly problematic if the undesirable MPE process is resonantly enhanced, leading to a much greater fraction of hot electrons. The ultrafast red laser can access four states in the relevant wavelength range that could potentially induce a resonant enhancement in the red-only MPE electron yield. The $5P_{1/2}$ and $5P_{3/2}$ states can cause a "1+2" REMPE transition [117], where there is a resonant enhancement for the first absorbed photon, with the second two photons being absorbed via a virtual

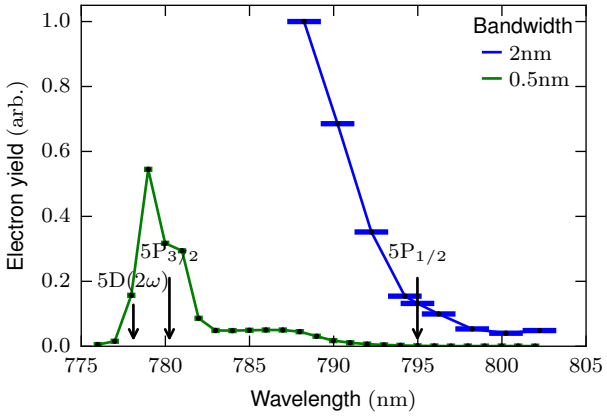

Figure 5.5: Electron yield from REMPE processes. The number of hot electrons produced by a REMPE process varies with the relative detuning from different states. The horizontal bars indicate the wavelength components present in the ultrafast laser pulse. The plots are normalised to the peak value of the 2 nm bandwidth scan.

state. This resonance is also problematic because any population induced in the P states can lead to electron pulse lengthening as previously discussed. There is also a "2+1" resonance [118], where two photons are absorbed via a virtual state resulting in the population of the $5D_{3/2}$ and $5D_{5/2}$ states, before a final photon is absorbed promoting the atom to an ionising state.

Figure 5.5 shows the electron yield produced using only the ultrafast red laser as its central wavelength was tuned across the possible resonances. Two scans are shown in the figure, where the bandwidth of the laser pulse was changed using the slit width on the pulse shaper, with one scan taken at a bandwidth of 0.5 nm (shown in green) and another at 2 nm (shown in blue). The spectral density was kept approximately constant by maintaining a constant pulse energy within each bandwidth scan. The energy in the 2 nm bandwidth pulses was set to approximately four times that of the 0.5 nm pulse in order to maintain the same spectral density.

The feature that stands out most clearly in the 0.5 nm scan is the strong enhancement around the $5D$ and $5P_{3/2}$ resonances, though there is insufficient resolution to separate the individual resonances. There is an obvious absence of any resonance peak at the $5P_{1/2}$ state, but there is a clear shoulder off the main peak out towards this state. In an attempt to observe any resonance around the $5P_{1/2}$ state, the bandwidth was increased to 2 nm so as to increase intensity. While many more electrons were generated near the $5P_{1/2}$ state, the feature still appeared to be part of the shoulder previously observed.

The increased bandwidth scan illustrates the huge effect that bandwidth can

have when considering nonlinear optical transitions. Increasing the bandwidth of the laser pulse by a factor of 4 increases pulse energy by the same factor (assuming a flat spectral density profile), but it also reduces the duration of a transform-limited pulse by a factor of 4 as can be seen in equation 2.3. These combined factors increase the peak intensity by a factor of 16. Because a two photon transition rate is proportional to the square of intensity, an increase in bandwidth by a factor of 4 can increase the transition rate by a factor of 256, which is the correct order of magnitude for the electron yield enhancement seen in Figure 5.5.

The main message that can be taken from Figure 5.5 is that to avoid generating hot, red-only MPE electrons when attempting to produce cold TCMPE electrons, it is best to use a wavelength less than 775 nm, or greater than 800 nm. It had been assumed that using an ultrafast red laser wavelength halfway between the two $5P$ transitions would be sufficient to avoid any resonant behaviour, so 787 nm was typically used in TCMPE electron generation throughout this chapter. However, given that 787 nm is on the REMPE 'shoulder' as seen in Figure 5.5, it would have been better to use a wavelength that was less strongly resonant, as this would have resulted in fewer hot electrons being generated.

To determine which of the $5P_{3/2}$ or $5D$ states contribute more strongly to the hot MPE electron signal, a higher resolution scan was performed across the relevant wavelength range using a reduced bandwidth of 0.2 nm (Figure 5.6). In this scan, the 2+1 resonance via the $5D$ states form a narrow peak, with no such peak observable at wavelength corresponding to the $5P_{3/2}$ state. However, there is an increased electron yield extending between the $5D$ and $5P_{3/2}$ wavelengths, which shows some similarity to the region of higher electron yeild observed between the $5D/5P_{3/2}$ and $5P_{1/2}$ positions in Figure 5.5.

The resolution of the scan is insufficient to differentiate the $5D_{3/2}$ and $5D_{5/2}$ states, given that the separation of the states is less than the minimum achievable laser bandwidth. There is also an uncertainty in the absolute wavelength of around 0.2 nm, so the peak may well be centred directly over the $5D$ states, rather than being slightly offset to the right.

The variation in electron yield between the different REMPE channels can be explained by considering the detuning of the intermediate virtual state from nearby real states in the 2 photon absorption step. When the laser wavelength is tuned to excite the atom to the $5D$ resonances, the intermediate virtual state has a detuning of around 2×10^4 natural line widths from the $5P_{3/2}$ state. Even with this large detuning, at high laser powers the proximity to a real state can

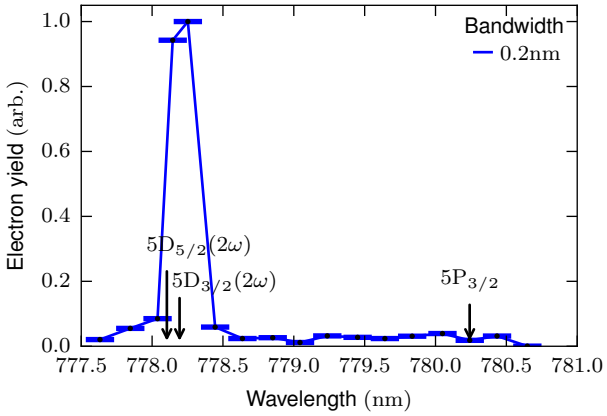

Figure 5.6: Electron yield from REMPE processes using narrowest ultrafast bandwidth. The strongest resonant enhancement is from a 2+1 excitation channel via the $5D$ states.

resonantly enhance the excitation to the $5D$ states, in effect leading to a double resonantly enhanced excitation pathway to the final ionising state. Where the wavelength is tuned to excite directly to the $5P_{3/2}$ state for a 1+2 excitation channel, the virtual state of the 2 photon absorption step is detuned from the $5D$ states by around 5×10^5 natural line widths. This much larger detuning reduces the effect of the double resonance relative to the 2+1 channel, so leads to a reduced electron yield for a given laser intensity. The 1+2 excitation channel that is directly resonant with the $5P_{1/2}$ has a virtual state that is even further detuned from the $5D$ states (4×10^6 natural line widths), so this channel generates even fewer electrons, as shown in Figure 5.5. So while the $5D$ states form the strongest resonance, which is observable with the lowest power, the $5P_{3/2}$ and $5P_{1/2}$ resonances should also be avoided, as they also resonantly enhance the MPE electron yield, albeit to a lesser extent.

The electron yield generated from blue laser MPE appeared relatively constant across the accessible range of wavelengths. The lack of a resonant response was expected given that the nearest accessible transition from the ground state is to the $6P_{1/2}$ level [119], requiring a wavelength of 422 nm which corresponds to a detuning of 10^7 natural line widths using 480 nm light [120].

5.1.4 Alternative to TCMPE

Temporal pulse broadening by population of intermediate states, low yield of cold electrons, and generation of hot electrons by competing processes are all significant problems of the TCMPE method used to generate ultrafast cold electrons.

It was necessary to use this excitation scheme because the only ultrafast laser available to our group had a nominal wavelength of 800 nm. Ideally, the ultrafast laser pulse would drive a single photon transition from a pre-prepared excited state to the ionising state. The much higher transition probability of single photon transitions would greatly enhance the possible electron yield, and eliminate the need for very high laser powers, and the problems that come along with it.

Such an excitation scheme has been employed elsewhere [58,121], where a CW laser was used to deliberately populate the $5P_{3/2}$ intermediate state of rubidium, and an ultrafast blue laser pulse further excited the atoms to an ionising state. The only disadvantage of this scheme is that generation of ultrafast laser pulses at blue wavelengths requires frequency doubling optics or an optical parametric oscillator, which marginally increases the complexity of the optical setup.

If the ultrafast blue laser pulse was to also cause a transition from the ground state to an intermediate state, then the CW laser could further excite atoms in this state to an ionising one, leading to the same electron pulse broadening which was a problem with our excitation scheme. However, if ground state rubidium is exposed to a pulse of 480 nm (blue) light, the nearest accessible real intermediate state is the $6P_{1/2}$ level, at a detuning of more than 10^7 natural line widths. Such a large detuning means there will effectively be zero probability of excitation to this state using the relatively modest laser pulse powers required.

5.2 Energy Dependence of Ionisation Duration

Regardless of the excitation scheme, rapid excitation of the atom to an ionising state is not sufficient to generate ultrafast electron bunches: the electron liberation from that state must itself be an ultrafast process.

Electrons extracted from Stark-shifted Coulomb potentials have lower transverse momentum spread than would be expected for a given excess energy because the shape of the potential causes anisotropic emission, preferentially directing electrons in the forward direction, along the external electric field [122,123]. The reduction in transverse momentum spread creates electron bunches with higher transverse coherence. The coldest most coherent electrons have typically been generated by tuning the excitation lasers to, or just below, the ionisation threshold [58,105]. The results of streaking experiments detailed below show that generating electrons with very low, or negative, excess energy can have a detrimental affect on electron liberation time.

5.2.1 Below Threshold Ionisation

Below the classical ionisation threshold, electrons can escape the atomic potential through tunnelling, but the small probability amplitude on the free side of the barrier increases the time it takes to deplete the ionising state. The sensitivity of tunnelling rate to excess energy has important consequences for generating ultrafast electron pulses, because the ionisation rate of below-threshold Stark states can vary by many orders of magnitude over energy scales that are comparable to the bandwidth of an ultrafast laser pulse. Above the classical ionisation threshold, the probability amplitude on the free side of the barrier is greater, and ionisation proceeds rapidly. The exact ionisation rate depends on which states are excited and the strength of the external field, but typical ionisation times are in the tens of picoseconds [101–103].

For ultrafast bunch generation using broadband laser pulses, excitation near the classical ionisation threshold populates a superposition of Stark states, where states from both above and below threshold contribute. Figure 5.7(a) shows the temporal profile of an electron pulse produced by TCMPE, with the ultrafast red laser tuned so that Stark states were excited with both positive and negative ΔE. A fast initial peak is generated from Stark states with positive ΔE, followed by a very slowly decaying tail from lower-lying states.

To study the effects of Stark state lifetime on bunch duration in more detail, the broadband ultrafast red laser was replaced with the narrow-linewidth CW red laser, and the pulsed blue laser was used to excite electrons from the $5P_{3/2}$ state. Figure 5.7(b) shows a resulting streak for $\Delta E = -0.5\,\mathrm{eV}$, which might be considered an optimum energy for applications like electron diffraction because of the low resulting electron temperature, and high electron yield. However, the pulses exhibit long tails with decay time $17\,\mu\mathrm{s}$ containing 70% of the total electron charge, corresponding to an increase in bunch length by nearly a factor of 10^6 relative to a bunch generated from purely above-threshold states. It should be noted that the deflector potential sweep time has been greatly increased in Figure 5.7(b) compared to 5.7(a), in order to observe the full temporal profile of the electron pulse. The increase in deflector sweep time results in a corresponding decrease in the temporal resolution of the streak.

It is not totally clear why the bunch in Figure 5.7(b) has an initial peak, since it might be expected that all atoms should tunnel out with the same characteristic time of $17\,\mu\mathrm{s}$. The peak must be caused by some atoms ending up in rapidly ionising Stark states, which could result from the spread of wavelengths in the

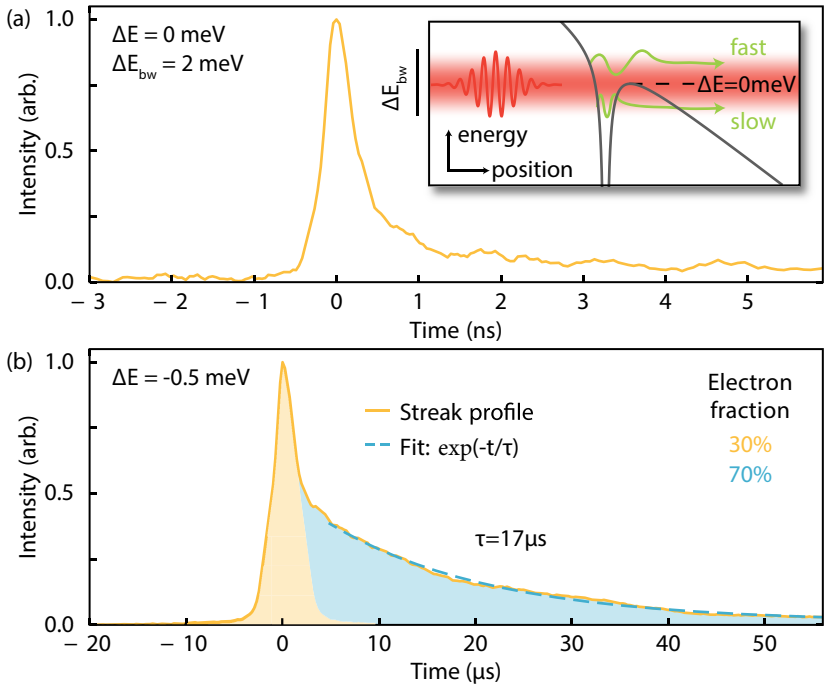

Figure 5.7: Slow ionisation resulting from tunnelling. (a) Temporal profile of the first few nanoseconds of an electron bunch consisting of a fast initial peak due to above threshold excitation and a slow tail from below threshold excitation. Ionisation process illustrated in the inset. (b) Complete microsecond-scale profile of an electron bunch generated by below threshold excitation. Electrons liberated in the initial pulse make up only 30% of the total yield, with the remainder being liberated in the long tail.

blue laser pulse due to a component of amplified spontaneous emission. However the long tail contributes to the majority of the electrons in the pulse, which probably originate from a single Stark state given the good fit between the tail decay rate and the exponential fit.

5.2.2 Ionising State Lifetime Spectroscopy

To see in more detail how the ionisation time was affected by electron excess energy, the total electron flux was measured as the electric field strength was varied. By changing the electric field strength, the excess energy of the excited electrons is shifted according to equation 5.2. Varying the excess energy in this way was more precise and repeatable than keeping a constant electric field strength and changing the laser wavelength, because the laser could not reliably be adjusted by such small increments. It should be clarified that in this context, the ionisation time for tunnelling states simply refers to the inverse of the ionisation rate, and is just the characteristic time it takes to deplete the Stark state. The time it takes for an electron to tunnel across a barrier is a question that still doesn't have a

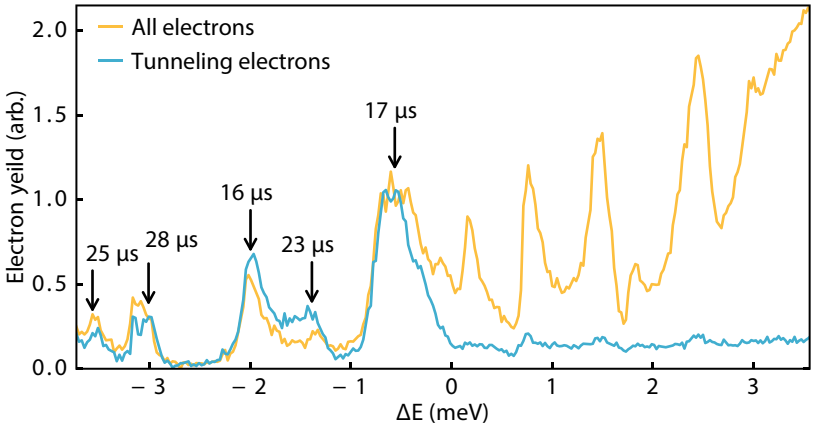

Figure 5.8: Electron yield as a function of excess energy. The yellow line shows the total electron yield at a given excess energy, and the blue line shows only the yield of electrons detected more than 200 ns after laser excitation. Labels indicate measured pulse decay times at that energy, with uncertainty $\pm 2\,\mu$s.

universally accepted answer [124, 125].

In one of the scans of electron yield vs. excess energy, all the electrons generated in each pulse were counted by integrating the intensity on the Micro-Channel Plate (MCP) captured with a camera (Figure 5.8, yellow trace). Many different peaks are visible, which may belong to individual Stark states, or groups of adjacent Stark states, with the total yield in each peak generally increasing with increased excess energy. A second scan was made under the same conditions, but included only electrons that were detected more than 200 ns after the blue laser pulse excited the atoms to an ionising state. Practically this was achieved by attaching the electrical output on the MCP to a pulse counter as described in chapter 2, and gating the input to only allow counts to be made in the desired time window. By counting electrons in this way, only the electrons in the tail of pulses like that in Figure 5.7(b) were included, essentially indicating where the ionisation time was drastically increased due to tunnelling. The resulting spectrum can be seen as the blue line in Figure 5.8. While the two spectra look essentially identical for negative values of excess energy, above $\Delta E = 0$ there is almost a complete absence of any electrons with an ionisation time of more than 200 ns.

For both scans the blue wavelength was fixed at 485.587 nm, and the electric field strength was varied from the calculated values of 1720 $\mathrm{Vcm^{-1}}$ to 2500 $\mathrm{Vcm^{-1}}$. These values of the electric field were calculated using the known potential and separation of the accelerator electrodes, and then adding an offset to account for the gradient in the field. The offset added to the calculated electric field was equivalent to adding an offset in excess energy of about -1.0 meV so that the

position of $\Delta E = 0$ corresponded to observed transition point between fast and slow ionisation lifetimes. The apertures in the electrodes result in a small position dependence in the electric field strength, but since the precise position of the ionisation volume was uncertain, the exact electric field at the atoms also had an uncertainty. It is common practice to use the electric field as a fitting parameter in spectroscopy of Stark states [126], but the specific value of the offset used here reflects the assumption that the transition from fast to slow ionisation should occur around $\Delta E = 0$, rather than a fit to the expected positions of particular known states. The precise value of the offset added does not affect conclusions of the current work, but the exact values on the energy scale in Figure 5.8 should be taken only as a guide.

Streak measurements were performed for each discernible state below the threshold, with all showing ionisation lifetimes in the tens of microseconds. It is well-known that field ionisation rates of atoms tend to increase as the excess energy is increased [127, 128], but Figure 5.8 makes it clear that this is not at all a smooth function. Ionisation time drops by at least a factor of 100 over less than 1 meV around the classical threshold energy, whereas the ionisation times remain relatively constant over the full range of negative excess energies shown, spanning about 4 meV. This step function in ionisation time shows that there is a meaningful transition from tunnelling ionisation to above threshold ionisation. Determining the precise magnitude of the decrease in ionisation time on the positive energy side of this step would require a greater temporal resolution than was accessible with out current streaking system.

Analytic estimates exist for ionisation rates of Stark states in hydrogen, though these estimates become increasingly less accurate at higher energies and particularly for the red states where more probability amplitude is located on the free side of the Coulomb barrier. Accurate modelling of Stark state ionisation rates in rubidium is even more complex, because the nonhydrogenic component of the Hamiltonian can lead to coupling between degenerate blue and red states. Blackbody induced transitions can further distribute the population among many Stark states, even if external electric field and laser photon energy are accurately known. Ultimately, the hydrogenic theory predicts that the ionisation time for states at the energy and electric field used in these experiments can vary by a few tens of orders of magnitude [55, 114, 115], with the observed ionisation times of tens of microseconds being approximately in the middle of this range.

The ionisation lifetimes of the below threshold states were determined by fitting a decaying exponential to the tail of the streaks, an example of which is

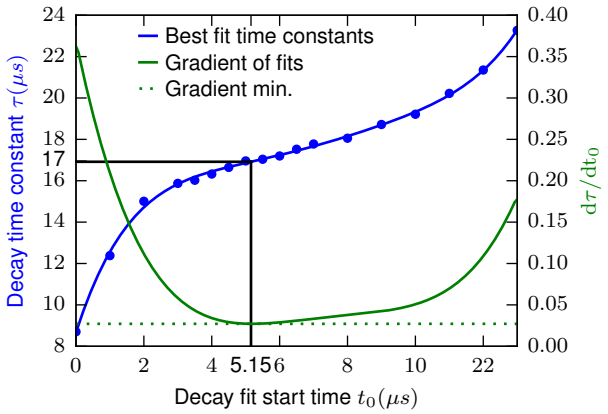

Figure 5.9: Determination of tunnelling time constant. τ was determined by finding the best fit exponential decay curves for a range of start times. The start time was chosen where the rate of variation in the recovered decay constant was the lowest.

shown in Figure 5.7(b). To get a reliable value for the decay constant τ, the start time t_0, of the decaying exponential was not used as one of the fitting parameters in the automated fitting routine. Allowing t_0 to be used as a fitting parameter in an automated fitting algorithm changes the number of data points that can be used in the fit, which confused the error metric. The optimal t_0 was instead determined manually, by finding the best fit exponential decay curves for a range of t_0 values. The final value of τ was chosen where the rate of variation in the best fit τ with respect to t_0 was the lowest, as illustrated in Figure 5.9.

5.2.3 Implications of Tunnelling Ionisation for the CAES

The demonstration that electron bunch duration changes as a function of excess energy has significant consequences for the ability of CAES systems to generate electrons that are both cold and ultrafast. It implies that the bandwidth-duration relationship of the optical excitation pulse has a corresponding temperature-duration relationship for the generated electron bunches, though the relationship is complicated and highly dependent on the exact states that are excited. There is good reason to believe that cold electron bunches can still be extracted on ultrafast time scales, but this must be done carefully, without assumption of a linear response to excess energy for either temperature or duration. In particular, the drastic changes in bunch duration around the classical ionisation threshold energy shows that it is critically important to avoid coupling to below-threshold states if generation of ultrashort electron bunches is desired. The basic conclusions of this work have been recently confirmed by Franssen et al. [121], who

performed similar streaking measurements but with greater time resolution and lower energy resolution.

5.3 High-Resolution Rydberg Spectroscopy

Many applications for photoionised cold atoms, such as ion microscopy and milling, do not require ultrafast ionisation, and hence slow tunnelling from below threshold Stark states is not always problematic. In fact, a rapid change in ionisation rate as electric field strength is varied is the basis of a proposed method for reducing the energy spread of ions generated in these systems, known as selective field ionisation [129, 130].

The majority of the energy spread in ion beams generated by photoionisation of cold atoms in a static electric field is due to the longitudinal size of the ionisation volume, which is defined by the laser focus size. Ions generated closer to the downstream accelerator electrode will end up with less energy than those generated further away, and this energy spread can seriously degrade the achievable focal spot size of the ion beam [131].

In selective field ionisation, energy spread is reduced by first exciting atoms to a high-lying Stark state in a region of electric field strength where the ionisation rate of the atoms is very low. As the atoms drift through a region of high electric field gradient, they will encounter an electric field strength that results in very rapid ionisation at a very specific location, ultimately decreasing the total volume over which ionisation occurs [131]. A number of different mechanisms can result in a sudden increase in ionisation rate [132, 133], but accurate prediction of the ionisation rate of high lying Stark states, particularly for red states near the classical threshold energy, is a theoretically challenging task [134–137]. A pragmatic approach to finding States that display large changes in ionisation rate is to experimentally measure the location and rates for Starks states at a range of different electric field strengths, and identify those that show the desired behaviour.

To perform the spectroscopic scans, the system was modified to use narrow linewidth CW red and blue excitation lasers. Both lasers illuminated the atoms in a direction perpendicular to the static electric field, with polarisation parallel to the field. The red laser was tuned to couple the atoms from the $5S_{1/2}$ to the $5P_{3/2}$ transition, and was spatially overlapped with the blue laser, which was expected to couple the $5P_{3/2}$ state to any of the $nS_{1/2}$, $nD_{3/2}$ or $nD_{5/2}$ levels, for an unknown n. The arrangement of laser direction and polarisation was chosen

to minimise coupling to states with high projection of angular momentum in the direction of the external electric field, reducing the total number of states observed, and making potential comparison with theoretically calculated energy levels easier. Such a comparison is not shown here, but was performed for similar scans presented in reference [131].

The MOT and Zeeman slower were not used to cool atoms in this experiment, as any magnetic field would further split the energy levels into Zeeman substates. Instead, atoms were photoexcited directly from the beam of rubidium gas emitted from the effusive oven. The generated ion signal was collected using the electrical output of the MCP attached to the pulse counter as before.

An example scan showing ion yield as excitation energy and electric field strength are varied can be seen in Figure 5.10. The intention was to excite states near the ionisation threshold energy, but the entire region shown is actually below the threshold. The total excitation energy was known with high accuracy because the laser wavelength was measured with a highly accurate wavemeter, but there was a significant discrepancy between the electric field strength calculated from the known electrode potentials, and actual strength at the position of the ionisation volume. However the exact electric field offset in these experiments could be inferred by comparing the locations of individual Stark states with the locations predicted by theory. This comparison was demonstrated in reference [131] for data taken under the same conditions to that shown in Figure 5.10, and the calculated offset applied to the data shown here.

Some of the states in Figure 5.10 do show noticeable variation in their count rate for fairly small changes in electric field strength, which is the behaviour desired for selective field ionisation. However interference effects between two adjacent Stark states around avoided crossings can, in some circumstances result in a far greater increase in the ionisation rate at specific electric field strengths, so finding regions where this occurs offers the largest potential gains in beam monochromaticity [131, 138]. None of the states in the measured Stark map display obvious interference narrowing, however the map only covers an extremely small region of the potentially useful parameter space of excitation energy and electric field strength.

Although the Stark map in Figure 5.10 shows no obvious candidate state with which to perform selective field ionisation, it does demonstrate that our system can be used to perform high resolution Rydberg spectroscopy. It also gives insight into the precise nature of the states that yield electrons when using pulsed excitation, clarifying the underlying physics of electron generation with

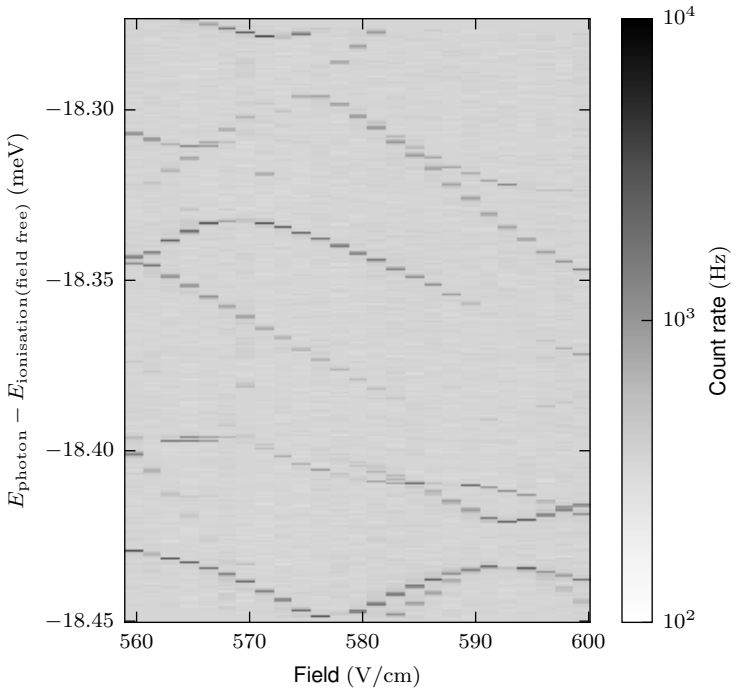

Figure 5.10: High precision spectroscopy of tunnel-ionising Stark states showing the detected ion yield. Spectroscopy using narrow linewidth excitation lasers reveals the multiplicity of closely spaced Stark states, where the signal is recorded by measuring the flux of ions produced. Lines of high count rate represent the energy level of tunnel-ionising Stark states, which can be seen to change in energy as the electric field strength is varied.

these systems.

5.4 Conclusion

The work presented in this chapter clarifies the conditions required to generate cold electron bunches from a CAES, that are actually ultrashort in duration. The effects that certain excitation schemes have on electron bunch duration were not necessarily appreciated in previous CAES experiments, which in a number of cases have led to the assumption that electron bunches were ultrafast, where the results presented here suggest that they could not have been.

Specifically, it has previously been suggested that picosecond duration bunches could be generated using an excitation scheme which was essentially sequential excitation, using an ultrafast laser to couple the ground and intermediate states [105]. The evidence presented in support of this claim was a very fast rise time of the voltage pulse produced at the electrical output of the MCP which detected the electron bunches. The pulse had a slow fall time on the scale of a few nanoseconds, which was attributed to the electrical characteristics of the detector. In light of the work presented in section 5.1, it now seems likely that the electron pulses themselves actually had a temporal profile with a sharp initial rise, and a decay time on the nanosecond, not picosecond timescale, exactly as can be seen in Figure 5.3(c).

A different experiment by Engelen et al. used ultrafast excitation to an ionising state [58], which certainly should produce ultrashort electron bunches if the excitation energy is sufficiently high to avoid the slow tunnelling ionisation discussed in section 5.2. However, they reported that the coldest electrons produced using "femtosecond photoionisation" was when the ultrafast photoionisation laser spectrum was centred on the threshold energy. Given that the laser had a 20 meV bandwidth, this certainly would have excited slowly ionising below-threshold states, increasing the duration of the electron bunches to microseconds. Electron bunches they produced at higher excess energies would have been in the ultrafast domain, however they also had a higher temperature than the 30 K achieved around the threshold energy. More recent work from the same group shares this conclusion: ultrafast electron generation requires above threshold excitation [121].

In summary, this chapter presents direct measurements of the temporal distribution of electron bunches extracted from cold atomic gases. Several distinct processes involved in the excitation and ionisation of cold atoms have been de-

scribed, including how each of these processes contributes to the duration of the extracted electron bunches. Experiments confirmed that it is possible to produce simultaneously ultrafast and cold electron bunches, and the conditions required to achieve this were identified.

Both the transverse and temporal properties of CAES electron bunches have now been characterised. In the next chapter, these electron bunches of known coherence and pulse duration will be used in proof-of-concept electron diffraction experiments, which will demonstrate some of the advantages of cold atom electron sources over traditional photocathode sources.

Chapter 6

Electron Diffraction

While ionising cold atomic gases may turn out to have a multitude of applications, from ion beam milling and microscopy [108,139,140] to electron bunch injectors in particle accelerators [43, 44], a driving motivation for their development has been their potential use as an electron source for ultrafast electron diffraction [141,142]. It was shown in Chapter 5 that it is certainly possible to produce ultrafast bunches of cold electrons from a Cold Atom Electron Source (CAES), and Chapter 4 described efforts to control brightness-destroying space-charge expansion. Here, we demonstrate our first successful electron diffraction experiments using electrons generated in the CAES, including using verifiably ultrafast bunches. The goal of this work was not to demonstrate the holy grail of diffractive imaging: single-shot ultrafast electron coherent diffractive imaging of nanoscale objects, but rather to demonstrate certain elements of this final goal individually.

Experimental results are presented in Section 6.1, where diffraction was demonstrated from large crystalline samples, using traditional crystallographic techniques of transmission and reflection Bragg diffraction. In Section 6.2, close-to-realistic simulations of coherent diffractive imaging using the CAES are presented, including both forward propagation and phase retrieval.

The task remains to combine all the elements that have been demonstrated individually, though only future development of CAES technology will tell if there are fundamental or practical barriers to doing so. Diffraction with this novel class of electron source is still in its infancy, with only one other demonstration reported [143]. The results presented here represent an incremental, but important step towards establishing the cold atom electron source as a real alternative to current sources used in ultrafast electron diffraction.

6.1 Crystallography

Electron diffraction from single crystals was demonstrated more than a hundred years ago [1], but far from being an obsolete science, it is arguably more productive than it has ever been. Constant refinements and new techniques are allowing structural determination of ever more complex samples, and the ease with which electron beams can be manipulated often makes electron diffraction techniques more versatile than those of X-rays [144].

Despite the multitude of techniques now available, it is the simplicity of basic electron crystallography that makes it an ideal first experiment with which to demonstrate a practical use of electrons generated from the CAES. All diffraction experiments were performed using pulses of electrons, rather than a continuous beam. The practical reason for using electron pulses is that in the current setup, the Magneto-Optical Trap (MOT) magnetic fields make it effectively impossible to propagate a collimated electron beam to the sample chamber. More generally though, the benefit of generating electrons from atomic gases is only clear when a pulsed source is desired, since current field emission tip Direct Current (DC) electron sources are already approaching fundamental limits to brightness. With this in mind, the present section focuses on demonstrating electron diffraction using a CAES, and the specific issues and benefits that arise, rather than comparing the quality of the results obtained with those that could be generated from a typical electron microscope.

6.1.1 Kinematic Theory of Electron Diffraction

A perfect infinite crystal is made up of a periodic set of points, the lattice, with an identical arrangement of atoms, the basis, positioned around each lattice point. The lattice is made from a set of basis vectors $\mathbf{a}$, $\mathbf{b}$, and $\mathbf{c}$, with each point on the lattice described by translations from each other by:

$$\mathbf{t} = u\mathbf{a} + v\mathbf{b} + w\mathbf{c}, \tag{6.1}$$

where u, v and w are integers [145–147]. A unit cell is some volume that can fill all space simply through translations by the vector $\mathbf{t}$. A primitive unit cell contains exactly one primitive lattice point, but it is common to use other unit cells which contain more than one primitive lattice point if they more clearly illuminate the symmetry of the crystal structure.

Diffraction maxima from crystals occurs when a wave is reflected in phase from the same atom in every unit cell. These atoms will line up along planes in the crystal, and these planes are described by the points in the reciprocal lattice. The points of the reciprocal lattice can be found by linear combinations of the reciprocal basis vectors, $\mathbf{a}^*$, $\mathbf{b}^*$, and $\mathbf{c}^*$, which are related to the real basis vectors by:

$$\mathbf{a}^* = \frac{2\pi \mathbf{b} \times \mathbf{c}}{\mathbf{a} \cdot (\mathbf{b} \times \mathbf{c})} \qquad \mathbf{b}^* = \frac{2\pi \mathbf{c} \times \mathbf{a}}{\mathbf{a} \cdot (\mathbf{b} \times \mathbf{c})} \qquad \mathbf{c}^* = \frac{2\pi \mathbf{a} \times \mathbf{b}}{\mathbf{a} \cdot (\mathbf{b} \times \mathbf{c})}, \tag{6.2}$$

where the 2π comes from the convention we have chosen for the wave-vector: $|\mathbf{k}| = 2\pi/\lambda$. Reciprocal lattice points are then given by the reciprocal lattice vector, $\mathbf{g}$

$$\mathbf{g} = h\mathbf{a}^* + k\mathbf{b}^* + l\mathbf{c}^*, \tag{6.3}$$

where h, k and l are integers known as Miller indices.

A scattering event of a wave can be described by the scattering vector, $\mathbf{q}$, which is the difference in the initial and final wavevectors, $\mathbf{k_0}$ and $\mathbf{k}$:

$$\mathbf{q} = \mathbf{k} - \mathbf{k_0}. \tag{6.4}$$

When a wave scatters elastically from a crystal (such that $|\mathbf{k}| = |\mathbf{k_0}|$), constructive interference only occurs where the difference in initial and final wavevectors is equal to a reciprocal lattice vector, which gives the scattering condition for crystals:

$$\mathbf{q} = \mathbf{g}. \tag{6.5}$$

It can be seen from Figure 6.1 that the relationship between the scattering vector and scattering angle is:

$$|\mathbf{q}| = 2|\mathbf{k_0}| \sin(\theta), \tag{6.6}$$

where θ is the half angle between the initial and final wavevectors. Our choice of wavevector convention more generally determines the relationship between distances in real and reciprocal space such that:

$$|\mathbf{g}| = 2\pi/d_{hkl}, \tag{6.7}$$

where d_{hkl} is the distance between the set of planes described by the corresponding Miller indices, though it should be noted that the other common convention which is used particularly in X-ray science is $|\mathbf{g}| = 1/d_{hkl}$. Combining equations 6.5, 6.6

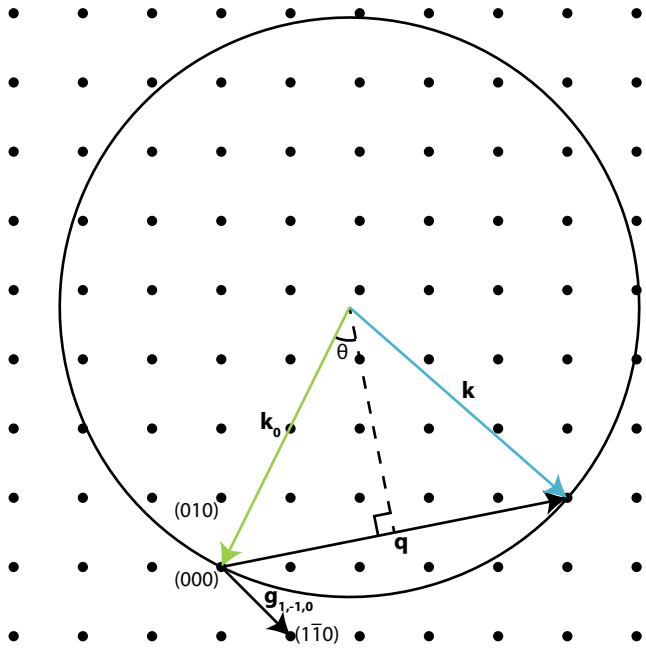

Figure 6.1: Ewald sphere construct in the reciprocal lattice. Diffraction spots appear wherever the scattered wave interferes constructively. This can only happen where the scattering vector $\mathbf{q}$ intersects a reciprocal lattice point. The reciprocal lattice of a crystal is made by the set of all reciprocal lattice vectors, an example of which is shown: $\mathbf{g_{1,-1,0}}$. Due to conservation of energy between the incident wave (wavevector $\mathbf{k_0}$) and scattered wave (wavevector $\mathbf{k}$), the scattered wave must point to a position on the Ewald sphere.

and 6.7 yield the familiar Bragg condition:

$$2d_{hkl} \sin\theta = n\lambda, \tag{6.8}$$

where n is the diffraction order.

The diffraction condition described by equation 6.5 can be represented graphically using the Ewald sphere construction shown in Figure 6.1. In this construction, the unscattered wavevector points to the origin of reciprocal space, with all possible elastically scattered directions being represented by a sphere. Waves scattered from a crystal lattice can interfere constructively only where the sphere intersects one of the reciprocal lattice points.

Equation 6.5 says nothing about the intensity of the diffraction spots from a crystal, since this condition only references the lattice, and a crystal also requires a basis. To determine the intensity of the diffraction spots (which includes intensity of zero, the so called forbidden reflections), the scattering potential of the actual crystal must be considered.

In the single-scattering approximation, the *relative intensity*, I of the wave

with scattering vector $\mathbf{q}$ is given by:

$$I(\mathbf{q}) = \left|\breve{V}(\mathbf{q})\right|^2, \tag{6.9}$$

where $\breve{V}(\mathbf{q})$ is the Fourier transform of the crystal potential evaluated at $\mathbf{q}$.

For an infinite crystal, the Fourier transform of the crystal potential can be written in terms of the *structure factors* $V_{\mathbf{g}}$:

$$\breve{V}^{\text{inf}}(\mathbf{q}) = (2\pi)^3 \sum_{\mathbf{g}} V_{\mathbf{g}} \delta(\mathbf{q} - \mathbf{g}), \tag{6.10}$$

where the sum takes into account the scattering contribution from all the reciprocal lattice points, and the Dirac delta plays the roll of the scattering condition (equation 6.5), ensuring only one reciprocal lattice point contributes to any given spot. Structure factors are also often written as F_{hkl}, particularly in the field of X-ray diffraction. The effect of the crystal basis comes in during calculation of the structure factors for each of the reciprocal lattice points. The structure factor for a particular reciprocal lattice point is calculated by taking into account the position $\mathbf{x}_j$ and scattering factors $\tilde{V}_j$ for each of the j atoms in the crystal basis:

$$V_{\mathbf{g}} = \frac{1}{V_{\text{cell}}} \sum_j \tilde{V}_j(\mathbf{g}) e^{-i\mathbf{g}\cdot\mathbf{x}_j}. \tag{6.11}$$

The scattering factors $\tilde{V}_j(\mathbf{k})$ are the Fourier transform of an isolated atomic potential, and are not to be confused with the Fourier transform of the whole crystal potential, $\breve{V}(\mathbf{k})$. Equation 6.11 is in a convenient form, because $\tilde{V}_j(\mathbf{g})$ is just a number which relates to the probability that an isolated atom of type j will scatter an electron into a direction corresponding to $\mathbf{g}$. Scattering factors for the complete range of scattering angles are tabulated for almost all elements at a range of incident electron energies [148]. Scattering factors are often called *atomic form factors* in X-ray diffraction, and although they appear in the same place in kinematical theory, their numerical value is different for X-rays and electrons. V_{cell} is the volume of the chosen unit cell, and accounts for the many possible choices of unit cell.

Of particular consequence in our experiments is that we were required to use very thin samples in order to not unduly attenuate the electron beam. This requirement for thin samples means that the crystal potential deviates significantly from the case of an infinite crystal. The potential of the finite crystal can be

calculated by multiplying the infinite potential by the *shape function*, $S(\mathbf{x})$:

$$V(\mathbf{x}) = V^{\text{inf}}(\mathbf{x})S(\mathbf{x}), \tag{6.12}$$

where

$$S(\mathbf{x}) = \begin{cases} 1, & \text{for } \mathbf{x} \text{ in the crystal} \\ 0, & \text{otherwise.} \end{cases} \tag{6.13}$$

The Fourier transform of this potential can be represented in the same form as equation 6.10, where the delta functions have been softened to sinc functions:

$$\breve{V}(\mathbf{q}) = \sum_{\mathbf{g}} V_{\mathbf{g}} t_x t_y t_z \,\text{sinc}\left(\frac{(q_x - g_x)t_x}{2}\right) \text{sinc}\left(\frac{(q_y - g_y)t_y}{2}\right) \text{sinc}\left(\frac{(q_z - g_z)t_z}{2}\right), \tag{6.14}$$

where t_x, t_y, t_z are the sizes of the illuminated portions of the crystal in the indicated dimensions. In practice, we will only be using crystal foils, which are very thin in one dimension, but very large in the other two, resulting in the sinc terms limiting back toward delta functions in those dimensions. Crystal foils therefore result not in reciprocal lattice points, but in reciprocal lattice rods, or *relrods*. Equation 6.14 is important because it shows that the diffraction condition $\mathbf{q} = \mathbf{g}$ does not need to be perfectly satisfied in order to diffract electrons to a particular direction. It says that the intensity of the diffracted spot will be reduced the further you get from satisfying the diffraction condition.

Excitation Error

The distance from the perfect condition can be conveniently quantified by defining the excitation error: $\mathbf{s_g}(\mathbf{q}) = s_x\hat{\mathbf{x}} + s_y\hat{\mathbf{y}} + s_z\hat{\mathbf{z}}$, where the components are defined by the distance between the scattering vector and reciprocal lattice point:

$$s_x = q_x - g_x \qquad s_y = q_y - g_y \qquad s_z = q_z - g_z. \tag{6.15}$$

An excitation error is introduced in two ways in our diffraction setup: through the curvature of the Ewald sphere, and through beam tilt away from perfectly meeting the diffraction condition.

The direction orthogonal to a plane in reciprocal space that passes through any three (non-collinear) reciprocal lattice points is called a *Zone Axis*. For a beam incident along a given zone axis, the set of diffraction spots that will be

excited are, to a first approximation, the reciprocal lattice points that lie on this plane. However, as a result of the curvature of the Ewald sphere (which itself results from energy conservation of the incident beam), the larger the scattering vector $\mathbf{q}$, the greater the distance between $\mathbf{q}$ and a reciprocal lattice point $\mathbf{g}$, which would otherwise be excited. This distance is the excitation error as introduced previously, and modifies the diffraction condition in equation 6.5 to:

$$\mathbf{q} = \mathbf{g} + \mathbf{s}. \tag{6.16}$$

To find an expression for the size of $\mathbf{s}$, equation 6.16 can be rewritten as $\mathbf{s} = \mathbf{k} - \mathbf{k_0} - \mathbf{g}$. Now consider the case where illumination is along the z axis, such that $\mathbf{k_0} = 0\hat{\mathbf{x}} + 0\hat{\mathbf{y}} + k_0\hat{\mathbf{z}}$ as in Figure 6.2. If we look at the diffraction due to the reciprocal lattice point $\mathbf{g}$, by observing scatter to the direction $\mathbf{k}$, where $k_x = g_x$, $k_y = g_y$, then it can be shown that the components of the excitation error are given by:

$$\begin{aligned} s_x &= k_x - k_{0x} - g_x = k_x - g_x = 0 \\ s_y &= k_y - k_{0y} - g_y = k_y - g_y = 0 \\ s_z &= k_z - k_{0z} - g_z = k_z - k_0 - g_z = \sqrt{k_0^2 - g_x^2 - g_y^2} - k_0 - g_z. \end{aligned} \tag{6.17}$$

The diffraction spots resulting from the first row of reciprocal lattice points are called the *zeroth order Laue zone*, and the intensity of these spots will be reduced at larger $\mathbf{q}$ because of the increasing size of s_z. However, for reciprocal lattice points in the second (or higher) rows, s_z can decrease with increasing $\mathbf{q}$. This can result in the appearance of alternating dark and light bands of spots, as the Ewald sphere cuts through *higher order Laue zones*.

Another way that excitation error can be introduced is by tilting the beam away from a zone axis. For an incident beam that is tilted at an angle α to a zone axis, an excitation error is introduced due to the Ewald sphere being shifted away from reciprocal lattice points. As the scattering vector increases, the curvature of the Ewald sphere increases (or decreases) the size of the tilt-induced excitation error, but for a small magnitude of $\mathbf{q}$ it can be seen from Figure 6.3 that

$$s_z = |\mathbf{q}| \sin(\alpha). \tag{6.18}$$

While a more sophisticated analysis can take advantage of diffraction data to accurately determine the shape of the illuminated crystal, equations 6.14, 6.16

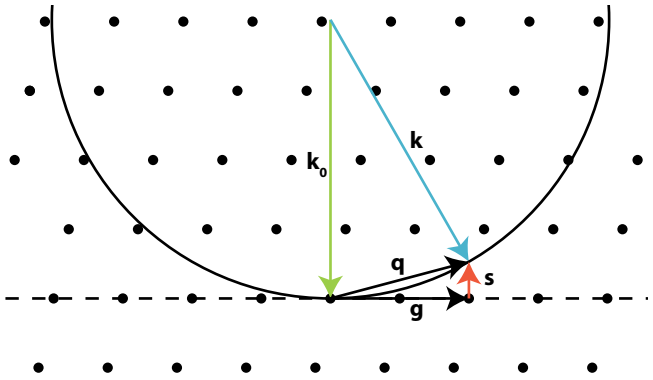

Figure 6.2: Excitation error from Ewald sphere curvature. The curvature of the Ewald sphere introduces an excitation error **s**, even if illumination is also along a zone axis (the plane corresponding to a zone axis is shown as the dotted line).

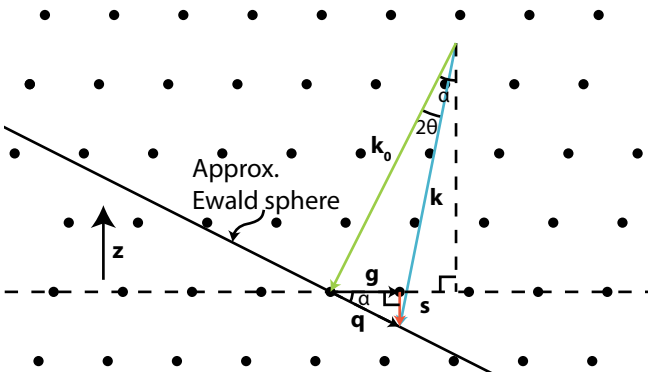

Figure 6.3: Excitation error from beam tilt. Tilting the incident beam by an angle α away from a zone axis (corresponding to the plane shown by the dotted line) introduces an excitation error **s**.

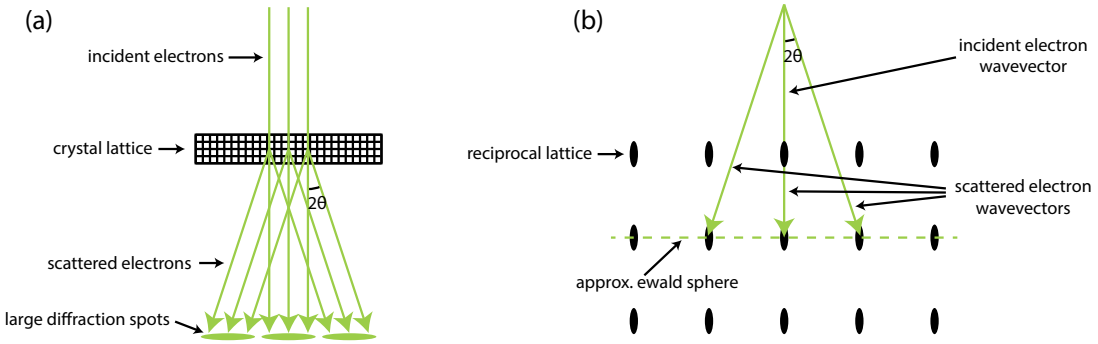

Figure 6.4: Parallel beam diffraction in (a) real space and (b) reciprocal space. Simple parallel beam illumination means the whole beam can perfectly meet the condition $\mathbf{q} = \mathbf{g}$, but creates large diffraction spots if the beam is large at the sample.

and 6.18 combined with the Ewald sphere construct, are sufficient to analyse the effect that different diffraction geometries will have on the expected diffraction pattern.

6.1.2 Diffraction Geometry

The archetypal transmission electron diffraction experiment involves directing a collimated beam of electrons through a sample, and observing the angle to which they diffract, giving information about the crystal such as lattice spacing. Because the beam is collimated, the picture in reciprocal space is very clear, with any electron diffracted to a particular reciprocal lattice point being scattered into the same direction (Figure 6.4). In real space, the result is a set of beamlets exiting the sample which correspond to the set of excited reflections. Each diffracted beamlet is also collimated, with the same transverse size as the incident beam. There are two ways to retrieve the desired angular distributions of the transmitted electrons. The first is to simply propagate into the far field, so that each beamlet will be spatially well-resolved. To be in the far field, the Fraunhofer condition (equation 3.29) requires that either the transverse size of the initial beam is very small (which requires precise beam control), or the propagation distance is very large (which can require an impractically large propagation distance.)

The second way to detect the angular distribution is to pass the transmitted beam through a lens and to detect it in the focal plane, effectively Fourier transforming the field. This is the method used in traditional Transmission Electron Microscopes (TEMs), and when combined with the usual complement of extra lenses and beam apertures, these microscopes become very versatile, able to perform diffraction and real space imaging in a variety of geometries. The obvious

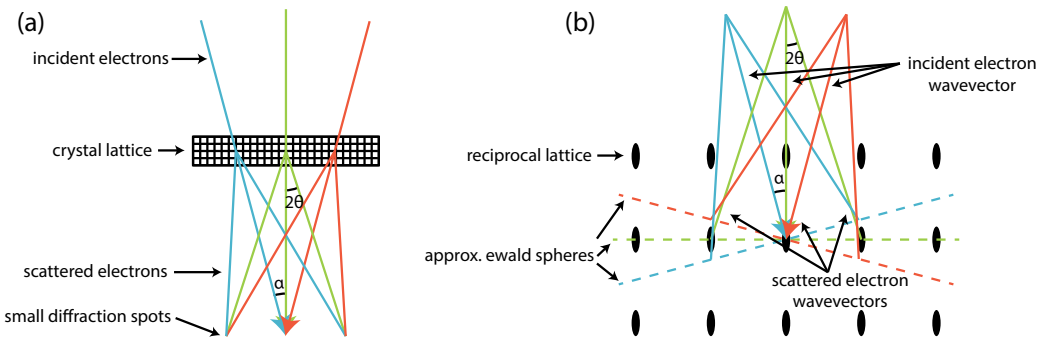

Figure 6.5: Slightly convergent beam diffraction in (a) real space and (b) reciprocal space. Focusing the primary beam on the detector ensures that sharp diffraction spots are seen using only a single lens. Because the beam is no longer parallel through the sample, a small excitation error is introduced for some fraction of the beam, reducing the intensity of the diffraction spots at larger $\mathbf{q}$.

downside to using lenses to transform the transmitted beam is the added complexity of the setup. Indeed, a modern TEM is a collection of extremely precise lenses and electron optics, with a relatively simple (though also very precise) electron source connected to it.

In contrast to a TEM, our setup is primarily a sophisticated electron source connected to some primitive electron optics. Using a single condenser lens close to the source, we focus the beam to a minimum transverse spot size on the detector. Because of the long focal length, the beam only has a small converging angle, thought it is certainly not collimated. This converging beam is incident on the sample as shown on the left in Figure 6.5, meaning there is a spread of incident angles at the crystal. If the crystal were infinite, only the small fraction of the beam that was directed exactly down a zone axis would contribute to any (non-zeroth order) diffracted beams. However, because the crystal is a foil, the resulting reciprocal lattice rods can be intersected by the Ewald spheres of the imperfectly aligned portion of the beam. The increasing excitation error at higher beam angles will only serve to decrease the proportion of these electrons diffracted by a particular scattering vector. Those electrons that *are* scattered, will be scattered *by* the same angle (as opposed *to* a particular angle) as those electrons that were perfectly aligned with the zone axis. This behaviour is illustrated on the right side of Figure 6.5. The result is that the electrons scattered by a set of planes in the crystal form a beamlet that has the same convergence angle as the original incident beam, and so will also be focused to a minimum spot size at the detector. The size of the beam at the sample does not influence the size of the final detected Bragg spots.

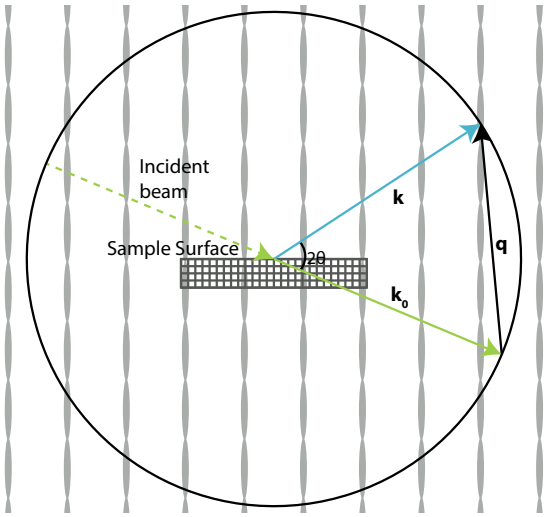

Figure 6.6: Ewald sphere construct and the reciprocal lattice in a RHEED configuration. Diffraction is performed with grazing incidence electrons. The reciprocal lattice points get stretched into very long rods in the direction normal to the surface, because the electrons only penetrate a very short distance into the sample. The same focusing arguments that were used in transmission electron diffraction also apply to RHEED.

This single condenser lens diffraction setup provides an extremely simple and effective means to generate diffraction patterns from thin samples with a large area. The major drawback is that when a sample has only a small transverse area (or it is desired to collect diffraction information from only a small region), then the single lens system is largely ineffective, because the beam size at the sample is fixed by the requirement that the focus be at the detector.

Many of the geometry considerations relating to the formation of transmission electron diffraction patterns also apply to the case of reflection electron diffraction. In Reflection High-Energy Electron Diffraction (RHEED), electrons are directed at a grazing incidence to the sample, so the area of the sample exposed to the beam is much larger. Also, where a crystal foil in transmission diffraction is very thin in the direction parallel to the incident beam, in reflection mode, the sample is *effectively* extremely thin in the direction approximately perpendicular to the incident beam. This is because even if the sample is physically very thick, the grazing electron beam only penetrates to a depth of a few nanometers. The effective sample thinness results in the reciprocal lattice points being stretched into very long rods (which can even overlap) in the direction normal to the sample's surface as illustrated in Figure 6.6.

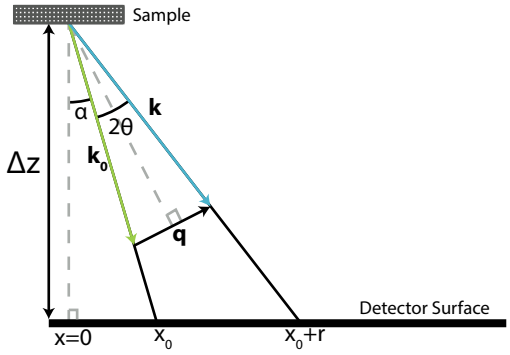

Figure 6.7: Determination of the scattering vector from real space detector measurement. The scattering vector of an electron can be calculated from its detected real space position through an analysis of the vectors.

Determining scattering vector from real space measurements

In our setup, for both transmission and reflection modes, the scattered electrons are detected on a planar detector several centimetres from the sample. This detection is a real-space measurement, with a one-to-one correspondence between the real space detector position and the scattering vector of the electrons. Consider the case where the unscattered electron beam is incident on the detector with known angle α to the detector normal, and is detected at position x_0 as in Figure 6.7. Electrons with scattering vector $\mathbf{q}$ will then be incident with angle $(\alpha + 2\theta)$, and be detected at $(x_0 + r)$. From the figure it can be seen that:

$$\tan(\alpha) = \frac{x_0}{\Delta z}, \qquad \tan(\alpha + 2\theta) = \frac{x_0 + r}{\Delta z}. \tag{6.19}$$

Using trigonometric addition formula for the tangent function, and combining the above two equations, an expression for θ can be found in terms of the detected position, propagation distance, and unscattered incident angle (beam tilt):

$$2\theta = \arctan\left(\frac{r}{\Delta z + \Delta z \tan^2(\alpha) + r\tan(\alpha)}\right). \tag{6.20}$$

The magnitude of the scattering vector can then be calculated using equation 6.6, and the excitation error due to the Ewald curvature and beam tilt can be deduced from equations 6.16 and 6.18.

The science behind electron scattering is complex, and an accurate quantitative description requires a far more detailed analysis than presented here. The basic kinematic theory provides sufficient insight into electron diffraction to allow the geometry of the diffraction system to be understood, and simple crystalline samples to be characterised. It will be seen in the following sections that even a

qualitative explanation of some features of the diffraction data requires the dynamical theory of electron diffraction. However, these features will be touched on only briefly as the main goals of the experiments are studying the possible benefits and disadvantages of performing diffraction using electron bunches obtained from a cold atom electron source.

6.1.3 Transmission Electron Diffraction from Single Crystal Gold

One of the first samples from which we successfully demonstrated transmission electron diffraction was a thin foil of single crystal gold. The 11 nm thick foil came mounted on a standard 3 mm diameter TEM grid, which was placed in the sample holder described in chapter 2. Nanosecond pulses of electrons were used, with the aim of generating a high bunch charge.

To generate the bunches we used a Gaussian excitation laser beam with a Full Width At Half Maximum (FWHM) width of 80 μm at the focus. However, as our intention was to ionise as many atoms as possible we used a very high power in the beam. This high power resulted in significant excitation a long way from the centre of the beam, as well as significant fluorescence and reabsorption, which both had the effect of increasing the excitation area as discussed in chapter 4. The excited area was ultimately determined by measuring the unfocused electron bunch size at the detector, along with the known magnification of the beam path. Using this method, the electron bunch at the source was determined to be approximately Gaussian in shape, with a FWHM width of 1.4 mm. Electrons generated using this method have been measured with a source divergence of $\sigma_{\theta_x} = 0.3\,\mu$rad [105], resulting in a source emittance for the bunch generated here of $\epsilon_x = 50\,\text{nm rad}$. The electrons were focused to a minimum spot size at the Micro-Channel Plate (MCP) as shown in Figure 6.5, resulting in a beam width at the sample of approximately 300 μm, with a corresponding coherence length at this point of $\ell_c = 2\,\text{nm}$.

To ionise as many atoms as possible, the power in the peak of the excitation beam was made to be thousands of times higher than the saturation intensity. At such high powers, it is possible to ionise more of the atoms than the 50% that can be in the excited state at any one time (assuming a steady state population), because during the 5 ns that the blue ionisation laser is depleting the excited state, the excitation laser can excite a non-negligible population from the ground state to the excited state (where it is rapidly ionised by the blue laser). Using a

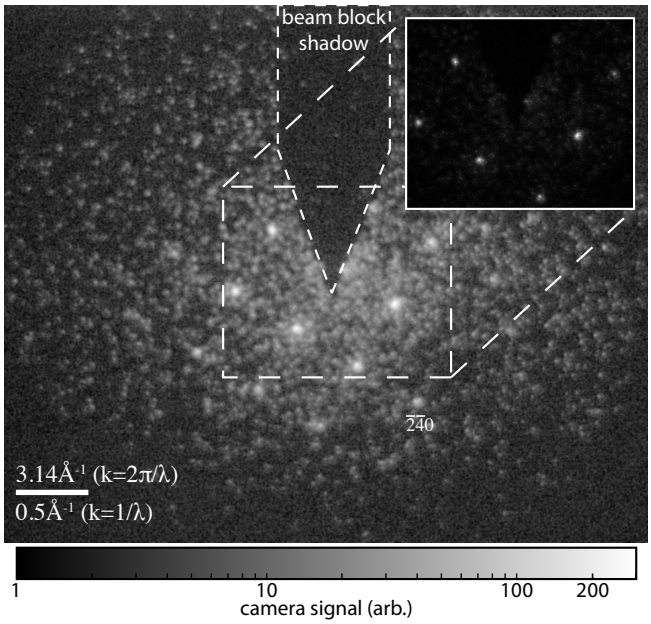

Figure 6.8: Single-shot transmission electron diffraction from gold, formed from a 5 ns pulse of cold electrons. Main image is logarithmically scaled, inset is linearly scaled. Both the quantum mechanical (top) and crystallographic (bottom) conventions for reciprocal space distance are shown.

Faraday cup, the number of electrons per pulse was measured to be 5×10^5 (80 fC), corresponding to an average ionisation fraction of approximately 50% within the ionisation region of the atom cloud when taking into account the density of the cloud, and the volume of the illuminated region.

Single-shot diffraction

The detected diffraction pattern from a single shot directed at normal incidence to the gold foil can be seen in Figure 6.8. Around 10 Bragg reflections can be seen, although the reflections at higher scattering angle become increasingly difficult to distinguish from the diffuse background scatter. The shadow of the beam block can also be seen.

To obtain a higher signal-to-noise ratio, 2000 single shots were averaged (Figure 6.9). In this average, Bragg reflections can be seen all the way out to the edge of the detector, corresponding to a resolution of around 12.5 Å^{-1} (using the quantum mechanical convention for length in reciprocal space, as used elsewhere in this thesis). Closer inspection of the directly averaged image reveals that the Bragg spots have been significantly broadened when compared to the single-shot case, indicating that the transverse coherence of the time-averaged electron beam is reduced compared to any single constituent bunch. This loss of coherence stems

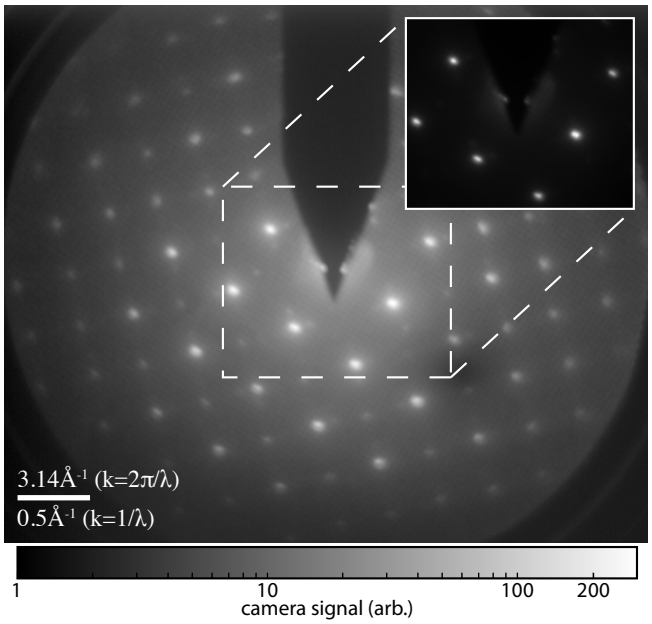

Figure 6.9: 2000 diffraction shots from gold, directly averaged. Averaging results in a higher signal-to-noise ratio, but shot-to-shot beam instabilities lead to a broadening of the Bragg peaks. Main image is logarithmically scaled, inset is linearly scaled.

from a slight beam wobble due to small variations in the decay of the quadrupole magnetic field of the MOT after it is switched off.

The magnitude of this drift was investigated by removing the gold sample from the beam path, and identifying the location of the beam focus on the MCP over 1000 shots. A scatter plot of these locations can be seen in Figure 6.10, which shows the beam drifts by about half a millimetre over 100 seconds. It can also be seen that the distribution of shot positions isn't a Gaussian as might be expected if the deflection was a fully stochastic process. The presence of two main lobes connected by three observable paths indicates that the source of the deflection is periodic, with a characteristic magnitude. It can also be seen that the general pattern is elongated diagonally, as seen in Bragg spots of the averaged diffraction pattern.

The most likely sources of the periodic deflection are magnetic fields induced by the switch-off of the quadruple coils at 10 Hz, and those generated by the 50 Hz mains power. Further characterisation of the cause of this periodic deflection was not deemed worthwhile, since in either case fixing the problem would have required a fundamental redesign of the CAES.

To compensate for the beam wobble, successive single-shot images were registered. The eleven brightest spots were used to adjust the alignment by performing a cross correlation of the individual images g, and the unregistered average f, in

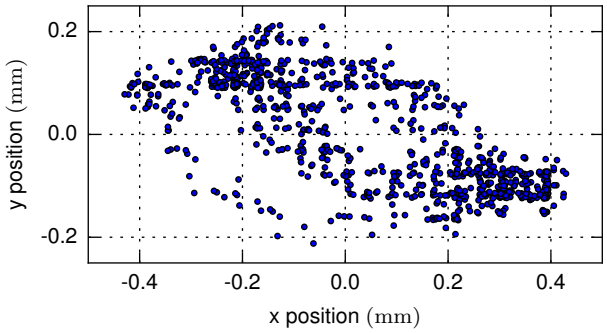

Figure 6.10: Beam drift over 100 seconds. The beam focus drifts around on the MCP due to the beam interacting with stray magnetic fields. The detected positions of 1000 shots are shown, acquired at 10 shots per second.

the region $\mathbb{S}$ surrounding the spots:

$$(f \star g)(u, v) = \iint_{\mathbb{S}} f^*(x, y) g(x + u, y + v)\, dy\, dy. \tag{6.21}$$

Each individual image was correctly aligned by transversely offsetting the image by a number of pixels equal to the values of u and v for which $(f \star g)(u, v)$ was a maximum.

Because the peaks in the unregistered average were relatively broad, the cross correlation between the unregistered average and each single shot also had a maximum which was somewhat broad (in u and v). This broadening of the peak in the cross correlation increased the uncertainty in the optimum values of u and v to use to correctly align single images. To increase the accuracy of alignment, two rounds of cross correlation were performed: the first between each of the single images and the unregistered average, and the second between each of the single images using the new, registered average, which had significantly sharper peaks. In practice, the second round of cross correlation resulted in a negligible improvement in image alignment.

The region $\mathbb{S}$, over which integration was performed was the set of x, y values contained in circles centred on the brightest Bragg spots, with radius slightly larger than double the maximum size of the blurred spots. Only a small region around the brightest Bragg spots was integrated, because it was not expected that there would be any correlated signal away from these reflections, so integrating over the whole image would only serve to degrade the fidelity of the alignment process. This form of image registration only accounts for relative translations in each single image, and not for rotations or stretching that may result from the scattered electrons interacting with a varying magnetic field. In practice, it

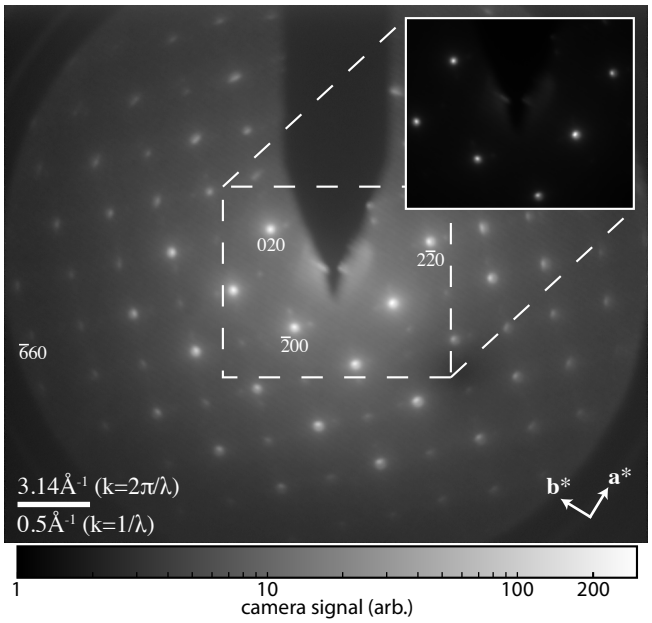

Figure 6.11: 2000 diffraction shots from gold averaged by registering individual images. Registration is possible due to the high signal-to-noise ratio in the single shots, and recovers the sharpness in Bragg peaks lost in direct averaging. The reciprocal lattice vectors $\mathbf{a}^*$, $\mathbf{b}^*$ are drawn to scale. Main image is logarithmically scaled, inset is linearly scaled.

appeared that the beam deflection did occur before the beam interacted with the sample, so only translations were expected.

The resulting registered average can be seen in Figure 6.11, showing notably sharper Bragg spots. Additionally, the spots in the registered image appear circular, as would be expected from the shape of the beam, and not elliptical as in the unregistered average.

An improvement in the signal-to-noise ratio is apparent from the integral of one of the brighter Bragg spots in the direction orthogonal to that of greatest broadening (Figure 6.12). The single shot shows a sharp Bragg peak, but also a significant amount of noise, as can be expected given the relatively small number of electrons per shot. The noise being considered in this case is not background signal in the MCP or image sensor, but the probabilistic variation in the number of electrons landing in any given region given the finite number of samples (which will be Poisson distributed). This noise is largely eliminated in the direct average containing 2000 single shots, but the peak is broadened, and the peak height reduced. The registered average on the other hand, maintains the reduced noise of the direct average, while fully recovering peak height and narrow width. The peak heights in each case have been normalised by dividing the counts in each lineout by the counts at the top of the peak in the single shot.

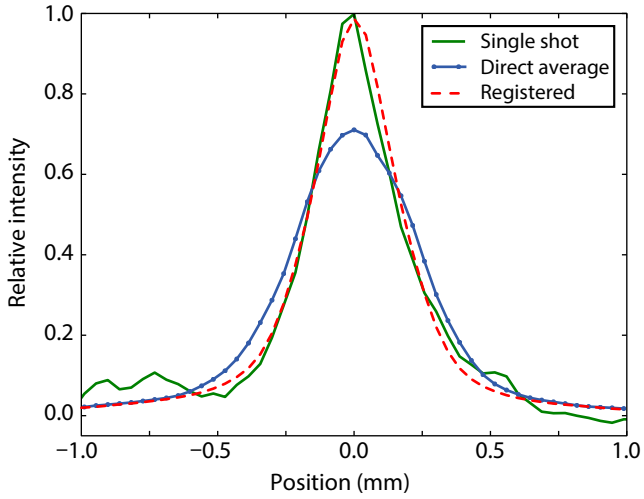

Figure 6.12: A lineout of the $(\bar{2}00)$ Bragg reflection in the $\mathbf{b}^*$ direction of the gold reciprocal lattice. Registering multiple single-shot images averages the noise without resulting in Bragg spot broadening, as happens when shots are directly averaged.

It is significant that single images contain sufficient information to align successive shots, because it gives some credibility to the claim that they are truly "single-shot" images. In the context of imaging single macromolecules using Coherent Diffractive Imaging (CDI), it has been proposed that many single shots of many individual, randomly aligned molecules can be combined to form the full reciprocal space representation [23, 149]. This is only possible if each individual image has enough signal to allow correct alignment relative to the other images [21, 150].

Our experiment forms a simple analogue of this type of alignment problem. While we know that our sample orientation is fixed, it is our beam that changes orientation. The signal in any individual image however, is sufficient to correctly align it with successive images.

Kinematic diffraction from gold

To explain the features of the diffraction pattern shown in Figure 6.11, we can use some of the kinematic theory described previously. The first step involves determining the expected relative intensities of the Bragg reflections by calculating the structure factors $V_{\mathbf{g}}$ of gold, for each reciprocal lattice point.

The conventional choice to describe the crystal structure of gold is to use a face-centred cubic (*fcc*) unit cell, which contains four primitive lattice points. The four primitive lattice points are conventionally placed in the centre of the cube faces, and on the cube vertices (with the appropriate fraction of each primitive lattice point contributing to the total number enclosed). The primitive basis

contains one gold atom, conventionally located on the origin of the primitive lattice points.

The length of the cubic basis vectors (sometimes called the *lattice parameter*) of gold is $|\mathbf{a}| = a = 0.40782\,\text{nm}$ at 25°C [151]. In a cartesian basis, the lattice basis vectors become:

$$\mathbf{a} = a\hat{\mathbf{x}} \qquad \mathbf{b} = a\hat{\mathbf{y}} \qquad \mathbf{c} = a\hat{\mathbf{z}}, \tag{6.22}$$

where $\hat{\mathbf{x}}$, $\hat{\mathbf{y}}$, $\hat{\mathbf{z}}$ are unit vectors. The corresponding reciprocal lattice vectors are calculated using equation 6.2:

$$\mathbf{a}^* = \frac{2\pi}{a}\hat{\mathbf{x}} \qquad \mathbf{b}^* = \frac{2\pi}{a}\hat{\mathbf{y}} \qquad \mathbf{c}^* = \frac{2\pi}{a}\hat{\mathbf{z}}. \tag{6.23}$$

Rather than placing a fraction of an atom at each of 8 partial primitive lattice sites within a cell, complete primitive lattice points can equivalently be placed at one vertex, and in the centre of the closest 3 faces. The cubic lattice then has a four atom basis, with positions, $\mathbf{x}_j$ given by:

$$\mathbf{x}_1 = \mathbf{0} \qquad \mathbf{x}_2 = \frac{1}{2}\mathbf{a} + \frac{1}{2}\mathbf{b} \qquad \mathbf{x}_3 = \frac{1}{2}\mathbf{a} + \frac{1}{2}\mathbf{c} \qquad \mathbf{x}_4 = \frac{1}{2}\mathbf{b} + \frac{1}{2}\mathbf{c}. \tag{6.24}$$

We can now write an expression for the structure factor for a given reciprocal lattice vector $\mathbf{g}_{hkl}$. Since all the atoms in the unit cell are gold, they all have the same value for the scattering factor when scattered to a given direction, i.e. $\tilde{V}_j(\mathbf{g}_{hkl}) = \tilde{V}_{\text{gold}}(\mathbf{g}_{hkl})$. Equation 6.11 then becomes:

$$\begin{aligned} V_{\mathbf{g}_{hkl}} &= \frac{1}{\mathbf{a}\cdot(\mathbf{b}\times\mathbf{c})}\tilde{V}_{\text{gold}}(\mathbf{g}_{hkl})\left[e^{-i\mathbf{g}_{\mathbf{hkl}}\cdot\mathbf{x}_1} + e^{-i\mathbf{g}_{\mathbf{hkl}}\cdot\mathbf{x}_2} + e^{-i\mathbf{g}_{\mathbf{hkl}}\cdot\mathbf{x}_3} + e^{-i\mathbf{g}_{\mathbf{hkl}}\cdot\mathbf{x}_4}\right] \\ &= \begin{cases} \dfrac{4\tilde{V}_{\text{gold}}(\mathbf{g}_{hkl})}{a^3}, & \text{for } h,\, k,\, l \text{ all even or all odd} \\ 0, & \text{for } h,\, k,\, l \text{ mixed even and odd.} \end{cases} \end{aligned} \tag{6.25}$$

The relative intensity of the Bragg reflections is directly related to the structure factor (equation 6.9), so equation 6.25 states that only those reciprocal lattice points with all even, or all odd Miller indices should be visible. Since the electron beam is nominally directed along the $\langle 001\rangle$ zone axis, it would be expected that only the $\{hk0\}$ spots are observed, where h and k are even. The full linearly scaled diffraction image confirms this, as can be seen in Figure 6.13(a). However, when looking at the logarithmically scaled image in Figure 6.13(b), many more spots can be seen, including diffraction orders *between* the expected (h, k, l = even)

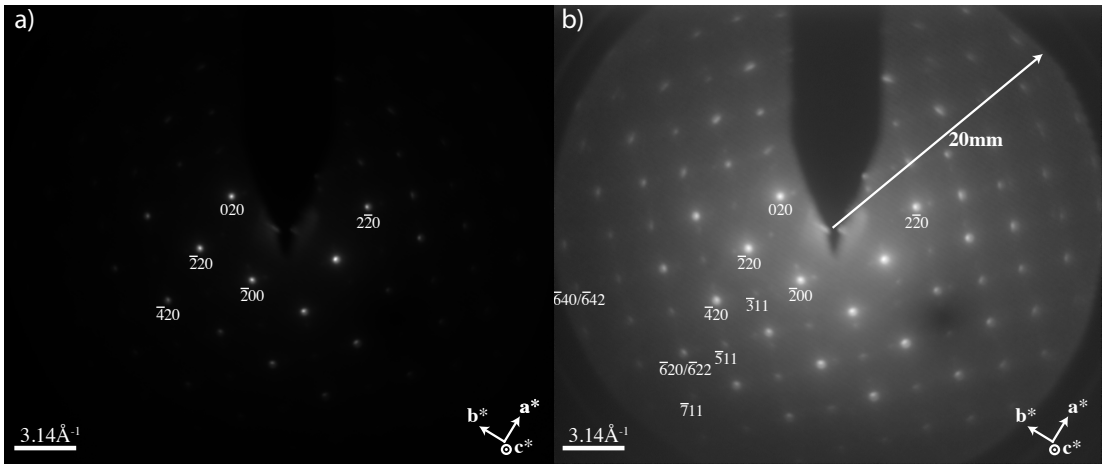

Figure 6.13: Diffraction pattern from gold along the ⟨001⟩ zone axis. (a)A linearly scaled image shows only the expected Bragg reflections for $k = 0$, with all Miller indices being even. (b)A logarithmically scaled image shows that at larger detector radii, Bragg spots appear with all odd Miller indices, which happens because of the curvature of the Ewald sphere.

spots.

The extra diffraction spots are visible because of the curvature of the Ewald sphere. The sphere curves away from the $l = 0$ reciprocal lattice points (Zeroth Order Laue Zone, ZOLZ), towards the $l = 1$ points (First Order Laue Zone, FOLZ), as $\mathbf{q}$ increases. In the $l = 1$ plane, only odd h and k values have non-zero structure factors. The extent of the curvature is illustrated by considering the excitation error in the $\mathbf{c}^*$ direction for the $l = 0, 1$ reciprocal lattice points as a function of radial detector position as shown in Figure 6.14, which is calculated using equation 6.16.

The figure shows that at detector positions with radius greater than about 13 mm, the excitation error from the FOLZ is lower (in magnitude) than that for the ZOLZ. The effect that the excitation error has on the relative intensity of the Bragg spots can be calculated using equation 6.14, which takes into account the elongation of the reciprocal lattice points due to the small thickness of the sample. The expected intensity also depends on the value of the scattering factor which decreases markedly as scattering angle increases [148] as shown in Figure 6.15.

Taking into account both the angular dependence of the scattering factor, and the excitation error due to the curvature of the Ewald sphere, the expected Bragg spot intensities for both the ZOLZ and FOLZ were calculated (Figure 6.16). The results suggest that the combined intensity of the diffraction spots from the ZOLZ and FOLZ should dip to less than 10^{-4} of the maximum at a radius of around 14 mm before increasing again as the excitation error of the FOLZ reduces to

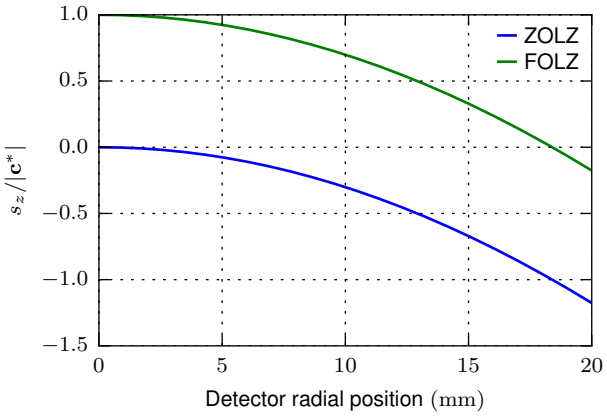

Figure 6.14: Excitation error from Ewald sphere curvature. As scattering angle increases, the Ewald sphere curves away from the reciprocal lattice points with $l = 0$ (ZOLZ), and towards the $l = 1$ points (FOLZ). Higher scattering angles are detected at increasing radial positions on the detector.

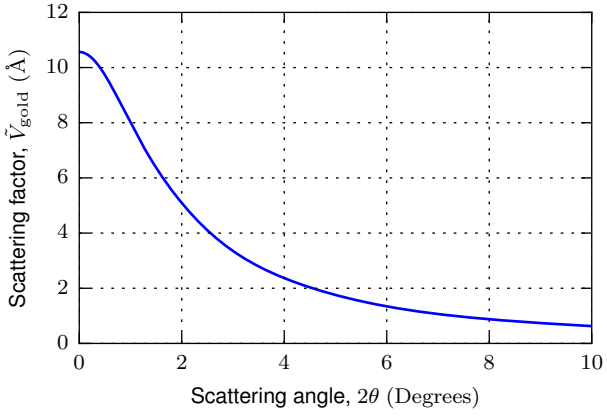

Figure 6.15: Electron scattering factor of gold. The scattering amplitude of an electron scattering off an isolated gold atom decreases as scattering angle increases.

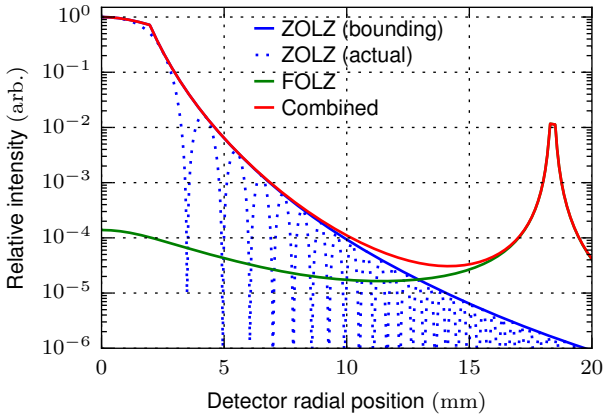

Figure 6.16: Kinematically expected relative intensity of Bragg reflections. The expected intensity takes into account excitation error caused by Ewald sphere curvature, and the angular dependence of the scattering factor. The intensity is modulated by a $\mathrm{sinc}(x)$ function, which is bounded by a $1/x$ function at larger scattering angles.

zero. This would indicate that there should be a clear ring of much dimmer spots between the two Laue zones, which is not seen in Figure 6.13(b).

The main reason for the departure from the expected intensity profile is that the single scattering approximation of kinematical theory is a very bad approximation in this experiment (which is further discussed below). However, another factor that works to reduce the modulation depth of intensity profile is that the beam is not collimated as it passes through the crystal. This leads to a spread of excitation errors for any given Bragg reflection, which can be calculated using the known beam semiangle and equation 6.3. The semiangle of the electron beam used in these experiments was $\alpha = 0.13°$, which leads to a position dependent excitation error shown in Figure 6.17. The excitation error resulting from the non-zero beam semiangle is small compared to that caused by the curvature of the Ewald sphere, so the effect it has on expected intensity is modest, shown in Figure 6.18.

While kinematic theory would predict a modulation in the intensity of the Bragg spots by more than a factor of 10^4, the actual decrease in modulation is closer to 10^2 based on the intensity of the spots in Figure 6.11. The disparity between theory and experiment is due to the high probability that electrons undergo multiple elastic and inelastic scattering events, which can be explained using dynamical scattering theory [145], but which is beyond the scope of this thesis.

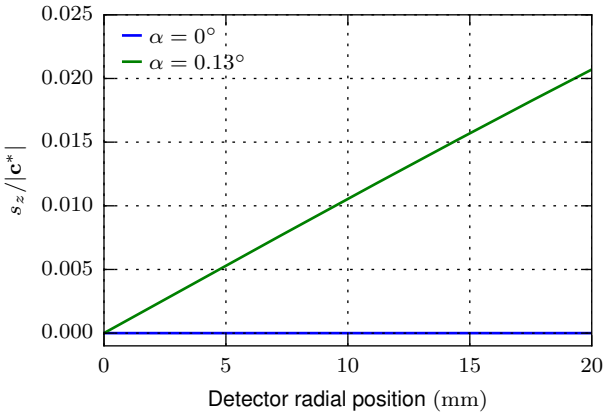

Figure 6.17: Excitation error due to uncollimated beam. The diffraction geometry used results in a range of beam angles passing through the sample. The beam semiangle is $\alpha = 0.13°$, leading to a small range of excitation errors as scattering angle increases.

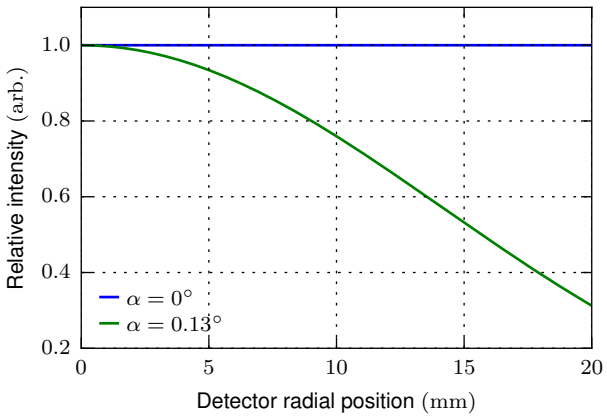

Figure 6.18: Kinematically expected intensity variation due to uncollimated beam. As scattering angle increases, some portion of the beam has an increasingly large excitation error, resulting in reduced Bragg spot intensity.

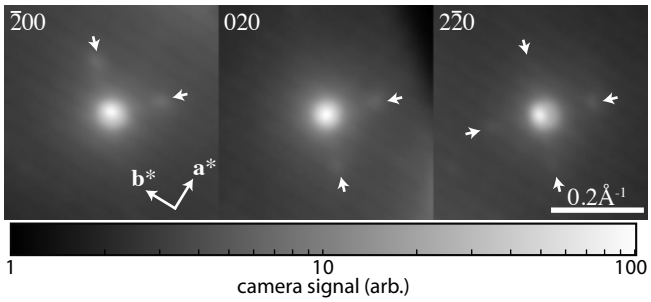

Figure 6.19: Diffraction from crystal twins. The two satellite spots around the $(\bar{2}00)$ and (020) reflections, and the rightmost spot around the $(2\bar{2}0)$ reflection, are due to diffraction from crystal twins. The other spots visible around the $(2\bar{2}0)$ reflection are due to the electron diffracting twice: once each from two different twins. The small arrows indicate the positions of the faint satellite spots. The reciprocal lattice vectors are not to scale.

Non-kinematic features

The most obvious departure from kinematic diffraction in the gold sample is the lack of any clear separation between the zeroth and first order Laue zones. Multiple scattering can reduce the expected modulation in Bragg spot intensity by the same mechanism as uncollimated illumination of the sample. After an electron is scattered once, it is travelling along a different direction to the original beam, so its Ewald sphere for subsequent scattering events is oriented differently from the unscattered illumination beam.

Another departure from the case of single elastic scattering is the presence of significant background electron signal between the Bragg spots, which can be seen in the logarithmically scaled diffraction images. This inter-spot background is largely caused by inelastically scattered electrons, many of which will have scattered multiple times.

The Bragg reflections are also accompanied by two or more satellite spots, offset from the main reflection at 45° from the direction of the reciprocal basis vectors, which can be more clearly seen in Figure 6.19. These satellites are the result of {111} crystal twinning, which can form when (100) gold films are prepared by evaporation [152].

There are two different mechanisms behind the satellite creation. The two relatively strong satellites that can be seen around the $(\bar{2}00)$ and (020) Bragg reflections are created directly by diffraction from the crystal twins, which also produces the rightmost spot around the $(2\bar{2}0)$ reflection. These satellite spots are not a result of multiple scattering, they simply correspond to diffraction of gold crystals that are not in the assumed (100) orientation. The other satellites

around the $(2\bar{2}0)$ reflection *are* a direct result of multiple scattering. They arise from double diffraction, where electrons are first diffracted by a (100) oriented domain, and then diffracted again by one of the twins.

Dynamical effects would not normally be seen to such a large extent with the very thin gold foil because electron energies used in a transmission electron microscope are typically ten times greater than used here, resulting in a much lower scattering cross section, and interactions that more closely match the simple kinematic theory.

Ultrafast electron diffraction from gold

As discussed in chapter 5, it was possible to produce ultrafast cold electron bunches using a Two-Colour Multiphoton Excitation (TCMPE) process provided atoms were excited above the classical ionisation threshold to ensure fast electron liberation. While the TCMPE process yielded only a few hundred electrons per shot, this was still sufficient to obtain clear diffraction patterns from gold by averaging many shots. A logarithmically scaled 1000 shot average generated using these ultrafast electron bunches can be seen in Figure 6.20. This image was averaged using the same registration method as before, however only a region around the central spot was included in the cross correlation because the other diffraction maxima did not contain sufficient signal for alignment. Each diffraction spot is surrounded by an obvious halo, which arises from unfocused hot electrons produced by single colour multiphoton excitation.

While the electron pulses used in this diffraction experiment were not themselves streaked to verify that they were ultrafast, the calculated total photon energy means that they should have an excess energy between 0 and +2 meV. Even small positive excess energies were shown to lead to ultrafast electron liberation in the work described in chapter 5, so it is reasonable to assume that these bunches were truly ultrafast. However, it is possible that small changes in the field strength caused by day-to-day movement of the excitation lasers could lead to a situation where the excess energy would be less than that calculated. Under these circumstances, the electron pulses would be much slower, though the resulting images would appear identical for a static target, such as the gold foil.

The generation of diffraction patterns using ultrafast electron bunches represents the fulfilment of a significant aim of the CAES project, however the immediate impact is likely to be limited. While the individual electron bunches lasted only a few tens of picoseconds, the very low bunch charges meant that single-shot images could not be produced. Since one of the potential advantages

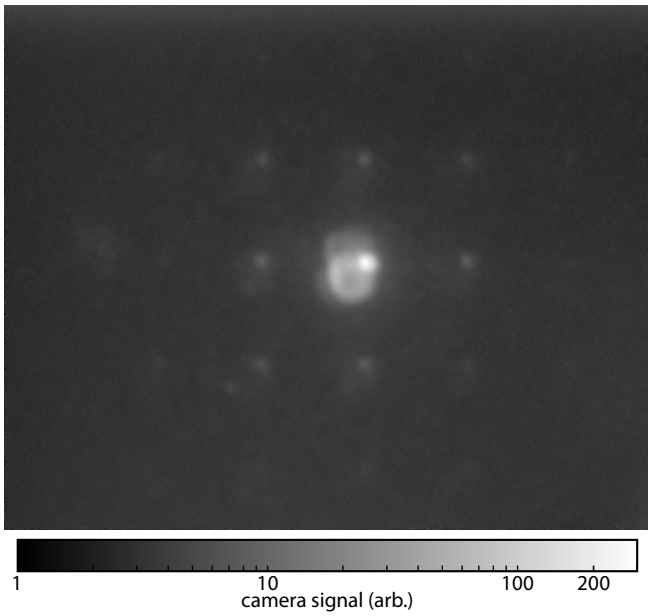

Figure 6.20: Ultrafast electron diffraction from gold. The image is a registered average of 1000 shots. Electron bunched were produced using TCMPE, but some hot electrons produced from single colour MPE can also be seen as a halo around the Bragg reflections.

of cold bunches is that the deleterious effects of space-charge expansion may be alleviated for high charge bunches, the current inability to produce these large bunches is a significant impairment. Where experiments only require small numbers of electrons per bunch, it is likely that solid state photocathodes combined with appropriate aperturing will continue to be the source of choice due to their relative simplicity.

It is important to note however, that while the ultrafast electron bunches generated using the excitation method employed here did not contain sufficient charge to produce single-shot images, other excitation methods should be capable of doing so. Thus, while ultrafast single-shot diffraction patterns have not yet been generated using a cold atom electron source, it now seems that doing so will require only incremental progress from what has been achieved so far.

6.1.4 Diffraction from Graphite

In addition to gold, a variety of other off-the-shelf TEM calibration samples were tested to see if any diffraction patterns could be observed. These calibration samples covered a range of lattice spacings and morphologies, from polycrystalline aluminium films, to thin crystals of catalase, a large biomolecule [153–155]. For a number of reasons, none of these samples showed any visible diffraction maxima

(either Bragg spots or Debye-Scherrer rings). For the samples with large lattice spacing, it was calculated that the resolution of the detector was not sufficient to resolve any generated Bragg reflections, since the scattering angle would be small, and the propagation distance was only around 8 cm.

Some of the samples, such as crocidolite (a type of asbestos) were known to be made of a large number of isolated crystal fragments, which possibly cover only a small fraction of the total TEM grid area. For these samples, it is likely that any diffraction spots produced by the crystals would not be visible above the signal produced by the amorphous diffraction from the underlying carbon support. Compared with a modern TEM, our electron beam is very large (and unstable), which prevents targeting of any region less than 300 μm or so in diameter, which can be thousands of times the area of a desired crystal.

The relatively low energy of the electrons was suspected to be the biggest limitation with respect to seeing diffraction from most of the samples. Lower energy electrons scatter more strongly than high energy electrons, and it was suspected that most of the samples were simply too thick, so that absorption or multiple elastic and inelastic scattering events prevented formation of the diffraction pattern expected from a kinematical approximation.

One workaround to the low electron energy problem was to use only very thin samples. The thinnest possible sample is a single atomic layer, which can be realised by suspended graphene sheets. Samples of graphene on TEM grids were obtained from *Graphene Supermarket*, which were stated to have 60 to 90% coverage of 1 to 6 layer graphene suspended on a lacy carbon mesh [156]. Most the samples showed no clear signs of diffraction, however one region of one particular sample did display clear diffraction peaks as can be seen in Figure 6.21. Graphene can be considered structurally as the Two-Dimensional (2D) form of graphite, which consists of alternating layers of graphene in an AB sequence. Graphite is described by a hexagonal lattice system with a four atom basis (2 atoms for each of the two layers within the unit cell). The real and reciprocal basis vectors are respectively given by:

$$\mathbf{a} = \frac{a\sqrt{3}}{2}\hat{\mathbf{x}} - \frac{a}{2}\hat{\mathbf{y}} \qquad \mathbf{b} = \frac{a\sqrt{3}}{2}\hat{\mathbf{x}} + \frac{a}{2}\hat{\mathbf{y}} \qquad \mathbf{c} = c\hat{\mathbf{z}} \tag{6.26}$$

$$\mathbf{a}^* = \frac{2\pi}{a\sqrt{3}}\hat{\mathbf{x}} - \frac{2\pi}{a}\hat{\mathbf{y}} \qquad \mathbf{b}^* = \frac{2\pi}{a\sqrt{3}}\hat{\mathbf{x}} + \frac{2\pi}{a}\hat{\mathbf{y}} \qquad \mathbf{c}^* = \frac{2\pi}{c}\hat{\mathbf{z}}, \tag{6.27}$$

where $a = 0.246\,\text{nm}$ and $c = 0.671\,\text{nm}$ [157].

The diffraction pattern in Figure 6.21, shows that the sample is not a sin-

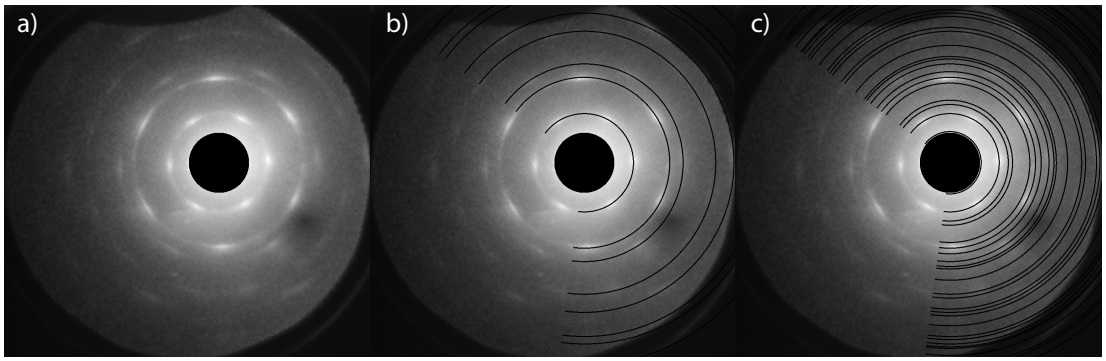

Figure 6.21: Diffraction from the graphene/graphite sample. (a) 100 shot average of the graphene/graphite sample. (b) Data overlaid with rings indicating expected diffraction angles for graphene, or for graphite that is illuminated only along the ⟨001⟩ zone axis. (c) Data overlaid with the many rings expected from totally randomly oriented graphite domains.

gle crystal, as evidenced by the appearance of rings, but neither is it a set of completely randomly aligned domains. There are obvious maxima in the ring structure which show the six-fold rotational symmetry expected from graphene. The predicted diffraction angles for graphene (or graphite when illuminated along the ⟨001⟩ zone axis) is shown in Figure 6.21(b), which clearly matches the observed diffraction angles.

Given that no other graphene sample displayed any discernible diffraction at all, it is probable that the scattering from the underlying carbon support dominated any diffracted signal from the graphene sheets. It is likely that the observed diffraction was from a chunk of many layer graphene, ie. a piece of graphite. While the domains of the graphite chunk had some disorder in their **a** and **b** lattice vector alignment, it appears as though all chunks had the same **c** alignment. This can be seen from Figure 6.21(c), which shows the expected diffraction rings from a set of randomly aligned graphite domains. The extra rings come from the additional atomic planes possible in a three dimensional crystal compared with the 2D graphene sheet. The total lack of these extra planes can be seen even more clearly in Figure 6.22, which shows the radially averaged diffracted intensity for the graphite sample. The only peaks present perfectly match those expected from graphene or **c** axis aligned graphite. The non-orthogonal nature of the graphite basis vectors mean that crystallographically equivalent planes can be defined by Miller indices that are not obviously related. The labeled diffraction peaks in Figure 6.22 therefore represent only one of many possible sets of labels.

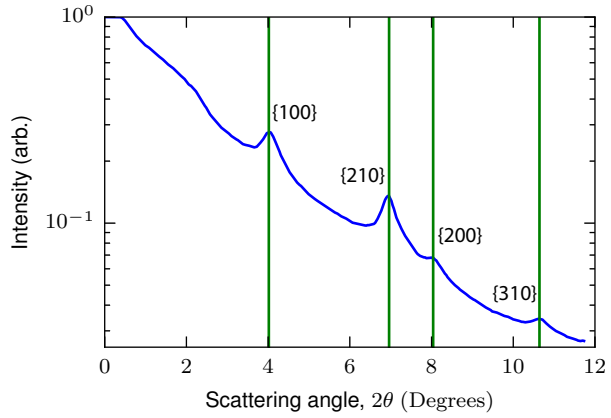

Figure 6.22: Radially averaged diffraction intensity of graphite. The only peaks observed correspond to either graphene, or grains of graphite with their **c** axis all aligned in the same direction.

6.1.5 Diffraction from Aluminium using a Biasing Potential

High energy electron beams could not be generated in the Cold Atom Electron and Ion Source (CAEIS) because the accelerator electrodes would undergo electrical breakdown at high potentials. This electrical breakdown limited the possible electron energy to about 11.6 keV at the exit of the accelerator, which in turn limited the thickness of sample from which diffraction could be observed. To boost the maximum achievable electron energy, modifications were made to the sample holder to allow the samples to be electrically biased. By applying a positive potential to the sample, the electron energy could be increased as they passed through the sample, allowing thicker samples to be studied.

To test the effectiveness of increasing the electron energy, a polycrystalline evaporated aluminium foil was illuminated at a range of biases. The sample was quoted to be 31 nm thick [158], and had previously shown no conclusive evidence of diffraction when illuminated with 11.6 keV electrons. Figure 6.23 shows the scattered electron intensity as the sample bias was increased from 0 to +8.5 kV. With the sample held at ground, only faint hints of rings can be seen, which could easily be interpreted as amorphous diffraction rings due to short range order in any underlying support. As the bias was increased, the rings become visibly more defined and separated. This was accompanied by a drift in the overall beam position, as the beam path was distorted by the fields generated from the biased sample holder.

The relative positions of the rings show good agreement with that expected from aluminium (Figure 6.24). The effective propagation distance for the pre-

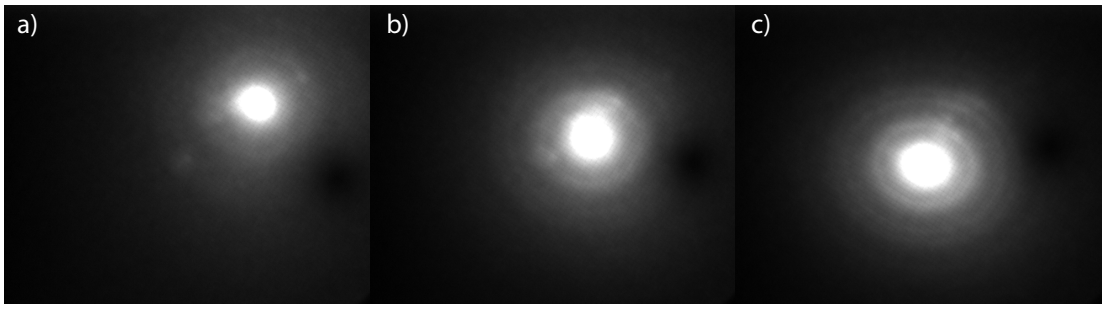

Figure 6.23: Diffraction from aluminium at increasing positive bias. (a) No bias. Diffraction rings barely visible. (b) +4.2 kV bias. Ring structure enhanced, but still very unclear. (c) +8.5 kV bias. Clearer ring structure with multiple rings discernible.

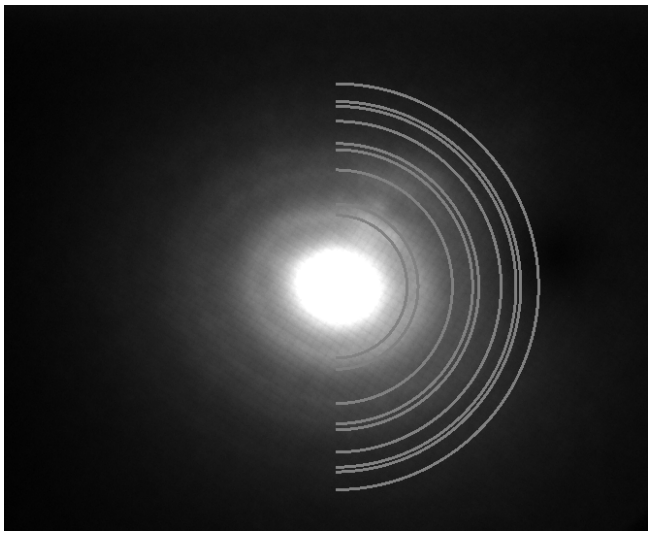

Figure 6.24: Diffraction from aluminium with a +8.5 kV bias applied. The observed rings correspond well to those expected from the known structure of aluminium (overlaid on right half of image), though the biasing results in some post-sample distortion of the diffracted beam.

dicted rings was adjusted to fit the observed ring positions, since the electron trajectory after scattering off the biased sample was curved. Also, the rings have been slightly warped out of the normal circular shape due to the post-sample field. Despite this warping, the sample clearly shows the rings expected from polycrystalline face-centred cubic aluminium [159].

Even at a total electron energy of 20.1 keV, the detected electron profile is dominated by non-kinematically scattered electrons. The improvement in the visibility of the diffraction pattern confirms that electron energy is a limiting factor in our electron diffraction setup. The biasing potential could not be increased further due to electrical breakdown, meaning that biasing the sample increased the maximum usable sample thickness only modestly.

While the cold atom electron source has been shown to produce electron

bunches with favourable temporal and coherence characteristics, the implementation and integration of the source with the electron optics impose severe limitations in terms of performing transmission electron diffraction experiments. Nevertheless, simple proof-of-principle transmission diffraction experiments were successfully performed, and limitations and advantages of the source were identified, which will provide a basis for future development.

6.1.6 Reflection High Energy Electron Diffraction

To circumvent the problems of limited sample choice associated with transmission electron diffraction, we investigated reflection mode diffraction experiments. Reflection electron diffraction typically refers to one of two categories: low energy (electron energy ∼50 eV), which detects back-scattered electrons, or high energy (electron energy ∼10 keV), which operates at a grazing incidence. Both methods have been operated in ultrafast modes to observe surface dynamics resulting from ultrafast pump lasers [160, 161].

RHEED is a surface-sensitive diffraction technique routinely used to monitor crystal surface quality and epitaxial crystal growth [162, 163]. RHEED is a useful technique to further demonstrate diffraction from our source, both because the electron energies typically required fall into the range we can easily generate, and because high quality single crystals are more readily available as bulk wafers than as the nanometre-thick foils needed for transmission electron diffraction.

To adjust the system for RHEED, all that was required was to rotate the sample through 90 degrees such that the electron beam was incident on the sample surface at a glancing angle. Experiments were performed at an electron energy of 11.6 keV. Figure 6.25 shows RHEED patterns from a ⟨100⟩ silicon wafer, which was HF etched to remove the native oxide layer immediately prior to transfer to the vacuum chamber. The beam was nominally incident on the crystal from the [110] direction at 0° polar angle. Since the sample stage could not be rotated in the azimuthal direction, it is likely that the wafer was slightly misaligned, which would account for the apparent horizontal asymmetry of the Bragg reflections at any particular polar angle. For clarity the RHEED patterns shown are 100 shot averages, however Bragg reflections were easily visible from a single shot as shown by the inset.

Using RHEED, Bragg peaks were clearly observable for every monocrystalline sample tested, including ⟨100⟩ silicon, ⟨111⟩ silicon, sapphire, and diamond. While the silicon samples were originally HF etched before being placed in the

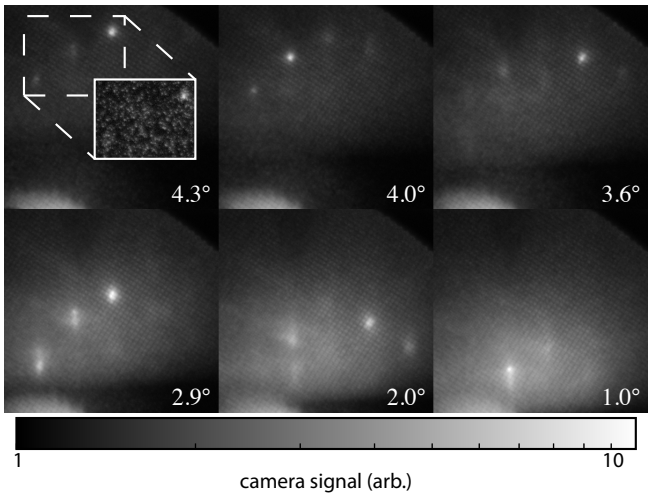

Figure 6.25: 100 shot averages of RHEED from silicon ⟨100⟩ at a range of polar angles. Inset: a single shot of the region indicated, clearly showing a Bragg reflection.

vacuum chamber, subsequent removal and replacement saw only a modest reduction in the quality of the diffraction images due to the amorphous oxide layer on the surface. This is promising for future experiments, because it should allow any highly polished monocrystalline sample to be used, even if it is prone to forming thin oxide layers. Such flexibility in sample choice should permit future pump-probe, or spin-polarised electron experiments.

Cold electron RHEED offers a promising opportunity to investigate near-surface dynamics on nanosecond time scales. The high transverse coherence of the beam should also allow coherent scattering to be observed from structures tens of nanometres wide, such as quantum dots and optical metamaterials. Cold electron sources with bunch shaping to control space-charge induced brightness degradation are perhaps uniquely placed to perform these studies, due to their potential to deliver high bunch charges and high coherence at relatively low electron energies. Using very high electron energies to mitigate space-charge effects is not an option for RHEED, since very energetic electrons penetrate too deeply to accurately probe surface structure.

6.1.7 Summary of Electron Diffraction Experiments

This section presented results of initial electron diffraction experiments performed with the CAES. Using a single pulse of electrons with nanosecond-duration, diffraction patterns from a thin gold foil were obtained that had enough signal to allow registration of multiple images, compensating for a shot-to-shot variation in the beam direction. Many potential applications of cold atom electron sources

require high bunch charge, so successful demonstration of single-shot diffraction is an important step forward. Diffraction images of the gold foil were also generated using ultrafast electron bunches, but only very low bunch charges could be achieved due to limitations of the available ultrafast excitation pathway, as discussed in chapter 5.

Diffraction from a limited number of other transmission samples was also observed, but the low limit on electron energy imposed by the accelerator design meant that thicker samples did not produce observable Bragg spots because of strong multiple electron scattering. The ability to operate with electron energies in the 100 keV range used in typical transmission electron diffraction experiments will be an important consideration in future CAES designs, and incorporating high potential accelerators with atom trapping optics could prove challenging.

Instability in electron beam trajectory caused by the changing magnetic fields from the MOT and Zeeman slower also reduced sample choice, as the beam could not be stably positioned over a small region at the sample. While this instability allowed demonstration of single-shot diffraction pattern registration, it generally had negative impacts on experimental results. Future CAES designs will need to take into account the requirement of high beam stability, which could be achieved either by removing the need to switch magnetic fields, or by switching them more rapidly as is possible in alternating-current MOTs [164]. RHEED was also successfully demonstrated from for a variety of single crystal samples, with the accessible electron energy being in the desirable range to perform this sort of reflection mode diffraction.

While the high transverse coherence of electrons generated in the CAEIS resulted in the production of sharply defined Bragg peaks without the need to aperture the beam, none of the diffraction experiments demonstrated explicitly required a highly coherent beam. In the next section, simulations are presented of electron diffraction from nanoscale milled apertures, which do require high transverse coherence in the sample plane, and so benefit from the high initial coherence of electrons produced in the CAES.

6.2 Coherent Diffractive Imaging Simulations

Coherent Diffractive Imaging (CDI) aims to reconstruct both the amplitude and phase of a wavefield after it has passed through a sample, by measuring only the propagated intensity. Retrieving the lost phase information can be achieved using computational methods which iteratively improve an initial guess of the phase [165–167].

CDI is an attractive technique when using X-rays because only rudimentary lenses can be created, making traditional microscopy difficult [25]. Such "lensless" imaging can be performed with any wavefield, including electrons, though the advantages of doing so with electrons are less pronounced, since high quality electron lenses are readily available, and real-space images can easily be produced with very high magnification. Electron Coherent Diffractive Imaging (eCDI) has some advantages over traditional electron microscopy, because the reduced reliance on lenses means the ultimate resolution is not limited by lens aberrations [168]. However the many other complications of eCDI mean that it is unlikely to replace regular transmission electron microscopy in the foreseeable future.

One situation where eCDI potentially has an application is in high bunch charge pulsed experiments, where space-charge interactions within the beam become considerable. While bunch shaping can help maintain bunch brightness before it interacts with a sample, the bunch shape after the sample is inevitably irregular. Allowing the irregular bunch to propagate directly to the detector would minimise the distortion caused by the Coulomb repulsion, whereas refocusing the bunch after the sample would increase the intrabeam forces, potentially making the resulting image unusable. Such high bunch charge pulsed experiments have been proposed for structural determination of biological macromolecules that from micro-crystals [39], and also as a way to observe dynamical processes [28, 169].

The immediate motivation for performing eCDI using electron bunches generated in the CAES was not to overcome space-charge induced distortions in microscope images, but rather as a demonstration that utilised the inherently high coherence of the bunches. The proposed experiment was to demonstrate eCDI from nano-apertures, milled into an appropriate substrate. Unfortunately the experiment was not realised because early investigations indicated there would be several technical difficulties, both with generating the required sample, and using it in our system.

The remainder of this chapter details simulations showing what could possi-

bly be achieved, provided some of the technical difficulties can be overcome in the future. Ultimately these simulations show that it should be possible to perform CDI using electrons generated in the CAES under fairly realistic conditions. However, unless sufficient electron number in a single bunch can be obtained to make very fast imaging feasible, a regular continuous illumination electron beam is probably more appropriate for this application. Such continuous-mode electron CDI from nano-apertures was performed at least as early as 2002 [170], however interference experiments are the most rigorous test of coherence, so performing such experiments would still be useful.

6.2.1 Diffraction Simulations

The first consideration needed to assess the plausibility of performing CDI with the CAES is geometric: for realistic aperture size, electron wavelength, propagation distance, and detector resolution, does the detected diffraction patten contain sufficient information to perform phase retrieval? The achievable aperture size is determined by the resolution limits of the focused ion beam milling used to create the nano-apertures. Early attempts at creating pairs of 10 nm wide slits in a substrate of silicon nitride resulted in significant tearing of the substrate. Arrays of holes with diameter 30 nm spaced 200 nm apart were milled without difficulty, indicating that it was probably a combination of the length of the slits, and their narrow separation that caused the tearing, rather than the width of each individual slit. For this reason, the simulated aperture used throughout this section has a feature resolution of approximately 10 nm, and a fairly compact overall size as shown in Figure 6.26(a). The specific shape of the aperture was chosen to have low symmetry, both to give a more complicated diffraction pattern, and to ease identification of different parts of the reconstructed images.

The electron energy in the simulation was set to 8.5 keV, which corresponds to an effective electron wavelength of 13 pm when analysing electron interference. The propagation distance between the sample and the detector was set to 70 cm, which is the maximum propagation distance possible for our apparatus when a fully extended bellows is inserted between the sample chamber and MCP. The detector resolution in the simulation was set by making the element size in the detector plane equal to 43 μm, which is equal to the length of the phosphor screen imaged by each pixel in the camera (in both x and y directions). The actual detector resolution in the experiment is limited by the point spread function of the MCP and phosphor screen, which will be discussed later.

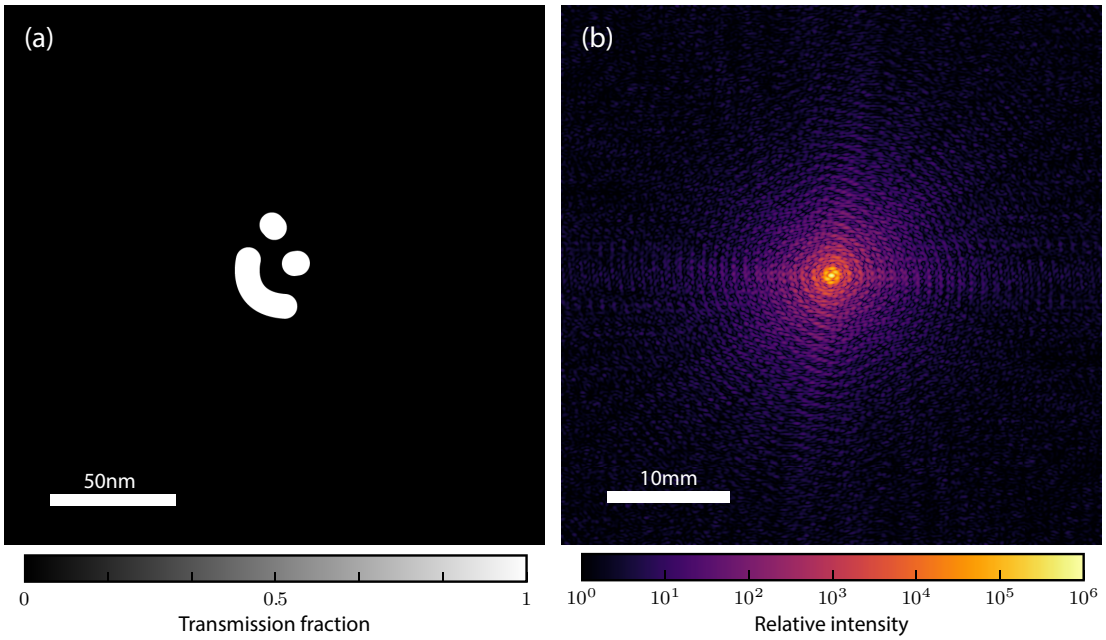

Figure 6.26: Simulated electron diffraction from nanoapertures in the far-field. Electrons propagating through an aperture shown in (a) should result in a diffracted intensity at the detector shown in (b).

Simulations were performed assuming parallel beam illumination, which is simple to achieve experimentally, and allows Fraunhofer propagation of the wavefield from one plane to another, which is given by equation 3.30. The validity of the Fraunhofer approximation is contingent on the aperture being sufficiently small according to the condition in equation 3.29, meaning the aperture must be less than about 2 μm across, much larger than the approximately 40 nm aperture simulated here.

The simulated detected intensity of the wavefield diffracted by the aperture in Figure 6.26(a) is shown in Figure 6.26(b). There are well-separated diffraction maxima and minima in the calculated diffraction pattern, which is unsurprising given the high sampling resolution of the simulated aperture, which can be seen by the smooth, unpixelated features in Figure 6.26(a). Both the simulated aperture and detector contain 1024×1024 pixels. The well-separated diffraction maxima indicate that at least from a geometrical perspective, it should be possible to see a diffraction pattern using experimentally achievable parameters.

Effect of partial coherence

The simulated diffraction pattern shown in Figure 6.26(b) assumes a fully coherent wavefield incident on the aperture. The effect of partial coherence is to blur the detail of the diffraction pattern, decreasing the visibility of the minima and

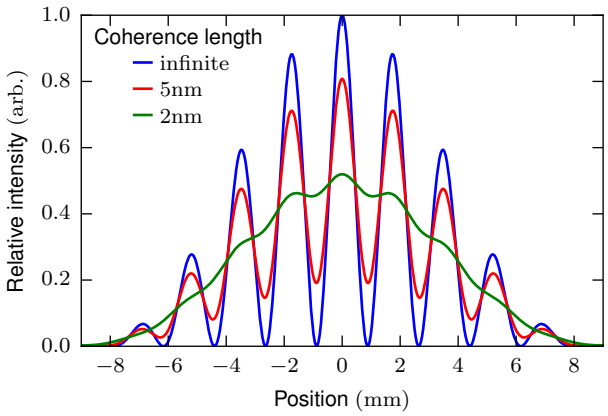

Figure 6.27: Partial coherence. Simulated two-slit diffraction pattern illuminated by electrons with varying coherence lengths. The slits are 1 nm wide, with a centre-to-centre separation of 5 nm.

maxima as discussed in section 3.2. The effect is most easily visualised by looking at the effect of decreasing coherence length on the diffraction pattern resulting from double slit diffraction, as shown in Figure 6.27. The parameters of the simulation are the same as for Figure 6.26, but the aperture has been replaced with two slits, each 1 nm wide, with a centre-to-centre separation of 5 nm. The propagated partially coherent intensity was calculated using equation 3.32, assuming a Gaussian complex coherence factor as in equation 3.19, which precisely defines the coherence length ℓ_c. It can be seen that with coherence length equal to the slit separation, the visibility of the fringes is still relatively clear, but as the coherence length drops below half the separation, the fringes are almost completely lost.

Electrons generated in the CAES have a coherence length of around 10 nm at the point of generation, but this coherence length is altered by changing the beam size according to equation 3.21. Since the simulated aperture in Figure 6.26 is 40 nm across, a coherence length of 40 nm was used to simulate the effect of partial coherence. This would require the beam to be expanded by a factor of 4, reducing the intensity at the aperture by a factor of 16. The resulting partially coherent diffraction pattern is shown in Figure 6.28(b), which shows the expected reduction in visibility of the interference minima and maxima.

The true resolution of the detector is not only determined by the effective pixel size of the camera, but also by the Point Spread Function (PSF) of the MCP and phosphor screen assembly. The PSF is easily found by looking at single electron impact events recorded by the camera, which is possible because of the very high gain of the MCP/phosphor system. The PSF was found to be approximately

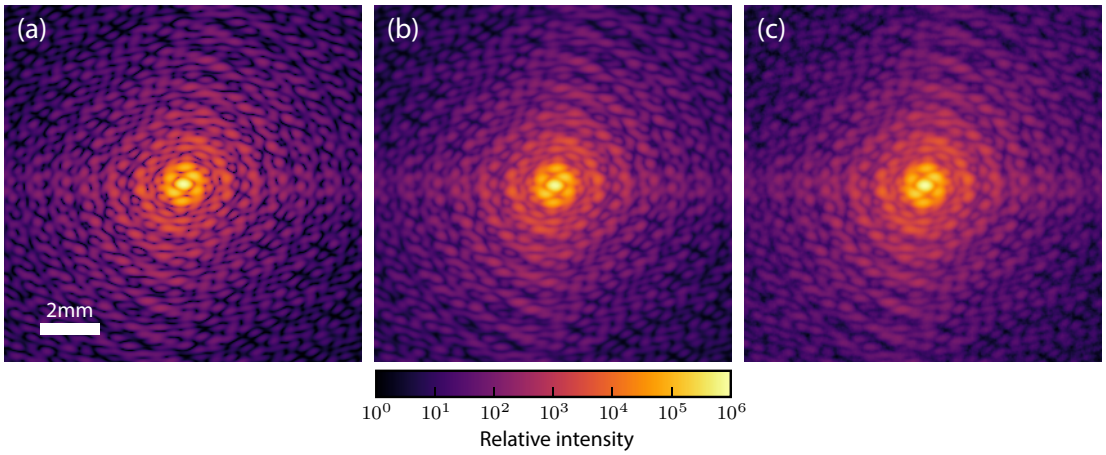

Figure 6.28: Simulated electron diffraction including effects of partial coherence and detector PSF. (a) Fully coherent intensity. (b) Partially coherent intensity, $\ell_c = 40\,\text{nm}$. (c) Partially coherent intensity, $\ell_c = 40\,\text{nm}$ and blurring due to the point spread function of the MCP/phosphor screen assembly.

Gaussian, with standard deviation around $35\,\mu\text{m}$.

The effect of this finite detector resolution was incorporated into the simulated diffraction pattern by convolving the partially coherent intensity with the Gaussian PSF. This has the effect of further blurring the detected diffraction pattern as can be seen from Figure 6.28(c), however individual diffraction maxima lobes are still clearly resolved.

6.2.2 Phase Retrieval

A forward-propagating wavefield directly after a scattering or emitting object can be completely reconstructed if both the amplitude and phase of the wavefield is measured over a plane at some distance downstream. Amplitude and phase detection is achievable with radio or acoustic waves for example, because the frequencies are relatively low, and so the amplitude of the wave can be recorded at many points over a single cycle, allowing the relative phase at different points on the plane to be measured. For optical or higher frequency electromagnetic waves, the frequency is simply too high to allow multiple amplitude measurements to be taken in a single cycle, so all than can be measured is the intensity (as defined by equation 3.6). For electron wavefields, the wavevector and frequency can be changed arbitrarily by inclusion of extra irrotational vector potentials and constant scalar potentials in the Hamiltonian, so direct measurement of absolute electron phase at a single point is a meaningless concept [145]. However, measurement of relative phase across a set of points can be achieved through intensity

measurements of interfering fields, exactly as for electromagnetic waves.

The inability to measure the phase constitutes a loss of information about the wavefield, and means the wavefield over a plane immediately after an object cannot be directly determined by detecting the intensity of the propagated wavefield over a plane downstream. This is known as the *phase problem*, and is the motivation for attempting to retrieve the phase. Broadly speaking, the relative phase of the wavefield over the detection plane can be determined in one of two ways. Firstly, interfering the wavefield of interest with a known reference wave can allow the phase to be deduced from the resulting interference patten, as in holography. The second approach to retrieving the phase is computational, and generally works by iteratively refining an initial guess of the phase. The work presented in this chapter focuses only on computational phase retrieval.

The Gerchberg-Saxton iterative phase retrieval algorithm [171] determines the phase of a wavefield at both the object and diffraction planes, but requires the intensity to be measured at both planes. While this has many potential applications, it does not solve the more general (and arguably much more useful) problem of determining the complete exit wavefield at the object, from a measurement of the diffracted intensity alone. A plethora of other phase retrieval algorithms have been developed [172], many of which can determine the full exit wavefield with little or no information beyond the diffraction intensity measurement, however one of the workhorses now used to solve this problem is the Shrinkwrap algorithm [173].

The core of the Shrinkwrap algorithm is the Hybrid Input-Output (HIO) algorithm, which is summarised by steps 3 to 6 of Figure 6.29. In essence, the algorithm propagates an initial guess of the field back and forth between the object and detector/diffraction planes, applying constraints on the amplitude (but not phase) at each plane, in each iteration. In the detector plane, amplitude is set by the measured intensity I_{det}, but in the object plane a weaker constraint is applied by the *support*, $\mathbb{S}$.

The support is the region in the object plane, outside of which the amplitude of the wavefield is known to be zero. There are many ways to construct a support, but generally speaking the tighter the support, the better the reconstruction of the wavefield. A tight support is one which includes very little area where the amplitude of the wavefield is zero. That it, a good support traces the outline of the object being imaged. There are many ways to estimate a support, including using a priori knowledge of the object, such as a low resolution microscope image [174].

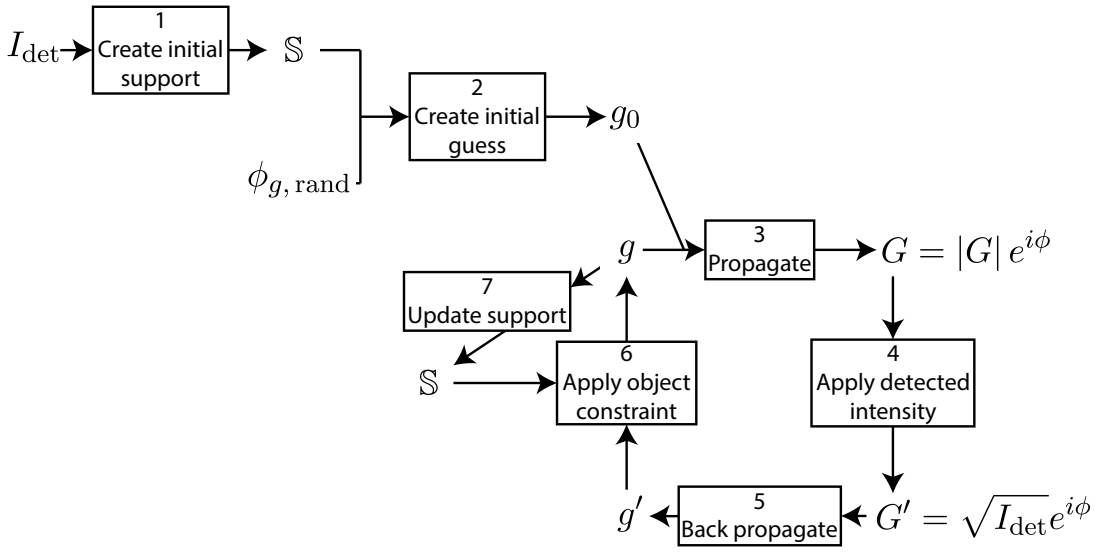

Figure 6.29: The Shrinkwrap algorithm. The amplitude and phase of the exit wave, g, are determined iteratively. The support, $\mathbb{S}$, is periodically updated based on g, and tends to shrink and conform around the non-zero region of the exit wave.

The Shrinkwrap algorithm gets its name from the way it updates the support based on the most recent approximation of the wavefied amplitude at the object plane. Starting with a large support area, the support tends to shrink around the object as the algorithm progresses through many iterations. The initial support is often estimated from the diffraction pattern alone, a technique which is usually considered part of the Shrinkwrap algorithm.

In the following summary of the algorithm depicted in Figure 6.29, it is assumed that the intensity is measured in the far field, so the Fraunhofer approximation can be made when propagating the wavefield to and from the object and detector planes. Furthermore, while equation 3.30 shows that the wavefield in the detector plane has a spherical modulation to the phase, as well as a constant phase offset determined by the propagation distance, these two phases are ignored. These additional phase terms have no effect on the detected intensity, and are simply added to and removed from the field each time it is propagated to and from the detector plane. By ignoring these phase terms, the field can be propagated to and from the detector and object planes using nothing more than a forward, and inverse Fourier transform respectively. The scaling of the position variables between the two planes also has no practical effect, so is safely ignored. This allows a compact notation to be adopted, where the exact fields in the object and detector planes are f, and F respectively, where $F = \mathscr{F}\{f\}$, and we wish to recover f. The approximations to f and F are g and G respectively, where g' represents g before the object plane constraint is applied, and G' represents G

after the detector plane constraint is applied. We seek to make g as close to f as possible, and the algorithm proceeds according to the steps in Figure 6.29:

1. An initial support, $\mathbb{S}$, is created from the detected intensity, I_{det}, alone. Inverse Fourier transforming the detected intensity produces the autocorrelation R, of the original object according to the autocorrelation theorem [175] (Wiener-Khinchin theorem):

$$R(\mathbf{x}) = \mathscr{F}^{-1}\{|F(\mathbf{k})|^2\}, \tag{6.28}$$

   where we identify $|F(\mathbf{k})|^2 = I_{\text{det}}$. To obtain $\mathbb{S}$, R is blurred by convolution with a narrow Gaussian (σ of 3 pixels) to reduce very high frequency oscillations, and then the result is thresholded. The regions greater than the threshold value are elements of $\mathbb{S}$, and regions less than the threshold are not. Setting a low threshold of 4% ensures the initial support area is larger than the object, so the support can shrink around it.

2. An initial guess of g is created by choosing a field with random phase and amplitude, and then applying the support constraint:

$$g_0(\mathbf{x}) = \begin{cases} |g_{\text{rand}}|\, e^{i\phi_{g,\,\text{rand}}}, & \text{if } \mathbf{x} \in \mathbb{S} \\ 0, & \text{otherwise.} \end{cases} \tag{6.29}$$

   The amplitude of g_0 must then be normalised such that there is the same probability (integral of intensity) in both the object and detector planes. Note that the initial guess need not be random, as (almost) any initial guess can result in a successful reconstruction, though the convergence time can vary.

3. Propagate the current object plane field to detector plane by Fourier transforming: $G_n = \mathscr{F}\{g_n\} = |G|\, e^{i\phi}$.

4. Apply the amplitude constraint imposed by the intensity in the detector plane: $G'_n = \sqrt{I_{\text{det}}} e^{i\phi}$.

5. Back-propagate the current detector plane field to object plane by inverse Fourier transforming: $g'_n = \mathscr{F}^{-1}\{G'_n\}$.

6. Apply the amplitude constraint imposed by the support according to the

HIO method:

$$g_{n+1}(\mathbf{x}) = \begin{cases} g'_n(\mathbf{x}), & \text{if } \mathbf{x} \in \mathbb{S} \\ g_n(\mathbf{x}) - \beta g'_n(\mathbf{x}), & \text{otherwise.} \end{cases} \tag{6.30}$$

The feeback parameter β is set between 0 and 1, with $\beta = 0.9$ usually working well.

7. The support is updated every few iterations (all phase retrieval examples in this chapter update every 5 iterations). The new support is obtained by convolving $|g|$ with a Gaussian and thresholding the result (using the most recent g). The σ of the Gaussian starts at 3 pixels, but is reduced by 1% every time the support is updated, down to a minimum of 1.5 pixels. The threshold level is set at 20% the maximum value of $|g|$.

Modifications to the above algorithm exist such that the input parameters are automatically optimised, however the core process remains the same.

The above detailed Shrinkwrap algorithm was applied to the simulated fully coherent intensity shown in Figure 6.26(b), and the progress of the phase retrieval is demonstrated in Figure 6.30. It can be seen that the symmetry of the initial support given by the object autocorrelation function is quickly broken, with the support becoming steadily tighter as the algorithm progresses. The object is fairly well reconstructed after 40 iterations, with very little observable error after 300 iterations.

6.2.3 Sources and Effect of Noise

The success or failure of the phase retrieval algorithm is dependent on how it manages to deal with factors such as partial coherence, limited amounts of signal that is discrete in nature (shot noise), and additional sources of noise. The effects of experimentally expected partial coherence, and of limited electron number contributing to the detected intensity, are shown in Figure 6.31. While the scale used in the image presenting only partially coherent intensity is somewhat arbitrary, for the images which simulate different numbers of electrons contributing to the signal, a value of unity was ascribed to the peak of the Gaussian PSF caused by a single electron impact.

The simulated detected intensity containing 8.7 million electrons appears to be continuous, but the discrete nature of the electron signal becomes very apparent in the simulations containing only 87,000 and 870 electrons. The reasons

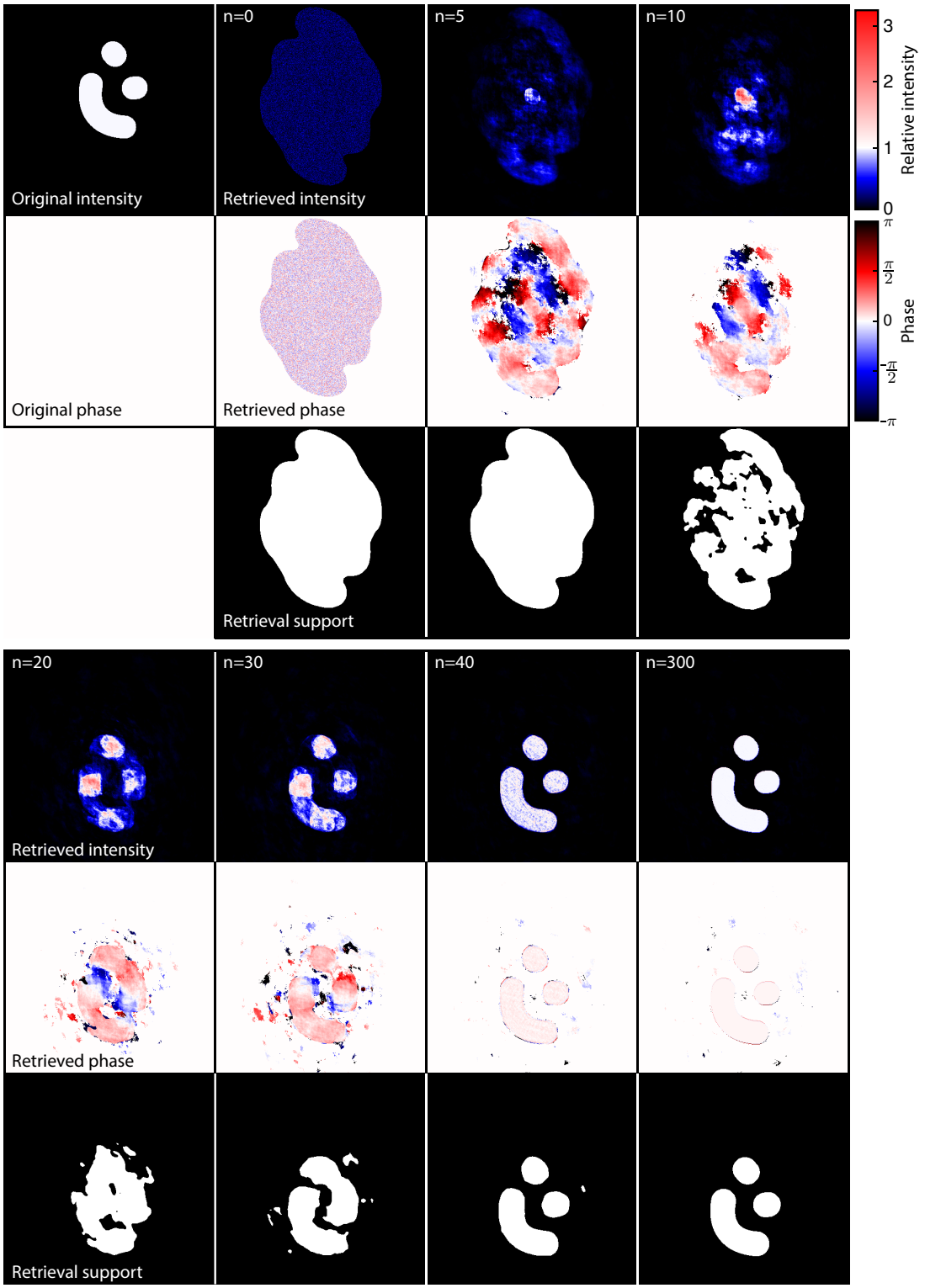

Figure 6.30: Progression of phase retrieval using the Shrinkwrap algorithm. The retrieved object plane intensity, phase, and support are continually updated as the Shrinkwrap algorithm progresses through n iterations.

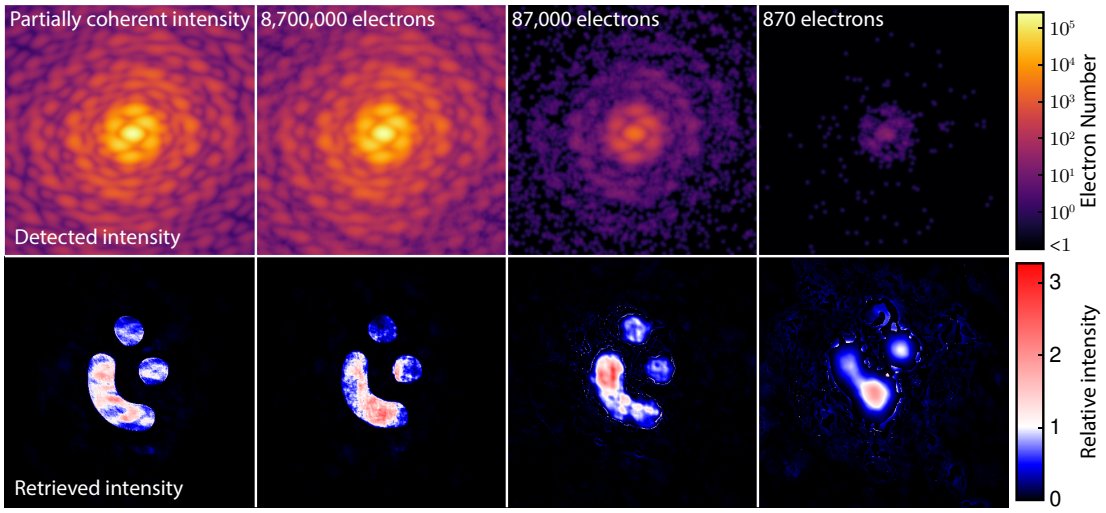

Figure 6.31: Simulated electron diffraction with partial coherence and limited electron flux, and corresponding retrieved object plane intensity. The retrieval is still fairly successful using the partially coherent intensity, and with millions of simulated electron impacts, but begins to fail with very low signal level. The retrieved intensity shown is after 100 iterations of the Shrinkwrap algorithm.

for choosing to test these specific electron numbers are discussed in greater detail later in the section, but in general they are the result of assuming 100,000 electrons per shot, along with realistic estimates for possible exposure number and aperture array size. The electron impact positions were determined by a random number generator with a probability density function determined by the simulated intensity. Practically, the easiest way to achieve this was to scale the partially coherent intensity such that the sum of all pixels equaled the required number of electrons, and then for each pixel calculate a Poisson random integer using the pixel value as the expected value. The Gaussian blur caused by the MCP point spread function was then applied to that array to generate expected detector image.

Figure 6.31 also shows the recovered object plane intensity after 100 iterations for each of the simulated detected images. The retrieval algorithm in each case was actually run for 10,000 iterations, but it was found that the retrieved intensity stagnated after about 100 iterations. The recovered intensities corresponding to the cases of continuous partially coherent intensity, and of 8.7 million discrete electron impacts, both show good qualitative agreement with the shape of the original object, but contain significant errors in the magnitude. For the case of 87,000 electrons, the general shape of the object is still fairly well recovered, but the reconstruction becomes almost unrecognisable when only 870 electrons are detected.

While surprisingly few electrons are required to obtain at least a rudimentary reconstruction of the object intensity, it is clear that the reconstructions made using fewer than 8.7 million suffer from a loss of high spatial frequency information, which can be attributed to the lack of electrons scattered to high angles. Importantly, these simulations assume absolutely no noise. While the positions of the electrons are determined stochastically, they only appear in positions allowed by the diffracted intensity so every additional electron improves the eventual reconstructed object plane intensity. Sources of actual noise however, will produce a signal at positions not determined by the diffraction pattern, and so will make the reconstruction worse.

The relative strength of the desired signal, and that produced by sources of noise, will determine whether it is possible to observe any diffraction pattern, and whether this can then be used to reconstruct the object plane intensity. Given the relative clarity of the reconstruction formed from a detected intensity containing 8.7 million electrons, this number will be used as a target for the total number of electrons contributing to the actual signal, with noise overlaid on top of this.

Two major sources of noise are considered: the MCP firing in response to anything other than electrons emanating from the sample, and electrons transmitted through the sample substrate where the transmission fraction was assumed to be zero in simulations up until now. Sources of noise in the image sensor of the camera can be ignored, because the MCP/phosphor assembly produce so much light per electron impact that a small dark current or digitisation noise in the sensor has negligible effect.

To determine how much noise came from the MCP, images were taken when the electron beam was inactive. Individual MCP firings could be seen in the images, and were manually counted over a known area. In reality, the amount of light caused by a single MCP firing event varied considerably, so a thorough analysis would involve finding the distribution of intensities for the noise firings, however this was deemed unnecessary since only an average rate of noise accumulation was required. Over a square centimetre in a 4 ms exposure, it was found that there were around 10 distinguishable firing events. The physical origin of the MCP noise is a combination of spontaneous firings, firings caused by a collision from background gas, and those caused by electrons shed from the accelerator electrodes and ion pump, though the origin of the firing is not of particular importance to including its effect.

The noise contribution from electrons transmitted through the aperture substrate depends on the transmission properties of the substrate, as well as the total

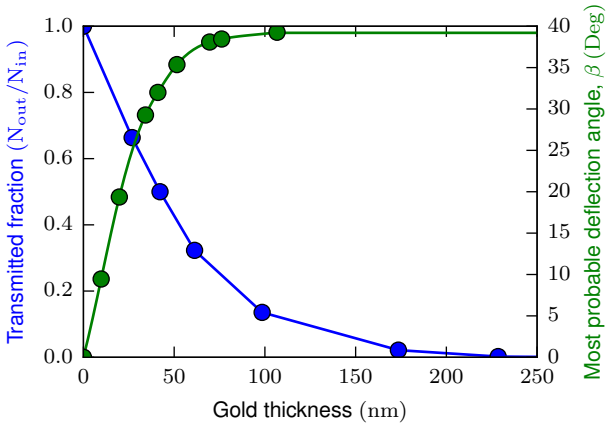

Figure 6.32: Electron transmission fraction and most probable deflection angle when penetrating through gold. An electron beam penetrating through gold is both attenuated, and the angular distribution of electron trajectories increases. Data taken from reference [179].

area illuminated. A common method of making nano-apertures for illumination in electron microscopy is to use focused ion beam milling to create a hole of the desired shape in a silicon nitride membrane around 100 nm thick [176]. The fairly low atomic numbers of silicon and nitrogen means the membrane itself is fairly transparent to an electron beam, so a layer of heavy metal such as gold is then deposited on top to make the aperture more opaque [177, 178].

The total fraction of electrons transmitted through a gold film rapidly reduces as the depth increases as can be seen in Figure 6.32, which is adapted from experimental data taken by Cosslett et al. [179]. In addition to flux attenuation, the angular spread of electron trajectories of an initially collimated beam increases as it penetrates the solid. The result can be approximately described by a Gaussian angular distribution, with a standard deviation which increases with greater depth. Under this assumption, the fraction of the beam η, collected in a cone of semi-angle θ, is given by

$$\eta(\theta) = 1 - \exp \frac{-\theta^2}{2\beta^2}, \tag{6.31}$$

where β is the most likely angle for an electron to have been scattered to by the time it reaches a given depth, which can also be found in Figure 6.32.

Calculation of the expected detected intensities including noise, required estimates of realistic experimental parameters. The beam profile at the sample was estimated to be Gaussian with a standard deviation of 100 μm, which is on the smaller side of what has been measured experimentally when creating a fairly collimated beam. Since the beam size is much larger than the size of a single aper-

ture, a square array of apertures was simulated, which allows more flux through the open area, minimising the acquisition time (which would increase the relative amount of noise acquired). The total size of the array was set to a square 100 μm to a side, which should only minimally blur the resulting diffraction pattern since 100 μm is approximately the same size as the point spread function of the detector. The pitch of the aperture array was set to 200 nm, which is as low as possible while still ensuring the limited coherence length results in no observable interference between electrons passing through adjacent apertures. With these parameters the array contains 250,000 elements. Assuming 100,000 electrons per pulse, 40,000 shots would be needed to obtain 8.7 million electrons passing through the apertures. Milling such a large number of apertures over such a large area could be very time consuming, but is otherwise no different to the milling of the array holes already achieved.

The calculated detected intensities using the above parameters, including all discussed sources of noise, are shown in Figure 6.33, for several thicknesses of gold substrate. An attempt has also been made to subtract the noise produced by the random MCP firings and electrons transmitted through the gold substrate. For the case of MCP noise only, and where 100 nm and 10 nm of gold substrate has been simulated, the value subtracted from each pixel was constant across the array, and was taken as the median pixel value. The resulting background subtracted images at least superficially appear to be more similar to the idealised intensity in Figure 6.26 than before the background was subtracted, however at higher scattering angles the signal becomes increasingly indistinguishable from random noise. The inclusion of noise becomes worse for thinner the gold substrates. With only 1 nm of gold, the number of electrons transmitted through the substrate noticeably varies with scattered angle. To subtract the noise in this case, a two-dimensional Gaussian was fit to the intensity and then subtracted, with any resulting negative values being set to zero. As can be seen from the resulting intensity, only a small disk of recognisable signal remains in the central region of the image. The outer ring of intensity is much brighter than the corresponding region in the simulated fully coherent noiseless intensity, so is almost completely composed of noise. This ring was not subtracted out of the image because of an imperfect guess at the distribution of the noise.

Despite the high noise levels, in all cases the object plane intensity was reconstructed with surprisingly high fidelity. In large part this is due to the simple structure and relatively large size of the object, which results in the majority of the diffracted electrons ending up in a few lobes near the centre of the diffraction

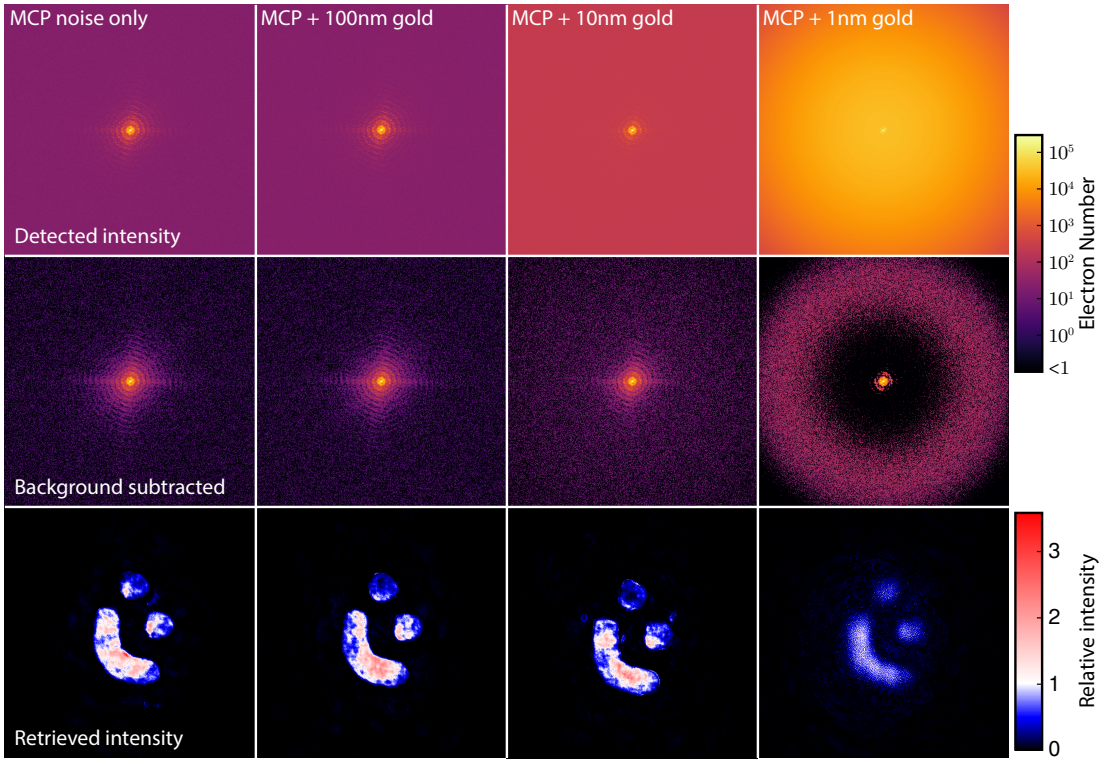

Figure 6.33: Simulated electron CDI from the CAES including noise. The detected intensity includes the noise from the MCP, as well as electrons transmitted through the gold substrate itself (for various thicknesses of gold, indicated in nanometers). An attempt at noise subtraction is made before phase retrieval is performed. The reconstructed object plane intensity is shown after 100 iterations, and resembles the true object surprisingly well in all cases, though an increase in noise always makes the reconstruction worse.

pattern. The electrons scattered to larger angles contribute to the higher spatial frequency components, but are not important in determination of the general shape of the aperture. In this respect, it is likely that the reconstruction could be significantly improved by only utilising a small disk of the detected intensity near the centre of the diffraction pattern, thereby avoiding all the artefacts introduced by the unsubtracted noise at higher scattering angles.

These simulations show that even with a relatively thin gold substrate, it should not only be possible to observe interference from realistic sized nano-apertures, but it should be possible to use iterative phase retrieval to reconstruct the shape of those apertures. One potentially significant factor that was ignored was the beam drift that was discussed in previous sections. It is tempting to say that the beam drift simply reduces the effective coherence length of the time averaged beam, which can be ameliorated simply by expanding the beam, however this only fixes the problem under certain conditions. If the electron trajectory is altered because of a deflected at the source, then the beam will tend to wander off the desired region of the sample. This form of beam drift reduces the total number of electrons through the apertures (increasing the required number of exposures), but otherwise causes no harm. If however, the deflection happens some distance from the source, then any electrons that do make it through the aperture will no longer be heading directly down the optic axis (even if the beam was perfectly coherent originally), and so the diffraction pattern will be shifted laterally. This shift cannot be removed by simply expanding the beam, with the problem becoming worse the closer the point of deflection is to the sample.

The effects of beam drift caused by deflection close to the sample can be overcome by combining successive images thorough registration on the condition that sufficient detail is present in each single image. For the parameters described above, approximately 200 electrons would be directly transmitted through the apertures each shot, the majority of which would be detected in or near the central diffraction lobe. This should be a sufficient number to allow registration, however if uncertainties in previous estimates combine to make the transmitted number a factor of 10 lower, then image registration would likely become impossible.

6.2.4 Outlook for Electron CDI in the CAES

These simulations show that it should be possible to perform CDI from an array of nano-apertures using electron bunches generated in the CAES. While this would be an exciting achievement, the ability to generalise this experiment to image

other samples of current interest is limited. While the electron bunches produced are short in duration, they are not ultrashort, and though each pulse itself has high peak brightness, the time averaged beam is not ultrabright. Therefore, electron CDI at atomically relevant length or time scales requires an electron source with different characteristics to the current generation CAES, though improvements implemented in future generations of the device could change this. Necessary improvements would include elements investigated in previous chapters, such as an ultrafast excitation pathway capable of producing ultrafast bunches with high electron number, and also bunch shaping that can reduce brightness degrading space-charge effects. Probing sup-picosecond atomic timescales would also require techniques not explored in this thesis, such as radio-frequency bunch compression.

Chapter 7

Conclusions

The Cold Atom Electron Source (CAES) was originally conceived as an electron source with many of the characteristics of a photocathode source, but with the potential to have a greatly increased electron bunch brightness. This increase in brightness was to come from the far lower thermal energy that would be imparted to the electrons upon photoionisation of isolated gas atoms when compared to what could be achieved by illuminating a metal or semiconducting solid, along with the potential to overcome space-charge induced brightness degradation through 3D bunch shaping. Early experiments produced favourable results, with the coldest electrons routinely extracted from these cold atom sources having a temperature around 10 K, much lower than the thousands of Kelvin typical of electrons produced from solid photocathodes.

Following the encouraging CAES electron temperature results, an ambitious set of experiments were proposed, ultimately working towards an electron based equivalent of the holy grail in X-ray structural determination: single-shot, ultrafast, Coherent Diffractive Imaging (CDI) of single molecules. The progress towards this goal, and some of the intermediate steps taken, has been the focus of this thesis.

Descriptions of the CAES and some of the associated subsystems were presented in chapter 2. Details were given of modifications made to various systems over the course of this project, including upgrades to the laser system, changes required to perform diffraction experiments, and additions of beam diagnostic equipment. Given that much of the promise surrounding CAES technology references the intrinsically excellent beam quality, specifically the high transverse electron coherence, some technical explanation of the formalism surrounding these quantities was presented in chapter 3.

From the outset it was known that one of the major challenges for single-shot

ultrafast diffraction experiments was to overcome the brightness degrading effects of space-charge repulsion. The proposed solution has long been to use uniformly filled ellipsoidal bunches, which do not experience brightness degradation under space-charge expansion. The CAES had already been shown capable of producing electron bunches of arbitrary 2D profile (and limited control in the third dimension), and the low thermal diffusion of the cold electrons resulted in the bunches maintaining their shape during propagation. Such bunches were considered ideal for use in initial demonstrations of meaningfully reduced brightness degradation after space-charge expansion, and so actualising such a demonstration was one of the first goals of this project, and was the focus of chapter 4.

For reasons that were not initially understood but which were elucidated in chapter 5, electron bunches that were assumed to be ultrafast in duration did not undergo space-charge expansion to anywhere near the degree expected from simulation, if at all. However it was noted that the ions remaining after the electrons were extracted did undergo profound space-charge expansion. It was also determined that the trajectories of ions in a bunch should be identical to those of electrons in a bunch, where the only difference is a scaling factor in time, based on the difference in mass between the two particle types. This scaling factor was such that a 5 ns ion bunch (which was easy to generate) should be equivalent to a 12.5 ps electron bunch, which is in the ultrafast regime. Furthermore, the initial temperature of the ions was on the millikelvin level, which enabled almost complete separation of thermal diffusion and space-charge induced effects. Ion bunches therefore allowed experimental investigation of the effects of bunch shaping on space-charge expansion, with the results being directly transferrable to ultrafast electron bunches.

In section 4.1, some initially unexpected results of the first ion bunch shaping experiments were investigated. It was shown that single initially point-like ion bunches expanded into a shape with a high charge density around the perimeter, which was not predicted by particle tracking simulations. The rings also formed collisional boundaries which did not pass through each other when interacting with neighbouring simultaneously produced ion bunches.

The mechanism of ring production was explained by Dene Murphy [84], who proposed that the rings resulted from a complication of photoionising atoms with light resonant with a strong atomic transition. The atoms that were directly illuminated by the excitation laser were absorbing light from the beam, and re-emitting the light isotropically. This scattered light was then being reabsorbed by nearby atoms, resulting in a diffuse halo of excited state atoms, which were

subsequently ionised by the ionisation laser beam. The resulting diffuse halo of ions was swept up as the high density core expanded under space-charge forces, forming the high density ring observed.

In later experiments which I conducted, it was found that ion ring formation could be avoided by reducing the delay between the excitation and ionisation laser beam pulses, which greatly reduced the total light that was scattered by the desired core of atoms. This understanding was critical in the next experiment, which aimed to control the ion bunch distribution much more precisely so that uniformly charged ellipsoid bunches could be created.

Section 4.2 presented the first experimental demonstration of using a Cold Atom Electron and Ion Source (CAEIS) to reduce space-charge induced emittance growth through generation of uniformly filled ellipsoidal bunches. The reduction was relative to the emittance growth of other, non-ellipsoidal distributions, and was determined using a simple focal width measurement.

The relative reduction in emittance growth for the ellipsoidal bunch compared to the Gaussian bunch was modest at around 50% for the maximum charge measured, though the difference appeared to become larger as the total charge was increased. The importance of this result lies in the verification that the method used to produce the ellipsoidal bunches can actually result in measurable improvements in beam quality in a CAES. Further refinements to the method, particularly in the precision of defining the initial shape, and increases in total bunch charge, are likely to yield more pronounced improvements to beam quality.

A notable limitation to this demonstration of reducing emittance growth using bunch shaping, is that there are few applications requiring high brightness bunches of ions. High energy particle colliders aside, the most pressing need for reduction in space-charge induced emittance growth is in applications requiring high charge electron bunches, such as single-shot electron diffraction, or free electron lasers. While a strong case is made for why cold ion bunches are a good analogue for cold electron bunches, there are important differences between the two. The first is that the ions are initially significantly colder than similarly produced electrons, which could be of some consequence, particularly where the bunch shape must be maintained for an extended period. Even assuming that the somewhat higher temperature of electrons produced in the CAEIS does not invalidate the use of ions as a means of testing space-charge induced effects in electrons, the achievable bunch duration, and the corresponding longitudinal size of the bunch, are consequential. If gains from bunch shaping can only be realised using cold *and* ultrafast electron bunches, then the shaping demonstration is only

meaningful if the CAES can ultimately satisfy both criteria simultaneously.

The question of duration of electron bunches produced in the CAES was the topic of chapter 5. In section 5.1, the effect that different photoexcition processes had on electron pulse duration was investigated, with the basic finding that ultrafast electrons could only be produced if the ultrafast laser was involved in the *final* stage of excitation to an ionising state. While on reflection this is perhaps unsurprising, at the time there was some indication in the literature that ultrafast electrons could be generated even if the ultrafast laser was involved only in excitation from the ground state to an intermediate state, a position which is contradicted by work presented in this thesis. An ultrafast excitation pathway was identified that could produce both fast and cold electron bunches, which involved the atom absorbing two photons simultaneously from two different laser fields via a virtual state. The significance of the findings about different excitation pathways is somewhat limited, since other groups were already using pathways that reliably resulted in ultrafast excitation, and had advantages in terms of required laser power, achievable electron yield, and reduced simultaneous generation of undesirable hot electrons.

Of more general consequence were the findings about the speed of ionisation after the atoms had been excited to an ionising state, as presented in section 5.2. It was shown that any fraction of atoms excited to below the classical threshold energy could slowly tunnel ionise over the course of tens of microseconds: a million times slower than desired. The transition from ultrafast to ultraslow appeared to be abrupt, though the relatively low temporal resolution of our system only allowed an upper limit to be placed on the duration of the ultrafast electrons, which we found to be 130 ps.

The significance of the ionisation findings lie in the relationship between achievable electron bunch temperature, and bunch duration. The requirement that excitation energies only be positive places constraints on ultrafast laser bandwidth, which in turn limits the excitation speed because of the time-bandwidth product of the laser pulse. Concurrently, the spread of excitation energies produces a spread in the resulting electron energies, ultimately forming a time-temperature relation. This time-temperature relation is highly nonlinear because of the complex physics behind ionisation rate of above threshold Stark states (explored to a limited extent in the spectroscopy experiments in section 5.3), but it will ultimately determine the achievable brightness of ultrafast electron bunches produced in cold atom sources. The limited temporal resolution of our system combined with the coarse temperature measurements made, mean that we did

not explore this time-temperature relation with any accuracy, so this work remains for future investigations. The outcomes of these further studies may well determine if there is any future for this type of source, as they will resolve the question of whether cold atom sources or traditional solid photocathode sources can produce brighter electron bunches. However it may turn out that the achievable values for a combination of other properties such as total bunch charge, minimum pulse duration, and ability to implement shaping, mean that the two technologies complement each other, with one or the other being the best choice for a specific application.

The results of ionisation duration experiments in chapter 5 confirmed that the current implementation of The University of Melbourne CAES was incapable of producing cold electron bunches that were simultaneously both ultrafast, and of high electron number, as would be required for single-shot ultrafast electron diffraction. However, it was definitely capable of producing cold bunches that were *either* ultrafast *or* high charge, which was sufficient to perform initial demonstration experiments of electron diffraction, which was the topic of chapter 6.

Section 6.1 presented crystallographic type experiments, first summarising some considerations of geometry and kinematic diffraction theory as they applied to our implementation of the CAES. A number of diffraction experiments were performed, on a variety of samples, though the most significant example was demonstration of true single-shot diffraction from a gold foil. The importance of this demonstration lay in the ability of the CAES to produce electron bunches of sufficiently high charge and low temperature such that even a single electron pulse produced diffraction images with sufficient information to reliably align it with successive shots, despite significant shot-to-shot variation in bunch trajectory. A reasonable analogy was drawn between this alignment problem and the type of alignment that will be required in future demonstration of ultrafast single-shot diffraction of single molecules.

Bragg diffraction was also observed in averaged images comprising many low-charge electron bunches generated using an ultrafast excitation scheme. It is likely that the individual bunches were in the tens of picosecond *ultrafast* regime, allowing us to make a fairly legitimate claim that we have successfully demonstrated ultrafast electron diffraction using the source. However, the particular bunches used were not verified to have been generated from above the classical threshold, and so were possibly liberated slowly from the atoms via tunnelling. The distinction is somewhat academic, since the resulting images would appear

identical in either case as the ultrafast nature of the bunches was not applied to recover any time dependent sample behaviour.

While we were able to cast the beam drift in an interesting and positive light which may be relevant to future experiments, ultimately the drift highlighted some serious inadequacies and design flaws in the CAES, at least in the context of using it to generate electron bunches. Much of the less-than-optimal design was a result of the device being relatively general purpose, allowing experiments on a wide array of topics ranging from high precision spectroscopy and fundamental atom-laser interactions, to electron diffraction and novel ion beam experiments. The specific problem of beam drift due to interactions with switching magnetic fields ultimately proved to be quite a large problem for diffraction experiments. However the conflicting demands involved in development of new technologies inevitably produce some unintended results, observations of which hint at refinements that can be made in future devices.

While it was hoped that the high coherence of the electrons produced from the CAES could be leveraged to perform CDI, technical difficulties - including, but not limited to beam drift - meant that this was ultimately not achieved. In section 6.2, realistic simulations were presented of how CDI could probably be accomplished using the CAES. Coherence theory that had been summarised in chapter 3 was used to incorporate effects of partial coherence, and sources of noise - some measured, some calculated - were included in the final simulated diffraction image from a realistically scaled nanoaperture. Ultimately it was determined that it should be possible to successfully achieve CDI using the CAES, but the impact of this result would be limited. Electron CDI of nanoscale binary objects has been achieved several times before using continuous sources, and the ultrafast, bunched nature of electrons generated in the CAES was not to be exploited in the proposed experiment. But again, demonstration of this basic experiment may yield further insight into potential design factors that should be considered in future optimised implementations of cold atom electron sources.

Improved performance from future CAES designs may be achieved by including many of the features suggested throughout this thesis. Avoidance of any design that requires magnetic fields to be rapidly switched is critical for high electron beam stability, which is a crucial element for precision experiments. Non-axially symmetric magnetic fields should also be avoided (for example, those produced from a non-axially aligned Zeeman slower), as such fields can cause beam astigmatisms which may increase the complexity of the required electron optics. An ultrafast excitation scheme should be employed using an ultrafast

laser pulse which excites a single photon transition to the ionising state, so that high excitation efficiencies can be achieved on ultrafast timescales with low laser powers. Using high-numerical-aperture lenses for the excitation laser would allow for more precise generation of uniformly filled ellipsoidal electron bunches, which could better reduce space-charge induced emittance degradation of high charge bunches. An optimised accelerator arrangement could decrease the electron energy spread, and allow for higher energy electrons to be generated, both of which can be advantageous for diffraction experiments. In addition to the above design considerations for the cold atom source itself, the shortest, brightest bunches will require electron optics that can also be employed after traditional photocathode sources, such as low aberration lenses and RF bunch compressors.

In conclusion, it is still an open question as to whether or not ultrafast near-threshold photoionisation of isolated atoms can generate electron bunches that have properties which are superior to those generated by solid photocathodes. However, work presented in this thesis has removed significant uncertainty about what can be achieved, and set constraints about how certain objectives can be accomplished. Even if it turns out that cold atom sources cannot produce electron bunches with superior properties to what can be achieved with other sources, it seems likely that the extreme brightness of ion beams that can also be extracted will find use in a new generation of ion microscopes.

Bibliography

[1] C. Davisson and L. H. Germer, "Diffraction of Electrons by a Crystal of Nickel", *Phys. Rev.*, **30**, pp. 705–740 (1927). 1, 80

[2] B. D. Cullity, *Elements of X-ray Diffraction*, Addison-Wesley Publishing Company, Inc. (1956). 1

[3] G. E. Bacon, *Neutron Diffraction*, Clarendon Press (1975). 1

[4] M. Levitt, "Nature of the protein universe", *Proceedings of the National Academy of Sciences*, **106**, no. 27, pp. 11079–11084 (2009). 1

[5] Z. Dauter, "Current state and prospects of macromolecular crystallography", *Acta Crystallographica Section D*, **62**, no. 1, pp. 1–11 (2006). 1

[6] R. Henderson, J. Baldwin, T. Ceska, F. Zemlin, E. Beckmann and K. Downing, "Model for the structure of bacteriorhodopsin based on high-resolution electron cryo-microscopy", *Journal of Molecular Biology*, **213**, no. 4, pp. 899 – 929 (1990). 1

[7] Z. H. Zhou, "Towards atomic resolution structural determination by single-particle cryo-electron microscopy", *Current Opinion in Structural Biology*, **18**, no. 2, pp. 218 – 228 (2008), theory and simulation / Macromolecular assemblages. 1

[8] D. L. Bish, D. F. Blake, D. T. Vaniman, S. J. Chipera, R. V. Morris, D. W. Ming, A. H. Treiman, P. Sarrazin, S. M. Morrison, R. T. Downs, C. N. Achilles, A. S. Yen, T. F. Bristow, J. A. Crisp, J. M. Morookian *et al.*, "X-ray Diffraction Results from Mars Science Laboratory: Mineralogy of Rocknest at Gale Crater", *Science*, **341**, no. 6153 (2013). 2

[9] D. I. Svergun, M. V. Petoukhov and M. H. Koch, "Determination of Domain Structure of Proteins from X-Ray Solution Scattering", *Biophysical Journal*, **80**, no. 6, pp. 2946 – 2953 (2001). 2

[10] M. Howells, T. Beetz, H. Chapman, C. Cui, J. Holton, C. Jacobsen, J. Kirz, E. Lima, S. Marchesini, H. Miao, D. Sayre, D. Shapiro, J. Spence and D. Starodub, "An assessment of the resolution limitation due to radiation-damage in X-ray diffraction microscopy", *Journal of Electron Spectroscopy and Related Phenomena*, **170**, no. 13, pp. 4 – 12 (2009). 2

[11] J. Hajdu, "Single-molecule X-ray diffraction", *Current Opinion in Structural Biology*, **10**, no. 5, pp. 569 – 573 (2000). 2

[12] E. R. Bodenstaff, F. J. Hoedemaeker, M. E. Kuil, H. P. M. de Vrind and J. P. Abrahams, "The prospects of protein nanocrystallography", *Acta Crystallographica Section D*, **58**, no. 11, pp. 1901–1906 (2002). 2

[13] L. X. Chen, X. Zhang and M. L. Shelby, "Recent advances on ultrafast X-ray spectroscopy in the chemical sciences", *Chem. Sci.*, **5**, pp. 4136–4152 (2014). 2

[14] C. J. Fecko, J. D. Eaves, J. J. Loparo, A. Tokmakoff and P. L. Geissler, "Ultrafast Hydrogen-Bond Dynamics in the Infrared Spectroscopy of Water", *Science*, **301**, no. 5640, pp. 1698–1702 (2003). 2

[15] M. M. Murnane, H. C. Kapteyn, M. D. Rosen and R. W. Falcone, "Ultrafast X-ray pulses from laser-produced plasmas", *Science*, **251**, no. 4993, p. 531 (1991). 2

[16] R. W. Schoenlein, W. P. Leemans, A. H. Chin, P. Volfbeyn, T. E. Glover, P. Balling, M. Zolotorev, K.-J. Kim, S. Chattopadhyay and C. V. Shank, "Femtosecond X-ray Pulses at 0.4$\mathring{A}$ Generated by 90° Thomson Scattering: A Tool for Probing the Structural Dynamics of Materials", *Science*, **274**, no. 5285, pp. 236–238 (1996). 2

[17] B. Abbey, R. A. Dilanian, C. Darmanin, R. A. Ryan, C. T. Putkunz, A. V. Martin, D. Wood, V. Streltsov, M. W. M. Jones, N. Gaffney, F. Hofmann, G. J. Williams, S. Boutet, M. Messerschmidt, M. M. Seibert *et al.*, "X-ray laser–induced electron dynamics observed by femtosecond diffraction from nanocrystals of Buckminsterfullerene", *Science Advances*, **2**, no. 9 (2016). 3

[18] I. D. Young, M. Ibrahim, R. Chatterjee, S. Gul, F. D. Fuller, S. Koroidov, A. S. Brewster, R. Tran, R. Alonso-Mori, T. Kroll, T. Michels-Clark, H. Laksmono, R. G. Sierra, C. A. Stan, R. Hussein *et al.*, "Structure of photosystem II and substrate binding at room temperature", *Nature*, **540**, no. 7633, pp. 453–457 (2016). 3

[19] J. R. Stagno, Y. Liu, Y. R. Bhandari, C. E. Conrad, S. Panja, M. Swain, L. Fan, G. Nelson, C. Li, D. R. Wendel, T. A. White, J. D. Coe, M. O. Wiedorn, J. Knoska, D. Oberthuer *et al.*, "Structures of riboswitch RNA reaction states by mix-and-inject XFEL serial crystallography", *Nature*, **541**, no. 7636, pp. 242–246 (2017). 3

[20] C. Gati, D. Oberthuer, O. Yefanov, R. D. Bunker, F. Stellato, E. Chiu, S.-M. Yeh, A. Aquila, S. Basu, R. Bean, K. R. Beyerlein, S. Botha, S. Boutet, D. P. DePonte, R. B. Doak *et al.*, "Atomic structure of granulin determined from native nanocrystalline granulovirus using an X-ray free-electron laser", *Proceedings of the National Academy of Sciences*, **114**, no. 9, pp. 2247–2252 (2017). 3

[21] G. Huldt, A. Szőke and J. Hajdu, "Diffraction imaging of single particles and biomolecules", *Journal of Structural Biology*, **144**, no. 12, pp. 219 – 227 (2003). 3, 96

[22] H. N. Chapman, A. Barty, M. J. Bogan, S. Boutet, M. Frank, S. P. Hau-Riege, S. Marchesini, B. W. Woods, S. Bajt, W. H. Benner, R. A. London, E. Plonjes, M. Kuhlmann, R. Treusch, S. Dusterer *et al.*, "Femtosecond diffractive imaging with a soft-X-ray free-electron laser", *Nat. Phys.*, **2**, pp. 839–842 (2006). 3, 4

[23] K. J. Gaffney and H. N. Chapman, "Imaging Atomic Structure and Dynamics with Ultrafast X-ray Scattering", *Science*, **316**, no. 5830, pp. 1444–1448 (2007). 4, 96

[24] J. Rodenburg, "The phase problem, microdiffraction and wavelength-limited resolution a discussion", *Ultramicroscopy*, **27**, no. 4, pp. 413 – 422 (1989). 3

[25] H. N. Chapman and K. A. Nugent, "Coherent lensless X-ray imaging", *Nat Photon*, **4**, no. 12, pp. 833–839 (2010). 3, 112

[26] H. N. Chapman, "X-ray imaging beyond the limits", *Nat Mater*, **8**, no. 4, pp. 299–301 (2009). 4

[27] R. F. Egerton, "Outrun radiation damage with electrons?", *Advanced Structural and Chemical Imaging*, **1**, no. 1, p. 5 (2015). 4, 6

[28] J. Yang, M. Guehr, T. Vecchione, M. S. Robinson, R. Li, N. Hartmann, X. Shen, R. Coffee, J. Corbett, A. Fry, K. Gaffney, T. Gorkhover, C. Hast, K. Jobe, I. Makasyuk *et al.*, "Diffractive imaging of a rotational wavepacket in nitrogen molecules with femtosecond megaelectronvolt electron pulses", *Nat. Commun.*, **7**, no. 11232 (2016). 5, 112

[29] H. Ihee, B. M. Goodson, R. Srinivasan, V. A. Lobastov and A. H. Zewail, "Ultrafast electron diffraction and structural dynamics: Transient intermediates in the elimination reaction of C2F4I2", *Journal of Physical Chemistry A*, **106**, no. 16, pp. 4087–4103 (2002). 5

[30] C.-Y. Ruan, F. Vigliotti, V. A. Lobastov, S. Chen and A. H. Zewail, "Ultrafast electron crystallography: Transient structures of molecules, surfaces, and phase transitions", *Proceedings of the National Academy of Sciences of the United States of America*, **101**, no. 5, pp. 1123–1128 (2004). 5

[31] M. Gulde, S. Schweda, G. Storeck, M. Maiti, H. K. Yu, A. M. Wodtke, S. Schäfer and C. Ropers, "Ultrafast low-energy electron diffraction in transmission resolves polymer/graphene superstructure dynamics", *Science*, **345**, no. 6193, pp. 200–204 (2014). 5

[32] P. Musumeci, J. T. Moody, C. M. Scoby, M. S. Gutierrez, H. A. Bender and N. S. Wilcox, "High quality single shot diffraction patterns using ultrashort megaelectron volt electron beams from a radio frequency photoinjector", *Review of Scientific Instruments*, **81**, no. 1, p. 013306 (2010). 5

[33] S. Tokita, M. Hashida, S. Inoue, T. Nishoji, K. Otani and S. Sakabe, "Single-Shot Femtosecond Electron Diffraction with Laser-Accelerated Electrons: Experimental Demonstration of Electron Pulse Compression", *Phys. Rev. Lett.*, **105**, p. 215004 (2010). 5

[34] T. van Oudheusden, P. L. E. M. Pasmans, S. B. van der Geer, M. J. de Loos, M. J. van der Wiel and O. J. Luiten, "Compression of Subrelativistic Space-Charge-Dominated Electron Bunches for Single-Shot Femtosecond Electron Diffraction", *Phys. Rev. Lett.*, **105**, p. 264801 (2010). 5, 58

[35] J. Cao, Z. Hao, H. Park, C. Tao, D. Kau and L. Blaszczyk, "Femtosecond electron diffraction for direct measurement of ultrafast atomic motions", *Applied Physics Letters*, **83**, no. 5, pp. 1044–1046 (2003). 5

[36] R. Li, W. Huang, Y. Du, L. Yan, Q. Du, J. Shi, J. Hua, H. Chen, T. Du, H. Xu and C. Tang, "Note: Single-shot continuously time-resolved MeV ultrafast electron diffraction", *Review of Scientific Instruments*, **81**, no. 3, p. 036110 (2010). 5

[37] K. Mukojima, S. Kanzaki, K. Kawanishi, K. Sato and T. Abukawa, "Streak-camera reflection high-energy electron diffraction for dynamics of surface crystallography", *Surface Science*, **636**, pp. 25 – 30 (2015). 5

[38] J. S. Baskin, H. Liu and A. H. Zewail, "4D multiple-cathode ultrafast electron microscopy", *Proceedings of the National Academy of Sciences*, **111**, no. 29, pp. 10479–10484 (2014). 6

[39] S. C. Bell, *Cold electrons extracted from an ultracold plasma*, Ph.D. thesis, School of Physics, The University of Melbourne (2011). 6, 12, 112

[40] A. A. Ischenko, V. V. Golubkov, V. P. Spiridonov, A. V. Zgurskii, A. S. Akhmanov, M. G. Vabischevich and V. N. Bagratashvili, "A stroboscopical gas-electron diffraction method for the investigation of short-lived molecular species", *Applied Physics B*, **32**, no. 3, pp. 161–163 (1983). 6

[41] A. Feist, N. Bach, N. R. da Silva, T. Danz, M. Möller, K. E. Priebe, T. Domröse, J. G. Gatzmann, S. Rost, J. Schauss, S. Strauch, R. Bormann, M. Sivis, S. Schäfer and C. Ropers, "Ultrafast transmission electron microscopy using a laser-driven field emitter: Femtosecond resolution with a high coherence electron beam", *Ultramicroscopy*, **176**, pp. 63 – 73 (2017). 6

[42] D. T. Pierce and F. Meier, "Photoemission of spin-polarized electrons from GaAs", *Phys. Rev. B*, **13**, pp. 5484–5500 (1976). 6

[43] C. Hernandez-Garcia, P. G. O'Shea and M. L. Stutzman, "Electron sources for accelerators", *Physics Today*, **61**, pp. 44–49 (2008). 7, 79

[44] B. J. Claessens, S. B. van der Geer, G. Taban, E. J. D. Vredenbregt and O. J. Luiten, "Ultracold Electron Source", *Phys. Rev. Lett.*, **95**, p. 164801 (2005). 7, 79

[45] D. H. Dowell and J. F. Schmerge, "Quantum efficiency and thermal emittance of metal photocathodes", *Phys. Rev. ST Accel. Beams*, **12**, p. 074201 (2009). 7

[46] S. Pastuszka, M. Hoppe, D. Kratzmann, D. Schwalm, A. Wolf, A. S. Jaroshevich, S. N. Kosolobov, D. A. Orlov and A. S. Terekhov, "Preparation and performance of transmission-mode GaAs photocathodes as sources for cold dc electron beams", *Journal of Applied Physics*, **88**, no. 11, pp. 6788–6800 (2000). 7

[47] C. Limborg-Deprey and P. R. Bolton, "Optimum electron distributions for space charge dominated beams in photoinjectors", *Nuclear Instruments and Methods in Physics Research Section A: Accelerators, Spectrometers, Detectors and Associated Equipment*, **557**, no. 1, pp. 106 – 116 (2006). 7

[48] S. B. VAN DER GEER, O. J. LUITEN and M. J. DE LOOS, "DESIGN OF A 2 kA, 30 fs RF-PHOTOINJECTOR FOR WATERBAG COMPRESSION", *International Journal of Modern Physics A*, **22**, no. 22, pp. 4000–4005 (2007). 7

[49] O. J. LUITEN, B. J. CLAESSENS, S. B. VAN DER GEER, M. P. REIJNDERS, G. TABAN and E. J. D. VREDENBREGT, "ULTRACOLD ELECTRON SOURCES", *International Journal of Modern Physics A*, **22**, no. 22, pp. 3882–3897 (2007). 7, 49

[50] P. Musumeci, J. T. Moody, R. J. England, J. B. Rosenzweig and T. Tran, "Experimental Generation and Characterization of Uniformly Filled Ellipsoidal Electron-Beam Distributions", *Phys. Rev. Lett.*, **100**, p. 244801 (2008). 8, 50

[51] L. Serafini, "The short bunch blow-out regime in RF photoinjectors", *AIP Conference Proceedings*, **413**, no. 1, pp. 321–334 (1997). 8

[52] A. J. McCulloch, D. V. Sheludko, S. D. Saliba, S. C. Bell, M. Junker, K. A. Nugent and R. E. Scholten, "Arbitrarily shaped high-coherence electron bunches from cold atoms", *Nat. Phys.*, **7**, pp. 785–788 (2011). 8, 43

[53] G. Xia, M. Harvey, A. J. Murray, L. Bellan, W. Bertsche, R. B. Appleby, O. Mete and S. Chattopadhyay, "An ultracold low emittance electron source", *Journal of Instrumentation*, **9**, no. 06, p. P06011 (2014). 8

[54] W. Engelen, E. Smakman, D. Bakker, O. Luiten and E. Vredenbregt, "Effective temperature of an ultracold electron source based on near-threshold photoionization", *Ultramicroscopy*, **136**, pp. 73 – 80 (2014). 8

[55] L. Y. Baranov, R. Kris, R. D. Levine and U. Even, "On the field ionization spectrum of high Rydberg states", *The Journal of Chemical Physics*, **100**, no. 1, pp. 186–196 (1994). 8, 72

[56] D. Dowell, S. Bethel and K. Friddell, "Results from the average power laser experiment photocathode injector test", *Nuclear Instruments and Methods in Physics Research Section A: Accelerators, Spectrometers, Detectors and Associated Equipment*, **356**, no. 23, pp. 167 – 176 (1995). 9

[57] B. M. Sparkes, D. J. Thompson, A. J. McCulloch, D. Murphy, R. W. Speirs, J. S. J. Torrance and R. E. Scholten, "High-Coherence Electron and Ion Bunches From Laser-Cooled Atoms", *Microscopy and Microanalysis*, **20**, pp. 1008–1014 (2014). xiv, 9, 57

[58] W. J. Engelen, M. A. van der Heijden, D. J. Bakker, E. J. D. Vredenbregt and O. J. Luiten, "High-coherence electron bunches produced by femtosecond photoionization", *Nat Commun*, **4**, p. 1693 (2013). 9, 68, 77

[59] D. Murphy, R. W. Speirs, D. V. Sheludko, C. T. Putkunz, A. J. McCulloch, B. M. Sparkes and R. E. Scholten, "Detailed observation of space–charge dynamics using ultracold ion bunches", *Nature communications*, **5** (2014). xiv, 9, 46

[60] B. J. Claessens, M. P. Reijnders, G. Taban, O. J. Luiten and E. J. D. Vredenbregt, "Cold electron and ion beams generated from trapped atoms", *Physics of Plasmas*, **14**, no. 9, p. 093101 (2007). 9

[61] D. V. Sheludko, *Shaped electron bunches from ultracold plasma*, Ph.D. thesis, School of Physics, The University of Melbourne (2010). 12

[62] S. D. Saliba, *A cold atom electron source for diffractive imaging*, Ph.D. thesis, School of Physics, The University of Melbourne (2011). 12

[63] A. J. McCulloch, *Towards electron diffraction from a cold atom electron source*, Ph.D. thesis, School of Physics, The University of Melbourne (2012). 12

[64] K. B. MacAdam, A. Steinbach and C. Wieman, "A narrow-band tunable diode laser system with grating feedback, and a saturated absorption spectrometer for Cs and Rb", *American Journal of Physics*, **60**, no. 12, pp. 1098–1111 (1992). 14

[65] J. Kim and D. Cho, "Dark-spot magneto-optical trap of cesium atoms", *Journal of the Korean Physical Society*, **39**, no. 5, pp. 864–868 (2001). 14

[66] S. D. Saliba, C. T. Putkunz, D. V. Sheludko, A. J. McCulloch, K. A. Nugent and R. E. Scholten, "Spatial coherence of electron bunches extracted from an arbitrarily shaped cold atom electron source", *Opt. Express*, **20**, no. 4, pp. 3967–3974 (2012). 16

[67] A. Monmayrant, S. Weber and B. Chatel, "A newcomer's guide to ultrashort pulse shaping and characterization", *Journal of Physics B: Atomic, Molecular and Optical Physics*, **43**, no. 10, p. 103001 (2010). 17

[68] A. M. Weiner, "Femtosecond pulse shaping using spatial light modulators", *Review of Scientific Instruments*, **71**, no. 5, pp. 1929–1960 (2000). 17

[69] D. J. Griffiths, *Introduction to Electrodynamics*, Prentice Hall, 3rd edn. (1999). 18

[70] Beam4, Ver.168, Stellar Software, http://www.stellarsoftware.com. 19

[71] D. J. Thompson and R. E. Scholten, "Narrow linewidth tunable external cavity diode laser using wide bandwidth filter", *Review of Scientific Instruments*, **83**, no. 2, p. 023107 (2012). 19

[72] W. H. Press, S. A. Teukolsky, W. T. Vetterling and B. P. Flannery, *Numerical recipes: the art of scientific computing*, Cambridge University Press, 3rd edn. (2007). 21

[73] J. C. Simpson, J. E. Lane, C. D. Immer and R. C. Youngquist, "Simple analytic expressions for the magnetic field of a circular current loop", *NASA technical reports server* (2001). 22

[74] M. Reiser, *Theory and design of charged particle beams*, John Wiley & Sons (2008). 31

[75] A. J. McCulloch, B. M. Sparkes and R. E. Scholten, "Cold electron sources using laser-cooled atoms", *Journal of Physics B: Atomic, Molecular and Optical Physics*, **49**, no. 16, p. 164004 (2016). 34

[76] J. W. Goodman, *Statistical Optics*, John Wiley & Sons (1985). 35, 37, 41

[77] D. M. Paganin, *Coherent X-Ray Optics*, Oxford Science Publications (2006). 36

[78] E. Collett and E. Wolf, "Beams generated by Gaussian quasi-homogeneous sources", *Optics Communications*, **32**, no. 1, pp. 27 – 31 (1980). 38

[79] K. Nugent, "A generalization of Schell's theorem", *Optics Communications*, **79**, no. 5, pp. 267 – 269 (1990). 41

[80] K. A. Nugent, "Partially coherent diffraction patterns and coherence measurement", *J. Opt. Soc. Am. A*, **8**, no. 10, pp. 1574–1579 (1991). 41

[81] O. D. Kellogg, *Foundations of Potential Theory*, Springer-Verlag, Berlin (1929). 43

[82] I. M. Kapchinski and V. V. Vladimirski, in "Proceedings of the International Conference on High Energy Accelerators", CERN, Geneva (1959), (p. 274). 43

[83] N. Debernardi, M. P. Reijnders, W. J. Engelen, T. T. J. Clevis, P. H. A. Mutsaers, O. J. Luiten and E. J. D. Vredenbregt, "Measurement of the temperature of an ultracold ion source using time-dependent electric fields", *Journal of Applied Physics*, **110**, no. 2, p. 024501 (2011). 44

[84] D. Murphy, *Measurement and Modelling of Intrabeam Coulomb Interactions in Ultracold Ion Bunches*, Ph.D. thesis, School of Physics, The University of Melbourne (2017). 45, 130

[85] General Particle Tracer, Pulsar Physics, http://www.pulsar.nl. 46

[86] A. E. Kaplan, B. Y. Dubetsky and P. L. Shkolnikov, "Shock Shells in Coulomb Explosions of Nanoclusters", *Phys. Rev. Lett.*, **91**, p. 143401 (2003). 47

[87] D. Feldbaum, N. V. Morrow, S. K. Dutta and G. Raithel, "Coulomb Expansion of Laser-Excited Ion Plasmas", *Phys. Rev. Lett.*, **89**, p. 173004 (2002). 47

[88] O. J. Luiten, S. B. van der Geer, M. J. de Loos, F. B. Kiewiet and M. J. van der Wiel, "How to Realize Uniform Three-Dimensional Ellipsoidal Electron Bunches", *Phys. Rev. Lett.*, **93**, p. 094802 (2004). 49, 50

[89] J. T. Moody, P. Musumeci, M. S. Gutierrez, J. B. Rosenzweig and C. M. Scoby, "Longitudinal phase space characterization of the blow-out regime of rf photoinjector operation", *Phys. Rev. ST Accel. Beams*, **12**, p. 070704 (2009). 50

[90] P. Piot, Y.-E. Sun, T. J. Maxwell, J. Ruan, E. Secchi and J. C. T. Thangaraj, "Formation and acceleration of uniformly filled ellipsoidal electron bunches obtained via space-charge-driven expansion from a cesium-telluride photocathode", *Phys. Rev. ST Accel. Beams*, **16**, p. 010102 (2013). 50

[91] R. K. Li, K. G. Roberts, C. M. Scoby, H. To and P. Musumeci, "Nanometer emittance ultralow charge beams from rf photoinjectors", *Phys. Rev. ST Accel. Beams*, **15**, p. 090702 (2012). 50

[92] B. O'Shea, J. B. Rosenzweig, G. Asova, J. Bähr, M. Hänel, Y. Ivanisenko, M. Khojoyan, M. Krasilnikov, L. Staykov, F. Stephan and J. Rönsch-Schulenburg, "Measurement of self-shaped ellipsoidal bunches from a photoinjector with postacceleration", *Phys. Rev. ST Accel. Beams*, **14**, p. 012801 (2011). 50

[93] Y. Li, S. Chemerisov and B. Shen, "Ultrafast spatiotemporal laser pulse engineering using chromatic dispersion", *New Journal of Physics*, **12**, no. 12, p. 123011 (2010). 50

[94] D. J. Thompson, D. Murphy, R. W. Speirs, R. M. W. van Bijnen, A. J. McCulloch, R. E. Scholten and B. M. Sparkes, "Suppression of Emittance Growth Using a Shaped Cold Atom Electron and Ion Source", *Phys. Rev. Lett.*, **117**, p. 193202 (2016). xiv, 50

[95] C. J. Foot, *Atomic physics*, vol. 7, Oxford University Press (2005). 51, 64

[96] R. M. W. van Bijnen, C. Ravensbergen, D. J. Bakker, G. J. Dijk, S. J. J. M. F. Kokkelmans and E. J. D. Vredenbregt, "Patterned Rydberg excitation and ionization with a spatial light modulator", *New Journal of Physics*, **17**, no. 2, p. 023045 (2015). 52

[97] R. van Bijnen, *Quantum engineering with ultracold atoms*, Ph.D. thesis, Technische Universiteit Eindhoven (2013). 52

[98] I. V. Bazarov, B. M. Dunham, Y. Li, X. Liu, D. G. Ouzounov, C. K. Sinclair, F. Hannon and T. Miyajima, "Thermal emittance and response

time measurements of negative electron affinity photocathodes", *Journal of Applied Physics*, **103**, no. 5, 054901 (2008). 57

[99] W. Engelen, E. Vredenbregt and O. Luiten, "Analytical model of an isolated single-atom electron source", *Ultramicroscopy*, **147**, pp. 61 – 69 (2014). 57

[100] W. Engelen, *Coherent electron bunches from laser-cooled gases*, Ph.D. thesis, Technische Universiteit Eindhoven (2013). 57

[101] B. Broers, J. F. Christian, J. H. Hoogenraad, W. J. van der Zande, H. B. van Linden van den Heuvell and L. D. Noordam, "Time-resolved dynamics of electronic wave packets above the classical field-ionization threshold", *Phys. Rev. Lett.*, **71**, pp. 344–347 (1993). 57, 69

[102] B. Broers, J. F. Christian and H. B. van Linden van den Heuvell, "Experimental investigation of rubidium atoms above the field-ionization limit using a time-resolved wave-packet approach", *Phys. Rev. A*, **49**, pp. 2498–2507 (1994). 57, 69

[103] G. M. Lankhuijzen and L. D. Noordham, "Frequency- and time-resolved study of the dynamics of rubidium Rydberg wave packets in an electric field", *Phys. Rev. A*, **52**, pp. 2016–2028 (1995). 57, 69

[104] W. J. Engelen, D. J. Bakker, O. J. Luiten and E. J. D. Vredenbregt, "Polarization effects on the effective temperature of an ultracold electron source", *New Journal of Physics*, **15**, no. 12, p. 123015 (2013). 57

[105] A. J. McCulloch, D. V. Sheludko, M. Junker and R. E. Scholten, "High-coherence picosecond electron bunches from cold atoms", *Nat. Commun.*, **4**, no. 1692 (2013). 57, 60, 68, 77, 91

[106] R. W. Speirs, A. J. McCulloch, B. M. Sparkes and R. E. Scholten, "Identification of competing ionization processes in the generation of ultrafast electron bunches from cold-atom electron sources", *Phys. Rev. A*, **95**, p. 053408 (2017). xiv, 57

[107] G. Sciaini and R. J. D. Miller, "Femtosecond electron diffraction: heralding the era of atomically resolved dynamics", *Reports on Progress in Physics*, **74**, no. 9, p. 096101 (2011). 58

[108] J. J. McClelland, A. V. Steele, B. Knuffman, K. A. Twedt, A. Schwarzkopf and T. M. Wilson, "Bright focused ion beam sources based on laser-cooled atoms", *Applied Physics Reviews*, **3**, no. 1, 011302 (2016). 58, 79

[109] B. Knuffman, A. V. Steele, J. Orloff and J. J. McClelland, "Nanoscale focused ion beam from laser-cooled lithium atoms", *New Journal of Physics*, **13**, no. 10, p. 103035 (2011). 58

[110] A. V. Steele, A. Schwarzkopf, J. J. McClelland and B. Knuffman, "High-brightness Cs focused ion beam from a cold-atomic-beam ion source", *Nano Futures*, **1**, no. 1, p. 015005 (2017). 58

[111] F. Hasselbach, "Progress in electron- and ion-interferometry", *Reports on Progress in Physics*, **73**, no. 1, p. 016101 (2010). 58

[112] L. Kime, A. Fioretti, Y. Bruneau, N. Porfido, F. Fuso, M. Viteau, G. Khalili, N. Šantić, A. Gloter, B. Rasser, P. Sudraud, P. Pillet and D. Comparat, "High-flux monochromatic ion and electron beams based on laser-cooled atoms", *Phys. Rev. A*, **88**, p. 033424 (2013). 58

[113] C. J. Joachain, N. J. Kylstra and R. M. Potvliege, *Atoms in intense laser fields*, Cambridge University Press (2012). 60

[114] K. D. Belfield, K. J. Schafer, Y. Liu, J. Liu, X. Ren and E. W. Van Stryland, "Multiphoton-absorbing organic materials for microfabrication, emerging optical applications and non-destructive three-dimensional imaging", *Journal of Physical Organic Chemistry*, **13**, no. 12, pp. 837–849 (2000). 60, 72

[115] M. B. Robin, "Multiphoton fragmentation and ionization", *Appl. Opt.*, **19**, no. 23, pp. 3941–3947 (1980). 60, 72

[116] T. F. Gallagher, *Rydberg Atoms*, Cambridge University Press (1994). 60, 61

[117] Z. Stryla and R. Parzynski, "Three-photon ionisation of potassium atoms near the 4 2 P 1/2,3/2 resonances", *Journal of Physics B: Atomic and Molecular Physics*, **19**, no. 5, p. 541 (1986). 64

[118] L. Deng, W. R. Garrett, M. G. Payne and D. Z. Lee, "Effect of the odd-photon destructive interference on laser-induced transparency and multi-photon excitation and ionization in rubidium", *Phys. Rev. A*, **54**, pp. 4218–4225 (1996). 65

[119] M. S. Safronova, C. J. Williams and C. W. Clark, "Relativistic many-body calculations of electric-dipole matrix elements, lifetimes, and polarizabilities in rubidium", *Phys. Rev. A*, **69**, p. 022509 (2004). 67

[120] C. E. Theodosiou, "Lifetimes of alkali-metal-atom Rydberg states", *Phys. Rev. A*, **30**, pp. 2881–2909 (1984). 67

[121] J. G. H. Franssen, T. L. I. Frankort, E. J. D. Vredenbregt and O. J. Luiten, "Pulse length of ultracold electron bunches extracted from a laser cooled gas", *Structural Dynamics*, **4**, no. 4, p. 044010 (2017). 68, 73, 77

[122] C. Bordas, "Classical motion of a photoelectron interacting with its ionic core: Slow photoelectron imaging", *Phys. Rev. A*, **58**, pp. 400–410 (1998). 68

[123] A. S. Stodolna, A. Rouzée, F. Lépine, S. Cohen, F. Robicheaux, A. Gijsbertsen, J. H. Jungmann, C. Bordas and M. J. J. Vrakking, "Hydrogen Atoms under Magnification: Direct Observation of the Nodal Structure of Stark States", *Phys. Rev. Lett.*, **110**, p. 213001 (2013). 68

[124] G. Nimtz, "Tunneling Confronts Special Relativity", *Foundations of Physics*, **41**, no. 7, pp. 1193–1199 (2011). 71

[125] E. H. Hauge and J. A. Støvneng, "Tunneling times: a critical review", *Rev. Mod. Phys.*, **61**, pp. 917–936 (1989). 71

[126] P. M. Koch and D. R. Mariani, "Precise Measurement of the Static Electric-Field Ionization Rate for Resolved Hydrogen Stark Substates", *Phys. Rev. Lett.*, **46**, pp. 1275–1278 (1981). 72

[127] M. G. Littman, M. M. Kash and D. Kleppner, "Field-Ionization Processes in Excited Atoms", *Phys. Rev. Lett.*, **41**, pp. 103–107 (1978). 72

[128] R. Haydock and D. R. Kingham, "The model dependence of the ionisation rate of hydrogen in a uniform electric field", *Journal of Physics B: Atomic and Molecular Physics*, **14**, no. 2, p. 385 (1981). 72

[129] U. Hollenstein, R. Seiler, H. Schmutz, M. Andrist and F. Merkt, "Selective field ionization of high Rydberg states: Application to zero-kinetic-energy photoelectron spectroscopy", *The Journal of Chemical Physics*, **115**, no. 12, pp. 5461–5469 (2001). 74

[130] M. Førre and J. P. Hansen, "Selective-field-ionization dynamics of a lithium $m = 2$ Rydberg state: Landau-Zener model versus quantal approach", *Phys. Rev. A*, **67**, p. 053402 (2003). 74

[131] A. J. McCulloch, R. W. Speirs, J. Grimmel, B. M. Sparkes, D. Comparat and R. E. Scholten, "Field ionization of Rydberg atoms for high-brightness electron and ion beams", *Phys. Rev. A*, **95**, p. 063845 (2017). xiv, 74, 75

[132] M. L. Zimmerman, M. G. Littman, M. M. Kash and D. Kleppner, "Stark structure of the Rydberg states of alkali-metal atoms", *Phys. Rev. A*, **20**, pp. 2251–2275 (1979). 74

[133] M. G. Littman, M. L. Zimmerman and D. Kleppner, "Tunneling Rates for Excited States of Sodium in a Static Electric Field", *Phys. Rev. Lett.*, **37**, pp. 486–489 (1976). 74

[134] D. S. Bailey, J. R. Hiskes and A. Riviere, "Electric field ionization probabilities for the hydrogen atom", *Nuclear Fusion*, **5**, no. 1, p. 41 (1965). 74

[135] R. J. Damburg and V. V. Kolosov, "A hydrogen atom in a uniform electric field. III", *Journal of Physics B: Atomic and Molecular Physics*, **12**, no. 16, p. 2637 (1979). 74

[136] J. W. Farley and W. H. Wing, "Accurate calculation of dynamic Stark shifts and depopulation rates of Rydberg energy levels induced by blackbody radiation. Hydrogen, helium, and alkali-metal atoms", *Phys. Rev. A*, **23**, pp. 2397–2424 (1981). 74

[137] J. Grimmel, M. Stecker, M. Kaiser, F. Karlewski, L. Torralbo-Campo, A. Günther and J. Fortágh, "Ionization spectra of highly Stark-shifted rubidium Rydberg states", *Phys. Rev. A*, **96**, p. 013427 (2017). 74

[138] W. van de Water, D. R. Mariani and P. M. Koch, "Ionization of highly excited helium atoms in an electric field", *Phys. Rev. A*, **30**, pp. 2399–2412 (1984). 75

[139] B. Knuffman, A. V. Steele and J. J. McClelland, "Cold atomic beam ion source for focused ion beam applications", *Journal of Applied Physics*, **114**, no. 4, 044303 (2013). 79

[140] K. A. Twedt, J. Zou, M. Davanco, K. Srinivasan, J. J. McClelland and V. A. Aksyuk, "Imaging nanophotonic modes of microresonators using a focused ion beam", *Nat Photon*, **10**, no. 1, pp. 35–39 (2016). 79

[141] R. W. Speirs, C. T. Putkunz, A. J. McCulloch, K. A. Nugent, B. M. Sparkes and R. E. Scholten, "Single-shot electron diffraction using a cold atom electron source", *Journal of Physics B: Atomic, Molecular and Optical Physics*, **48**, no. 21, p. 214002 (2015). xiv, 79

[142] S. van der Geer, M. de Loos, E. Vredenbregt and O. Luiten, "Ultracold Electron Source for Single-Shot, Ultrafast Electron Diffraction", *Microscopy and Microanalysis*, **15**, pp. 282–289 (2009). 79

[143] M. W. van Mourik, W. J. Engelen, E. J. D. Vredenbregt and O. J. Luiten, "Ultrafast electron diffraction using an ultracold source", *Structural Dynamics*, **1**, no. 3, 034302 (2014). 79

[144] J. M. Cowley, *Electron diffraction techniques*, Oxford University Press (1988). 80

[145] L. Reimer, *Transmission electron microscopy : physics of image formation and microanalysis*, Springer-Verlag (1984). 80, 100, 116

[146] P. E. Champness, *Electron diffraction in the transmission electron microscope*, Bios Scientific (2001). 80

[147] R. F. Egerton, *Physical principles of electron microscopy : an introduction to TEM, SEM, and AEM*, Springer (2005). 80

[148] L.-M. Peng, "Electron atomic scattering factors and scattering potentials of crystals", *Micron*, **30**, no. 6, pp. 625 – 648 (1999). 83, 98

[149] H. N. Chapman, P. Fromme, A. Barty, T. A. White, R. A. Kirian, A. Aquila, M. S. Hunter, J. Schulz, D. P. DePonte, U. Weierstall, R. B. Doak, F. R. N. C. Maia, A. V. Martin, I. Schlichting, L. Lomb *et al.*, "Femtosecond X-ray protein nanocrystallography", *Nature*, **470**, no. 7332, pp. 73–77 (2011). 96

[150] U. Adiga, W. T. Baxter, R. J. Hall, B. Rockel, B. K. Rath, J. Frank and R. Glaeser, "Particle picking by segmentation: A comparative study with SPIDER-based manual particle picking", *Journal of Structural Biology*, **152**, no. 3, pp. 211 – 220 (2005). 96

[151] A. Maeland and T. B. Flanagan, "Lattice Spacings of GOLD-PALLADIUM Alloys", *Canadian Journal of Physics*, **42**, pp. 2364–2366 (1964). 97

[152] D. W. Pashley and M. J. Stowell, "Electron microscopy and diffraction of twinned structures in evaporated films of gold", *Philosophical Magazine*, **8**, no. 94, pp. 1605–1632 (1963). 102

[153] A. McPherson and A. Rich, "Crystallographic study of beef liver catalase", *Archives of Biochemistry and Biophysics*, **157**, no. 1, pp. 23 – 27 (1973). 104

[154] D. L. Dorset and D. F. Parsons, "Electron diffraction from single, fully-hydrated, ox-liver catalase microcrystals", *Acta Crystallographica Section A*, **31**, no. 2, pp. 210–215 (1975). 104

[155] N. G. Wrigley, "The lattice spacing of crystalline catalase as an internal standard of length in electron microscopy", *Journal of Ultrastructure Research*, **24**, no. 5, pp. 454 – 464 (1968). 104

[156] "Graphene Transmission Electron Microscopy Support Films", GrapheneSupermatket®, http://www.graphene-supermarket.com/images/XC/TEM/GrapheneTEMgrids-General%20info.pdf, 2016-11-21. 105

[157] D. D. L. Chung, "Review Graphite", *Journal of Materials Science*, **37**, no. 8, pp. 1475–1489 (2002). 105

[158] "Diffraction Standard Evaporated Aluminum", TedPellaINC., https://www.tedpella.com/technote_html/619%20TN.pdf, 2016-11-21. 107

[159] D. W. Jepsen, P. M. Marcus and F. Jona, "Low-Energy-Electron-Diffraction Spectra from [001] Surfaces of Face-Centered Cubic Metals: Theory and Experiment", *Phys. Rev. B*, **5**, pp. 3933–3952 (1972). 108

[160] H. E. ElsayedAli and J. W. Herman, "Picosecond time-resolved surface-lattice temperature probe", *Applied Physics Letters*, **57**, no. 15, pp. 1508–1510 (1990). 109

[161] G. Storeck, S. Vogelgesang, M. Sivis, S. Schäfer and C. Ropers, "Nanotip-based photoelectron microgun for ultrafast LEED", *Structural Dynamics*, **4**, no. 4, p. 044024 (2017). 109

[162] J. Neave, B. Joyce, P. Dobson and N. Norton, "Dynamics of film growth of GaAs by MBE from Rheed observations", *Applied Physics A*, **31**, no. 1, pp. 1–8 (1983). 109

[163] A. Ichimiya and P. I. Cohen, *Reflection high-energy electron diffraction*, Cambridge University Press (2004). 109

[164] M. Harvey and A. J. Murray, "Cold Atom Trap with Zero Residual Magnetic Field: The ac Magneto-Optical Trap", *Phys. Rev. Lett.*, **101**, p. 173201 (2008). 111

[165] D. Sayre, "Some implications of a theorem due to Shannon", *Acta Crystallographica*, **5**, no. 6, p. 843 (1952). 112

[166] J. R. Fienup, "Phase retrieval algorithms: a comparison", *Appl. Opt.*, **21**, no. 15, pp. 2758–2769 (1982). 112

[167] R. Neutze, R. Wouts, D. van der Spoel, E. Weckert and J. Hajdu, "Potential for biomolecular imaging with femtosecond X-ray pulses", *Nature*, **406**, no. 6797, pp. 752–757 (2000). 112

[168] J. M. Zuo, I. Vartanyants, M. Gao, R. Zhang and L. A. Nagahara, "Atomic Resolution Imaging of a Carbon Nanotube from Diffraction Intensities", *Science*, **300**, no. 5624, pp. 1419–1421 (2003). 112

[169] J. Yang, V. Makhija, V. Kumarappan and M. Centurion, "Reconstruction of three-dimensional molecular structure from diffraction of laser-aligned molecules", *Structural Dynamics*, **1**, no. 4, 044101 (2014). 112

[170] U. Weierstall, Q. Chen, J. Spence, M. Howells, M. Isaacson and R. Panepucci, "Image reconstruction from electron and X-ray diffraction patterns using iterative algorithms: experiment and simulation", *Ultramicroscopy*, **90**, no. 23, pp. 171 – 195 (2002). 113

[171] R. W. Gerchberg and W. O. Saxton, "A practical algorithm for the determination of phase from image and diffraction plane pictures", *Optik*, **35**, p. 237 (1972). 117

[172] J. R. Fienup, "Phase retrieval algorithms: a personal tour", *Appl. Opt.*, **52**, no. 1, pp. 45–56 (2013). 117

[173] S. Marchesini, H. He, H. N. Chapman, S. P. Hau-Riege, A. Noy, M. R. Howells, U. Weierstall and J. C. H. Spence, "X-ray image reconstruction from a diffraction pattern alone", *Phys. Rev. B*, **68**, p. 140101 (2003). 117

[174] J. Miao, P. Charalambous, J. Kirz and D. Sayre, "Extending the methodology of X-ray crystallography to allow imaging of micrometre-sized non-crystalline specimens", *Nature*, **400**, no. 6742, pp. 342–344 (1999). 117

[175] J. R. Fienup, T. R. Crimmins and W. Holsztynski, "Reconstruction of the support of an object from the support of its autocorrelation", *J. Opt. Soc. Am.*, **72**, no. 5, pp. 610–624 (1982). 119

[176] G. Gronniger, B. Barwick, H. Batelaan, T. Savas, D. Pritchard and A. Cronin, "Electron diffraction from free-standing, metal-coated transmission gratings", *Applied Physics Letters*, **87**, no. 12, p. 124104 (2005). 124

[177] S. Frabboni, G. C. Gazzadi and G. Pozzi, "Nanofabrication and the realization of Feynman's two-slit experiment", *Applied Physics Letters*, **93**, no. 7, 073108 (2008). 124

[178] R. Bach, D. Pope, S.-H. Liou and H. Batelaan, "Controlled double-slit electron diffraction", *New Journal of Physics*, **15**, no. 3, p. 033018 (2013). 124

[179] V. E. Cosslett and R. N. Thomas, "Multiple scattering of 5-30 keV electrons in evaporated metal films: I. Total transmission and angular distribution", *British Journal of Applied Physics*, **15**, no. 8, p. 883 (1964). 124

[180] B. M. Sparkes, D. Murphy, R. J. Taylor, R. W. Speirs, A. J. McCulloch and R. E. Scholten, "Stimulated Raman adiabatic passage for improved performance of a cold-atom electron and ion source", *Phys. Rev. A*, **94**, p. 023404 (2016). xiv

Appendix A

Publications

This section contains copies of peer reviewed journal articles that I have contributed to as listed on page xiv.

IOP Publishing Journal of Physics B: Atomic, Molecular and Optical Physics
J. Phys. B: At. Mol. Opt. Phys. 48 (2015) 214002 (6pp) doi:10.1088/0953-4075/48/21/214002

Single-shot electron diffraction using a cold atom electron source

Rory W Speirs[1], Corey T Putkunz[1], Andrew J McCulloch[1], Keith A Nugent[2], Benjamin M Sparkes[1] and Robert E Scholten[1]

[1] School of Physics, The University of Melbourne, Victoria, 3010, Australia
[2] ARC Centre of Excellence for Advanced Molecular Imaging, Department of Physics, La Trobe University, Victoria 3086, Australia

E-mail: scholten@unimelb.edu.au

Received 4 June 2015, revised 30 July 2015
Accepted for publication 7 August 2015
Published 23 September 2015

Abstract

Cold atom electron sources (CAESs) are a promising alternative to traditional photocathode sources for use in ultrafast electron diffraction due to greatly reduced electron temperature at creation, and the potential for a corresponding increase in brightness. Here we demonstrate single-shot, nanosecond electron diffraction from monocrystalline gold using cold electron bunches generated in a CAES. The diffraction patterns have sufficient signal to allow registration of multiple single-shot images, generating an averaged image with significantly higher signal-to-noise ratio than obtained with unregistered averaging. Reflection high-energy electron diffraction was also demonstrated, showing that CAESs may be useful in resolving nanosecond dynamics of nanometre scale near-surface structures.

Keywords: cold atom electron source, ultrafast electron diffraction, diffraction imaging

(Some figures may appear in colour only in the online journal)

1. Introduction

Ultrafast single-shot diffraction is revolutionizing our understanding of materials science, chemistry, and biology, by imaging objects on atomic length and time scales simultaneously [1–3]. X-ray free electron lasers (XFELs) have been used to perform single-shot coherent diffractive imaging on micro- and nano-metre scale targets [4, 5], where the imaging pulse is briefer than the time scale of damage to the object [6, 7]. An alternative and complementary approach is ultrafast electron diffraction, which benefits not only from much stronger scattering of electrons relative to x-rays [8], but also significantly reduced damage per elastic scattering event [9]. To enable single-shot diffraction studies, the number of electrons per pulse must be of order 10^6 or greater to have sufficient signal per pixel at the detector [10]. This number is easily achievable with photocathode sources, and when combined with RF bunch compression, sub 100 fs pulses have been achieved [11]. The brightness of photocathode sources is limited by the high initial temperature of the extracted electrons (10^4 K), leading to a high transverse emittance [12]. The emittance required for single-shot imaging depends on the size of the object being imaged: larger object sizes or crystal periods require lower emittance to generate useful coherent diffraction patterns. Ultrafast single-shot electron diffraction has been achieved from large single crystal and polycrystalline samples using a variety of photocathode based sources [13–17], but insufficient source brightness has prevented demonstration for micro or nanocrystals, or single molecules.

Cold electron sources are a promising alternative to solid state photocathodes, producing electrons by near threshold photoionization of laser cooled atoms. Electrons from these sources have an intrinsic temperature as low as 10 K, which for a given flux leads to several orders of magnitude increase in brightness [18, 19]. The low electron temperature, together with the ability to spatially shape the beam [20], should allow these sources to produce uniformly filled ellipsoid bunches, which do not suffer emittance degradation resulting from nonlinear internal Coulomb forces [21].

A cold electron source was recently used for the first time to generate a transmission electron diffraction pattern [22]. In that experiment, cold, sub-picosecond electron pulses containing a few hundred electrons were scattered by graphite. To

J. Phys. B: At. Mol. Opt. Phys. **48** (2015) 214002 R W Speirs *et al*

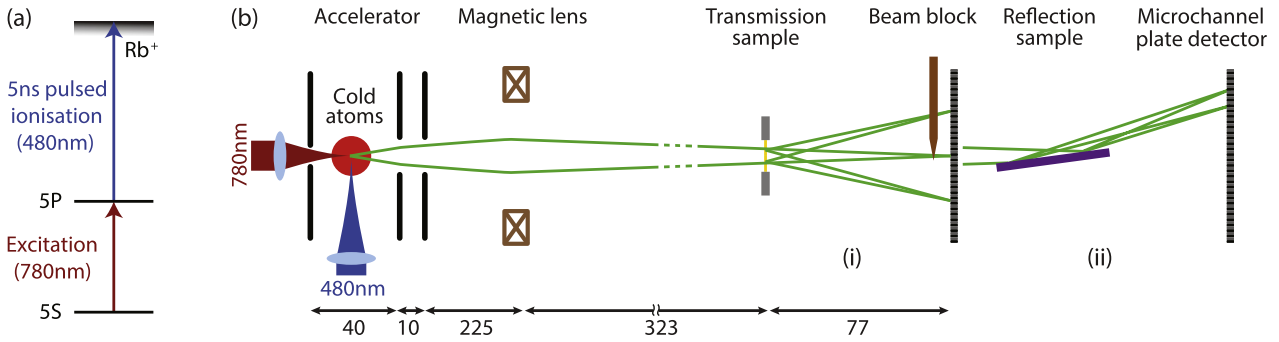

Figure 1. (a) Rubidium atoms are ionized in a two step process: 780 nm laser light drives them to the first excited state where they are ionized by a 5 ns pulse of 480 nm light. (b) The electrons produced are accelerated by a static electric field, focused, and scattered off a sample, either in transmission (i) or reflection (ii) geometries. Distances are in millimetres.

produce diffraction patterns with clearly discernible Bragg reflections, several thousand individual shots were integrated.

Here we present the first *single-shot* electron diffraction patterns obtained using a cold electron source. The patterns were obtained from a monocrystalline gold foil using a single 5 ns bunch of 5×10^5 electrons. No electron aperture was required due to the high spatial coherence of the electrons at the source. This allowed all generated electrons to contribute to the image, resulting in a single shot with sufficiently high signal-to-noise ratio for identification of the sample and registration of successive images. Single-shot reflection high-energy electron diffraction (RHEED) was also demonstrated from a wafer of monocrystalline silicon.

2. The cold atom electron source (CAES)

The CAES generates electrons by photoionization of rubidium-85 atoms in a magneto-optical trap, which is positioned between two accelerating electrodes as shown in figure 1(b).

The photoionization is a two-stage process (figure 1(a)). The atoms are excited from the $5S_{1/2}(F = 3)$ ground state to the $5P_{3/2}(F = 4)$ excited state using a 100 ns pulse of laser light of wavelength 780 nm. A 5 ns pulse from the ionization laser (wavelength 480 nm) then drives the atoms either to a Rydberg level, or directly to the continuum.

The excitation laser illuminates the atom cloud along the axis of electron propagation (longitudinal direction), and the focused intensity profile can be changed arbitrarily using a liquid crystal spatial light modulator, which defines the shape of the electron bunch in the two dimensions transverse to propagation [20]. The blue ionization laser illuminates the atom cloud transversely to the electron propagation axis, defining the longitudinal profile of the electron bunch which is generated in the region of overlap of the two laser beams such that the bunch is shaped in all three-dimensions.

The ionization time is determined by the temporal profile of the blue tunable dye laser pulse, with full width half maximum (FWHM) duration of 5 ns, pulse energy of 5 mJ at the cloud, and repetition rate of 10 Hz. The blue laser is focused with a cylindrical lens onto the atom cloud, so that the ionization region is defined by a ribbon of light with a FWHM width of 30 μm in the longitudinal direction.

Before ionization the atom cloud has a peak density of 10^{10} atoms cm^{-3} and temperature 100 μK. The quadrupole magnetic field is switched off and allowed to decay for 3.5 ms before ionization, but a remnant magnetic field alters the electron trajectory slightly from shot to shot.

The accelerator can be used in a two or three electrode configuration. The arrangement of applied potentials allows flexibility in determining the extraction electric field strength, the final energy of the electrons, and the diverging beam angle, which is defined in part by the lensing effect of the electrodes. In addition, the energy spread of the extracted electrons is determined by the combination of extraction electric field strength and longitudinal width of the ionization region. A standard configuration of potentials with field strength 2.6 kVcm^{-1} and a blue beam width of 30 μm results in an electron energy spread of 8 eV. This is a relatively high energy spread compared to sources used in conventional electron microscopes, where chromatic aberration in the strong objective lens drives the need for low energy dispersion. The contribution to the point spread function due to chromatic aberration is proportional to the beam semi-angle accepted into the lens, and for the single weak condenser lens used in our setup, this contribution is significantly smaller than the detector resolution. Polychromaticity also results in a spread of diffraction angles for any given sample spatial frequency, limiting the achievable resolution in coherent diffractive imaging. We typically use an electron energy of 8 keV for diffraction experiments, giving a fractional energy spread of $\Delta E/E < 0.001$, which contributes negligibly to the spread in diffraction angles from the sample, and would allow coherent diffractive imaging of 20 nm objects to a resolution of better than 1 Å [23]. The energy spread could be reduced further if required by tailoring the extraction field strength or reducing the focal spot size of the blue laser beam, though the latter would also reduce the number of electrons generated.

After the electron bunch leaves the accelerator, it traverses a solenoid magnetic lens at a distance of 225 mm, before drifting 323 mm to the sample. The low numerical aperture of the lens limits the ability to create very small beam sizes at the sample, but results in a highly collimated beam

without the need to introduce further electron optics. After the target sample the diffracted electrons propagate 77 mm to a phosphor-coupled microchannel plate (MCP) detector which is imaged with a camera.

3. Beam parameters

We used a Gaussian excitation laser beam of width 80 μm FWHM at the focus, with peak intensity thousands of times the saturation intensity to maximize the bunch charge. The effective excitation volume was increased by saturation broadening and reabsorption of radiative decay. The effective width of the source was 1.4 mm FWHM, determined from the unfocused electron bunch size at the detector and the known magnification of the electron optics. The source divergence of our source is $\sigma_{\theta_x} = 0.3$ μrad [18], giving a source emittance of $\epsilon_x = 50$ nm rad. The electrons were focused to a minimum spot size at the MCP as shown in figure 1, with beam width at the sample of approximately 300 μm, and corresponding coherence length at this point of $\ell_c = 2$ nm. Using a Faraday cup, the number of electrons per pulse was measured as 5×10^5 (80 fC), corresponding to an ionization fraction of approximately 50% within the ionization region. The bunch temporal profile was estimated to be Gaussian with a duration of 5 ns FWHM based on the shape of the blue laser pulse, leading to a peak beam current of 20 μA and peak brightness of $\mathscr{B} = 3 \times 10^8$ A m^{-2} sr^{-1} [18].

The emittance and bunch charge for the CAES are therefore approaching the values required for single-shot diffraction of microcrystals [24], but the pulse duration is up to six orders of magnitude too long to avoid degradation of the diffraction pattern due to beam induced damage of such small samples. Recent studies have suggested the constraints on pulse duration due to damage could be relaxed for electrons compared with x-rays, because of the differences between the scattering and damage-inducing processes [25]. To achieve sub-picosecond ultrafast electron diffraction, the ionization process can be modified to use femtosecond rather than nanosecond laser pulses [18, 19]. Picosecond to femtosecond duration electron bunches containing the same charge will require spatial beam shaping in order to avoid brightness degradation caused by the otherwise nonlinear space charge expansion of the bunch [26].

4. Single-shot electron diffraction

We demonstrated diffraction of electron bunches generated in the CAES from an 11 nm thick gold foil mounted on a 3 mm transmission electron microscopy grid, with an electron energy of 8 keV. Figure 2 shows the diffraction pattern from a single 5 ns electron bunch. The resulting Bragg reflections are clearly visible out to the $(\overline{2}40)$ spot at a resolution of 1.1 Å^{-1}, where the crystallographic convention has been adopted for reciprocal lattice vectors, such that $|\mathbf{g}_{hkl}| = 1/d_{hkl}$, where d_{hkl} is distance between atomic planes in real space.

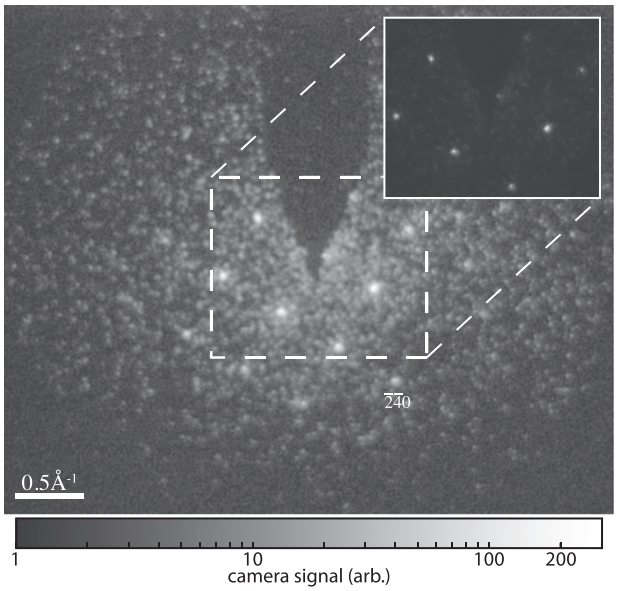

Figure 2. Single-shot transmission electron diffraction from gold, formed from a 5 ns pulse of cold electrons. Main image is logarithmically scaled, inset is linearly scaled.

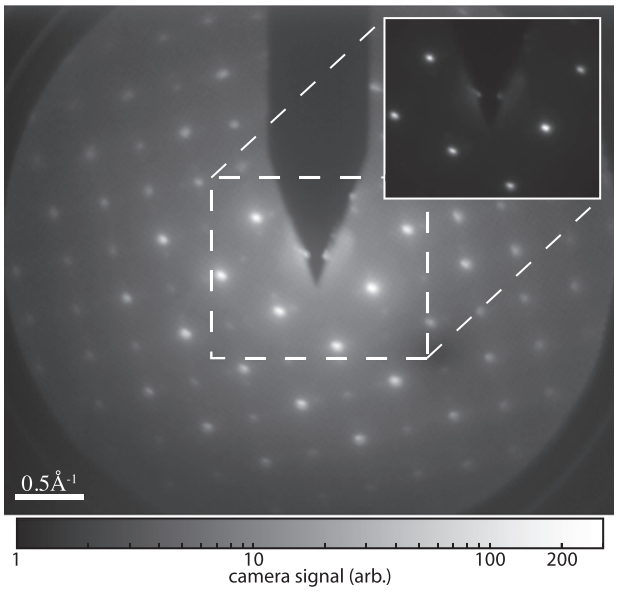

Figure 3. Two thousand diffraction shots from gold, directly averaged. Averaging results in a higher signal-to-noise ratio, but shot-to-shot beam instabilities lead to a broadening of the Bragg peaks. Main image is logarithmically scaled, inset is linearly scaled.

The reflections show the four-fold symmetry of the gold face-centered cubic (fcc) lattice, and the {200} and {220} reflections visible on the sides and corners of the inner square confirm the unit cell parameter as 0.407 nm, consistent with the accepted value for gold of 0.40782 nm at 25 °C [27]. To obtain a higher signal-to-noise ratio, 2000 shots were averaged. The result (figure 3) allows Bragg spots to be identified out to the $(\overline{6}60)$ reflection, with an effective resolution of 2.08 Å^{-1}, limited by the size of the detector.

J. Phys. B: At. Mol. Opt. Phys. **48** (2015) 214002 R W Speirs *et al*

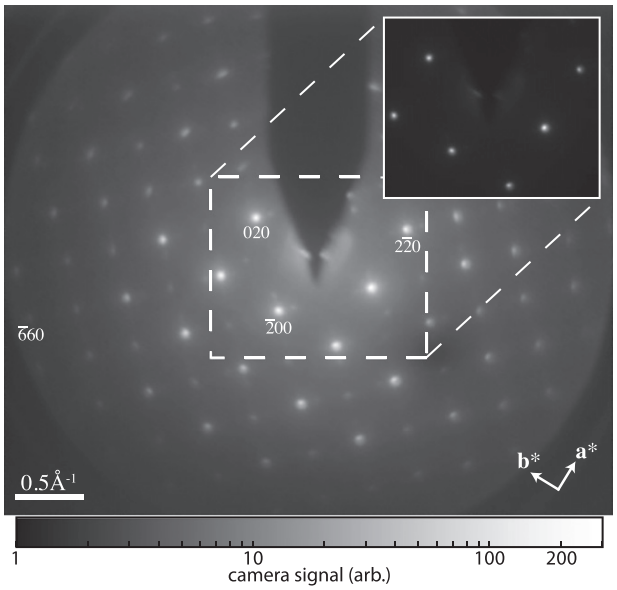

Figure 4. Two thousand diffraction shots from gold averaged by registering individual images. Registration is possible due to the high signal-to-noise ratio in the single shots, and recovers the sharpness in Bragg peaks lost in direct averaging. The reciprocal lattice vectors **a***, **b*** are drawn to scale. Main image is logarithmically scaled, inset is linearly scaled.

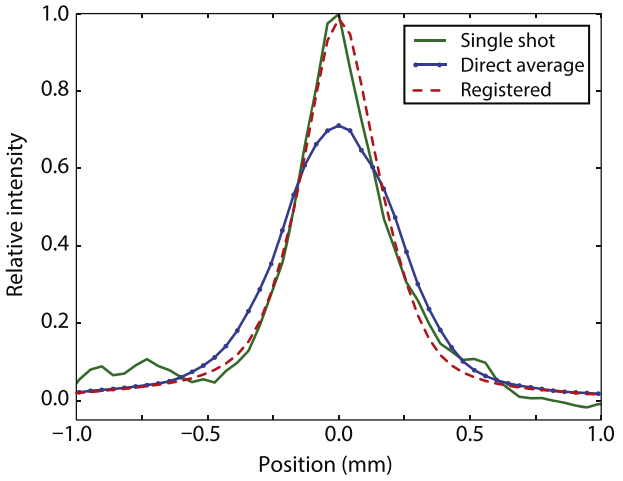

Figure 5. A lineout of the $(\bar{2}00)$ Bragg reflection in the **b*** direction. Registering the single shots averages out the noise without resulting in Bragg spot broadening, as happens when shots are directly averaged.

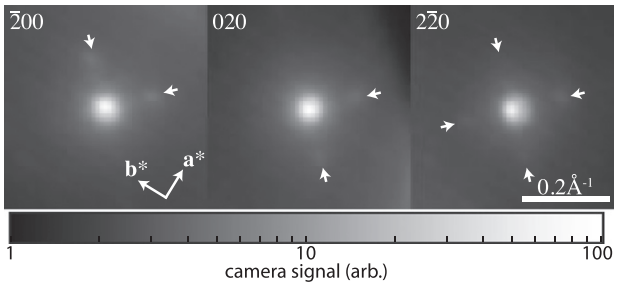

Figure 6. The two satellite spots around the $(\bar{2}00)$ and (020) reflections, and the rightmost spot around the $(2\bar{2}0)$ reflection, are due to diffraction from crystal twins. The other spots visible around the $(2\bar{2}0)$ reflection are due to the electron diffracting twice: once each from two different twins. The small arrows indicate the positions of the faint satellite spots. The reciprocal lattice vectors are not to scale.

Closer inspection reveals that the Bragg spots have been significantly broadened when compared to the single-shot case, indicating that the transverse coherence of the time-averaged electron beam is reduced compared to any single constituent bunch. This loss of coherence stems from variation in the bunch trajectory related to small variations in the remnant magnetic field of the magneto-optic trap. The effect of the beam drift on the diffraction pattern is analogous to the varying shot-to-shot diffraction patterns obtained in XFEL nanocrystal diffraction experiments, where diffraction patterns are obtained from millions of randomly aligned nanocrystals [28].

To compensate for the beam wobble, successive single-shot images were registered. The eleven brightest spots were used to adjust the alignment by performing a cross correlation of the individual images and the unregistered average in the region surrounding the spots. The resulting registered average can be seen in figure 4, showing notably sharper Bragg spots.

A lineout (figure 5) of the $(\bar{2}00)$ Bragg reflection in the **b*** direction shows how the direct average reduces the noise level compared to a single shot, at the expense of increasing peak width. The registered average maintains the low noise level of the direct average, while fully recovering the peak resolution. These results emphasize that the imaging is indeed effectively single-shot, with features clearly visible above the noise out to a resolution to 1.1 Å^{-1}.

Due to the structure amplitude of fcc gold, the only allowed reflections are those where the Miller indices h, k, l, are all even or all odd. The diffraction images of gold were taken along the $\langle 001 \rangle$ zone axis, where the lattice amplitude dictates that reflections are only allowed if h and k are even. While at low diffraction angles these rules are obeyed, it can be seen in figures 3 and 4 that some kinematically disallowed reflections are visible at higher angles. This is caused by a departure from the single scattering kinematic approximation, where both elastically, and inelastically scattered electrons are then re-scattered into directions which are forbidden to the unscattered incident beam. It can also be seen from figure 6 that the Bragg reflections are accompanied by two or more satellites, offset from the main reflection at 45° from the direction of the reciprocal basis vectors.

These satellites are the result of {111} crystal twinning, which can form when (100) gold films are prepared by evaporation [29]. There are two different mechanisms behind the satellite creation. The two relatively strong satellites that can be seen around the $(\bar{2}00)$ and (020) Bragg reflections are created directly by diffraction from the crystal twins. This also produces the rightmost spot around the $(2\bar{2}0)$ reflection. The other satellites around the $(2\bar{2}0)$ reflection arise from double diffraction, where electrons are first diffracted by a

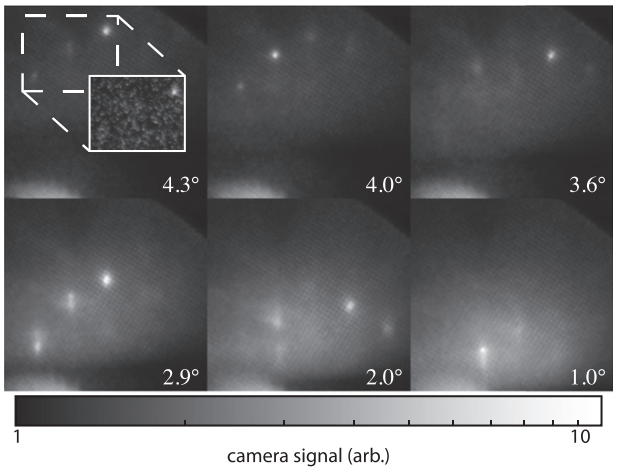

Figure 7. One hundred shot averages of RHEED from silicon ⟨100⟩ at a range of polar angles. Inset: a single shot of the region indicated, clearly showing a Bragg reflection.

(100) oriented domain, and then diffracted again by one of the twins. Dynamical effects would not normally be seen with such a thin sample because electron energies used in a transmission electron microscope are typically ten times greater than used here, resulting in a much lower scattering cross section and interactions that more closely match simple kinematic theory.

RHEED is a surface-sensitive diffraction technique routinely used to monitor crystal surface quality and epitaxial crystal growth [30], and has also been used to observe surface dynamics resulting from illumination by ultrafast lasers [31]. RHEED is a useful technique to further demonstrate diffraction from our source, both because the electron energies typically required are readily accessible, and because high quality single crystals are more readily available as bulk wafers than as the nanometre-thick foils needed for transmission electron diffraction. To adjust the system for RHEED required simple rotation of the sample by 90° as shown in figure 1(b)(ii). Figure 7 shows RHEED patterns from a ⟨100⟩ silicon wafer, which was HF etched to remove the native oxide layer immediately prior to transfer to the vacuum chamber. The beam was nominally incident on the crystal from the (110) direction at 0° polar angle. Since the sample stage could not be rotated in the azimuthal direction, it is likely that the wafer was slightly misaligned, which would account for the apparent horizontal asymmetry of the Bragg reflections at any particular polar angle. For clarity the RHEED patterns shown are 100 shot averages, however Bragg reflections were easily visible from a single shot as shown by the inset.

Cold electron RHEED offers a promising opportunity to investigate near-surface dynamics on nanosecond time scales. The high transverse coherence of the beam should also allow coherent scattering to be observed from structures tens of nanometres wide, such as quantum dots and optical metamaterials. Cold electron sources with bunch shaping to control space-charge induced brightness degradation are perhaps uniquely placed to perform these studies, due to their potential to deliver high bunch charges and high coherence at relatively low electron energies. Using very high electron energies to mitigate space-charge effects is not an option for RHEED, since very energetic electrons penetrate too deeply to accurately probe surface structure.

5. Summary

We have demonstrated single-shot electron diffraction using fast electron bunches produced with a CAES. The 5 ns bunches contained around 5×10^5 electrons, and because of their low temperature and high coherence, no beam aperture was required, allowing all generated electrons to contribute to imaging. When scattered by a single crystal of gold, the resulting single-shot diffraction pattern contained sufficient signal to give information about the crystal structure without averaging. The large signal-to-noise ratio allowed subsequent shots to be merged through image registration, which compensated for shot-to-shot beam drift that degraded the image quality when directly summing. Single-shot diffraction pattens have also been obtained in reflection mode, which may prove useful for investigating the dynamics of nanometre scale surface structures, where high beam coherence is necessary. Demonstrating single-shot diffraction is a significant step forward for CAESs, and supports the promise that they could complement solid state photocathode sources for use in ultrafast single-shot electron diffraction experiments.

Acknowledgments

We thank L J Allen for helpful discussions and advice. BMS gratefully acknowledges the support of a University of Melbourne McKenzie Fellowship. This work was supported by the Australian Research Council Discovery Project DP140102102.

References

[1] Barty A *et al* 2008 *Nat. Photonics* **2** 415–9
[2] Dwyer J R, Hebeisen C T, Ernstorfer R, Harb M, Deyirmenjian V B, Jordan R E and Miller R J D 2006 *Phil. Trans. R. Soc.* A **364** 741–78
[3] Zewail A H 2006 *Annu. Rev. Phys. Chem.* **57** 65–103
[4] Seibert M M *et al* 2011 *Nature* **470** 78–81
[5] Chapman H N *et al* 2006 *Nat. Phys.* **2** 839–42
[6] Neutze R, Wouts R, van der Spoel D, Weckert E and Hajdu J 2000 *Nature* **406** 752–7
[7] Quiney H M and Nugent K A 2011 *Nat. Phys.* **7** 142–6
[8] Carbone F, Musumeci P, Luiten O and Hebert C 2012 *Chem. Phys.* **392** 1–9
[9] Henderson R 1995 *Q. Rev. Biophys.* **28** 171–93
[10] Krivanek O and Mooney P 1993 *Ultramicroscopy* **49** 95–108
[11] van Oudheusden T, Pasmans P L E M, van der Geer S B, de Loos M J, van der Wiel M J and Luiten O J 2010 *Phys. Rev. Lett.* **105** 264801

[12] Claessens B J, van der Geer S B, Taban G, Vredenbregt E J D and Luiten O J 2005 *Phys. Rev. Lett.* **95** 164801
[13] Tokita S, Inoue S, Masuno S, Hashida M and Sakabe S 2009 *Appl. Phys. Lett.* **95** 111911
[14] Li R *et al* 2010 *Rev. Sci. Instrum.* **81** 036110
[15] Musumeci P, Moody J T, Scoby C M, Gutierrez M S, Bender H A and Wilcox N S 2010 *Rev. Sci. Instrum.* **81** 013306
[16] Sciaini G, Harb M, Kruglik S G, Payer T, Hebeisen C T, Heringdorf F J M z, Yamaguchi M, Hoegen M H v, Ernstorfer R and Miller R J D 2009 *Nature* **458** 56–59
[17] Siwick B J, Dwyer J R, Jordan R E and Miller R J D 2003 *Science* **302** 1382–5
[18] McCulloch A J, Sheludko D V, Junker M and Scholten R E 2013 *Nat. Commun.* **4** 1692
[19] Engelen W J, van der Heijden M A, Bakker D J, Vredenbregt E J D and Luiten O J 2013 *Nat. Commun.* **4** 1693
[20] McCulloch A J, Sheludko D V, Saliba S D, Bell S C, Junker M, Nugent K A and Scholten R E 2011 *Nat. Phys.* **7** 785–8
[21] Luiten O J, van der Geer S B, de Loos M J, Kiewiet F B and van der Wiel M J 2004 *Phys. Rev. Lett.* **93** 094802
[22] van Mourik M W, Engelen W J, Vredenbregt E J D and Luiten O J 2014 *Struct. Dyn.* **1** 034302
[23] Zurch M, Rothhardt J, Hadrich S, Demmler S, Krebs M, Limpert J, Tunnermann A, Guggenmos A, Kleineberg U and Spielmann C 2014 *Sci. Rep.* **4** 7356
[24] van Oudheusden T, de Jong E F, van der Geer S B, t Root W P E M O, Luiten O J and Siwick B J 2007 *J. Appl. Phys.* **102** 093501
[25] Egerton R F 2015 *Adv. Struct. Chem. Imaging* **1** 5
[26] Luiten O J, Claessens B J, van der Geer S B, Reijnders M P, Taban G and Vredenbregt E J D 2007 *Int. J. Mod. Phys.* A **22** 3882–97
[27] Maeland A and Flanagan T B 1964 *Can. J. Phys.* **42** 2364–6
[28] Chapman H N *et al* 2011 *Nature* **470** 73–77
[29] Pashley D W and Stowell M J 1963 *Phil. Mag.* **8** 1605–32
[30] Neave J, Joyce B, Dobson P and Norton N 1983 *Appl. Phys.* A **31** 1–8
[31] Elsayed-Ali H E and Herman J W 1990 *Appl. Phys. Lett.* **57** 1508–10

PHYSICAL REVIEW A **95**, 053408 (2017)

Identification of competing ionization processes in the generation of ultrafast electron bunches from cold-atom electron sources

Rory W. Speirs, Andrew J. McCulloch, Ben M. Sparkes, and Robert E. Scholten*
School of Physics, The University of Melbourne, Parkville, Victoria 3010, Australia
(Received 22 August 2016; revised manuscript received 4 April 2017; published 17 May 2017)

We make direct measurements of the duration of ultrafast cold-electron bunches produced by photoionization of laser-cooled atoms. We show that the bunch duration can vary by up to six orders of magnitude for relatively small changes in laser wavelength that enhance or inhibit specific photoexcitation pathways and below-threshold tunneling. By selecting a two-color multiphoton excitation process, bunches with durations as low as the measurement resolution limit of 130 ps are measured using a streak technique. Verification that ultrafast cold-electron bunches can be generated by photoionization of cold atoms is an important step towards their application in high-brightness ultrafast electron diffraction and injectors for particle accelerators.

DOI: 10.1103/PhysRevA.95.053408

I. INTRODUCTION

High-brightness ultrashort electron bunches are a critical requirement for free-electron lasers [1,2], particle colliders [3], and ultrafast electron diffraction [4–8]. Photocathode sources are the current state of the art in producing bright, ultrafast electron bunches, but ultimately their brightness is limited by the high initial temperature of the electrons produced, typically 10^3–10^4 K [9]. Electron sources based on near-threshold photoionization of laser-cooled atomic gases by ultrafast lasers offer potentially large increases in brightness by greatly reducing the temperature of the electrons generated. These cold-atom electron sources (CAESs) have been shown capable of producing electron bunches with temperatures as low as 10 K [10] and bunch charges up to 80 fC [11], which are approaching values required for the next milestone in nanoimaging: single-shot electron diffraction from micocrystals of large weakly scattering biomolecules [12].

While low temperature and high charge have been demonstrated, the temporal characteristics of electron bunches from a CAES have been largely neglected, even though bunch duration is a critical parameter of sources intended for ultrafast applications [13–15]. It has been implicitly assumed that electron liberation in a CAES takes at most a few picoseconds and the bunch duration is then usually determined by geometrical factors. Time-resolved measurements for single-photon direct photoionization of atoms [16–18] and classical particle tracking simulations of electrons in Stark-shifted Coulomb potentials [19] provide some insight into the processes involved in electron liberation but do not model the many complex electron generation mechanisms active in a CAES. Pulsed electric field ionization of highly excited atoms has been used to create electron bunches from cold atoms with durations of hundreds of picoseconds [20], but offers little prospect of reducing pulse lengths to the ultrafast regime that can be accessed by ultrafast lasers, due to the difficulty of rapidly changing the potential of accelerator electrodes.

Recently, it has been shown that a radio-frequency cavity deflector [21] can resolve the bunch temporal profile of a CAES with picosecond resolution, also allowing identification of the competing excitation and ionization processes. Here we describe direct measurements of the temporal profile of cold-electron bunches produced from a CAES using a simple streak deflection method. We find that photoexcitation to an ionizing state and field ionization of that state can both take significantly longer than the ultrafast excitation laser pulse duration. We show that excitation and ionization are both highly sensitive to small changes in ultrafast laser wavelength and bandwidth, resulting in a variation of electron pulse duration by up to six orders of magnitude. With detailed consideration of these processes, we demonstrate the production of ultrafast cold-electron bunches with duration less than the measurement resolution of 130 ps, consistent with the expected value of a few tens of picoseconds. Such pulses are short enough for compression to 100 fs [22], which will enable the observation of dynamic diffraction on atomically relevant time scales [8].

II. EXPERIMENT

In our experiment, ^{85}Rb atoms are loaded into a mageto-optical trap (MOT) positioned in a static external electric field variable between 1700 and 2600 V cm^{-1}, created by accelerator electrodes separated by 50 mm. The atom cloud is cooled to approximately 100 μK, with a peak density of 10^{10} atoms cm^{-3} and diameter of a few millimeters. After ionization of the trapped atoms, the accelerated electron bunches are focused with a solenoid lens onto a phosphor-coupled microchannel plate detector imaged with a camera. Parallel plate electrodes deflect the beam with a time-varying potential to create a streak on the detector (Fig. 1). The spatial profile of the streak corresponds to the temporal profile of the electron bunches. The potential of the streaking electrodes is ramped using a pair of bipolar push-pull solid-state switches, with a fixed transition time of 10 ns.

To produce an electron bunch, the MOT laser beams were first extinguished to allow the rubidium atoms to decay into the $5S_{1/2}$ ground state and the atoms were then excited via absorption of two or more photons to a field-ionizing state close to the ionization threshold of $E_I = 4.18$ eV. The MOT magnetic coils were also switched off and the field was allowed to decay for 4 ms prior to photoexcitation. We used a dye laser tunable from 460 nm (2.7 eV) to 490 nm

*scholten@unimelb.edu.au

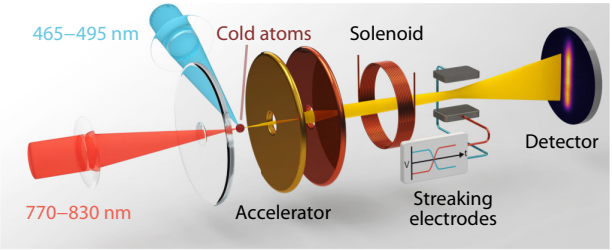

FIG. 1. Electron bunches are produced by photoionization of laser-cooled rubidium gas. The temporal bunch length is determined by applying a time-varying deflection to the bunch while it is drifting and measuring the length of the resulting streak on the detector. Laser-cooling beams and magneto-optic trap coils are not shown; details are in [10].

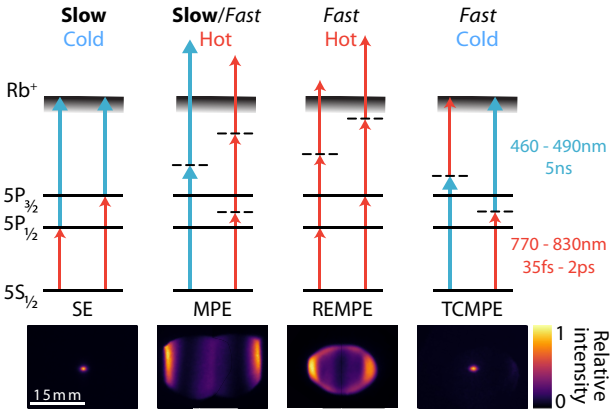

FIG. 2. Simultaneous illumination with two laser pulses can result in several excitation pathways: sequential excitation (SE), multiphoton excitation (MPE), resonance-enhanced multiphoton excitation (REMPE), and two-color multiphoton excitation (TCMPE). Only TCMPE produces electron bunches that are both cold and ultrashort. Virtual states are indicated as dashed lines. The false-color images show transverse momentum distributions of the detected bunches for the associated excitation pathways.

(2.5 eV) to produce blue pulses with a full width at half maximum (FWHM) duration of 5 ns. Red light was provided by either a continuous wave (cw) diode laser tuned to the 780.2 nm $5S_{1/2} \rightarrow 5P_{3/2}$ transition (1.59 eV), pulsed using an acousto-optic modulator with a rise time of a few hundred nanoseconds, or a mode-locked Ti:sapphire amplified pulsed laser. The latter provided wavelengths from 770 to 830 nm and a minimum pulse width of 35 fs. A folded $4f$ pulse shaper [23] selected the central wavelength and bandwidth of the 35-fs pulse with 0.2-nm resolution. The slit selects a wavelength range with a sharp cutoff and if the bandwidth selected is much less than the original 26-nm FWHM, then the spectral density is approximately flat over the selected range. Upon exiting the pulse shaper the pulse intensity profile is given by $I(t) \propto \Delta\omega^2 \mathrm{sinc}^2(\Delta\omega t/2)$, where $\Delta\omega$ is the FWHM frequency range selected. For transform-limited pulses of this form, the time-bandwidth product is given by $\Delta\omega\Delta t = 5.57$, where Δt is the FWHM duration. All laser beams were focused to overlapping waists of approximately 100-μm FWHM within the atomic cloud, with the cw and pulsed red beams illuminating collinearly to electron propagation and the blue beam incident transversely as shown in Fig. 1.

III. EXCITATION PATHWAYS

Atoms can be excited by several different pathways (see Fig. 2), separately or in parallel, with each pathway resulting in different electron bunch temperature and duration. All processes are observed, but each can be isolated by appropriate control of laser wavelength and intensity.

Sequential excitation (SE) [24] uses a single-photon transition from the ground state to an intermediate state and another single-photon transition from the intermediate state to a field-ionizing state. The duration of the excitation process is determined by the duration of the laser pulse driving the transition to the ionizing state, depletion of the intermediate state through that process, or the lifetime of the intermediate state, whichever is shortest.

Even with the relatively-low-energy laser pulses used in our experiments, focusing of the laser beams can easily produce sufficient intensity to cause nonlinear optical transitions. Multiphoton excitation (MPE) [25] occurs when two or more photons are absorbed without the atom transitioning to a real intermediate state. The transition rate is proportional to the nth power of optical intensity, where n is the number of photons absorbed before the atom reaches its final ionizing state [26]. The lifetimes of intermediate virtual states are very short [27,28], so the excitation period is determined only by the duration of the laser pulse.

Resonance-enhanced multiphoton excitation (REMPE) [25] is a combination of sequential excitation and multiphoton excitation, where m photons are absorbed to excite the atom to a real intermediate state and then a further p photons are absorbed in the transition to the final state. The reduction in the required number of photons for each transition, relative to the number required for a single n-photon transition, can significantly increase the overall transition rate. The excitation duration is limited by the same factors as for sequential and multiphoton excitation.

Two-color multiphoton excitation (TCMPE) [29] is an MPE process where one photon is absorbed from each of two different laser fields. The excitation duration is then determined by the shorter of the two laser pulses.

Cold-electron bunches are produced when the extracted electrons have small excess energy ΔE above the barrier formed by the Stark-shifted Coulomb potential $V = ke/r + Fz$, where r is the distance to the ion core, z is the position in the direction of the external electric field of strength F, k is the Coulomb constant, and e is the elementary charge. The energy of an electron relative to the classical ionization threshold energy is given by

$$\Delta E(F) = -E_I + \sum_{i=1}^{n} \frac{hc}{\lambda_i} + 2\sqrt{ke^3F}, \qquad (1)$$

where E_I is the field-free ionization energy of the ground-state atom, the middle term is the total energy of the n photons involved in excitation, each with wavelength λ_i,

the third term is the Stark shift of the classical ionization threshold corresponding to the saddle point energy, h is the Planck constant, and c is the speed of light. This assumes a hydrogenlike system, which is an excellent approximation on the condition that $E_I \gg 2\sqrt{ke^3F}$, since at energies near the field-free ionization threshold the shielding effect of the inner electrons has little effect on the energy of the Stark saddle. With our lasers, both SE and TCMPE produce cold-electron bunches with small transverse momentum spread as shown in Fig. 2, but only for TCMPE is the expected excitation duration determined by the ultrafast laser pulse duration.

Directly imaging the unfocused, unstreaked electron bunches after propagation gives a good indication of their temperature. While not technically in the far field, the transverse electron profile imaged on the microchannel plate is approximately equal to the transverse momentum distribution of the constituent electrons scaled for the necessary time of flight and particle mass, convolved with the transverse spatial profile of the bunch at the time of creation, ignoring the magnification due to the accelerator structure. In Fig. 2, the size of the detected bunches generated by both SE and TCMPE processes is dominated by the size of the original bunches, signifying that the election temperature is so low that meaningful values cannot be extracted with this method. The electron temperature can be estimated based on the calculated excess energy and equating energy to temperature using $\Delta E = k_B T$, where k_B is the Boltzmann constant. The SE and TCMPE generated electrons shown in Fig. 2 were both calculated to have a ΔE around 1 meV based on the wavelengths used and field strength of 2140 V cm^{-1}, which corresponds to a temperature of order 10 K. This value is consistent with previous temperature measurements made using the SE process, which was shown to generate electrons with temperature as low as 10 K [10].

The REMPE-generated electrons resulted from the absorption of three photons from the ultrafast laser with wavelength around 780.2 nm, exciting the $5P_{3/2}$ resonance. These electrons had a calculated ΔE of 625 meV, which corresponds to a temperature of 7200 K. Electrons produced via MPE using two blue photons of wavelength 482.1 nm had a calculated ΔE of 1000 meV corresponding to a temperature of 11 600 K. Given the calculated excess energies, the maximum transverse velocity of the MPE electrons is expected to be 1.3 times that of the REMPE electrons. This is supported by the transverse profiles shown in Fig. 2, where the ratio of maximum MPE to REMPE bunch diameters is 1.5. The discrepancy between the expected and calculated diameters is attributed to uncertainties in aligning the composite image for the MPE profile, which was required because the MPE electrons were so hot that any single bunch was partially occluded by apertures in the beamline.

To investigate how the different photoexcitation processes that result in cold electrons affect the duration of generated bunches, electrons were generated under a variety of laser illumination conditions and streaked to determine their duration. Figure 3(a) shows the temporal profile of an electron bunch produced by sequential excitation, using the cw laser to excite atoms to the intermediate state and the pulsed blue laser for excitation to the ionizing state. The bunch duration is 5 ns, mirroring the profile of the blue laser pulse as expected. These

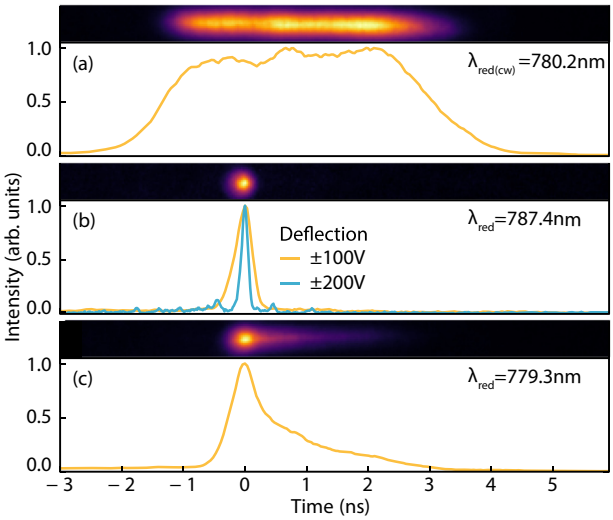

FIG. 3. Electron streak profiles showing pulse broadening by intermediate-state population. (a) Resonant cw excitation. The electron pulse profile mirrors the 5-ns blue laser pulse profile. (b) Far from resonance with intermediate states. TCMPE results in ultrafast bunches (profile in blue produced using higher streaking voltages). (c) Red photons from the ultrafast laser addressing an intermediate state lead to a slow sequential excitation component. The images show false-color detected streaks.

bunches typically contain around 10^5 electrons, with a peak ionization efficiency of greater than 50% [30].

Ultrafast TCMPE was achieved by increasing the intensity of the blue laser pulse and replacing the cw laser beam with a pulse from the ultrafast red laser tuned to 787.4 nm, far from resonance with real intermediate states. The ultrafast laser bandwidth was set to 1 nm and the blue laser was tuned to 482.1 nm, resulting in a small positive ΔE with a 2-meV bandwidth. The measured duration for the resulting electron bunch was 320-ps FWHM as shown in Fig. 3(b), much shorter than the blue laser pulse, thus showing the expected suppression of SE and enhancement of TCMPE in the excitation process.

The actual pulse length of our TCMPE bunches is expected to be much shorter than the 320 ps measured because the temporal resolution of the electron streak is limited by the transverse focal spot size of the detected electron bunch and the achievable deflector slew rate. The focal spot size is fixed by the combination of the bunch transverse emittance, and the numerical aperture and aberrations of the solenoid lens, but temporal resolution can be altered by varying the supply voltages to the deflector electrodes. Doubling the amplitude of the deflector potential, we observed a bunch duration of 130-ps FWHM [Fig. 3(b), blue curve], but again this is limited by the measurement resolution since the image of the streak still appeared circular [as is the case in Fig. 3(b)], indicating that the pulse was so short that the deflection distance was much less than the focal spot size. The deflector potential could not be increased further without inducing electrical breakdown.

The true bunch temporal profile will be given by a convolution of the ultrafast laser pulse profile, the temporal

profile of electron extraction from the ionizing state, and the temporal point spread function due to the spread of electron velocities caused by position-dependent energy imparted by the accelerator. To a first approximation, the actual duration at the streaking electrodes will simply be a sum of the duration of each of these three processes. The ultrafast laser duration is $\Delta t = 1.8$ ps with 1-nm bandwidth centered around 787 nm. Electron extraction time from the excited state is discussed in more detail below, but it is expected to take a few tens of picoseconds for the positive ΔE used here, based on high-resolution streaking experiments [21,31] and classical particle tracking simulations of electrons in Stark-shifted Coulomb potentials [19].

The temporal point spread function (TPSF) represents the change in duration of a hypothetical instantaneously created bunch as it propagates. The bunch spreading is caused by differences in kinetic energy ΔT gained by electrons generated along the length of the ionization region Δz in the accelerator: $\Delta T = eF\Delta z$. The TPSF was calculated assuming constant acceleration in each of the two accelerator regions and ignoring the effects of fringing fields caused by the holes in the electrodes through which the electrons pass.

The field strength in the first acceleration region where the electrons were created was 2140 V cm^{-1} and the mean acceleration distance was 25 mm. The field strength in the second region was 6300 V cm^{-1} with a 10-mm separation between electrodes. Assuming a Δz of 100 μm in the first accelerator region, the TPSF upon exiting the last electrode is 2.1 ps.

The TPSF has a minimum value of 2.6 fs at 153 mm from the last electrode. It is likely that the fringing fields would have some effect on the TPSF at such small time scales, making this value a lower limit. The bunch duration measurement was made at the position of the deflectors, 265 mm after the accelerators, where the calculated TPSF was 1.8 ps. Electron thermal energy, of order 1 meV, is negligible compared to the beam energy spread of 21 eV and so does not contribute to the TPSF. Space charge effects are also negligible since the ultrafast bunches consist of only around 100 electrons.

The true duration of the bunch generated by the TCMPE process is therefore likely dominated by the time it takes for the electrons to escape the ionic cores, which depends on the excitation energy and field strengths as previously mentioned. Using a value of several tens of picoseconds for electron extraction, consistent with values in the literature [19,21,31], the actual electron pulse duration at the deflectors is expected to be less than 50 ps, much shorter than the resolution-limited measurement of 130 ps.

Shifting the central wavelength of the ultrafast laser close to the $5S_{1/2} \rightarrow 5P_{3/2}$ resonance at 780.2 nm results in the generation of electrons by both SE and TCMPE processes, even though the ultrafast laser spectrum does not directly overlap with the resonance. The contribution from both processes is clearly seen from the profile in Fig. 3(c), where there is a fast initial peak but a slow tail of electrons excited from the populated $5P_{3/2}$ state.

The observed pulse broadening shown in Fig. 3(c) is strongly influenced by the wavelength of the ultrafast red laser. Figure 4 shows the pulse duration of electron bunches as the central wavelength of the ultrafast red laser was scanned over

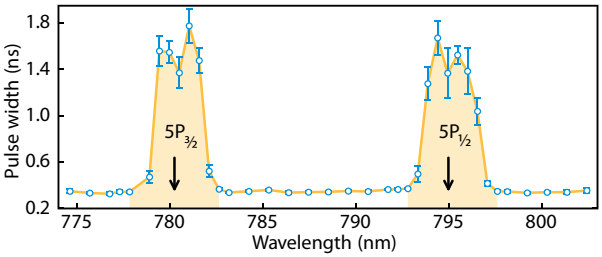

FIG. 4. Measured $1/e$ pulse durations of electron bunches as the ultrafast red laser is scanned over $5P_{3/2}$ and $5P_{1/2}$ resonances. The positions of the resonances are shown with arrows. The shaded area indicates detectable broadening.

both $5P$ resonances. The ultrafast laser bandwidth was set to 0.5 nm and the blue laser wavelength was adjusted such that the total combined photon energy was kept constant, with minimum combined photon energy still resulting in a positive ΔE. Pulse widths of less than 350 ps correspond to resolution-limited durations and the electrons generated in these regions are almost exclusively produced by TCMPE. Pulse widths larger than 350 ps indicate that electrons are being generated after the ultrafast red pulse via SE.

It can be seen that the laser wavelength must be a few nanometers from resonance before broadening by sequential excitation drops below detectable levels, which corresponds to a detuning of around 10^4 natural linewidths. The decrease in bunch duration as the predominant excitation process changes from SE to TCMPE is accompanied by a reduction in total electron yield. Around 10^5 electrons per bunch are created when the ultrafast laser wavelength directly overlaps with a resonance, but only around 100 are produced when exclusively TCMPE electrons are generated.

A complementary excitation scheme that is potentially capable of producing ultrafast bunches with greater electron number uses a slow laser to deliberately populate an intermediate state and an ultrafast laser pulse to further excite the atoms to an ionizing state [32]. The scheme also has the advantage of a reduced likelihood of electron pulse broadening by slow laser excitation to an ionizing state. For example, with rubidium the nearest accessible intermediate state for a pulse of 480-nm (blue) light is the $6P_{1/2}$ level, at a detuning of more than 10^7 natural linewidths [33]. The very large detuning, combined with the lower laser intensities required for the desired single-photon transitions, results in a negligible probability that the excitation process will take longer than the time of the ultrafast laser pulse.

IV. BELOW-THRESHOLD TUNNELING

Regardless of the excitation scheme, rapid excitation of the atom to an ionizing state is not sufficient to generate ultrafast electron bunches: The electron liberation from that state must itself be an ultrafast process. Electrons extracted from Stark-shifted Coulomb potentials have lower transverse momentum spread than would be expected for a given excess energy because the shape of the potential causes anisotropic emission, preferentially directing electrons in the forward direction, along the external electric field. The transverse

momentum spread is therefore reduced and the electron bunches are effectively colder for imaging applications. The coldest electrons, most suitable for high-resolution imaging, have typically been generated by tuning the excitation lasers to, or just below, the ionization threshold. However, our observations show that the duration of electron bunches generated in this way can be increased to an extent that prevents their application to ultrafast imaging.

Below the classical ionization threshold, electrons can escape the atomic potential through tunneling, but the small probability amplitude on the free side of the barrier increases the time it takes to deplete the ionizing state. The sensitivity of tunneling to energy has important consequences for generating ultrafast electron pulses, because the ionization rate of below-threshold Stark states can vary by many orders of magnitude over energy scales that are comparable to the bandwidth of an ultrafast laser pulse.

Above the classical ionization threshold, the probability amplitude on the free side of the barrier is greater and ionization proceeds rapidly. The exact ionization rate depends on which states are excited and the strength of the external field [34], but ionization times in the tens of picoseconds are typical [16–18].

For ultrafast bunch generation with inherently broadband laser pulses, excitation near the classical ionization threshold populates a superposition of Stark states, where electrons from both above and below threshold contribute. Figure 5(a) shows the temporal profile of an electron pulse produced by TCMPE, with the ultrafast red laser tuned so that Stark states were excited with both positive and negative ΔE. A fast initial peak is generated from Stark states with positive ΔE, followed by a very slowly decaying tail from lower-lying states. To study the effects of Stark state lifetime on bunch duration in more detail, the broadband ultrafast red laser was replaced with a narrow-linewidth cw red laser and the pulsed blue laser was used to excite electrons from the $5P_{3/2}$ state. Figure 5(b) shows a resulting streak for $\Delta E = -0.5$ eV, near optimum for imaging because of the resulting low electron temperature. The pulses exhibit long tails with a decay time of 17 μs containing 70% of the total electron charge, corresponding to an increase in bunch length by nearly a factor of 10^6 relative to a bunch generated from purely above-threshold states.

Varying the excess energy ΔE allowed identification of slowly ionizing states as shown in Fig. 5(c). Data in this figure were acquired by varying the electric field strength between 1720 and 2500 V cm^{-1}, using a constant blue laser wavelength of 485.587 nm for excitation to the ionizing state. Variation of the electric field rather than laser wavelength allowed higher-resolution control and avoided laser mode hops.

Electrons produced more than 200 ns after laser excitation were counted by measuring the electrical current to the phosphor screen, while the total electron signal was determined by looking at the integrated light signal generated by the phosphor itself and captured by the camera. Simultaneously capturing both the total and the delayed signal allowed identification of very slowly ionizing excited states. The precise value of ΔE was unknown due to uncertainty in the electric field in the accelerator, so a constant offset was applied to all values of ΔE such that $\Delta E = 0$ corresponded to the onset of states with tunneling times greater than 200 ns. With an excitation energy

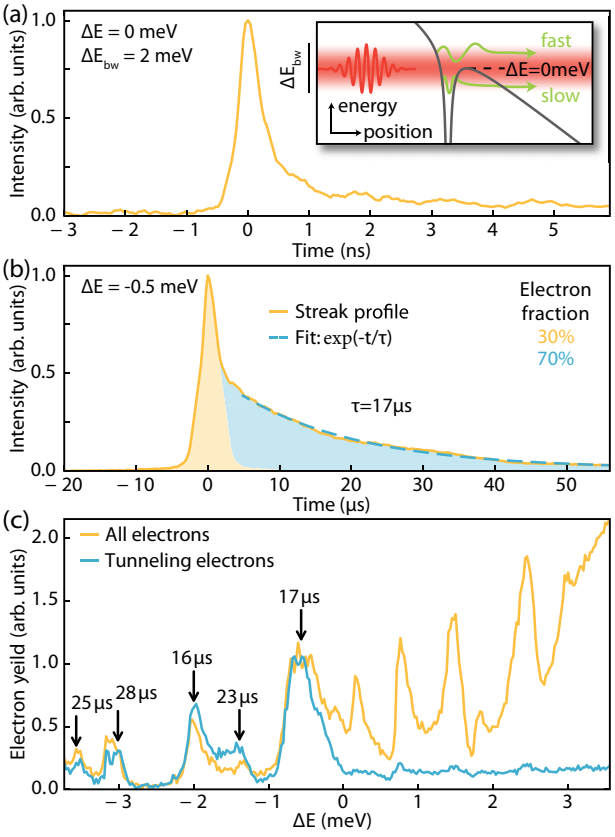

FIG. 5. Slow ionization resulting from tunneling. (a) Temporal profile of the first few nanoseconds of an electron bunch consisting of a fast initial peak due to above-threshold excitation and a slow tail from below-threshold excitation. The ionization process is illustrated in the inset. (b) Complete microsecond-scale profile of an electron bunch generated by below-threshold excitation. (c) Electron yield as a function of excess energy. The yellow line shows the total electron yield and the blue line shows only the yield of electrons detected more than 200 ns after laser excitation. Labels indicate measured pulse decay times at that energy with an uncertainty of ± 2 μs.

below the saddle point energy, the yield of slow electrons rapidly increased. Streak measurements were performed for each discernible state below the threshold, with all showing ionization lifetimes in the tens of microseconds. These ionization time scales are consistent with values reported elsewhere [21] for electrons excited to below threshold energies. Such a drastic and sudden increase in bunch duration shows that it is critically important to avoid coupling to below-threshold states to ensure generation of ultrashort electron bunches.

The slow ionization times observed at lower energies are attributed to tunneling [35] but may also be affected by a combination of other slow internal atomic processes, for example, blackbody-induced transitions to above-threshold states [36] or to below-threshold states with much higher tunneling rates. Regardless of the process, the implications of the slow ionization rates and the requirement to excite to higher energy remain unchanged.

V. CONCLUSION

In summary, we have presented direct measurements of the temporal distribution of electron bunches extracted from cold atomic gases. We have described several distinct processes involved in the excitation and ionization of cold atoms and how each of these processes contributes to the duration of the extracted electron bunches. By identifying the conditions required to ensure that both photoexcitation and electron liberation occur on ultrashort time scales while maintaining favorably low electron temperature, we have verified that it is possible to produce simultaneously ultrafast and cold-electron bunches. Further development of cold-atom electron source technology to increase the bunch charge and ameliorate Coulomb-driven emittance growth [37] could qualitatively change the way ultrafast electron bunches are generated and used, stimulating new developments in ultrafast imaging and particle accelerator design.

ACKNOWLEDGMENTS

B.M.S. acknowledges the support of a University of Melbourne McKenzie Fellowship. This work was supported by the Australian Research Council Discovery Project No. DP140102102.

[1] J. Fraser and R. Sheffield, IEEE J. Quantum Electron. **23**, 1489 (1987).
[2] P. Emma *et al.*, Nat. Photon. **4**, 641 (2010).
[3] C. Hernandez-Garcia, P. G. O'Shea, and M. L. Stutzman, Phys. Today **61**(2), 44 (2008).
[4] M. Eichberger, N. Erasmus, K. Haupt, G. Kassier, A. von Flotow, J. Demsar, and H. Schwoerer, Appl. Phys. Lett. **102**, 121106 (2013).
[5] B. J. Siwick, J. R. Dwyer, R. E. Jordan, and R. J. D. Miller, Science **302**, 1382 (2003).
[6] V. R. Morrison, R. P. Chatelain, K. L. Tiwari, A. Hendaoui, A. Bruhács, M. Chaker, and B. J. Siwick, Science **346**, 445 (2014).
[7] T. Ishikawa, S. A. Hayes, S. Keskin, G. Corthey, M. Hada, K. Pichugin, A. Marx, J. Hirscht, K. Shionuma, K. Onda, Y. Okimoto, S.-y. Koshihara, T. Yamamoto, H. Cui, M. Nomura, Y. Oshima, M. Abdel-Jawad, R. Kato, and R. J. D. Miller, Science **350**, 1501 (2015).
[8] G. Sciaini and R. J. D. Miller, Rep. Prog. Phys. **74**, 096101 (2011).
[9] B. J. Claessens, S. B. van der Geer, G. Taban, E. J. D. Vredenbregt, and O. J. Luiten, Phys. Rev. Lett. **95**, 164801 (2005).
[10] A. J. McCulloch, D. V. Sheludko, S. D. Saliba, S. C. Bell, M. Junker, K. A. Nugent, and R. E. Scholten, Nat. Phys. **7**, 785 (2011).
[11] R. W. Speirs, C. T. Putkunz, A. J. McCulloch, K. A. Nugent, B. M. Sparkes, and R. E. Scholten, J. Phys. B **48**, 214002 (2015).
[12] T. van Oudheusden, E. F. de Jong, S. B. van der Geer, W. P. E. M. Op't Root, O. J. Luiten, and B. J. Siwick, J. Appl. Phys. **102**, 093501 (2007).
[13] R. P. Chatelain, V. R. Morrison, B. L. M. Klarenaar, and B. J. Siwick, Phys. Rev. Lett. **113**, 235502 (2014).
[14] C. Kealhofer, W. Schneider, D. Ehberger, A. Ryabov, F. Krausz, and P. Baum, Science **352**, 429 (2016).
[15] I. V. Bazarov, B. M. Dunham, Y. Li, X. Liu, D. G. Ouzounov, C. K. Sinclair, F. Hannon, and T. Miyajima, J. Appl. Phys. **103**, 054901 (2008).
[16] B. Broers, J. F. Christian, J. H. Hoogenraad, W. J. van der Zande, H. B. van Linden van den Heuvell, and L. D. Noordam, Phys. Rev. Lett. **71**, 344 (1993).
[17] B. Broers, J. F. Christian, and H. B. van Linden van den Heuvell, Phys. Rev. A **49**, 2498 (1994).
[18] G. M. Lankhuijzen and L. D. Noordham, Phys. Rev. A **52**, 2016 (1995).
[19] W. Engelen, Coherent electron bunches from laser-cooled gases, Ph.D. thesis, Technische Universiteit Eindhoven, 2013.
[20] B. M. Sparkes, D. Murphy, R. J. Taylor, R. W. Speirs, A. J. McCulloch, and R. E. Scholten, Phys. Rev. A **94**, 023404 (2016).
[21] J. Franssen, T. Frankort, E. Vredenbregt, and O. Luiten, Struct. Dyn. **4**, 044010 (2017).
[22] T. van Oudheusden, P. L. E. M. Pasmans, S. B. van der Geer, M. J. de Loos, M. J. van der Wiel, and O. J. Luiten, Phys. Rev. Lett. **105**, 264801 (2010).
[23] A. Monmayrant, S. Weber, and B. Chatel, J. Phys. B **43**, 103001 (2010).
[24] B. Barrett, I. Chan, C. Mok, A. Carew, I. Yavin, A. Kumarakrishnan, S. Cahn, and T. Sleator, Adv. At. Mol. Opt. Phys. **60**, 119 (2011).
[25] K. Kulander, in *Springer Handbook of Atomic, Molecular, and Optical Physics*, edited by G. W. F. Drake (Springer, Berlin, 2006), pp. 1077–1089.
[26] C. J. Joachain, N. J. Kylstra, and R. M. Potvliege, *Atoms in Intense Laser Fields* (Cambridge University Press, Cambridge, 2012).
[27] M. B. Robin, Appl. Opt. **19**, 3941 (1980).
[28] K. D. Belfield, K. J. Schafer, Y. Liu, J. Liu, X. Ren, and E. W. Van Stryland, J. Phys. Org. Chem. **13**, 837 (2000).
[29] M. Dörr, R. M. Potvliege, D. Proulx, and R. Shakeshaft, Phys. Rev. A **44**, 574 (1991).
[30] D. Murphy, R. W. Speirs, D. V. Sheludko, C. T. Putkunz, A. J. McCulloch, B. M. Sparkes, and R. E. Scholten, Nat. Commun. **5**, 4489 (2014).
[31] G. M. Lankhuijzen and L. D. Noordam, Phys. Rev. Lett. **76**, 1784 (1996).
[32] W. J. Engelen, M. A. van der Heijden, D. J. Bakker, E. J. D. Vredenbregt, and O. J. Luiten, Nat. Commun. **4**, 1693 (2013).
[33] M. S. Safronova, C. J. Williams, and C. W. Clark, Phys. Rev. A **69**, 022509 (2004).
[34] L. Y. Baranov, R. Kris, R. D. Levine, and U. Even, J. Chem. Phys. **100**, 186 (1994).
[35] M. G. Littman, M. L. Zimmerman, and D. Kleppner, Phys. Rev. Lett. **37**, 486 (1976).
[36] I. Glukhov, E. Nekipelov, and V. Ovsiannikov, J. Phys. B **43**, 125002 (2010).
[37] D. J. Thompson, D. Murphy, R. W. Speirs, R. M. W. van Bijnen, A. J. McCulloch, R. E. Scholten, and B. M. Sparkes, Phys. Rev. Lett. **117**, 193202 (2016).

nature COMMUNICATIONS

ARTICLE

Received 9 May 2014 | Accepted 24 Jun 2014 | Published 17 Jul 2014

DOI: 10.1038/ncomms5489

Detailed observation of space-charge dynamics using ultracold ion bunches

D. Murphy[1], R.W. Speirs[1], D.V. Sheludko[1], C.T. Putkunz[1], A.J. McCulloch[1], B.M. Sparkes[1] & R.E. Scholten[1]

Control of Coulomb expansion in charged particle beams is of critical importance for applications including electron and ion microscopy, injectors for particle accelerators and in ultrafast electron diffraction, where space-charge effects constrain the temporal and spatial imaging resolution. The development of techniques to reverse space-charge-driven expansion, or to observe shock waves and other striking phenomena, have been limited by the masking effect of thermal diffusion. Here we show that ultracold ion bunches extracted from laser-cooled atoms can be used to observe the effects of self-interactions with unprecedented detail. We generate arrays of small closely spaced ion bunches that interact to form complex and surprising patterns. We also show that nanosecond cold ion bunches provide data for analogous ultrafast electron systems, where the dynamics occur on timescales too short for detailed observation. In a surprising twist, slow atoms may underpin progress in high-energy and ultrafast physics.

[1] ARC Centre of Excellence for Coherent X-ray Science, School of Physics, The University of Melbourne, Parkville, Victoria 3010, Australia. Correspondence and requests for materials should be addressed to R.E.S. (email: scholten@unimelb.edu.au).

Coulomb interactions can lead to instabilities and emittance growth in charged particle beams, limitting the ultimate performance of electron and ion microscopes[1,2] and high-energy particle accelerators[3]. In ultrafast electron diffraction[4–6], space–charge effects constrain the capacity to obtain diffraction information. For example, in bunches containing just 18 electrons, Coulomb repulsion was shown to increase the bunch duration by 50% and energy spread sevenfold[7]. Coulomb repulsion before[8] and after[9] the specimen thus place an ultimate limit on the ability to extract useful diffraction information. For strongly coupled systems, Coulomb interactions mediate interesting collective effects including the formation of Wigner crystals[10], self-organization[11] and shock wave phenomena[12–14]. Thus, although the underlying physics of the two-particle Coulomb interaction is simple, the behaviour of beams with complicated spatial and temporal structure can be difficult to predict. Particle trajectory calculations are straightforward for a few particles or even a few million, but become intractable for high-density high-current systems. The development of useful models of self-field effects has been limited by a lack of detailed comparative experimental data where the space–charge and thermal effects are clearly distinguishable.

Cold charged particle sources based on near-threshold photoionization of laser-cooled atoms[15–18] produce electrons and ions with temperatures as low as a few kelvin and millikelvin, respectively, allowing detailed investigation of self-field and strong coupling effects. The ability to arbitrarily shape the initial charged particle distribution[18] enables flexible investigation of the spatial dependence of inter-particle dynamics.

The effects of space–charge interactions are enhanced in ion bunches compared with electron bunches. Owing to their high mass, they have comparatively low velocities and hence retain a high charge density following the ionization. The ion temperature is also three to four orders of magnitude lower, allowing distinct measurement of space–charge effects without significant loss of detail due to thermal expansion.

During an ionizing laser pulse of time t_i in a static electric field, the ion bunch will grow longitudinally as the ions are produced, but the elongation is less than that of an electron bunch created over the same duration due to the larger ion mass. The equivalent-length electron bunch pulse duration t_e in the same field is then $t_e = t_i\sqrt{m_e/m_i}$, where $m_{e,i}$ are the electron and ion mass. The visibility of the space–charge effect is enhanced in ions compared with that in the equivalent-time electron bunches because the ion temperature remains low, with the excess ionization energy predominantly transferred to the photoelectrons. Thus, ion bunches created with ionization pulse durations of a few nanoseconds demonstrate space–charge effects equivalent to those in electron bunches created on picosecond timescales, comparable to the fast electron beams created using cold atom sources[19,20].

Pioneering work with cold atom sources has shown evidence of space–charge effects[21,22], and the role of Coulomb interactions in cold ion beams has been studied in detail for continuous-mode low charge density operation[23–25]. In this paper we investigate space–charge effects in arbitrarily shaped nanosecond duration cold ion bunches produced by near-threshold photoionization of laser-cooled atoms. We study in detail a complex ion distribution as an example of the subtle space–charge dynamics that can be observed, in particular the formation of shock wave structures where a halo of cold ions is compressed by the space–charge-driven expansion of a small high-density ion bunch. We observe collective behaviour including high-density caustics and the formation of complex patterns from long-range interaction between small charge bunches. The detail allowed us to systematically test and develop a comprehensive model of the system including self-field effects, illustrating the advantages of observation without thermal diffusion.

Results

Generating ultracold ion bunches. In our experiments (see Methods), ion bunches were formed by photoionization of an ensemble of laser-cooled rubidium atoms in a magneto-optical trap (Fig. 1). The two-colour ionization process allows ions to be created in an arbitrary charge density profile[18]. The intensity profile of an excitation laser beam (wavelength $\lambda = 780$ nm, Ω_{12}) was shaped using a reflective phase-shifting spatial light modulator. A second tunable laser (wavelength $\lambda = 480$ nm, Ω_{23}) was used to couple the excited atoms to a selectable Rydberg state. With the addition of an external static electric field (20–80 kV m^{-1}) the atoms are ionized in the region of overlap of the two laser beams. Control of the bunch charge was varied by changing the excitation laser beam power. The ions were accelerated in the static field over a distance of 2.5 cm before drifting 21.5 or 70 cm to a phosphor-coupled microchannel-plate and CCD camera to image the charge density profile of each bunch.

Ring formation. At low charge densities, the bunches expand linearly, driven by thermal diffusion. With increasing charge,

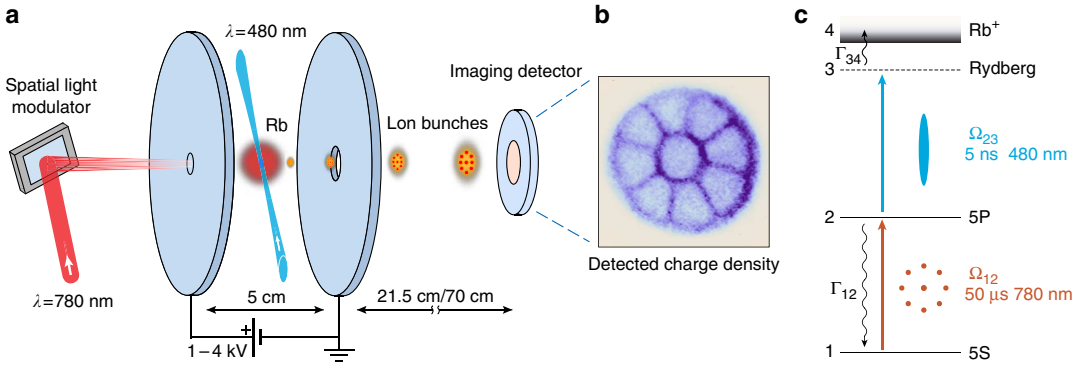

Figure 1 | Measurement of space-charge dynamics in ultracold ion bunches. (**a**) Cold rubidium atoms are prepared in a magneto-optical trap. Ions are produced by two-colour near-threshold photoionization. The cold ions are accelerated by a static electric field before drifting 21.5 or 70 cm in a zero-field region to an imaging detector to record their transverse spatial profile. (**b**) Ion bunch transverse spatial distribution; density shown in false colour. (**c**) Rubidium energy levels with optical couplings labelled by the Rabi rates Ω, decay rates Γ and schematic transverse laser intensity profiles for relevant states in the two-colour ionization process.

NATURE COMMUNICATIONS | DOI: 10.1038/ncomms5489 ARTICLE

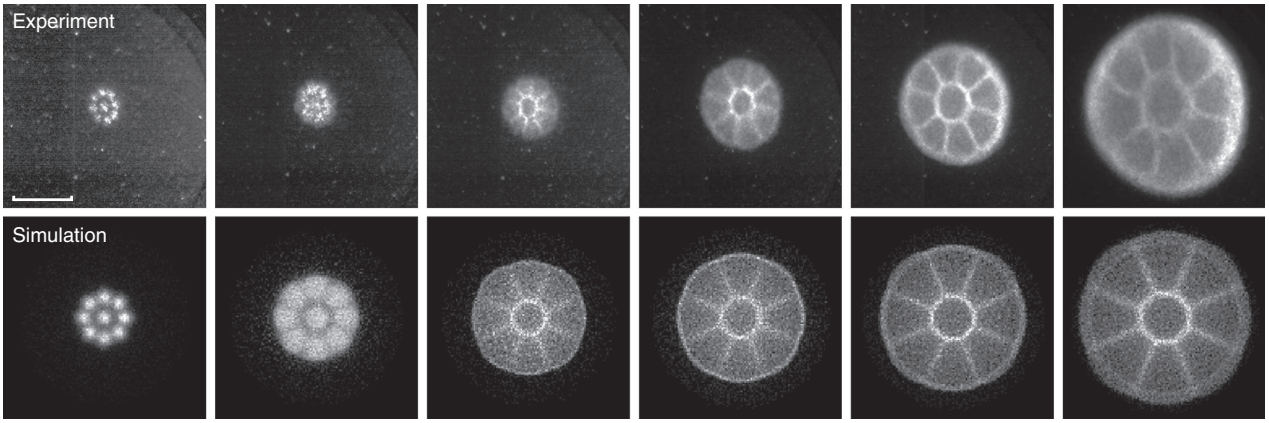

Figure 2 | Space-charge interactions between ion bunches. Ion beam density profiles imaged 24 cm (7.9 μs) from the source region, for nine closely spaced bunches each of 100 μm diameter. Upper panel: experimentally measured profiles for increasing bunch charge, showing increased expansion and the emergence of high-density regions due to intra-beam space-charge effects. Left to right: shaped excitation laser beam with total power of <1, 70, 210, 340, 640 and 980 μW. Lower panel: simulated bunch structure for ion bunches with spatial profiles calculated with laser profile and powers as used in the experimental images. Total bunch charges of 0 C, 2 fC, 8 fC, 10 fC, 13 fC and 19 fC. The greyscale density profiles are normalized individually to maximize contrast. Scale bar, 5 mm.

rather than the simple expansion and loss of detail that might be expected, Coulomb interactions accelerate the growth and induce nonlinear transformation of the bunch structure. Figure 2 shows experimentally measured projected ion bunch densities, for nine small closely spaced ion bunches. At low-excitation laser power (low bunch charge; left column) the measured distribution after propagation closely matches the intensity profile of the excitation laser and original bunch shape. Increased laser power and bunch charge induce surprisingly complex structure due to Coulomb interactions within and between the bunches. In particular, we observe the formation of high-density rings and collision boundaries between bunches.

The rings are visually similar to those formed by the interplay between self-fields and external focusing elements in electron storage rings[26], but in our case are found for all high-density initial distributions regardless of beam size and internal profile. The rings are also suggestive of phase–space wave-breaking phenomena, which have been predicted for particle beams[27–29], and similar to shock-shell formation predicted, but not yet experimentally observed, for Coulomb explosion of strongly coupled plasmas formed from cold ions[13] and in laser-irradiated nanoclusters[30].

We also observe high-density layers at the collision between expanding bunches. These layers have an apparent stickiness or adherence, in that the separate rings do not expand through each other, but compress to form collision boundaries. The compression layers have not been observed in studies of merging electron beams[31], illustrating the insight available through investigation of space–charge effects with cold and heavy ions.

Simulation and modelling. The evolution of the ion bunches was simulated using General Particle Tracer[32], which propagates point particles through the known accelerator field structures and the dynamically evolving self-field. The initial charge distributions were determined from the measured laser spatial profiles by calculation of the atomic excitation. For two-step ionization at a high 480-nm pulse energy, the probability of ionization is proportional to the probability of being in the intermediate 5P state before the 480-nm laser pulse[18,24,33], but the usual expectations of saturation for a two-level transition[34] are not applicable since we must include loss via field ionization. Indeed, experimentally, we can infer the number of ions produced from the space–charge-induced bunch expansion (Fig. 2) and we did not observe saturation of ion production even at several hundred times saturation intensity for the 480-nm transition. We developed a four-level model of the excitation and ionization process (see Methods), with field ionization included as a fixed rate loss. The extension accounts for laser-induced transitions from the ground to excited state during the 5-ns ionizing laser pulse, such that the ionization fraction is not limited by the saturated excited-state fraction before the ionization pulse. The spatial charge distribution of the ion bunches was calculated by numerical solution of four-level optical Bloch equations, given the known laser intensity profiles. We included the effects of fluorescence and reabsorption of the 780-nm photons, which lead to the formation of a halo of ions at large distances from the laser intensity maxima. The overall effect for a Gaussian excitation beam is an ion charge distribution that is radially broadened from the laser profile with a long, smoothly decreasing tail at large radius.

The experimentally observed high-density rings that surround the ion bunches were reproduced in simulation. Figure 3a shows the axially averaged radial distribution calculated for expanding ion bunches of varying charge density. The rings are formed by the dense inner core of ions, expanding rapidly due to Coulomb repulsion, until they interact with cold low-density ions in the halo generated by the reabsorption of fluorescence during the excitation phase. This behaviour is consistent with analytic predictions of the Coulomb explosion of dense nanoclusters irradiated by ultra-intense laser fields on very short timescales, which are studied in the context of laser-triggered nuclear fusion[30,35–37].

Figure 3b shows the simulated phase–space structure of a high-density bunch, in particular showing the large radius and momentum ring that are akin to shock wave formation in strongly interacting media. Modelling of a similar initial distribution of cold ions, in one dimension and without the halo formed by reabsorption of spontaneous emission, has also predicted an expanding shock front[13], but the formation of high-density boundary layers at the collision of the expanding ion shells has not been previously reported[31]. The negligible thermal diffusion of the ions in our experiments allows direct observation

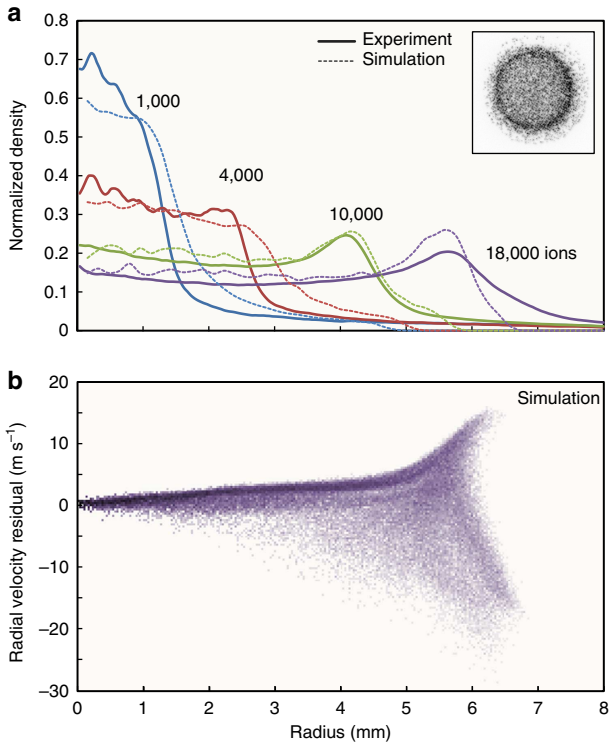

Figure 3 | Ion bunch profiles. (**a**) Measured and calculated radial dependence of the ion density. (**b**) Logarithm of the ion phase-space density, showing two orders of magnitude in density from light to dark, for a single bunch of 18,000 cold ions at propagation distance and time of 70 cm and 10.8 μs, respectively. The formation of a shock front at the outer edge of the bunch is illustrated by the caustic in the phase-space distribution. Inset of **a** shows typical measured density profile for a single bunch.

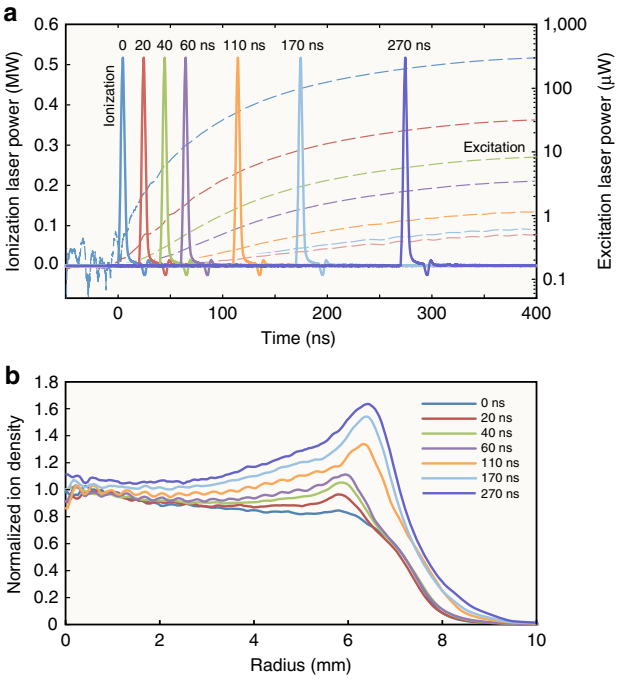

Figure 4 | Halo formation via fluorescence. Variation in density of halo ions with excitation laser pulse temporal separation. (**a**) Solid lines (left) and dashed lines (right) show the blue ionization and red excitation laser pulse timing. The excitation laser rise time is limited by the acousto-optical modulator used to modulate the laser beam. (**b**) Measured ion bunch radial profiles for varying ionization delay, for free-propagation distance of 70 cm. Owing to the slow rise of the excitation laser intensity, the charge density of the beam 'core' was kept constant for different timings by adjusting the power of the excitation laser. With a constant core density the expansion rate is approximately constant, but the 5P–5S fluorescence increases with pre-ionization excitation delay, increasing the halo density.

of the shells and high-density boundary layers despite the comparatively low density and long timescales. Simulations of the equivalent-time electron bunches show the same structures forming at very low initial electron temperature, but loss of visibility at a few kelvin, the lowest electron temperatures currently achievable[18,20].

Model verification. The high-density rings of our ion bunches are formed as the expanding core interacts with a halo of surrounding cold ions produced from reabsorbed spontaneous emission. The link between spontaneous emission and ring structure was tested by varying the duration of spontaneous emission before ionization and measuring the effect on ring density. The spontaneous emission time was determined by the delay between the 780- and 480-nm laser pulses used in the two-step ionization process. The first laser excites atoms to the $5P_{3/2}$ state, which has a natural lifetime of 26 ns. The second laser, with pulse length of 5 ns, excites the 5P atoms to a resonant auto-ionizing state in the static ambient electric field. The fluorescence from the intermediate 5P state can therefore be controlled by varying the delay between the two laser pulses, allowing variation of the density of excited and subsequently ionized atoms in the halo. Figure 4 shows the variation in visibility of the outer rings in the propagated bunch with changing time between pulses, showing increasing visibility with increased duration of spontaneous emission.

The evolution of the multi-beamlet ion bunch is shown in an animation (Supplementary Movie 1), where each frame is the calculated charge density profile for one charge bunch, in a plane transverse to the bunch propagation direction. The simulated ion bunch contains nine mini-bunches of 10^4 ions each, plus 2×10^4 simulated halo ions, for an accelerating field of 20 kV m^{-1} over 2.5 cm and free propagation of 14 cm (5 μs). The space–charge-driven bunch expansion and formation of the halo rings and colliding beamlets are readily apparent.

Discussion

Cold atom-charged particle sources are a promising new approach to producing high-brightness beams for applications in ultrafast imaging and high-resolution nanoscale fabrication. Achieving that promise will require detailed understanding of the Coulomb interactions within charge bunches and we have shown here that cold ion bunches can be a powerful tool for investigating such charged particle beam behaviour. The detailed measurements that are possible with cold ions have allowed us to test predictions of complex interactions in high-density charge bunches. Our observations highlight the importance of the initial charge density resulting from the photoionization process and identify the origin of features such as high-density caustics and inter-bunch boundary layers, which indicate nonlinear fields that lead to the emittance growth. The ability to arbitrarily shape the bunches in three dimensions has made it possible to mimic the

NATURE COMMUNICATIONS | DOI: 10.1038/ncomms5489 ARTICLE

density distributions for complex and diverse source configurations and probe the associated beam quality degradation related to space–charge effects. The low temperature of cold ion sources, and the scaling of time due to the electron/ion mass ratio, allows precise measurement of previously inaccessible space–charge dynamics relevant to high-density electron bunches used in accelerators and ultrafast electron diffraction imaging.

Methods

Experimental apparatus and techniques. A magneto-optical trap loaded from an effusive oven source and a Zeeman slower[38] was used to collect neutral rubidium-85 atoms at a temperature of 70 μK in a region ~5 mm in diameter, with a peak density of $1.2\times10^{10}\,\mathrm{cm}^{-3}$. The atoms were ionized by two-step, near-threshold photoionization. A $\lambda=780$ nm laser beam was used to drive the first-step excitation transition. This beam consisted of two laser frequencies, with 900 μW of power tuned to the $5^2S_{1/2}(F=3)\rightarrow5^2P_{3/2}(F=4)$ transition and 100 μW acting as a repumper on the $5^2S_{1/2}(F=2)\rightarrow5^2P_{3/2}(F=3)$ transition. The excitation laser beam intensity profile was shaped with a spatial light modulator to control the spatial distribution of the intermediate excited-state atoms in two dimensions. Atoms in the 5P state were then excited to a field-ionizing state, equivalent in energy to an $n\simeq30$ Rydberg state in a null field, by a $\lambda=480$ nm, 2–6 mJ laser pulse of 5 ns duration focused to a 100 μm × 8 mm (full width at half maximum) ribbon propagated perpendicular to the excitation laser beam, defining the profile of the ions along the direction of ion propagation. The atoms were excited and ionized in a static electric field of 20–80 $\mathrm{kV\,m}^{-1}$ between a pair of parallel plate electrodes. During and shortly after ionization, heating processes such as disorder-induced heating increase the ion temperature to a few millikelvin[39]. The ion bunches were accelerated over a distance of 2.5 cm, traversed an aperture in the grounded electrode and expanded due to the strong lens effect of the aperture, then drifted in a field-free region for 21.5 (Fig. 2) or 70 cm (Figs 3 and 4) to a phosphor-coupled microchannel plate and the spatial charge density was imaged with a CCD camera.

Modelling and simulation. To simulate the propagation of the cold ions with space–charge effects included, we first calculated the initial spatial profile of the bunches. The atomic state was described with a four-state density matrix for the electronic ground and intermediate excited states, the resonant self-ionizing state and the final ionized state. The states were coupled by laser fields with position- and time-dependent intensities and by spontaneous decay (see Fig. 1c). Field ionization was represented by rate Γ_{34}, which was determined from calculated near-threshold ionization cross-sections[40].

The evolution of ρ, the density matrix for the four-level atom, is given by

$$\dot{\rho}=-\frac{i}{\hbar}[\hat{H},\rho]+\hat{\mathcal{L}}(\rho) \tag{1}$$

where the indices are associated with the atomic levels given in Fig. 1. The Hamiltonian for the laser–atom interaction is

$$\hat{H}=\frac{\hbar}{2}\begin{bmatrix}0&\Omega_{12}&0&0\\ \Omega_{12}&0&\Omega_{23}&0\\ 0&\Omega_{23}&0&0\\ 0&0&0&0\end{bmatrix}. \tag{2}$$

The decay terms are:

$$\hat{\mathcal{L}}(\rho)=\frac{\Gamma_{21}}{2}\begin{bmatrix}2\rho_{22}&-\rho_{12}&0&0\\ -\rho_{21}&-\rho_{22}&-\rho_{23}&-\rho_{24}\\ 0&-\rho_{32}&0&0\\ 0&-\rho_{42}&0&0\end{bmatrix}+\frac{\Gamma_{34}}{2}\begin{bmatrix}0&0&-\rho_{13}&0\\ 0&0&-\rho_{23}&0\\ -\rho_{31}&-\rho_{32}&-\rho_{33}&-\rho_{34}\\ 0&0&-\rho_{43}&2\rho_{33}\end{bmatrix} \tag{3}$$

The optical Bloch equations for the four-level system were derived following standard approaches[34,41] and solved numerically for the spatially varying time derivative of the population of the ionized state. The total bunch charge was adjusted to optimize the agreement with the measured density distribution.

Particle tracking simulations[32] were used to calculate the evolution of the ion bunches under the influence of the external accelerator fields and internal Coulomb self-fields, as shown in the animation (Supplementary Movie 1). The tracking simulations reveal the time dependence of the bunch evolution, and two-dimensional projections of the particle density can be compared with experimental results as in Fig. 2. The essential features of the calculated initial bunch profiles produced good qualitative agreement with the observed bunch behaviour.

Simulations were performed using a three-dimensional particle mesh method to calculate the self-field, and also by calculating the interactions between all ion pairs. The bunch evolution was identical for the two approaches, showing that for our initial distributions, the evolution was dominated by space–charge effects rather than statistical Coulomb (Boersch) effects, which would not be apparent with the mesh method.

The effects of fluorescence and reabsorption of the quasi-continuous excitation beam were included using a first-order single-scattering approximation. Assuming steady-state conditions before the ionizing laser pulse, the excited-state spatial profile without fluorescence $\rho_{22}(\mathbf{x})$ was calculated from the laser intensity. Excited atoms spontaneously emit photons at the natural decay rate Γ_{21}, so the scattered light intensity is

$$I_{\mathrm{scat}}(\mathbf{x}')=\hbar\omega\Gamma_{21}\int\frac{N(\mathbf{x})\rho_{22}(\mathbf{x})}{4\pi|\mathbf{x}'-\mathbf{x}|^2}\mathrm{d}V \tag{4}$$

assuming isotropic emission, where $\hbar\omega$ is the energy per photon and $N(\mathbf{x})$ is the atomic number density. The scattered intensity is then added to the laser intensity to calculate the initial conditions of the excited-state profile corrected for reabsorption. Saturation and reabsorption cause broadening of the excited-state profile compared with the excitation laser profile, and the appearance of a halo of excited-state atoms that decrease in density smoothly from the beam core out to long distances. This excitation halo is ionized, becoming responsible for the formation of a density wave at the edge of an exploding ion bunch.

References

1. Buckanie, N. M. *et al.* Space charge effects in photoemission electron microscopy using amplified femtosecond laser pulses. *J. Phys. Condens. Matter* **21,** 314003 (2009).
2. Orloff, J. High-resolution focused ion beams. *Rev. Sci. Instrum.* **64,** 1105–1130 (1993).
3. Bernal, S. *et al.* Beam experiments in the extreme space-charge limit on the University of Maryland electron ring. *Phys. Plasmas* **11,** 2907–2915 (2004).
4. Dwyer, J. R. *et al.* Femtosecond electron diffraction: 'making the molecular movie'. *Philos. Trans. A Math. Phys. Eng. Sci.* **364,** 741–778 (2006).
5. Siwick, B. J., Dwyer, J. R., Jordan, R. E. & Miller, R. D. Ultrafast electron optics: Propagation dynamics of femtosecond electron packets. *J. Appl. Phys.* **92,** 1643–1648 (2002).
6. Qian, B.-L. & Elsayed-Ali, H. E. Electron pulse broadening due to space charge effects in a photoelectron gun for electron diffraction and streak camera systems. *J. Appl. Phys.* **91,** 462–468 (2002).
7. Kirchner, F. O., Gliserin, A., Krausz, F. & Baum, P. Laser streaking of free electrons at 25 kev. *Nat. Photon.* **8,** 52–57 (2014).
8. Tao, Z., Zhang, H., Duxbury, P. M., Berz, M. & Ruan, C. Space charge effects in ultrafast electron diffraction and imaging. *J. Appl. Phys.* **111,** 044316 (2012).
9. Chatelain, R. P. *et al.* Ultrafast electron diffraction with radio-frequency compressed electron pulses. *Ultramicroscopy* **116,** 86–94 (2012).
10. Mitchell, T. B., Bollinger, J. J., Huang, X.-P. & Itano, W. M. Direct observations of the structural phases of crystallised ion plasmas. *Phys. Plasmas* **6,** 1751–1758 (1999).
11. Kugland, N. L. *et al.* Self-organized electromagnetic field structures in laser-produced counter-streaming plasmas. *Nat. Phys.* **8,** 809–812 (2012).
12. Remington, B. A., Arnett, D., Drake, R. P. & Takabe, H. Modeling astrophysical phenomena in the laboratory with intense lasers. *Science* **284,** 1488–1493 (1999).
13. Feldbaum, D., Morrow, N. V., Dutta, S. K. & Raithel, G. Coulomb expansion of laser-excited ion plasmas. *Phys. Rev. Lett.* **89,** 173004 (2002).
14. Kulin, S. *et al.* Plasma oscillations and expansion of an ultracold neutral plasma. *Phys. Rev. Lett.* **85,** 318–321 (2000).
15. Killian, T. C. Ultracold neutral plasmas. *Science* **316,** 705–708 (2007).
16. Claessens, B. J., van der Geer, S. B., Taban, G., Vreden-bregt, E. J. D. & Luiten, O. J. Ultracold electron source. *Phys. Rev. Lett.* **95,** 164801 (2005).
17. Hanssen, J. L., Dakin, E. A., McClelland, J. J. & Jacka, M. Using laser-cooled atoms as a focused ion beam source. *J. Vac. Sci. Technol. B* **24,** 2907–2910 (2006).
18. McCulloch, A. J. *et al.* Arbitrarily shaped high-coherence electron bunches from cold atoms. *Nat. Phys.* **7,** 785–788 (2011).
19. McCulloch, A. J., Sheludko, D. V., Junker, M. & Scholten, R. E. High-coherence picosecond electron bunches from cold atoms. *Nat. Commun.* **4,** 1692 (2013).
20. Engelen, W. J., van der Heijden, M. J., Bakker, D. J., Vre-denbregt, E. J. D. & Luiten, O. J. High-coherence electron bunches produced by femtosecond photoionization. *Nat. Commun.* **4,** 1693 (2013).
21. Claessens, B. J., Reijnders, M. P., Taban, G., Luiten, O. J. & Vredenbregt, E. J. D. Cold electron and ion beams generated from trapped atoms. *Phys. Plasmas* **14,** 093101 (2007).
22. Reijnders, M. P. *et al.* Low-energy-spread ion bunches from a trapped atomic gas. *Phys. Rev. Lett.* **102,** 034802 (2009).
23. Steele, A. V., Knuffman, B. & McClelland, J. J. Inter-ion coulomb interactions in a magneto-optical trap ion source. *J. Appl. Phys.* **109,** 104308 (2011).
24. Knuffman, B., Steele, A. V. & McClelland, J. J. Cold atomic beam ion source for focused ion beam applications. *J. Appl. Phys.* **114,** 044303 (2013).

25. Kime, L. *et al.* High-flux monochromatic ion and electron beams based on laser-cooled atoms. *Phys. Rev. A* **88,** 033424 (2013).
26. Kishek, R. A. *et al.* Simulations and experiments with space-charge-dominated beams. *Phys. Plasmas* **10,** 2016–2021 (2003).
27. Anderson, O. A. Internal dynamics and emittance growth in space charge dominated beams. *Part. Accel.* **21,** 197–226 (1987).
28. Gluckstern, R. L. Analytic model for halo formation in high current ion linacs. *Phys. Rev. Lett.* **73,** 1247–1250 (1994).
29. Rizzato, F. B., Pakter, R. & Levin, Y. Wave breaking and particle jets in intense inhomogeneous charged beams. *Phys. Plasmas* **14,** 110701 (2007).
30. Kaplan, A. E., Dubetsky, B. Y. & Shkolnikov, P. L. Shock shells in coulomb explosions of nanoclusters. *Phys. Rev. Lett.* **91,** 143401 (2003).
31. Haber, I., Kehne, D., Reiser, M. & Rudd, H. Experimental, theoretical, and numerical investigation of the homogenization of density nonuniformities in the periodic transport of a space-charge dominated electron beam. *Phys. Rev. A* **44,** 5194–5205 (1991).
32. General Particle Tracer http://www.pulsar.nl/gpt/.
33. Killian, T. C., Pattard, T., Pohl, T. & Rost, J. M. Ultracold neutral plasmas. *Phys. Rep.* **449,** 77–130 (2007).
34. Allen, L. & Eberly, J. H. *Optical Resonance and Two-Level Atoms* (Dover, 1987).
35. Peano, F., Fonseca, R. A. & Silva, L. O. Dynamics and control of shock shells in the coulomb explosion of very large deuterium clusters. *Phys. Rev. Lett.* **94,** 033401 (2005).
36. Kovalev, V. F. & Bychenkov, V. Y. Quasimonoenergetic ion bunches from exploding microstructured targets. *Phys. Plasmas* **14,** 053103 (2007).
37. Saalmann, U., Mikaberidze, A. & Rost, J. M. Laser-driven nanoplasmas in doped helium droplets: local ignition and anisotropic growth. *Phys. Rev. Lett.* **110,** 133401 (2013).
38. Bell, S. C. *et al.* A slow atom source using a collimated effusive oven and a single-layer variable pitch coil Zeeman slower. *Rev. Sci. Instrum.* **81,** 013105 (2010).
39. Debernardi, N. *et al.* Measurement of the temperature of an ultracold ion source using time-dependent electric fields. *J. Appl. Phys.* **110,** 024501 (2011).
40. Petrov, I. D., Sukhorukov, V. L., Leber, E. & Hotop, H. Near threshold photoionization of excited alkali atoms Ak(np) (Ak = Na, K, Rb, Cs; n = 3-6). *Eur. Phys. J. D* **10,** 53–65 (2000).
41. Maguire, L. P., van Bijnen, R. M. W., Mese, E. & Scholten, R. E. Theoretical calculation of saturated absorption spectra for multi-level atoms. *J. Phys. B At. Mol. Opt. Phys.* **39,** 2709–2720 (2006).

Acknowledgements

This work was supported by the Australian Research Council Discovery Project DP1096025.

Author contributions

D.M., R.W.S., D.V.S., C.T.P. and A.J.M. executed the experiments, acquired and analysed the data; BMS contributed to the execution of the experiments; D.V.S. and A.J.M. designed and constructed the apparatus; D.M. generated the simulations; D.M., C.T.P. and R.E.S. wrote the manuscript with contributions from all authors; RES conceived and directed the project.

Additional information

Supplementary Information accompanies this paper at http://www.nature.com/naturecommunications

Competing financial interests: The authors declare no competing financial interests.

Reprints and permission information is available online at http://npg.nature.com/reprintsandpermissions/

How to cite this article: Murphy, D. *et al.* Detailed observation of space–charge dynamics using ultracold ion bunches. *Nat. Commun.* 5:4489 doi: 10.1038/ncomms5489 (2014).

PHYSICAL REVIEW A **95**, 063845 (2017)

Field ionization of Rydberg atoms for high-brightness electron and ion beams

A. J. McCulloch,[1] R. W. Speirs,[1] J. Grimmel,[2] B. M. Sparkes,[1] D. Comparat,[3] and R. E. Scholten[1,*]

[1]*School of Physics, The University of Melbourne, Victoria, 3010, Australia*

[2]*CQ Center for Collective Quantum Phenomena and their Applications, Physikalisches Institut, Eberhard-Karls-Universität Tübingen, Auf der Morgenstelle 14, D-72076 Tübingen, Germany*

[3]*Laboratoire Aimé Cotton, CNRS, Université Paris-Sud, ENS Cachan, Bât. 505, 91405 Orsay, France*

(Received 2 November 2016; published 28 June 2017)

We present an ionization mechanism for use in a cold atom electron source with the goal of producing highly monochromatic electron beams. We experimentally produce a map of the Stark states of ^{85}Rb below the ionization threshold and identify states that undergo selective field ionization. The properties of an electron beam produced by field-assisted ionization of such states are quantified. A theoretical framework is established to predict the improvement to beam quality when ionization is conducted above the ionization threshold, where ionization conditions are typically more favorable than below the threshold. Calculations suggest that selective ionization of Rydberg states may offer a pathway to the production of high-brightness, highly monochromatic ion and electron beams.

DOI: 10.1103/PhysRevA.95.063845

I. INTRODUCTION

Monochromatic electron beams are critically important for structuring and analysis of materials, from nanofabrication via electron-beam milling to compositional and structural analysis using electron energy loss spectroscopy (EELS). The advent of aberration-corrected optical systems has reduced limitations previously placed on electron-beam probe sizes by polychromatic beams at high energies (>100 keV), but at low energies, chromatic aberration is usually the limiting parameter [1]. High-resolution electron energy loss spectroscopy (HREELS), which combines EELS with highly monochromatic beams, can produce elemental maps with atomic resolution and probe the nature of atomic bonds in a variety of materials. The current standard for a highly monochromatic beam is an energy spread of less than 0.2 eV, which allows for observation of surface plasmons of gold nanoparticles [2] and the spectroscopic detection of single atoms [3]. More recently, monochromatic electrons have allowed atomic resolution to be realized in a transmission electron microscope operating with a beam energy of 15 keV [4].

Electron energy resolution of less than 0.1 eV is required to control and orient chemicals in the condensed phase [5,6]. State-of-the-art cold field emitting sources produce 100 keV electrons with an energy spread $\Delta U = 0.3$ eV [7] and hence still require energy filtering. Monochromators are well developed but nevertheless complicated and, critically, rely upon removing a significant fraction of the electrons from the beam, thus limiting the beam current.

Recently, a new source of electrons based on the ionization of laser-cooled atoms has emerged. Careful ionization of an atomic ensemble, either directly or via a field-assisted process, produces inherently cold electron bunches, giving an impressively small transverse energy spread [8,9]. Electron beams with energies of $U = 1$–10 keV [10,11] have been produced by ionizing atoms in a static electric field, with the finite size of the ionization volume giving rise to a longitudinal energy spread on the order of 0.01% of the beam energy ($\Delta U = 0.1$–1 eV). One possible mechanism to achieve reduced energy spread is field ionization of highly excited Rydberg atoms [12]. Under certain conditions, Rydberg atoms will ionize only at a specific value of the electric field. By using high field gradients, the length scale over which a beam of atoms will ionize can be very small, greatly reducing the energy spread of the beam.

Here we investigate the suitability of field-assisted ionization of rubidium Rydberg atoms for creating highly monochromatic electron and ion beams. We produce a high-resolution map of the Stark states below the ionization threshold and observe states which selectively ionize. For a particular selectively ionizing state, we predict the expected reduction in energy spread for an electron beam produced via selective field ionization. Finally, we model the effects of selective-state ionization for above-threshold Stark states, which are known to have higher ionization rates, to investigate the possibilities for further reducing the energy spread.

II. BACKGROUND

In HREELS, the energy resolution of the electron beam is not only critical to determining the structure that can be resolved, but also for improving the spatial resolution of bright field images [13], which is often limited by chromatic aberration. For a focused electron beam, the combination of beam emittance and aberrations arising from the source and the optical system determine the minimum achievable spot size. The dominant aberrations in the context of focused beams are spherical and chromatic. Spherical aberrations are a consequence of the optical system used, whereas chromatic aberrations and beam emittance are properties of the source. A common measure for the minimum achievable spot size is the beam diameter d_{50}, which is the diameter within which 50% of the beam current is encapsulated. With Gaussian distributions of both the beam energy U and the convergence angle α,

$$d_{50} = \sqrt{\left(d_{50,\mathrm{s}}^{1.3} + d_{50,\epsilon}^{1.3}\right)^{2/1.3} + d_{50,\mathrm{c}}^{2}}, \quad (1)$$

*scholten@unimelb.edu.au

where $d_{50,s}$, $d_{50,\epsilon}$, and $d_{50,c}$ are the beam diameters arising from the spherical aberration, emittance, and chromatic aberration, respectively [14]. Spherical aberration arises due to a differing focal length as a function of position from the optic axis. Emittance is a measure of the transverse phase-space volume occupied by the beam, which characterizes both the lateral size and angular divergence of the beam, and thus its inherent focusability. Chromatic aberration is the variation in focal length for particles of different energy. The chromatic aberration spot size $d_{50,c}$ is proportional to the energy spread of the beam ΔU and is given by [15]

$$d_{50,c} = \zeta C_c \Delta\alpha \frac{\Delta U}{U_0}, \tag{2}$$

where ζ is a numerical constant for a given system [16], C_c is the aberration coefficient of the lensing system, and U_0 is the mean beam energy. It is clear that increasing the beam energy will reduce $d_{50,c}$ but for many applications higher beam energies are not desirable. Consequently, the only method to minimize $d_{50,c}$ is to reduce ΔU.

The Cold Atom Electron Source (CAES) produces inherently cold electron bunches. The transverse beam properties have been investigated in detail, and the beam emittance measured to be a few nmrad for millimeter-sized beams [17,18], orders of magnitude lower than other sources. Consequently, the CAES will have a much smaller value of $d_{50,\epsilon}$ and given comparable values of $d_{50,s}$ and $d_{50,c}$, the CAES promises values of d_{50} below the current state-of-the art [19]. In contrast to the transverse beam properties, the longitudinal beam properties have hitherto remained largely unstudied, despite the relative simplicity with which the CAES can produce highly monochromatic electron beams.

In a CAES, ionization typically occurs in a region with width Δ_z determined by the spot size of the ionizing laser beam and can be as small as 10 μm. Given an extraction field of strength F which is created by electrodes separated by distance d the energy spread can be expressed as

$$\frac{\Delta U}{U_0} = \frac{\Delta_z}{d}. \tag{3}$$

Reduction of this value could in principle be achieved by reducing the photoionization laser beam size through the use of high-numerical-aperture optical systems, but these are not always feasible and the ionization width Δ_z will still be constrained by the diffraction-limited spot size. Using Rydberg atoms and the combination of a high-gradient electric field with a rapidly ionizing state may allow ionization widths of hundreds of nanometers or below, reducing the fractional energy spread by one to two orders of magnitude. If achieved, a system would effectively be "super-resolution," with electron emission spot sizes below the optical diffraction-limited spot sizes of the photoexcitation lasers.

Use of Rydberg atoms for the creation of monochromatic beams was first proposed in Ref. [20], but its application in the context of CAESs was first proposed in Ref. [12]. The scheme proposed there involves the creation of a beam of Rydberg atoms that enters into a high-gradient electric field. The atoms are ionized once the field value is large enough to permit field-assisted ionization. In principle, the Δ_z would then be limited by the gradient of the electric field. In practice, the evolution of Rydberg states through the electric field results in state mixing, leading to a range of threshold electric-field values and ionization rates. The degree to which Rydberg states mix is highly variable. Selective field ionization occurs when a state displays minimal mixing, and also rapidly ionizes near a specific value of the electric field [21]. By addressing states that undergo selective field ionization, it may be possible to reduce Δ_z well below optical diffraction-limited spot sizes.

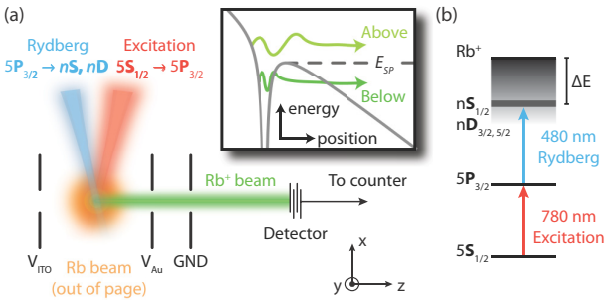

FIG. 1. A schematic of the experiment to produce Stark maps of ^{85}Rb. (a) A neutral beam of rubidium propagates along y, before entering a region of electric field produced between plates separated by 50 mm. Coupling to the Stark states is achieved with excitation and Rydberg laser beams, which are directed perpendicular to the field with polarizations parallel to the field. Ions are detected 680 mm downstream. Inset shows a plot of the electron potential versus position, showing the saddle-point energy E_{sp}. (b) The energy-level diagram for ^{85}Rb.

A key parameter in the study of the ionization of Rydberg atoms is the saddle-point energy $E_{sp} = -2\sqrt{F}$ (see Fig. 1), below which an electron cannot classically escape the ionic potential. Quantum mechanically, this corresponds to the energy below which only tunneling ionization can occur. Ionization occurs when the quasidiscrete hydrogenic basis states (Stark states) couple to the continuum. This coupling arises from the nonhydrogenic component of the Hamiltonian which, in turn, gives rise to anticrossings in the Stark spectrum. Near anticrossings, the behavior of state lifetimes can be dramatically altered, especially in the case of interference narrowing, where a stable state may have an avoided crossing with an unstable state, resulting in a reduction in the ionization rate of the unstable state by many orders of magnitude [22–29]. Interference narrowing has previously been used for selective field ionization of helium [20] and precision mapping of electric fields [30]. By applying selective field-ionization techniques to the CAES, it should be possible to produce a highly monochromatic electron beam, provided the appropriate state and selective ionization channel can be found. Here we map the Stark states of rubidium in the region around commonly used field strength values to identify states that selectively ionize and investigate their suitability for the production of highly monochromatic electron beams.

III. MAPPING STARK STATES

We performed a search for states which experience selective field ionization in the region below the saddle-point energy for $F = 600$ V/cm. A schematic of the experiment is shown

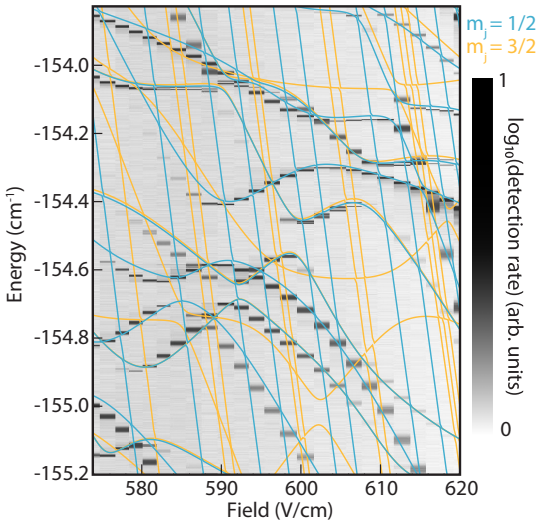

FIG. 2. A map of the Stark states, presented as a waterfall diagram, produced near the ionization threshold at $F = 600\,\mathrm{V/cm}$. The grayscale image shows the logarithm (base 10) of the rate of detected ionization events and the lines depict the calculated Stark states for both $m_j = 1/2$ [blue (dark gray)] and $m_j = 3/2$ [yellow (light gray)].

in Fig. 1. A neutral beam of rubidium effuses from an oven before passing through an aperture of $\phi 2$ mm (where ϕ denotes diameter) and subsequently a 70 mm differential pumping tube of $\phi 7.5$ mm, and free-space propagates for 940 mm before entering the ionization region. An electric field is produced between two electrodes separated by 50 mm with $\phi 20$ mm holes to allow ion extraction. Excitation to Stark states was performed by using a two-color process, with a continuous-wave (CW) excitation laser beam resonantly coupling the $5S_{1/2}F = 3$ and $5P_{3/2}F = 4$ states, and a CW probe laser beam coupling the exited $5P$ state to a high-lying Rydberg state. The laser beams are directed perpendicular to the electric field, with the polarization parallel to the field. The beams are focused as to intersect with the neutral atom beam as shown in Fig. 1 with spot sizes for the excitation and probe laser beams of 30 and 10 μm, respectively. Ions are accelerated towards a charge amplifying detector located 680 mm from the ionization region, where the current is amplified and filtered, with the discrimination of single-ionization events.

To map Stark states, an adjustable potential difference between the plates fixes the electric field, before the probe laser wavelength was scanned and the number of ionization events at a given wavelength recorded. The probe laser (linewidth $<$500 kHz) was scanned at 5000 discrete frequencies over 40 GHz and the number of ionization events were recorded for 750 ms at each point. For each change in the value of the electric field, the laser wavelength was reset and allowed 10 ms to respond and stabilize to avoid counting spurious ionization events. Upon completion of the laser scan, the electric field was adjusted and the wavelength scan repeated. Each scan took approximately one hour to complete and an entire Stark map took approximately one day to generate.

Figure 2 shows the map of Stark states for ^{85}Rb, both measured and calculated. The density plot displays the log (base 10) of the detected rate of ionization events, which has been normalized so the most rapidly ionizing state (measured at a rate of 17 kHz) appears black, with white indicating that no counts were detected. Background counts are expected from photoionization of Rydberg states and blackbody ionization while Penning ionization is not expected to contribute due to the low density. The measured rates of ionization are overlaid with the calculations of Stark states, with $m_j = 1/2$ states shown in blue (dark gray) and $m_j = 3/2$ states in yellow (light gray). Because the value of the electric field at the position of the atoms is not known precisely, a single value offset was applied to the measured field values to obtain agreement between the data to the calculations. It should be noted that the electric-field values used to produce the density plot in Fig. 2 are the mean of the measured field values recorded over the duration of each given scan. The variation in the measured field values relative to the mean-field value was approximately 0.1%. There is good agreement between predictions and observations, with mismatch attributable to field jitter, field inhomogeneity, and drift in the wavelength calibration.

The theoretical locations of Stark states were computed following the method detailed in Ref. [31]. The method numerically calculates the energy eigenvalues for a Hamiltonian of the form

$$\hat{H} = \hat{H}_0 + F\hat{z}, \tag{4}$$

where $\hat{H}_0$ is the Hamiltonian for the valence electron in the presence of the ionic core and $F\hat{z}$ is a perturbation due to the electric field of strength F directed along z. For excitation from the $5P_{3/2}$ states, we expect coupling to the $nS_{1/2}$, $nD_{3/2}$, and $nD_{5/2}$ states. With the probe laser polarization parallel to the electric field, we expect minimal coupling to $m_j = 5/2$ states, which are not observed in Fig. 2. The states were computed for 400 field values between $F = 550\,\mathrm{V/cm}$ and $F = 650\,\mathrm{V/cm}$ with 2000 states included in the calculation.

IV. SELECTIVE FIELD IONIZATION

Critical to the production of a monochromatic beam is the identification of states that experience a rapid growth in the ionization rate or, equivalently, a dramatic broadening of the resonance peak. One such process that can result in localized growth in the ionization rate is interference narrowing, which occurs when two Stark states that are coupled to the continuum with the same autoionization rates experience an anticrossing [32]. The coupling to the continuum for one of the eigenstates will vanish and the coupling for the other eigenstate will be enhanced due to the interference between the coupling amplitudes that govern their ionization. Such observations have been made previously in sodium [24,29], rubidium [33,34], and in cesium [35,36].

Another process that can result in localized growth in the ionization rate is when a stable "blue" state ($\Gamma \approx 0$) couples to a degenerate "red" state(s) ($\Gamma \gg 0$) which is (are) unbound, resulting in rapid ionization around the crossing [24]. An example of this latter behavior can be seen in Fig. 3, which shows a section of the Stark diagram in the region around

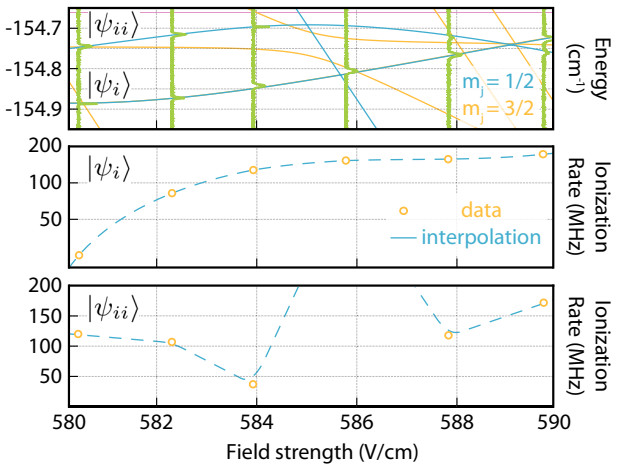

FIG. 3. Experimental Stark map in the region of 585 V/cm. The measured ion counts are shown in green (thick), and the calculated Stark states for $m_j = 1/2$ are shown in blue (dark gray) and for $m_j = 3/2$ are shown in yellow (light gray). State $|\psi_i\rangle$ undergoes monotonic growth in the ionization rate with respect to the electric field whereas, in contrast, state $|\psi_{ii}\rangle$ experiences a dramatic growth near a predicted anticrossing at $F = 585$ V/cm. The measured ionization rates for $|\psi_i\rangle$ and $|\psi_{ii}\rangle$ are shown in yellow (light gray) with the blue line (dark gray, dashed) showing the interpolation of the linewidth as a function of field strength. As no peak is present near the anticrossing, the linewidth of $|\psi_{ii}\rangle$ near $F = 586$ V/cm is not well known; a value of $\eta = 10$ (see text) was used to estimate the linewidth.

$F = 585$ V/cm. State $|\psi_{ii}\rangle$ shows a stable state evolving into a rapidly ionizing state near the crossing with a highly unstable state, which returns to a relatively stable state over a small change in field strength. This is in contrast to state $|\psi_i\rangle$, an initially stable state which becomes unstable with increasing field strength.

The state $|\psi_{ii}\rangle$ in Fig. 3, and other states in Fig. 2, show qualitatively the desired traits for producing a monochromatic beam; namely, a stable state which transitions to rapidly ionizing state over a small change in field. In the following section we model the ionization probability given to predict the effectiveness of selective field ionization for the minimization of energy broadening and therefore determine how monochromatic the electron beam can be.

V. BEAM MONOCHROMATICITY

To model the energy spread of the beam, the range of field values over which the beam is ionized must be calculated. We consider an apparatus optimized for field ionization by using high-gradient fields, such as the apparatus outlined in Ref. [12] or the apparatus currently under construction in our research group. These systems are similar to Fig. 1, but the electrode system is oriented along the same axis as the neutral atom beam propagation direction. They are optimized for the production of monochromatic electron beams with electrodes that can create a very uniform electric field in one region and high-gradient electric fields in adjacent regions, required for precise excitation and ionization, respectively. The combination of an optimized neutral atomic beam and adjacent regions of highly uniform electric fields with regions of high field gradient should allow creation of a high-quality beam of Rydberg atoms that can be efficiently ionized with a small ionization region (small Δ_z).

We assume an atom within the atomic beam traveling at speed v is excited to a Rydberg state $|\mathscr{R}\rangle$ in a uniform field of strength F_0 and propagates through a region with a high field gradient. Assuming the field is aligned along the z axis with a gradient of ζ, the field is then given by $F(z) = F_0 + \zeta z$. We define the effective ionization width $\Delta_{\text{eff}} \equiv 1/2(z_{\sigma^+} - z_{\sigma^-})$ as the region over which 68.2% of the atoms are ionized:

$$\Delta_{\text{eff}} = \tfrac{1}{2}[(z|\mathscr{P}(F) = 0.841) - (z|\mathscr{P}(F) = 0.159)], \quad (5)$$

allowing for direct comparison with Δ_z, typically defined as the standard deviation of the ionization laser spatial profile. $\mathscr{P}(F)$ denotes the cumulative probability that the atom will be ionized at a field between F_0 and F after having been excited in a field of strength F_0:

$$\mathscr{P}(F) = 1 - \exp\left[\frac{1}{\zeta \bar{v}_z}\int_{F_0}^{F} \Gamma(F')dF'\right], \quad (6)$$

where $\bar{v}_z$ is the mean atomic velocity within the beam and $\Gamma(F)$ is the ionization rate of the Rydberg state $|\mathscr{R}\rangle$. In expressing the cumulative probability as a function of the field strength F, we assume the field is linear in z and also that $t = (z - z_0)/\bar{v}_z$. Provided the form of $\Gamma(F)$ is known, Eqs. (3) and (5) allow the energy spread of the beam to be calculated. We insist that, for an ionization scheme to be useful, that the cumulative ionization probability be near unity after the anticrossing. If this were not the case, any Rydberg atoms not ionized would continue to propagate into a high-field region where they would be ionized via an alternate mechanism, resulting in a complicated longitudinal energy distribution and a reduction in beam monochromaticity.

By using the above formulation, we can calculate Δ_{eff} for the state shown in Fig. 3, which shows the measured ionization rate as a function of the electric-field strength that was interpolated to produce an approximation of $\Gamma(F)$. The ionization rate is determined by the width σ of the observed ionization peaks. In our apparatus, the maximum field gradient we can produce is on the order of $\zeta = 1 \times 10^9$ V/m^2. This value was calculated by using detailed modeling of the electrode system in SIMION [37] and shows the length scale over which the field has an appreciable gradient is 5 mm. Given a neutral rubidium beam produced from an oven at 373 K and an excitation field of 580 V/cm, with excitation to state $|\psi_i\rangle$ (Fig. 3), we calculate the ionization probability as a function of F by using equation (6). A rapid growth in the ionization probability occurs over approximately 250 nm and as expected and continues to increase with increasing F. While a localized growth in ionization probability is observed over some hundreds of nanometers, the total number of ionization events in this region is extremely small, owing to the small ionization rates. Consequently, the majority of the ionization takes places at higher values of the electric field and hence results in a ionization over a range of positions (large Δ_{eff}).

In contrast, the scale over which state $|\psi_{ii}\rangle$ destabilizes is much shorter due to the highly localized growth of the

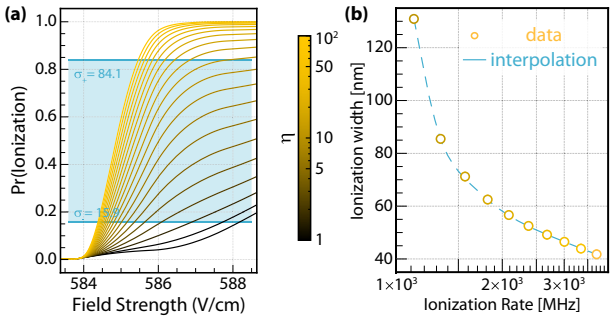

FIG. 4. Ionization properties of a selectively ionizing Rydberg state in rubidium. (a) Predicted cumulative ionization probability of $|\psi_{ii}\rangle$ as a function of electric-field strength around $F = 585\,\mathrm{V/cm}$. The blue shaded region from $\sigma_- = 15.9\%$ to $\sigma_+ = 84.1\%$ defines the region over which the beam ionizes. The color scale indicates the growth of ionization rate at the crossing, with $\eta = 1$ corresponding to 37 MHz. (b) Predicted ionization width as a function of the maximum ionization rate of $|\psi_{ii}\rangle$ at the crossing. The parameters for excitation and ionization are given in the text.

ionization rate. The exact growth in the ionization rate cannot be well predicted because no additional data were recorded in the region around the destabilization. Because there is no peak in the Stark map, we therefore include an enhancement of the ionization rate by a factor of η at the anticrossing. Previously, the ionization rate in the region of the crossing was measured by Ref. [24] to increase under similar conditions by two orders of magnitude relative to the stable state ($\eta = 10^2$), with a greater growth predicted but not measured. Assuming the value of Γ grows by a factor of η to a maximum rate Γ_M over the crossing, it is possible to calculate the expected value of Δ_{eff} given excitation to $|\psi_{ii}\rangle$, with all other parameters the same as were used to calculate the ionization width of $|\psi_i\rangle$.

Figure 4(a) shows the cumulative ionization probability for a rubidium atom excited to $|\psi_{ii}\rangle$ in the region around $F = 584\,\mathrm{V/cm}$. The different curves display how the cumulative ionization probability varies with the maximum ionization rate of $|\psi_{ii}\rangle$ at the anticrossing. It is clear that the ionization probability experiences highly localized growth and, as expected, with increased ionization rate the range of field values over which the ionization occurs decreases. In addition, a greater ionization rate also ensures near-unity ionization probability. For values of $\Gamma_M > 2.5 \times 10^9\,\mathrm{Hz}$, we calculate Δ_{eff} to be on the order of 50 nm, far below the tens of microns typically achieved by using photoionization and in the super-resolution regime (Δ_{eff} of order 100 nm). Figure 4(b) shows the ionization width Δ_{eff} as a function of the maximum ionization rate Γ_M. With greater values of Γ_M, the ionization width decreases, but it is clear that large growth in the ionization rate, at least $\eta > 30$, is required to produce super-resolution values of Δ_{eff}. For values of $\eta < 30$, values of Δ_{eff} near or below the diffraction limit are achievable; however, we are primarily interested in the super-resolution regime. A growth factor of $\eta = 30$, which corresponds to $\Gamma_M \approx 1 \times 10^9\,\mathrm{Hz}$ is not entirely unreasonable; in other work, a growth value of $\eta = 10^2$ has been measured [24], and separately a value of $\Gamma_M = 1 \times 10^9\,\mathrm{Hz}$ has been measured over a anticrossing [34]. A growth factor of $\eta = 30$ would yield a $\Delta_{\mathrm{eff}} = 130\,\mathrm{nm}$ and a higher growth rate, $\eta > 70$ (corresponding to $\Gamma_M > 2.5 \times 10^9\,\mathrm{Hz}$), is required to achieve $\Delta_{\mathrm{eff}} < 50\,\mathrm{nm}$. However, for growth rates less than $\eta \approx 80$, the cumulative ionization probability is below unity, meaning that any atoms not ionized will undergo ionization in the high-field region downstream, subsequently reducing the monochromaticity and increasing Δ_{eff}. This means that, for a monochromatic beam, we require a growth rate of at least $\eta = 80$, which would require an exceptional state with an ionization rate greater than that previously observed in Ref. [34]. Thus, in all likelihood, a sufficient value of Γ_M would not be reached to simultaneously ensure both efficient ionization and a small ionization width.

Further measurements of Γ_M are required to determine the suitability of state $|\psi_{ii}\rangle$ for monochromatic beam electron-beam production. The above results demonstrate that selective field ionization can result in ionization widths much smaller than conventional photoionization sources, but may come at the cost of ionization efficiency. One possible solution is to work in the region above the ionization threshold, where the transverse beam properties will be slightly degraded, but the ionization rates are typically many orders of magnitude higher. Provided an appropriate state with a localized growth in the ionization rate is used, a small ionization width could be combined with high-efficiency ionization. In the following section, we seek to validate this idea theoretically.

VI. MODELING ABOVE-THRESHOLD IONIZATION

The purpose of this section is to theoretically model the ionization rate for a state that experiences selective field ionization above the ionization threshold. We then seek to determine whether field ionization of Rydberg states is a viable method for highly monochromatic electron-beam production.

Calculation of the ionization width Δ_{eff} requires that one have precise knowledge of $\Gamma(F)$, and accurate prediction of the form of $\Gamma(F)$ is often difficult. In the case of hydrogen, the value of $\Gamma(F)$ can be calculated in a relatively straightforward manner [38], but for other atoms it is more complicated due to the coupling of states at the core and the associated avoided crossings of Stark states, though calculation of the lineshapes is possible [39]. For high-lying Rydberg states in alkali metals, the states of hydrogen provide a good approximation provided the quantum defect is small [40]. Since we are interested in the ionization rate of states near avoided crossings, we need only model the two-state system, provided the states are isolated.

More explicitly, to ensure the states are isolated, we require that the scale of the coupling between the states (V_c) is less than the difference in energy to neighboring states. Given the principal quantum number n, the separation of states to first order can be approximated by $(3/2)nF$, within an n manifold, before the first crossings with other n manifolds. The first crossings occur at a field strength of $1/(3n^5)$, hence the minimum energy separation for different values of n will vary as $1/(2n^4)$. The core coupling V_c can be approximated by using quantum-defect theory, where $V_c \approx \delta_m/n^4$ [21,41,42]. This suggests that, provided the quantum defect is small (less than 0.5), a two-level model should well approximate the system. In the case of rubidium, the δ_2 defect value for the

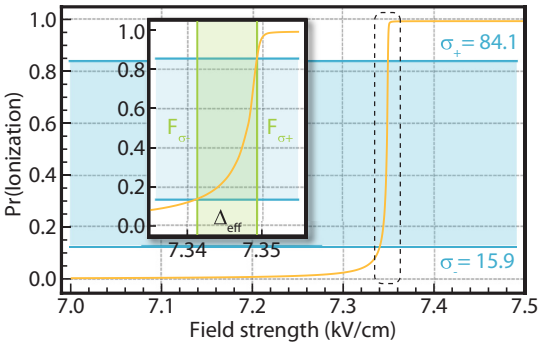

FIG. 5. Cumulative ionization probability of the $|17,0,13,3\rangle$ state for a rubidium beam (as detailed in Sec. V) as a function of electric-field strength. The blue shaded region from $\sigma_- = 15.9\%$ to $\sigma_+ = 84.1\%$ defines the region over which the beam ionizes. The inset shows a close up of the transition region, with the green area marking the range of the electric field over which the ionization occurs.

$nS_{1/2}$ states is approximately 0.18 and the values for $nP_{1/2,3/2}$ are approximately 0.29 [43], with the defect values for states of higher l being significantly smaller. Consequently, we use the two-level model to demonstrate the qualitative behavior, but do not expect quantitative agreement unless states of large l are considered.

Selective field-ionization processes above the ionization threshold usually occur when a stable "blue" state ($\Gamma \approx 0$) couples to degenerate "red" state(s) ($\Gamma \gg 0$) which are unbound, resulting in rapid ionization around the crossing; the field at which this occurs defines F_χ. We use a two-level model based on states of hydrogen A that allows for the calculation of $\Gamma(F)$ around F_χ. A similar model has been previously used to obtain excellent quantitative agreement for the ionization rate of sodium near the anticrossing of the $|12,6,3,2\rangle$ and $|14,0,11,2\rangle$ states [24] (labeled $|n,n_1,n_2,m\rangle$). By choosing states with a large value of $|m|$, we can ensure a small value of δ_2 and hence expect our model to be valid. The primary criterion for state selection is that a stable blue state crosses an unstable red state, which for even moderate electric fields is very common. We choose the states $|17,0,13,3\rangle$ and $|14,10,0,3\rangle$, but it should be emphasized that these are not unique. There are a multitude of states that display similar properties; we choose these simply because they are experimentally compatible with our system. In reality, the exact states to be used would, in great part, be determined by the core coupling V_c between the two states. The value of V_c is critical to determining the lineshape of state-selective ionization and hence the ionization width Δ_z but is not readily tunable, meaning that the crossing to be used must be selected for the appropriate value of V_c.

Using Eq. (6), it is again possible to calculate the cumulative ionization probability for a Rydberg atom propagating into an electric-field gradient as described above. We calculate the probability of ionization as a function of the electric field near the crossing of the $|17,0,13,3\rangle$ and $|14,10,0,3\rangle$ states (Fig. 5), by using $\bar{\Gamma}_-(F)$ [Eq. (A2)] [42] and an excitation field of 6 kV/cm, with the other parameters as in Sec. V. With a coupling strength of $V_c = \bar{\Gamma}_-(F_\chi)/4$ the rapid growth of the ionization rate near $F = F_\chi$ results in the rapid increase of the ionization probability, as was previously observed with below-threshold states. Due to the greatly increased ionization rate, on the order of 10^{10} Hz, a much higher ionization efficiency is predicted. From these data, we extract the ionization width of $\Delta_{\text{eff}} = 0.26\,\mu$m with unity probability for ionization. The value of Δ_{eff} is consistent with a previous estimate of the reduction of the ionization width via selective field ionization, which showed an improvement of one to two orders of magnitude compared with nonselective field ionization, with $\Delta_{\text{eff}} \approx 1\,\mu$m [12].

VII. CONCLUSION

Mapping of the Stark states below the ionization threshold allowed for the observation of selective field-ionization states, but insufficient resolution in the data around the localized growth of the ionization rate limited our ability to determine the states' suitability for the creation of a monochromatic electron beam. Further work is required to determine whether localized growth of the ionization rate below the ionization threshold is sufficient to allow for simultaneously efficient and localized ionization. It is possible that the low-ionization rates typical of states below the threshold will limit their usefulness in creation of monochromatic electron beams. Above the threshold, where ionization rates are much larger, we predict values of $\Delta_{\text{eff}} < 260$ nm are readily achievable. An ionization width on the order of hundreds of nanometers represents an improvement by a factor of at least ten compared with direct photoionization. Using high-numerical-aperture in-vacuum lenses permits laser spot sizes of the order a few microns, but getting below this limit represents a major challenge. By using field-assisted ionization of Rydberg atoms, any reduction in the ionization width linearly improves the beam monochromaticity, commensurate with a reduction of the value of d_{50}. If such a super-resolution ionization scheme were realized, it would result in an electron beam with a relative energy spread better than 1 part in 10^5, removing the need for a monochromator for many experiments. By implementing a high-efficiency photoexcitation scheme, for example, one similar to that already implemented in a cold atom source [44], this would allow for the creation of a high-current highly monochromatic electron beam. Additionally, the application of the same system to focused ion-beam science would be extremely powerful. For example, in a 30 kV cold atom beam ion source operating in low-current mode (0.1 pA), the expected value of d_{50} is 200 pm [19] when using photoionization. This value could potentially be reduced to $d_{50} = 50$ pm by using Rydberg ionization. Likewise, a field-ionization source operating in high-current mode (1 nA) could reach $d_{50} = 4$ nm, a factor ten below current state-of-the-art liquid-metal ion sources.

ACKNOWLEDGMENTS

The authors would like to thank Guyve Khalili for contributions to the two-level model and Francis Robicheaux for useful discussions. B.M.S. acknowledges the support of a University of Melbourne McKenzie Fellowship. This work was supported by the Australian Research Council Discovery

Project DP140102102 and by the EU through the FET-Open Xtrack Project HAIRS.

APPENDIX: MODELLING AVOIDED CROSSINGS

We seek to estimate the form of the ionization rate for a given state as a function of the electric field. We consider the two-state system of $|\phi_1\rangle$ and $|\phi_2\rangle$ with an energy separation $\hbar\delta = \mathscr{E}_1 - \mathscr{E}_2$, which experiences an anticrossing at a field of F_χ due to a coupling of strength V_c. Because we are interested in states that display selective field-ionization behavior, we consider the crossing of a stable blue state with an unstable red state. The Hamiltonian is then given by

$$\hat{H} = \begin{pmatrix} -\delta/2 & V_c \\ V_c & \delta/2 - i\Gamma/2 \end{pmatrix}, \tag{A1}$$

where Γ is the ionization rate of the dominant loss channel. At the anticrossing, the eigenstates will have the form $|\phi_1 \pm \phi_2\rangle$ where $|\phi_1\rangle$ and $|\phi_2\rangle$ are the eigenstates away from the crossing. The eigenvalues for the system can be extracted from the matrix $\hat{H}$, yielding the state energies $\bar{\delta}_\pm$ and ionization rates $\bar{\Gamma}_\pm$ for the upper and lower states of the mixed system:

$$\bar{\Gamma}_\pm = \tfrac{1}{4}\big(-\Gamma \pm \mathrm{Im}\big\{\sqrt{16V_c^2 - (\Gamma + 2i\delta)^2}\big\}\big),$$
$$\bar{\delta}_\pm = \pm\tfrac{1}{4}\mathrm{Re}\big\{\sqrt{16V_c^2 - (\Gamma + 2i\delta)^2}\big\}. \tag{A2}$$

The energy of the states $\mathscr{E}_1$ and $\mathscr{E}_2$ is calculated from the hydrogen Stark system, which we take to the fourth-order expansion [32]. The ionization rate Γ for the hydrogen Stark system can then be expressed as [45]

$$\Gamma = \frac{4R^{2n_2+m+1}}{n_1^3 n_2!(n_2+m)!}\exp\left\{-\frac{2R}{3} - \frac{n_1^3 F}{4}\left[34\big(n_2^2 + n_2 m\big) + 46n_2 + 7m^2 + 23m + \frac{53}{3}\right]\right\}, \tag{A3}$$

where $R = (-2\mathscr{E})^{3/2}/F$ and n_1, n_2, and m are the usual parabolic quantum numbers. By calculating $\mathscr{E}$, one can calculate a value of δ and, in conjunction with Eq. (A3), the ionization rates of the mixed system $\bar{\Gamma}_\pm$ can be calculated near the anticrossing.

By using quantum-defect theory one can estimate the expected core coupling [41] but, as a general trend, if the coupling is too weak, no strong state mixing is observed and narrowing either does not occur or only weakly occurs, resulting in no growth in the ionization rate. For stronger couplings, the effect begins to become delocalized and a growth in the ionization rate is seen over a range of field values. In the context of achieving highly localized ionization, the latter is highly undesirable. The maximum coupling rate occurs for any value of $V_c > \Gamma/4$, with the minimum ionization width and the maximum ionization rate simultaneously occurring for $V_c = \Gamma/4$. Physically, the actual value of coupling cannot be tuned as a simple parameter, but rather will be determined by the states in question. Some degree of tunability is present by changing the value of n_1 for the red state, moving to a neighboring crossing. If no states with desirable properties and appropriate coupling can be found, then the crossing of a different blue state should be considered. In practice a model, such as the one presented here, would be used to find potentially appropriate states and then a high-resolution scan performed experimentally to identify the optimum states.

[1] O. L. Krivanek, J. P. Ursin, N. J. Bacon, G. J. Corbin, N. Dellby, P. Hrncirik, M. F. Murfitt, and Z. S. Szilagyi, Philos. Trans. R. Soc., A **367**, 3683 (2009).

[2] B. Schaffer, K. Riegler, G. Kothleitner, W. Grogger, and F. Hofer, Micron **40**, 269 (2009).

[3] Q. M. Ramasse, C. R. Seabourne, D.-M. Kepaptsoglou, R. Zan, U. Bangert, and A. J. Scott, Nano Lett. **13**, 4989 (2013).

[4] S. Morishita, M. Mukai, K. Suenaga, and H. Sawada, Phys. Rev. Lett. **117**, 153004 (2016).

[5] A. Lafosse, M. Bertin, and R. Azria, Prog. Surf. Sci. **84**, 177 (2009).

[6] K. L. Moore, M. Schröder, Z. Wu, B. G. Martin, C. R. Hawes, S. P. McGrath, M. J. Hawkesford, J. F. Ma, F.-J. Zhao, and C. R. Grovenor, Plant Physiol. **156**, 913 (2011).

[7] P. E. Batson, *Transmission Electron Energy Loss Spectrometry in Materials Science and the EELS Atlas*, 2nd ed. (Wiley-VCH Verlag GmbH & Co KgaA, Weinheim, 2005), p. 353.

[8] B. J. Claessens, S. B. van der Geer, E. J. D. Vredenbregt, and O. J. Luiten, Phys. Rev. Lett. **95**, 164801 (2005).

[9] A. McCulloch, D. Sheludko, S. Saliba, S. Bell, M. Junker, K. Nugent, and R. Scholten, Nat. Phys. **7**, 785 (2011).

[10] R. W. Speirs, C. T. Putkunz, A. J. McCulloch, K. A. Nugent, B. M. Sparkes, and R. E. Scholten, J. Phys. B: At., Mol. Opt. Phys. **48**, 214002 (2015).

[11] A. J. McCulloch, B. M. Sparkes, and R. E. Scholten, J. Phys. B: At., Mol. Opt. Phys. **49**, 164004 (2016).

[12] L. Kime, A. Fioretti, Y. Bruneau, N. Porfido, F. Fuso, M. Viteau, G. Khalili, N. Šantić, A. Gloter, B. Rasser *et al.*, Phys. Rev. A **88**, 033424 (2013).

[13] P. C. Tiemeijer, M. Bischoff, B. Freitag, and C. Kisielowski, in *EMC 2008 14th European Microscopy Congress 1–5 September 2008, Aachen, Germany*, edited by M. Luysberg, K. Tillmann, and T. Weirich (Springer-Verlag, Berlin, Heidelberg, 2008), pp. 53–54.

[14] J. Barth and P. Kruit, Optik **101**, 101 (1996).

[15] P. W. Hawkes and E. Kasper, *Principles of Electron Optics* (Academic Press, London, 1996), Vol. 3.

[16] P. Hawkes and E. Kasper, *Principles of Electron Optics: Applied Geometrical Optics* (Academic Press, London, 1989).

[17] A. McCulloch, D. Sheludko, M. Junker, and R. Scholten, Nat. Commun. **4**, 1692 (2013).

[18] W. Engelen, M. van der Heijden, D. Bakker, E. Vredenbregt, and O. Luiten, Nat. Commun. **4**, 1693 (2013).

[19] J. J. McClelland, A. V. Steele, B. Knuffman, K. A. Twedt, A. Schwarzkopf, and T. M. Wilson, Appl. Phys. Rev. **3**, 011302 (2016).
[20] W. van de Water, D. R. Mariani, and P. M. Koch, Phys. Rev. A **30**, 2399 (1984).
[21] M. Førre and J. P. Hansen, Phys. Rev. A **67**, 053402 (2003).
[22] T. W. Ducas, M. G. Littman, R. R. Freeman, and D. Kleppner, Phys. Rev. Lett. **35**, 366 (1975).
[23] T. Gallagher, L. Humphrey, R. Hill, and S. Edelstein, Phys. Rev. Lett. **37**, 1465 (1976).
[24] M. G. Littman, M. L. Zimmerman, and D. Kleppner, Phys. Rev. Lett. **37**, 486 (1976).
[25] R. Damburg and V. Kolosov, Phys. Lett. A **61**, 233 (1977).
[26] T. F. Gallagher, L. M. Humphrey, W. E. Cooke, R. M. Hill, and S. A. Edelstein, Phys. Rev. A **16**, 1098 (1977).
[27] J.-L. Vialle and H. Duong, J. Phys. B: At. Mol. Phys. **12**, 1407 (1979).
[28] S. Liberman and J. Pinard, Phys. Rev. A **20**, 507 (1979).
[29] J.-Y. Liu, P. McNicholl, D. A. Harmin, J. Ivri, T. Bergeman, and H. J. Metcalf, Phys. Rev. Lett. **55**, 189 (1985).
[30] D.-H. Yang, D. Lieberman, P. van der Straten, T. Bergeman, and H. Metcalf, Phys. Rev. A **40**, 5026 (1989).
[31] J. Grimmel, M. Mack, F. Karlewski, F. Jessen, M. Reinschmidt, N. Sándor, and J. Fortágh, New J. Phys. **17**, 053005 (2015).
[32] M. L. Zimmerman, M. G. Littman, M. M. Kash, and D. Kleppner, Phys. Rev. A **20**, 2251 (1979).
[33] S. Feneuille, S. Liberman, J. Pinard, and A. Taleb, Phys. Rev. Lett. **42**, 1404 (1979).
[34] S. Feneuille, S. Liberman, E. Luc-Koenig, J. Pinard, and A. Taleb, J. Phys. B: At. Mol. Phys. **15**, 1205 (1982).
[35] C. Chardonnet, D. Delande, and J. C. Gay, Opt. Commun. **51**, 249 (1984).
[36] C. Chardonnet, D. Delande, and J. C. Gay, Phys. Rev. A **39**, 1066 (1989).
[37] SIMION, http://www.simion.com, Scientific Instrument Services, Inc., 1027 Old York Rd, Ringoes, NJ 08551, United States (2011).
[38] R. Damburg and V. Kolosov, J. Phys. B: At. Mol. Phys. **12**, 2637 (1979).
[39] D. A. Harmin, Phys. Rev. A **30**, 2413 (1984).
[40] T. Gallagher, *Rydberg Atoms* (Cambridge University Press, Cambridge, 2005), Vol. 3.
[41] I. Komarov, T. Grozdanov, and R. Janev, J. Phys. B: At. Mol. Phys. **13**, L573 (1980).
[42] G. Khalili, Ph.D. thesis, Université Paris Sud - Paris XI, 2015, https://tel.archives-ouvertes.fr/tel-01233284/.
[43] W. Li, I. Mourachko, M. W. Noel, and T. F. Gallagher, Phys. Rev. A **67**, 052502 (2003).
[44] B. M. Sparkes, D. Murphy, R. J. Taylor, R. W. Speirs, A. J. McCulloch, and R. E. Scholten, Phys. Rev. A **94**, 023404 (2016).
[45] R. Feynman, J. Hollingsworth, M. Vennettilli, T. Budner, R. Zmiewski, D. P. Fahey, T. J. Carroll, and M. W. Noel, Phys. Rev. A **92**, 043412 (2015).

PRL 117, 193202 (2016) PHYSICAL REVIEW LETTERS week ending 4 NOVEMBER 2016

Suppression of Emittance Growth Using a Shaped Cold Atom Electron and Ion Source

D. J. Thompson,[1] D. Murphy,[1] R. W. Speirs,[1] R. M. W. van Bijnen,[2] A. J. McCulloch,[1] R. E. Scholten,[1,*] and B. M. Sparkes[1]
[1]School of Physics, The University of Melbourne, Victoria 3010, Australia
[2]Eindhoven University of Technology, P.O. Box 513, 5600 MB Eindhoven, The Netherlands
(Received 20 May 2016; published 3 November 2016)

We demonstrate precise control of charged particle bunch shape with a cold atom electron and ion source to create bunches with linear and, therefore, reversible Coulomb expansion. Using ultracold charged particles enables detailed observation of space-charge effects without loss of information from thermal diffusion, unambiguously demonstrating that shaping in three dimensions can result in a marked reduction of Coulomb-driven emittance growth. We show that the emittance growth suppression is accompanied by an increase in bunch focusability and brightness, improvements necessary for the development of sources capable of coherent single-shot ultrafast electron diffraction of noncrystalline objects, with applications ranging from femtosecond chemistry to materials science and rational drug design.

DOI: 10.1103/PhysRevLett.117.193202

The elimination of Coulomb-driven emittance growth is crucial for the development of high brightness charged particle beam sources for high-energy accelerator injection [1], high-brightness x-ray sources [2], electron and ion microscopy [3,4], and ultrafast electron diffraction (UED) [5]. Single-shot UED experiments in particular require high bunch charge and short bunch duration, conditions that result in severe Coulomb-driven expansion [6,7]. For bunches with nonuniform charge density, the expansion leads to emittance growth and reduced bunch brightness and focusability. Overcoming Coulomb-driven emittance growth is, therefore, a key step towards achieving advances across fields ranging from femtosecond chemistry [8] to rational drug design [9,10] and materials science [5].

Uniformly filled three-dimensional (3D) ellipsoidal distributions, which have linear internal Coulomb fields, are ideal for the preservation of low emittance and high bunch brightness [11,12] because the bunch expansion can be fully reversed using linear electron optics. Three-dimensional ellipsoidal bunches have been created in thermal photocathode electron sources by using 2D laser pulse-shaping techniques to create "pancake" electron bunches which have a half-spherical transverse radial density profile. Provided the longitudinal profile is much narrower than the transverse radius, a pancake bunch will evolve into a uniformly filled ellipsoid under Coulomb-driven expansion [13]. The expansion properties of ellipsoidal bunches have been measured experimentally with photocathode sources [14–19], but demonstrating improved beam brightness has not been possible due to the inherently high electron temperature ($T > 1000$ K). At such temperatures, thermal diffusion quickly destroys the spatial structure of the bunch, preventing detailed observation of the effects of space-charge repulsion. High temperature also limits the initial bunch coherence, focusability and brightness of an electron source.

Cold atom electron and ion sources (CAEISs) are being developed [20–23] with the promise of orders of magnitude improvement in these key bunch metrics. The CAEIS is based on the photoionization of a laser-cooled atomic gas with two overlapping orthogonal laser beams, producing electrons and ions with low temperatures (10 K [21] and 1 mK [24], respectively), and correspondingly low emittance, high brightness, and high coherence. The initial charge distribution can be controlled by manipulating the laser beam profiles [21], allowing for full 3D shaping of the charged particle bunches at the optical resolution limit of a few micrometers [25]. Using this precise shaping ability to produce cold uniform ellipsoidal bunches is an important step towards creating a source capable of single-shot ultrafast coherent diffraction imaging of noncrystalline targets [26].

In this Letter, we describe experiments that demonstrate suppression of space-charge induced emittance growth for improved focusability and brightness, using shaped charged particle bunches from a CAEIS. Cold ions were used rather than electrons because their much lower temperature, and hence, negligible thermal diffusion, enhances the visibility of space-charge dynamics. In a CAEIS, measurements of the charge distribution for nanosecond duration ion bunches are directly analogous to picosecond electron bunches, because the heavier ion bunches disperse much more slowly than low-mass electrons within the accelerator region, retaining their high charge density and, therefore, exhibiting much stronger space-charge effects [27].

We quantify the beam expansion in terms of emittance, a measure of the phase-space volume occupied by the bunch, where low beam emittance corresponds to the desirable characteristics of high focusability and brightness. In thermal equilibrium, the transverse emittance can be defined along an axis x transverse to the beam propagation direction z, as

PRL **117,** 193202 (2016) PHYSICAL REVIEW LETTERS week ending 4 NOVEMBER 2016

$$\epsilon_x = \sigma_x \sqrt{\frac{k_B T_x}{mc^2}}, \tag{1}$$

where σ_x is the root mean square (rms) beam width, k_B is the Boltzmann constant, m is the mass of the beam particles, and c is the speed of light. The axial particle temperature can be defined as $T_x = m\sigma_{v_x}^2(1 - R_{x,v_x}^2)/k_B$, where σ_{v_x} is the rms velocity in the x axis and R_{x,v_x} is the correlation coefficient measuring the linearity of the particle position x and velocity v_x phase-space profile. Nonlinear space-charge forces cause distortion of the beam phase-space profile, increasing beam emittance. The normalized transverse beam brightness $\mathcal{B}_{n\perp}$ varies as ϵ_x^{-2}; hence, a reduction in the emittance will lead to an increase in the transverse beam brightness.

Ion bunches were created via two-color, near-threshold photoionization of an ensemble of rubidium atoms cooled to a temperature of 100 μK in a magneto-optical trap (see Fig. 1). The cloud of cold atoms had a Gaussian spatial density profile with a standard deviation of 500 μm and peak density of 3.0×10^{16} atoms m^{-3}. A 780 nm wavelength laser beam was used to excite atoms from the $5S_{1/2}$ ground state to the $5P_{3/2}$ excited state for 500 ns, with a transverse intensity profile shaped by a spatial-light modulator (SLM). Beam shaping was performed with a speckle-free protocol based on iterative feedback [25]. Atoms in the excited state were coupled to the ionization continuum with a 480 nm wavelength, 5 mJ, 5 ns laser pulse propagating through the atom cloud perpendicular to the excitation beam. The ionization beam was focused to a narrow ribbon at the cold atom cloud with rms intensity widths $\sigma_z = 15$ μm along the longitudinal direction of ion propagation and $\sigma_y > 1$ mm in the axis perpendicular to both the excitation and ionization laser propagation directions. The two-color ionization process produced ion bunches that initially had a very narrow longitudinal distribution compared to the length of the accelerator region (50 mm), ensuring that the longitudinal energy spread was only a few eV. Provided the intensity of the excitation laser beam is below the saturation intensity of the $5S \rightarrow 5P$ transition, the transverse excited atomic density profile $\rho_e(r)$ is proportional to $\Omega_e(r)$, the Rabi frequency for the driven transition. Control of the bunch charge was achieved by altering the excitation laser beam power and, thus, the overall population of the intermediate state prior to ionization by the 480 nm laser. The duration of the ion bunches was determined by the 480 nm laser pulse length

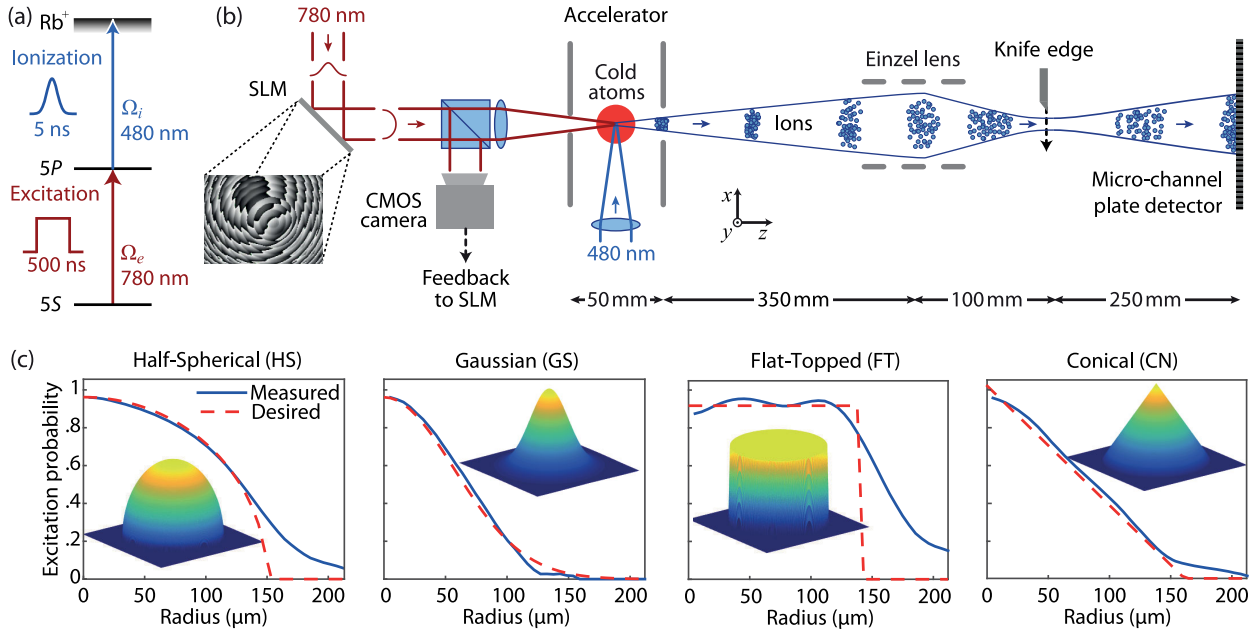

FIG. 1. (a) Two-color laser excitation scheme used to ionize laser-cooled ^{85}Rb atoms. (b) Cold atom electron and ion source with bunch shaping. The intensity profile of the excitation laser coupling the $5S$ ground state to the $5P$ intermediate state was shaped using a spatial-light modulator (SLM) with iterative feedback provided via a CMOS camera [25]. Atoms were ionized with a 5 ns pulsed blue laser, focused to a narrow ribbon perpendicular to the excitation laser. The ions were accelerated into a drift region and focused with an einzel lens. A knife edge was inserted into the bunch around the focus to determine the transverse focal spot width. Spatial bunch profiles and bunch charges were measured with a phosphor-coupled microchannel plate (MCP) detector combined with a CCD camera (not shown). (c) Measured radially averaged excitation laser profiles (solid lines) and desired profiles (dashed lines), plotted as the relative excitation probability. Insets show desired transverse bunch density profiles as shaded false-color renderings. All radial averages and density profiles are individually normalized.

(5 ns), analogous to an electron bunch duration of 13 ps [27].

To investigate the effect of transverse bunch shape on emittance growth, we studied four bunch distributions: half-spherical (HS), required to make pancake bunches; Gaussian (GS), i.e., an "unshaped" laser beam; flat-topped (FT), a uniform transverse profile with complementary application to pancake distributions [28]; and conical (CN), chosen as an example of a nonideal distribution. The excitation laser intensity profile $I_e(r) \propto \Omega_e^2$ was controlled by the SLM to create each initial transverse bunch distribution. Radial distributions of the excitation probability shown in Fig. 1(c) were calculated from each measured laser intensity profile. There was generally good agreement between the measured and desired distributions, with some loss of definition at the edges of the flat-topped and half-spherical distributions.

We initially studied the expansion of the shaped ion bunches for free propagation. Ion bunches with a range of charge densities were accelerated to 6 keV and propagated 700 mm to the detector where the transverse particle distributions were measured using a phosphor-coupled microchannel-plate (MCP) and camera. The initial radius encompassing 95% of the charge was $r_{95} = 139$ μm for all distributions, satisfying $r_{95} \gg \sigma_z$ required for the HS distribution to create a pancake bunch. Figure 2(a) shows the final transverse bunch distributions for ion numbers $N = 2.0 \times 10^3$, where there is negligible space-charge expansion, and $N = 7.1 \times 10^4$, where the growth is dominated by space-charge expansion. For higher charge, all distributions obtain a dense ring structure due to scattered 780 nm light absorbed by atoms outside the interaction region. These atoms were subsequently ionized by the 480 nm light pulse, creating a diffuse halo of electrons. The core ion bunch will expand much faster than the halo due to its higher charge density, resulting in transverse velocity bunching at the edges [27].

Bunches with linear space-charge forces undergo self-similar expansion, where the beam charge density profile is magnified by a single scaling factor. To assess the self-similarity of the CAEIS bunch expansion, we measured the transverse radii containing 50%, 75%, 90%, and 95% of the bunch charge for the different distributions at the detector. We then took the ratio of these radii to their initial values from the laser distribution to obtain the expansion factors denoted e_{50}, e_{75}, e_{90}, and e_{95} [Fig. 2(b)].

At low ion numbers, bunch expansion is mainly determined by lensing in the accelerator structure such that all shapes show approximately equal linear expansion by a factor of 20. As the ion number increases, and space-charge effects become more significant, the central radii expansion factors e_{50} and e_{75} of the GS and CN distributions increase more than the factors for the outer radii (e_{90} and e_{95}) due to the large initial central densities. The opposite behavior is true for the FT, with e_{50} and e_{75} increasing above e_{90} and

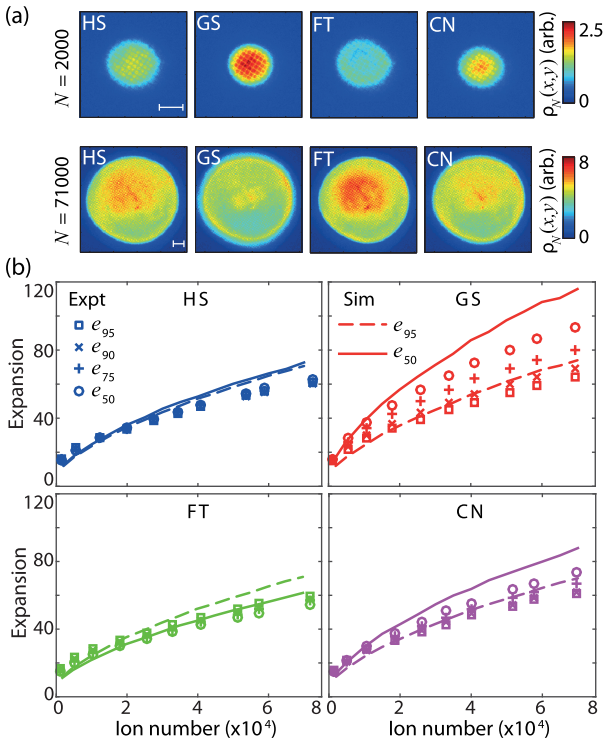

FIG. 2. (a) Experimentally measured transverse ion beam density profiles $\rho_N(x, y)$ for ion number $N = 2\,000$ and 71 000, for HS, GS, FT, and CN initial distributions (scale bar, 2 mm). (b) Radial expansion factors against ion number for each shape individually, with circle, plus, times, and square corresponding to the transverse radii containing 50%, 75%, 90%, and 95% of the bunch charge, respectively. The divergence of the expansion factors at high ion numbers indicate nonlinear space-charge forces, most prevalent in the GS and CN bunches. Simulated expansion factors e_{95} (dashed lines) and e_{50} (solid lines) for each shape are also shown. Measured radii are averaged from 100 ion bunches.

e_{95}, due to the lower initial central density. For the HS initial distribution, the expansion factors remain equal as the ion number increases, signifying linear self-similar space-charge expansion and formation of the desired uniform ellipsoid [13,29].

We simulated the acceleration, propagation, and expansion of the ion bunches using particle tracking software [30] for ideal spatial and measured temporal profiles, and an initial ion temperature of 1 mK. From these simulations, we extracted the expected expansion factors shown in Fig. 2(b). The simulations agree well with the experimental data, especially for the HS distribution. The smaller expansion of the experimental bunches at higher charge is attributed to the ions in the halo discussed earlier, which contribute to the measured ion number but not to the space-charge expansion. The greater deviation seen for the highly peaked GS and CN

distributions could also indicate saturation of the $5S \rightarrow 5P$ transition in the center.

At a beam waist, the transverse emittance [Eq. (1)] is the product of beam width and angular divergence. Measurement of the focal spot width for beams with different initial distributions, therefore, provides a measure of their relative emittance. To investigate the space-charge-induced emittance growth, an einzel lens situated 350 mm from the accelerator was used to focus the expanding bunches. The same transverse rms bunch width $\sigma_x = \sigma_y = 67\ \mu$m was used for all distributions to allow direct emittance comparison. A knife edge was scanned transversely through the propagating bunches at a range of z locations approximately 100 mm from the einzel lens. The rms width $\sigma_r(z)$ was determined from a fit of each profile to an error function (erf) [Fig. 3(a)]. The minimum focused bunch width σ_f was found from a parabolic fit of $\sigma_r(z)$ [Fig. 3(b)].

Figure 3(c) shows how σ_f varies for the different initial spatial distributions as the total ion number increases. The

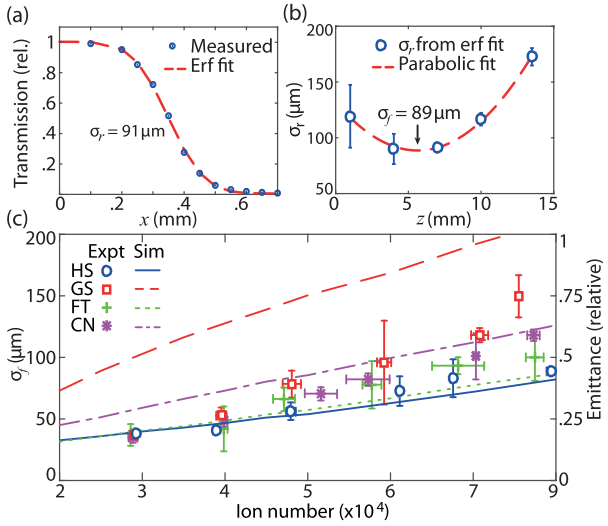

FIG. 3. (a) Example knife-edge plot of relative transmission (points) and erf fit (dashed line) to determine the transverse rms width σ_r at a given z position. (b) Example z scan of knife-edge transmission around the focus. Points indicate the knife-edge measurement and the dashed line is a weighted parabolic fit to determine the minimum rms width σ_f. Error bars are 95% confidence intervals determined from the fit in (a). (c) Experimentally measured minimum rms width (left-hand axis, points) and simulated emittance of freely expanding bunches (right-hand axis, lines) as a function of ion number for the four transverse spatial profiles: HS (blue, circles, solid line), GS (red, squares, dashed line), FT (green, crosses, dotted line), and CN (purple, stars, dashed-dotted line). Uncertainty in ion number is determined from standard deviation of ion numbers from all knife-edge measurements used to determine $\sigma_f(z)$, uncertainty in σ_f is determined from standard error of fitted parabolas in (b). Ion temperature for simulations was taken to be $T = 1$ mK.

GS and CN distributions, which demonstrated the most nonlinear growth in Fig. 2(c), show the greatest increase in emittance with bunch charge, while the linearly expanding HS distribution demonstrates the smallest increase as expected. Aperturing of the bunches in the accelerator structure limited the maximum number of ions to $N = 8 \times 10^4$, where we observe a 50% reduction in focused bunch width and, therefore, transverse emittance for the HS compared to GS distributions.

Particle tracking simulations of the free-expansion emittance for the four distributions exhibit the same behavior, though with a greater variation between the distributions. The greatest deviation is seen at low N, where space-charge expansion is negligible and bunch emittance will mostly be determined by accelerator aberrations and effects such as disorder-induced heating [31]. As N increases and space-charge dominates the emittance growth, there is much closer agreement between the experimental results and simulations, with the GS distribution showing the greatest difference. As with the free-expansion results, the discrepancies can be attributed to a combination of the formation of a ring structure, which will be more prominent for distributions created with higher peak 780 nm intensity, and saturation at the center. The separation between experimentally measured FT and HS waists is attributed to the imperfect flat-topped laser profile [Fig. 1(c)(ii)]. Nevertheless, the HS profile again matches very well with the simulations and shows that bunch shaping with a CAEIS can lead to a marked reduction in emittance growth relative to conventional Gaussian bunches.

In this Letter, we have experimentally demonstrated improvement of charged particle beam brightness through control of transverse bunch density distribution. The low temperature of the cold atom source has enabled detailed observation of space-charge effects, for the first time clearly distinguishing the variation in nonlinear growth for different initial particle distributions. For space-charge-dominated bunches with $N = 7.1 \times 10^4$ particles, a reduction in emittance growth of nearly 50% was achieved for a half-spherical rather than Gaussian transverse distribution, corresponding to a brightness increase by a factor of 4. Further improvements in beam brightness are expected if the spatial width of the pulsed blue laser beam is reduced to better satisfy the requirements for a half-spherical pancake distribution to transform into a uniformly filled ellipsoid [13].

The 5 ns ion bunches used for our demonstrations are directly analogous to ultrafast 13 ps electron bunches [27,31] with the same bunch charge. Achieving ultrafast single-shot diffraction will require much higher charge density, and much higher bunch charge such as the $N = 5 \times 10^5$ electron bunches we have previously produced with a cold atom source [32]. The effects of Coulomb-driven emittance growth will then severely limit the beam focus and brightness for unshaped Gaussian

bunches. Indeed, other cold atom sources using ultrafast electron bunches have been limited to a few hundred electrons per bunch due to the degrading effects of space charge, requiring thousands of bunches to create a satisfactory diffraction image [33]. Demonstrating the suppression of space-charge-induced emittance growth through shaping of the initial bunch profile is, therefore, a critical milestone in the development of cold electron sources, necessary for harnessing their inherent coherence, focusability, and brightness to perform single-shot ultrafast diffraction of noncrystalline targets.

B. M. S. acknowledges the support of a University of Melbourne McKenzie Fellowship. This work was supported by the Australian Research Council Discovery Project No. DP140102102.

*scholten@unimelb.edu.au

[1] S. Bernal, H. Li, T. Godlove, I. Haber, R. A. Kishek, B. Quinn, M. Reiser, M. Walter, Y. Zou, and P. G. O'Shea, Phys. Plasmas **11**, 2907 (2004).
[2] R. W. Schoenlein, W. P. Leemans, A. H. Chin, P. Volfbeyn, T. E. Glover, P. Balling, M. Zolotorev, K. Kim, S. Chattopadhyay, and C. V. Shank, Science **274**, 236 (1996).
[3] N. M. Buckanie, J. Göhre, P. Zhou, D. von der Linde, M. Horn-von Hoegen, and F. J. Meyer zu Heringdorf, J. Phys. Condens. Matter **21**, 314003 (2009).
[4] J. Orloff, Rev. Sci. Instrum. **64**, 1105 (1993).
[5] B. J. Siwick, J. R. Dwyer, R. E. Jordan, and R. J. D. Miller, Science **302**, 1382 (2003).
[6] Z. Tao, H. Zhang, P. M. Duxbury, M. Berz, and C.-Y. Ruan, J. Appl. Phys. **111**, 044316 (2012).
[7] F. O. Kirchner, A. Gliserin, F. Krausz, and P. Baum, Nat. Photonics **8**, 52 (2014).
[8] J. C. Williamson, J. Cao, H. Ihee, H. Frey, and A. H. Zewail, Nature (London) **386**, 159 (1997).
[9] L. W. Hardy, J. S. Finer-Moore, W. R. Montfort, M. O. Jones, D. V. Santi, and R. M. Stroud, Science **235**, 448 (1987).
[10] I. D. Kuntz, Science **257**, 1078 (1992).
[11] O. D. Kellogg, *Foundations of Potential Theory* (Springer-Verlag, Berlin, 1929).
[12] I. M. Kapchinskij and V. V. Vladimirskij, in *Proceedings of the International Conference on High Energy Accelerators* (CERN, Geneva, 1959), p. 274.
[13] O. J. Luiten, S. B. van der Geer, M. J. de Loos, F. B. Kiewiet, and M. J. van der Wiel, Phys. Rev. Lett. **93**, 094802 (2004).
[14] P. Musumeci, J. T. Moody, R. J. England, J. B. Rosenzweig, and T. Tran, Phys. Rev. Lett. **100**, 244801 (2008).
[15] J. T. Moody, P. Musumeci, M. S. Gutierrez, J. B. Rosenzweig, and C. M. Scoby, Phys. Rev. ST Accel. Beams **12**, 070704 (2009).
[16] Y. Li, S. Chemerisov, and B. Shen, New J. Phys. **12**, 123011 (2010).
[17] B. O'Shea, J. B. Rosenzweig, G. Asova, J. Bähr, M. Hänel, Y. Ivanisenko, M. Khojoyan, M. Krasilnikov, L. Staykov, F. Stephan *et al.*, Phys. Rev. ST Accel. Beams **14**, 012801 (2011).
[18] R. K. Li, K. G. Roberts, C. M. Scoby, H. To, and P. Musumeci, Phys. Rev. ST Accel. Beams **15**, 090702 (2012).
[19] P. Piot, Y. E. Sun, T. J. Maxwell, J. Ruan, E. Secchi, and J. C. T. Thangaraj, Phys. Rev. ST Accel. Beams **16**, 010102 (2013).
[20] B. J. Claessens, S. B. van der Geer, G. Taban, E. J. D. Vredenbregt, and O. J. Luiten, Phys. Rev. Lett. **95**, 164801 (2005).
[21] A. J. McCulloch, D. V. Sheludko, S. D. Saliba, S. C. Bell, M. Junker, K. A. Nugent, and R. E. Scholten, Nat. Phys. **7**, 785 (2011).
[22] A. J. McCulloch, D. V. Sheludko, M. Junker, and R. E. Scholten, Nat. Commun. **4**, 1692 (2013).
[23] W. J. Engelen, M. A. van der Heijden, D. J. Bakker, E. J. D. Vredenbregt, and O. J. Luiten, Nat. Commun. **4**, 1693 (2013).
[24] N. Debernardi, M. P. Reijnders, W. J. Engelen, T. T. J. Clevis, P. H. A. Mutsaers, O. J. Luiten, and E. J. D. Vredenbregt, J. Appl. Phys. **110**, 024501 (2011).
[25] R. M. W. van Bijnen, C. Ravensbergen, D. J. Bakker, G. J. Dijk, S. J. J. M. F. Kokkelmans, and E. J. D. Vredenbregt, New J. Phys. **17**, 023045 (2015).
[26] T. van Oudheusden, E. F. de Jong, S. B. van der Geer, W. P. E. M. Op't Root, O. J. Luiten, and B. J. Siwick, J. Appl. Phys. **102**, 093501 (2007).
[27] D. Murphy, R. W. Speirs, D. V. Sheludko, C. T. Putkunz, A. J. McCulloch, B. M. Sparkes, and R. E. Scholten, Nat. Commun. **5**, 4489 (2014).
[28] S. B. Van der Geer, M. J. De Loos, and O. J. Luiten, in *European Particle Accelerator Conference: Proceedings* (Genoa, Italy, 2008), Vol. 8, p. 151.
[29] L. Serafini, AIP Conf. Proc. **413**, 321 (1997).
[30] http://www.pulsar.nl/gpt/.
[31] D. Murphy, R. E. Scholten, and B. M. Sparkes, Phys. Rev. Lett. **115**, 214802 (2015).
[32] R. W. Speirs, C. T. Putkunz, A. J. McCulloch, K. A. Nugent, B. M. Sparkes, and R. E. Scholten, J. Phys. B **48**, 214002 (2015).
[33] M. W. van Mourik, W. J. Engelen, E. J. D. Vredenbregt, and O. J. Luiten, Struct. Dyn. **1**, 034302 (2014).

PHYSICAL REVIEW A **94**, 023404 (2016)

Stimulated Raman adiabatic passage for improved performance of a cold-atom electron and ion source

B. M. Sparkes, D. Murphy, R. J. Taylor, R. W. Speirs, A. J. McCulloch, and R. E. Scholten*
School of Physics, University of Melbourne, VIC 3010, Australia
(Received 10 March 2016; published 8 August 2016)

We implement high-efficiency coherent excitation to a Rydberg state using stimulated Raman adiabatic passage in a cold-atom electron and ion source. We achieve an efficiency of 60% averaged over the laser excitation volume with a peak efficiency of 82%, a 1.6 times improvement relative to incoherent pulsed-laser excitation. Using pulsed electric field ionization of the Rydberg atoms we create electron bunches with durations of 250 ps. High-efficiency excitation will increase source brightness, crucial for ultrafast electron diffraction experiments, and coherent excitation to high-lying Rydberg states could allow for the reduction of internal bunch heating and the creation of a high-speed single-ion source.

DOI: 10.1103/PhysRevA.94.023404

I. INTRODUCTION

Cold-atom electron and ion sources (CAEISs) [1–6], based on the photoionization of laser-cooled gases, offer the potential for dramatic improvements for electron diffraction, nanofabrication, and microscopy. One of the main drivers for the development of a CAEIS is the long-term goal of creating "molecular movies": to probe dynamic processes with atomic spatial and temporal resolution. Substantial advances towards this goal have been demonstrated with electron [7–13] and x-ray [14–20] single-shot ultrafast diffraction.

A key metric for ultrafast diffraction is the normalized beam brightness [21]. Conventional electron sources are not sufficiently bright for collecting single-shot diffraction signals from weakly scattering molecules or nanocrystals. Beam brightness is proportional to particle flux, which for a CAEIS depends linearly on the density of the cold-atom cloud and the photoionization probability or efficiency. To date, most CAEIS experiments have used photoexcitation with pulsed lasers in the presence of a static ionizing electric field. The incoherent nature of the excitation has limited the peak efficiency to 50%, while requiring high laser power due to saturation of the conventional excitation process.

Stimulated Raman adiabatic passage (STIRAP) [22] offers a mechanism for increasing the CAEIS excitation efficiency, particular in an optically dense cold atom target, and therefore improving source brightness. Here we are specifically interested in excitation to Rydberg states of rubidium-85 in a three-level ladder system (Fig. 1) [23]. By first illuminating the atoms with light of a frequency ω_{23}, resonant with the $|2\rangle \rightarrow |3\rangle$ transition, and then a second temporally overlapping light field of frequency ω_{12}, a dark state is formed by a coherent superposition of states $|1\rangle$ and $|3\rangle$. As the intensity of the light fields change, the atomic state transitions from state $|1\rangle$ to $|3\rangle$, bypassing $|2\rangle$. Figure 1 shows the population of the three states during the above-mentioned "counterintuitive" pulse sequence, simulated using optical Bloch equations for a ladder system [24] with Rabi frequencies Ω_{12} and Ω_{23}.

STIRAP is a robust technique and, provided the adiabatic condition is met ($\Omega_{\text{eff}}\,\tau > 10$, where $\Omega_{\text{eff}} = \sqrt{\Omega_{12}^2 + \Omega_{23}^2}$ is the effective Rabi frequency and τ is the interaction time), high-efficiency excitation is possible with a variety of different individual Rabi frequencies, pulse delays, and shapes. Experiments to date have demonstrated peak excitation efficiencies up to 90% [25–27], which would increase the brightness of a CAEIS by a factor of 1.8.

STIRAP also enables a method for producing very short bunches, and therefore for observing atomic-scale dynamics, by following excitation with pulsed-electric-field ionization [28]. This method will lead to a longitudinal compression of the bunch following ionization: the electrons liberated at later times will be accelerated by a larger field, allowing for ultra-short bunches at the sample without ultra-high electron densities, and therefore large Coulomb-driven expansion, at the source. Rydberg states have long lifetimes (tens to hundreds of microseconds) and relatively low ionization thresholds (600 V cm^{-1} for $30S_{1/2}$), easing experimental demands on the pulsed electric field supply. The coupling strength of Rydberg transitions is much higher in the absence of an electric field, so that much lower laser power is required with a pulsed electric field compared to excitation in a static field, making STIRAP excitation a viable option. Combining STIRAP excitation and fast pulsed-field ionization has the potential to create bunches that are cold, bright, and ultrafast, which is difficult to replicate with incoherent ultrafast laser ionization [4,29].

The large dipole moments of Rydberg atoms enable Rydberg blockade, where excitation of one atom inhibits the excitation of other atoms nearby [23,24]. Rydberg blockade can, in principle, reduce disorder-induced heating [30,31] and thereby reduce emittance and increase focusabiltiy in a CAEIS [32]. By enforcing a separation between Rydberg atoms larger than the laser excitation volume, blockade can allow selective excitation of discrete separated atoms and thereby create a deterministic single ion source [33–35].

With the much-reduced laser power required, STIRAP can also be used for high-efficiency continuous operation, with increased average current relative to pulsed trap-based CAEISs [36–39]. Continuous sources are preferred for sub-nanometer ion beam milling, imaging, and doping in semiconductor device fabrication. A continuous source of cold ions

*scholten@unimelb.edu.au

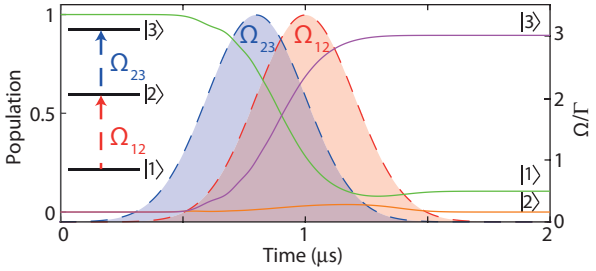

FIG. 1. Simulation of high-efficiency excitation using stimulated Raman adiabatic passage in a three-level ladder system. Solid lines represent atomic state populations (left-hand axis), dashed and filled lines represent Rabi frequencies Ω normalized to the intermediate state decay rate Γ (right-hand axis).

has recently been demonstrated using Rydberg excitation with a current of up to 130 pA [40], a 40-fold increase over direct, above-threshold ionization methods, illustrating the advantage of coherent excitation methods.

Here we present a CAEIS based on STIRAP excitation in a magneto-optical trap (MOT), with a volume-averaged excitation efficiency of 60% and a corresponding peak efficiency of 82%, 1.6 times the maximum possible with direct excitation. We also use a streak method to investigate the temporal profile of the bunches created via electric-field ionization, and finally we discuss how STIRAP could be implemented in an atomic beam-based CAEIS.

II. METHOD

The CAEIS setup is based around a MOT of rubidium-85 atoms located between two accelerator electrodes, as described in previous work [3,29] and shown in Fig. 2(a). A typical experimental sequence is shown in Fig. 2(b), starting with the MOT being loaded for approximately 100 ms. After this time all laser and magnetic fields are switched off and allowed to decay for 4 ms to ensure a field-free excitation region. The atomic density after 4 ms of expansion was measured to be $\rho_a = 5 \times 10^9$ atoms cm^{-3} using absorption imaging.

In contrast to previous CAEIS experiments, which used a large-bandwidth pulsed 480 nm blue laser for direct ionization via a Stark-shifted manifold [3,41–43], here we used a frequency-doubled and amplified 960 nm laser diode. The continuous laser provided a high-power (300 mW), narrow-linewidth (<500 kHz) source of 480 nm light to couple the intermediate $5P_{3/2}$ state to a Rydberg level ($28S_{1/2}$). The frequency was stabilized using an ultrastable optical reference cavity.

The STIRAP process [see level structure; Fig. 2(a)] was driven by an infrared 780 nm narrow-line width (200 kHz) diode laser with 60 nW of power and a frequency 27 MHz blue-detuned from the $5S_{1/2} \rightarrow 5P_{3/2}$ transition to reduce incoherent absorption by atoms outside the interaction volume. The continuous blue laser was red-detuned 27 MHz from the $5P_{3/2} \rightarrow 28S_{1/2}$ transition. We define the one-photon detuning as $\Delta = +27$ MHz.

Temporal control of the excitation fields was achieved via double-pass acousto-optic modulators. Rectangular pulses were used, as illustrated in Fig. 2(c), and we define the

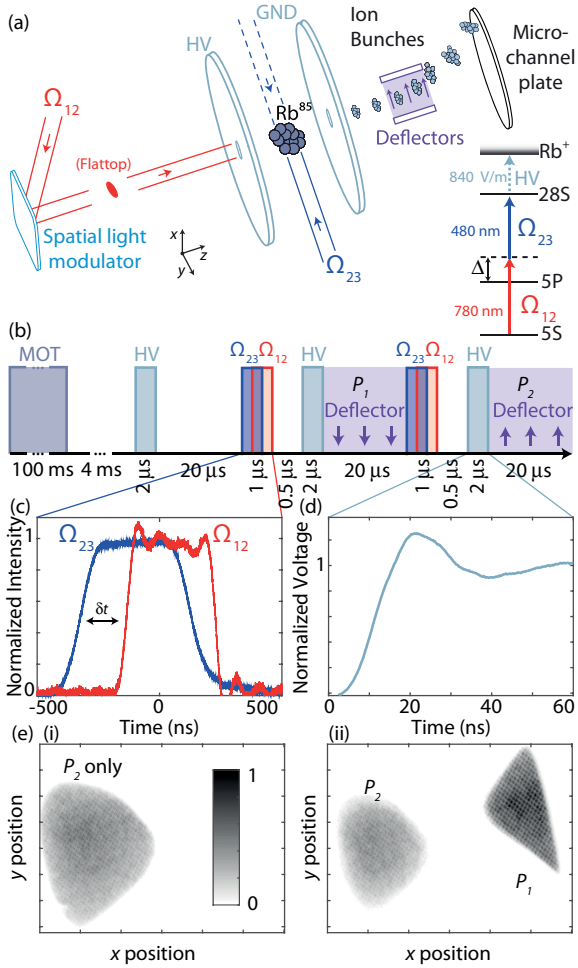

FIG. 2. (a) Cold-atom ion source: HV refers to the high-voltage supplied to the front accelerator plate; GND is the grounded plate; and Ω_{12} and Ω_{23} refer to the two STIRAP fields. Inset shows the level structure of Rb^{85} used here, including the electric field ionization strength required and the one-photon detuning Δ. (b) Timing sequence for STIRAP excitation, field ionization, and two-pulse measurements, using electrostatic deflectors to spatially separate the two pulses (P_1 and P_2). (c) STIRAP pulse sequence, with temporal separation $\delta t < 0$. (d) Time dependence of front accelerator potential, for $V_{max} = 100$ V. (e) Example MCP images showing (i) just pulse two (P_2) and (ii) both pulses. Color bar in (i) shows scaling used for both MCP images.

delay between the pulses δt to be negative if the blue pulse started before the red. The excitation region was determined by the spatial overlap of the two laser beams. The spatial profile of the infrared laser beam, controlled via a spatial-light modulator, was a uniform circular cross section with a radius of $R_r = 150$ μm in the plane perpendicular to the direction of charged particle propagation. The blue laser beam was focused to a ribbon with Gaussian standard deviations of approximately $\sigma_x = 150$ μm by $\sigma_z = 20$ μm in the perpendicular and longitudinal directions respectively. The optical excitation was driven without an external electric field to avoid Stark splitting and loss of coupling strength. A potential difference was then applied to the electrodes, with a rise time of 4 ns [Fig. 2(d)]. The threshold electric field strength required for ionization

of the $28S_{1/2}$ is 840 V cm^{-1}. Typically an accelerator field of 1400 kV cm^{-1} was applied to ensure complete ionization. The liberated electrons or ions (depending on the polarity of the electric field) propagated 70 cm before detection with a micro-channel plate (MCP) combined with a phosphor screen and CCD camera.

STIRAP was performed twice in quick succession using ion bunches to determine the ionization efficiency. The total charge in the first and second bunches, N_1 and N_2 respectively, are related to the efficiency $\mathcal{E}(x,z)$ by

$$N_1 \propto \iiint_V \mathcal{E}(x,z)\,dx\,dy\,dz, \tag{1}$$

$$N_2 \propto \iiint_V \mathcal{E}(x,z)[1-\mathcal{E}(x,z)]\,dx\,dy\,dz, \tag{2}$$

where the spatial dependence of $\mathcal{E}(x,z)$ comes from the intensity profile of the blue laser (the product of two independent Gaussians in x and z), and the interaction volume V is bounded by the size of the infrared laser ($x^2+y^2=R_r^2$). The total volume-averaged efficiency can be determined from the overall charge present:

$$\mathcal{E}_{\text{int}} = 1 - \frac{N_2}{N_1}. \tag{3}$$

This two-pulse method therefore provides a measure of efficiency that is independent of the atomic density, excitation volume and MCP efficiency [25,26] if we assume minimal atomic movement inside the MOT between the two STIRAP events.

$N_{1,2}$ are determined by area integration of the MCP images for pulses $P_{1,2}$ shown in Fig. 2(e). The phosphor screen on the MCP detector has a decay time on the order of milliseconds, too long to be able to temporally separate the signals from the two pulses. Instead, a deflector was used to spatially separate the two bunches. We used a variant on the two-pulse method to remove dependence on the MCP sensitivity, which is not perfectly uniform across the detector. Measurements were made with just the second pulse to give N_1 [Fig. 2(e)(i)], and then at the same location with both pulses spatially separated to determine N_2 [Fig. 2(e)(ii)].

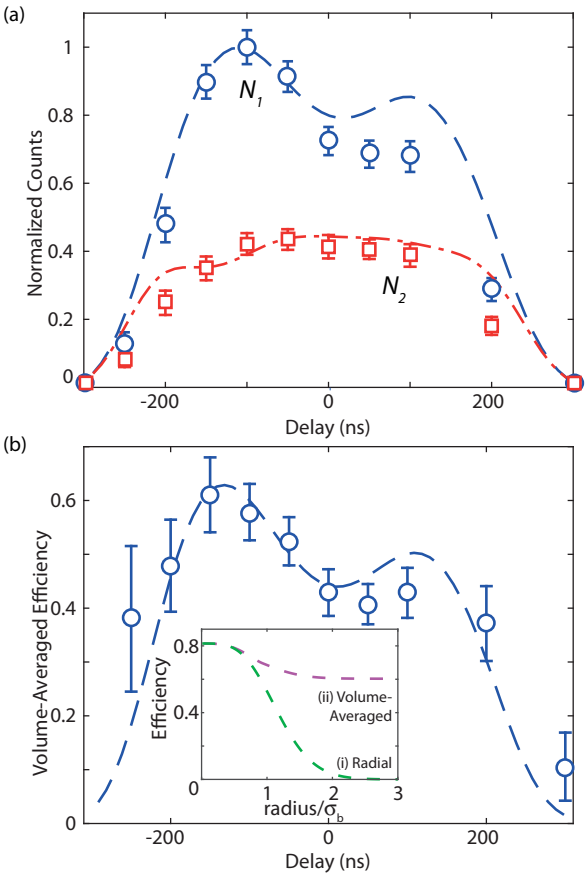

FIG. 3. (a) MCP Counts in first pulse (N_1, blue, circles) and second pulse (N_2, red, squares) as a function of the relative delay between the two excitation fields. Points indicate experimental data, with error bars determined from the standard deviation of 100 images, and lines indicate simulations using 200 ns flattop pulses, peak Rabi frequencies $\Omega_{12}=\Omega_{23}=15$ MHz, laser linewidths $\Gamma_{12}=\Gamma_{23}=500$ kHz, and $\Delta=27$ MHz. (b) Efficiency calculated from the ratio of N_2 to N_1 using Eq. (3). Points indicate experimental data, and lines indicate simulation. The inset shows (i) the calculated radial efficiency and (ii) the volume-averaged efficiency as a function of the blue laser beam radius, normalized to the Gaussian σ_b, at the optimal delay $\delta t=-150$ ns.

III. RESULTS AND ANALYSIS

A. STIRAP efficiency

Figure 3(a) shows the total integrated counts as a function of the delay between the pulses δt. Figure 3(b) shows the volume-averaged efficiency calculated from the relative signals using Eq. (3), with the characteristic high efficiency seen when $\delta t < 0$ (maximum of 60% at $\delta_t=-150$ ns).

Simulations were performed using optical Bloch equations [24] with experimentally realistic parameters (peak Rabi frequencies $\Omega_{12}=\Omega_{23}=15$ MHz, $\Delta=27$ MHz, intermediate state decay rate $\Gamma=6$ MHz, laser linewidths $\gamma_{12}=\gamma_{23}=500$ kHz, for 200 ns rectangular pulses with 100 ns linear rise and fall times). Inset (i) of Fig. 3(b) shows the simulated radial efficiency $\mathcal{E}[r]$ for a blue laser beam with Gaussian electric field profile with an arbitrary $1/e$ width of σ_b. Inset (ii) shows the volume-averaged efficiency $\int_0^r \mathcal{E}[r']\,dr'$ as the radius of integration increases to $\pm r$ in z and either $\pm r$ or $\pm R_r$ in x, whichever is smaller. In the inset we have scaled $\sigma_x=\sigma_z=\sigma_b$ for simplicity and used the fact that $R_r=\sigma_b$. These simulations of the volume-averaged efficiency agree well with the experimental data in Fig. 3. We can therefore infer a peak efficiency for STIRAP in the CAEIS of 82% at the maximum blue intensity. Increasing the blue power would increase the maximum efficiency obtainable. However, with increased intensity comes the possibility of adding random phase and amplitude noise, which can limit the maximum efficiency obtainable [44]. Even without increasing the maximum intensity, for a uniform blue laser profile with intensity such that the Rabi frequency is the same as at the peak of our Gaussian profile, then we expect both volume-averaged and peak efficiencies would be 82%. Nonuniform electric fields within the accelerator region, for example, caused by charged particle accumulation on the electrodes,

will also reduce the coupling strength, broaden the two-photon transition, and reduce the maximum efficiency.

The experimental results show a distinct reduction in signal compared to simulations for $\delta t > 0$. This reduction is the opposite of the increase in signal seen elsewhere [25,26], which was attributed to radiation trapping and Rydberg-Rydberg interactions. We use a large one-photon detuning to avoid absorption of the infrared laser outside the interaction zone. Any background absorption will lead to a large two-photon detuning for the re-radiated light interacting with the off-resonance blue light, causing a reduction in the excitation probability. The accompanying optical pumping of the background atoms into the lower ground state during the first excitation event will reduce the fraction of reradiating atoms for the second event, resulting mainly in a reduction of first pulse counts and, therefore, a reduction in the calculated efficiency.

B. Incoherent excitation efficiency

To quantify the improvement to CAEIS brightness provided by STIRAP, we measured the efficiency of pulsed 480 nm laser ionization using a variant of the two-pulse efficiency method. The pulsed and continuous blue laser beams were overlapped in counterpropagating directions [dashed lines in Fig. 2(a)], perpendicular to the direction of charged particle propagation. The same infrared laser was used for both excitation processes, though the power and detuning were optimized separately for each: on resonance for pulsed-laser excitation and 27 MHz detuned for STIRAP excitation. The accelerator field was applied before pulsed-laser excitation to reproduce "normal" ionization conditions for a CAEIS. N_1 was still defined as the signal for a single STIRAP pulse sequence, and N_2 as the signal for STIRAP excitation following excitation by the pulsed laser. Using this method, the efficiency of the pulsed blue laser as a function of infrared laser intensity and pulsed blue power was measured (Fig. 4).

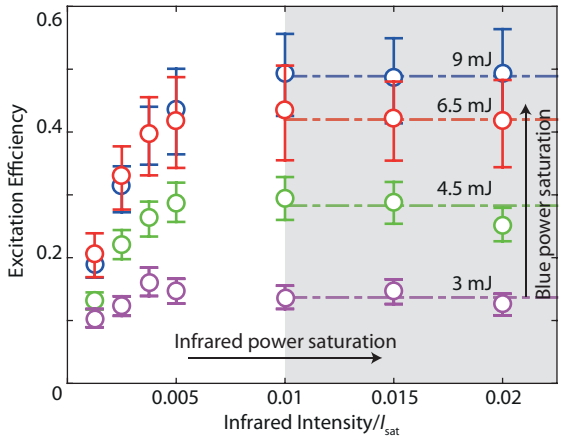

FIG. 4. Pulsed blue ionization efficiency as a function of infrared laser intensity normalized to saturation intensity (I_{sat}) for different blue pulse energies. Numbers indicate the power of the pulsed blue laser, dashed lines show the saturation of ionization efficiency, and shaded region denotes the region where the intermediate state becomes saturated.

The efficiency approaches 50%, the maximum efficiency for incoherent excitation in a two-level system, as infrared laser intensity and pulsed blue energy increase. This limit arises as the blue pulse duration (of order a few nanoseconds) is much faster than the infrared pumping rate, and so the intermediate state will not be refilled on the ionization time scale. Comparing the peak STIRAP excitation to this incoherent excitation peak gives an increase in efficiency by a factor of 60%.

C. Temporal profile

The duration of the electron or ion bunches is an important parameter for most applications of a CAEIS. Coulomb-driven spatial expansion of charged bunches leads to temporal expansion, but the expansion is not significant for electrons because the propagation time from bunch creation to detection is too short. Hence we investigated the temporal bunch shape using a streak method. The electron bunches propagated through deflectors with a rapidly varying transverse potential, causing the bunch to "streak" across the detector, with the position of an electron on the detector being dependent on the time at which it entered the deflector region. The temporal profile of the bunch was then determined from a line profile along the streak, calibrated to the known geometry and time-varying potential difference. The streak measurements are shown in Fig. 5 for bunches created with (a) STIRAP excitation followed by pulsed electric field ionization, and (b) pulsed blue ionization in a constant electric field.

For accelerator fields close to the electric-field ionization threshold of the $28S_{1/2}$ state, a broad secondary peak in the electron temporal distribution can be seen for the STIRAP bunches. This peak could be due to blackbody collisions transferring some atoms to lower energy states with a higher threshold ionization voltage [45]. The appearance of a much narrower secondary peak in both the 5.5 and 7.2 kV results also supports this explanation. Another possibility is nonideal behavior of the high-voltage switch, for example, by fast oscillations in the rising voltage.

The relative pulse heights show that a near-threshold voltage leads to only a small fraction of excited atoms being ionized. Once above the threshold voltage, this fraction approaches one, verified by the detection of only a very weak signal when performing a second electric field ionization pulse after a single STIRAP excitation sequence. The root mean square (RMS) duration of the STIRAP bunches, determined from the streak measurements of Fig. 5(a), was 250 ps, varying only slightly for different accelerator potentials.

With an accelerator rise time on the order of nanoseconds, ionization will be diabatic (hydrogenic). Modeling an accelerator profile on Fig. 2(d), the ionization rate for a "red" state of hydrogen (where Rydberg quantum numbers $m = n_1 = 0$, $n_2 = n - 1$) [46,47] gives an RMS pulse width of 170 ps [Fig. 5(a)], consistent with the initial rise in electron charge seen in the data of Fig. 5(a).

The measured duration of bunches produced with STIRAP excitation and field ionization compares favorably with that for pulsed blue excitation. The bunch duration for incoherent excitation is determined by the temporal profile of the pulsed laser, which has a quoted total pulse length of 5 ns and produces

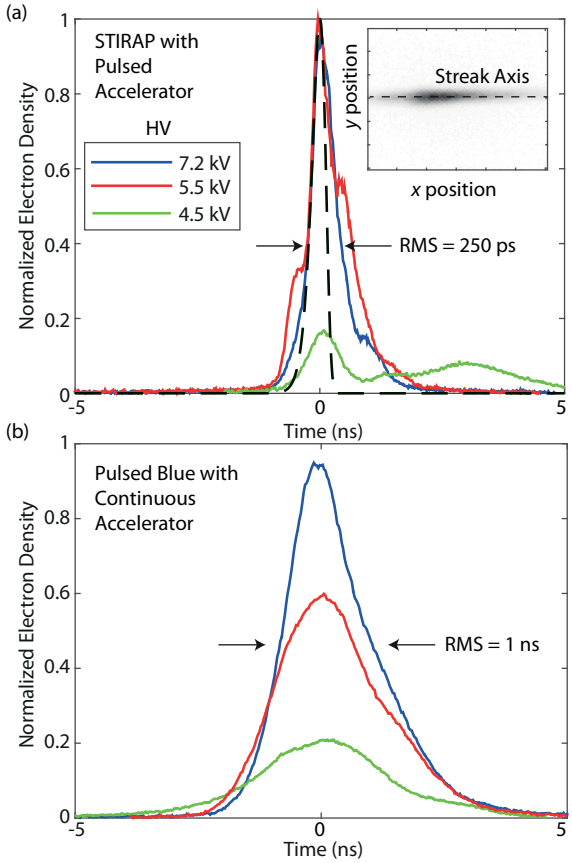

FIG. 5. Streak measurements of electrons created with: (a) STIRAP bunches with pulsed accelerator and (b) pulsed blue laser with continuous accelerator at different accelerator potential differences HV. Inset shows a false-color streaked electron bunch as measured by the MCP. All traces are normalized to the same peak value. Solid lines indicate experimental data, dashed line indicates theory for hydrogenic "red" state with field switching behavior from Fig. 2(d), normalized to height of experimental traces.

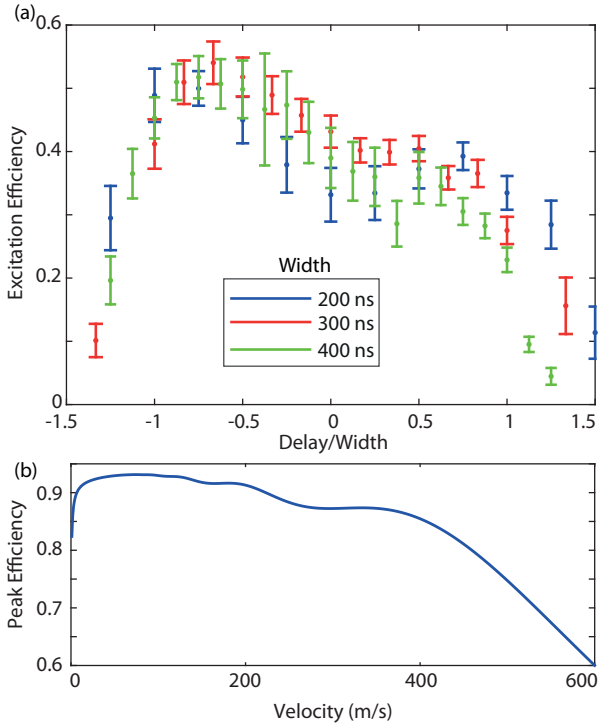

FIG. 6. (a) Efficiency as a function of the ratio of pulse delay δt to flattop pulse width w. (b) Simulated excitation efficiency of STIRAP for an cold atom-beam source, as a function of atomic velocity with $\Omega_{12} = \Omega_{23} = 15$ MHz, $\sigma_z = 15$ μm, and $\delta z = -\sigma_z$.

bunches with duration of order 1 ns RMS. Ultrafast electron diffraction requires subpicosecond pulses. With accelerator potentials of 30 kV and 30 ns electric field rise times, it has been shown that a bunch length of 80 ps can be achieved [28]. To reduce the bunch duration below 1 ps following STIRAP excitation, the maximum accelerator voltage would need to increase by an order of magnitude, and the switching time reduce to less than 1 ns [1]. Achieving such electric field switching requires careful design of the MOT chamber and accelerator to avoid electrical discharge [28] and a very fast high-voltage switch, potentially using laser-triggered spark gap technology [48]. Alternately, an RF bunch compressor could be used [12].

D. Robustness

The effect of different STIRAP pulse widths w was investigated [Fig. 6(a)]. The robustness of STIRAP excitation is apparent, since a difference in width by a factor of two has very little impact on either the maximum efficiency (50–55%), or the time at which this occurs ($\delta t/w = -0.75$ for the rectangular pulses used).

The robustness of STIRAP makes it ideally suited to next-generation cold-atom ion sources based on atomic beams [36–39]. The experimental situation described above, where atoms are stationary and the optical and electric fields are dynamic, is equivalent to an atomic beam system with atoms moving through spatially separated static optical fields and a region with an electric field gradient. The high temperature of the atoms along the direction of propagation will result in a large velocity spread. For instance, an experimentally practical atom beam temperature of 200 °C would lead to a most-probable velocity of $v_{zp} = 305$ m s^{-1} with standard deviation of 150 m s^{-1}. The different velocities of the atoms are equivalent to a static atom seeing STIRAP fields with different temporal widths but a constant $\delta t/w$. Figure 6(b) shows the peak efficiency calculated for such a system with Gaussian laser beam spatial profiles with $\sigma_z = 15$ μm and $\delta z = -\sigma_z$. The efficiency remains above 80% from 0 to 400 m s^{-1}, so that a large proportion of the atomic population (66%) will be excited with high efficiency.

High ion beam densities achieved using STIRAP excitation could lead to Coulomb explosion and a reduction in the focusability of the source. The density could be reduced by using Rydberg blockade with high principle quantum number $n \approx 100$ [23]. If the excitation volume is reduced to below one blockade radius, it will become possible to isolate separate ions spatially and temporally to create a quasideterministic highly focusable single ion source with heralding provided by the liberated electrons [34,35].

IV. CONCLUSIONS

We have shown that STIRAP can improve the excitation efficiency of a cold-atom electron and ion source by a factor of 1.6, from a peak efficiency of 50% with incoherent excitation, to 82%. Further improvements are expected with higher laser power, greater uniformity of the electric field within the excitation region, and reduced phase noise in the excitation lasers.

We have also shown that STIRAP excitation and fast switching of the ionization electric field produces bunches with an RMS duration of 250 ps. Subpicosecond bunches may be achievable with higher acceleration potentials and faster switching, and with an RF compressor, to satisfy the temporal criterion for imaging dynamic processes with atomic spatial and temporal resolution using ultrafast electron diffraction.

With continuous lasers and an atomic beam, STIRAP excitation will be directly applicable to next-generation continuous atom-beam based cold-electron and ion sources. Finally, by using high efficiency STIRAP excitation to reach higher Rydberg states, the phenomena of Rydberg blockade could be used to create spatial ordering, and therefore reduce the temperature and increase the focusability of the bunches, as well as enabling a new approach to creating a deterministic single ion source.

ACKNOWLEDGMENTS

B.M.S. gratefully acknowledges the support of a University of Melbourne McKenzie Fellowship. This work was supported by the Australian Research Council Discovery Project DP140102102.

[1] B. J. Claessens, S. B. van der Geer, G. Taban, E. J. D. Vredenbregt, and O. J. Luiten, Ultracold Electron Source, Phys. Rev. Lett. **95**, 164801 (2005).

[2] B. J. Claessens, M. P. Reijnders, G. Taban, O. J. Luiten, and E. J. D. Vredenbregt, Cold electron and ion beams generated from trapped atoms, Phys. Plasmas **14**, 093101 (2007).

[3] A. J. McCulloch, D. V. Sheludko, S. D. Saliba, S. C. Bell, M. Junker, K. A. Nugent, and R. E. Scholten, Arbitrarily shaped high-coherence electron bunches from cold atoms, Nature Phys. **7**, 785 (2011).

[4] W. J. Engelen, M. A. van der Heijden, D. J. Bakker, E. J. D. Vredenbregt, and O. J. Luiten, High-coherence electron bunches produced by femtosecond photoionization, Nature Comm. **4**, 1693 (2013).

[5] J. L. Hanssen, S. B. Hill, J. Orloff, and J. J. McClelland, Magneto-optical-trap-based, high brightness ion source for use as a nanoscale probe, Nano Lett. **8**, 2844 (2008).

[6] A. V. Steele, B. Knuffman, J. J. McClelland, and J. Orloff, Focused chromium ion beam, J. Vac. Sci. Technol. B **28**, C6F1 (2010).

[7] J. R. Dwyer, C. T. Hebeisen, R. Ernstorfer, M. Harb, V. B. Deyirmenjian, R. E. Jordan, and R. J. D. Miller, Femtosecond electron diffraction: 'making the molecular movie', Philosophical Transactions. Series A, Mathematical, Physical, and Engineering Sciences **364**, 741 (2006).

[8] B. J. Siwick, J. R. Dwyer, R. E. Jordan, R. J. D. Miller, R. S. Dwyer, R. E. Jordan, and R. J. D. Miller, An atomic-level view of melting using femtosecond electron diffraction, Science **302**, 1382 (2003).

[9] M. Harb, R. Ernstorfer, C. T. Hebeisen, G. Sciaini, W. Peng, T. Dartigalongue, M. A. Eriksson, M. G. Lagally, S. G. Kruglik, and R. J. D. Miller, Electronically Driven Structure Changes of Si Captured by Femtosecond Electron Diffraction, Phys. Rev. Lett. **100**, 155504 (2008).

[10] G. Sciaini, M. Harb, S. G. Kruglik, T. Payer, C. T. Hebeisen, F.-J. M. Z. Heringdorf, M. Yamaguchi, M. H. von Hoegen, R. Ernstorfer, and R. J. D. Miller, Electronic acceleration of atomic motions and disordering in bismuth, Nature (London) **458**, 56 (2009).

[11] S. Tokita, S. Inoue, S. Masuno, M. Hashida, and S. Sakabe, Single-shot ultrafast electron diffraction with a laser-accelerated sub-MeV electron pulse, Appl. Phys. Lett. **95**, 111911 (2009).

[12] T. van Oudheusden, P. L. E. M. Pasmans, S. B. van der Geer, M. J. de Loos, M. J. van der Wiel, and O. J. Luiten, Compression of Subrelativistic Space-Charge-Dominated Electron Bunches for Single-Shot Femtosecond Electron Diffraction, Phys. Rev. Lett. **105**, 264801 (2010).

[13] T. Ishikawa, S. A. Hayes, S. Keskin, G. Corthey, M. Hada, K. Pichugin, A. Marx, J. Hirscht, K. Shionuma, K. Onda, Y. Okimoto, S.-Y. Koshihara, T. Yamamoto, H. Cui, M. Nomura, Y. Oshima, M. Abdel-Jawad, R. Kato, and R. J. D. Miller, Direct observation of collective modes coupled to molecular orbital-driven charge transfer, Science **350**, 1501 (2015).

[14] H. N. Chapman, A. Barty, M. J. Bogan, S. Boutet, M. Frank, S. P. Hau-Riege, S. Marchesini, B. W. Woods, S. Bajt, W. H. Benner, R. A. London, E. Plönjes, M. Kuhlmann, R. Treusch, S. Düsterer, T. Tschentscher, J. R. Schneider, E. Spiller, T. Möller, C. Bostedt *et al.*, Femtosecond diffractive imaging with a soft-x-ray free-electron laser, Nature Phys. **2**, 839 (2006).

[15] H. N. Chapman, P. Fromme, A. Barty, T. A. White, R. A. Kirian, A. Aquila, M. S. Hunter, J. Schulz, D. P. DePonte, U. Weierstall, R. B. Doak, F. R. N. C. Maia, A. V. Martin, I. Schlichting, L. Lomb, N. Coppola, R. L. Shoeman, S. W. Epp, R. Hartmann, D. Rolles, A. Rudenko, L. Foucar, N. Kimmel, G. Weidenspointner, P. Holl, M. Liang, M. Barthelmess, C. Caleman, S. Boutet, M. J. Bogan, J. Krzywinski, C. Bostedt, S. Bajt, L. Gumprecht, B. Rudek, B. Erk, C. Schmidt, A. Hömke, C. Reich, D. Pietschner, L. Strüder, G. Hauser, H. Gorke, J. Ullrich, S. Herrmann, G. Schaller, F. Schopper, H. Soltau, K.-U. Kühnel, M. Messerschmidt, J. D. Bozek, S. P. Hau-Riege, M. Frank, C. Y. Hampton, R. G. Sierra, D. Starodub, G. J. Williams, J. Hajdu, N. Timneanu, M. M. Seibert, J. Andreasson, A. Rocker, O. Jönsson, M. Svenda, S. Stern, K. Nass, R. Andritschke, C.-D. Schröter, F. Krasniqi, M. Bott, K. E. Schmidt, X. Wang, I. Grotjohann, J. M. Holton, T. R. M. Barends, R. Neutze, S. Marchesini, R. Fromme, S. Schorb, D. Rupp, M. Adolph, T. Gorkhover, I. Andersson, H. Hirsemann, G. Potdevin,

H. Graafsma, B. Nilsson, and J. C. H. Spence, Femtosecond x-ray protein nanocrystallography, Nature (London) **470**, 73 (2011).

[16] M. M. Seibert, T. Ekeberg, F. R. N. C. Maia, M. Svenda, J. Andreasson, O. Jönsson, D. Odić, B. Iwan, A. Rocker, D. Westphal, M. Hantke, D. P. DePonte, A. Barty, J. Schulz, L. Gumprecht, N. Coppola, A. Aquila, M. Liang, T. A. White, A. Martin, C. Caleman, S. Stern, C. Abergel, V. Seltzer, J.-M. Claverie, C. Bostedt, J. D. Bozek, S. Boutet, A. A. Miahnahri, M. Messerschmidt, J. Krzywinski, G. Williams, K. O. Hodgson, M. J. Bogan, C. Y. Hampton, R. G. Sierra, D. Starodub, I. Andersson, S. Bajt, M. Barthelmess, J.C. H. Spence, P. Fromme, U. Weierstall, R. Kirian, M. Hunter, R. B. Doak, S. Marchesini, S. P. Hau-Riege, M. Frank, R. L. Shoeman, L. Lomb, S. W. Epp, R. Hartmann, D. Rolles, A. Rudenko, C. Schmidt, L. Foucar, N. Kimmel, P. Holl, B. Rudek, B. Erk, A. Hömke, C. Reich, D. Pietschner, G. Weidenspointner, L. Strüder, G. Hauser, H. Gorke, J. Ullrich, I. Schlichting, S. Herrmann, G. Schaller, F. Schopper, H. Soltau, K.-U. Kühnel, R. Andritschke, C.-D. Schröter, F. Krasniqi, M. Bott, S. Schorb, D. Rupp, M. Adolph, T. Gorkhover, H. Hirsemann, G. Potdevin, H. Graafsma, B. Nilsson, H. N. Chapman, and J. Hajdu, Single mimivirus particles intercepted and imaged with an x-ray laser, Nature (London) **470**, 78 (2011).

[17] S. Boutet, L. Lomb, G. J. Williams, T. R. M. Barends, A. Aquila, R. B. Doak, U. Weierstall, D. P. Deponte, J. Steinbrener, R. L. Shoeman, M. Messerschmidt, A. Barty, T. A. White, S. Kassemeyer, R. A. Kirian, M. M. Seibert, P. A. Montanez, C. Kenney, R. Herbst, P. Hart, J. Pines, G. Haller, S. M. Gruner, H. T. Philipp, M. W. Tate, M. Hromalik, L. J. Koerner, N. Van Bakel, J. Morse, W. Ghonsalves, D. Arnlund, K. Nass, L. Redecke, F. Stellato, N. Timneanu, D. Wang, J. C. H. Spence, H. N. Chapman, and I. Schlichting, High-resolution protein structure determination by serial femtosecond crystallography, Science **337**, 362 (2012).

[18] T. Kimura, Y. Joti, A. Shibuya, C. Song, S. Kim, K. Tono, M. Yabashi, M. Tamakoshi, T. Moriya, T. Oshima, T. Ishikawa, Y. Bessho, and Y. Nishino, Imaging live cell in micro-liquid enclosure by x-ray laser diffraction, Nature Comm. **5**, 3052 (2014).

[19] C. Kupitz, S. Basu, I. Grotjohann, R. Fromme, N. A. Zatsepin, K. N. Rendek, M. S. Hunter, R. L. Shoeman, T. A. White, D. Wang, D. James, J.-H. Yang, D. E. Cobb, B. Reeder, R. G. Sierra, H. Liu, A. Barty, A. L. Aquila, D. Deponte, R. A. Kirian *et al.*, Serial time-resolved crystallography of photosystem II using a femtosecond x-ray laser, Nature (London) **513**, 261 (2014).

[20] P. Nogly, I. Gushchin, A. Remeeva, A. M. Esteves, N. Borges, P. Ma, A. Ishchenko, S. Grudinin, E. Round, I. Moraes, V. Borshchevskiy, H. Santos, V. Gordeliy, and M. Archer, X-ray structure of a CDP-alcohol phosphatidyltransferase membrane enzyme and insights into its catalytic mechanism, Nature Comm. **5**, 4169 (2014).

[21] O. J. Luiten, B. J. Claessens, S. B. Van Der Geer, M. P. Reijnders, G. Taban, and E. J. D. Vredenbregt, Ultracold electron sources, Int. J. Mod. Phys. A **22**, 3882 (2007).

[22] K. Bergmann, H. Theuer, and B. W. Shore, Coherent population transfer among quantum states of atoms and molecules, Rev. Mod. Phys. **70**, 1003 (1998).

[23] R. Löw, H. Weimer, J. Nipper, J. B. Balewski, B. Butscher, H. P. Büchler, and T. Pfau, An experimental and theoretical guide to strongly interacting Rydberg gases, J. Phys. B **45**, 113001 (2012).

[24] S. Sevinçli, C. Ates, T. Pohl, H. Schempp, C. S. Hofmann, G. Günter, T. Amthor, M. Weidemüller, J. D. Pritchard, D. Maxwell, A. Gauguet, K. J. Weatherill, M. P. A. Jones, and C. S. Adams, Quantum interference in interacting three-level Rydberg gases: Coherent population trapping and electromagnetically induced transparency, J. Phys. B **44**, 184018 (2011).

[25] T. Cubel, B. Teo, V. Malinovsky, J. Guest, A. Reinhard, B. Knuffman, P. Berman, and G. Raithel, Coherent population transfer of ground-state atoms into Rydberg states, Phys. Rev. A **72**, 023405 (2005).

[26] J. Deiglmayr, M. Reetz-Lamour, T. Amthor, S. Westermann, A. L. de Oliveira, and M. Weidemüller, Coherent excitation of Rydberg atoms in an ultracold gas, Opt. Commun. **264**, 293 (2006).

[27] T. Takekoshi, L. Reichsöllner, A. Schindewolf, J. M. Hutson, C. R. Le Sueur, O. Dulieu, F. Ferlaino, R. Grimm, and H.-C. Nägerl, Ultracold Dense Samples of Dipolar RbCs Molecules in the Rovibrational and Hyperfine Ground State, Phys. Rev. Lett. **113**, 205301 (2014).

[28] G. Taban, M. P. Reijnders, S. C. Bell, S. B. van der Geer, O. J. Luiten, and E. J. D. Vredenbregt, Design and validation of an accelerator for an ultracold electron source, Phys. Rev. ST Accel. Beams **11**, 050102 (2008).

[29] A. J. McCulloch, D. V. Sheludko, M. Junker, and R. E. Scholten, High-coherence picosecond electron bunches from cold atoms, Nature Comm. **4**, 1692 (2013).

[30] M. S. Murillo, Using Fermi Statistics to Create Strongly Coupled Ion Plasmas in Atom Traps, Phys. Rev. Lett. **87**, 115003 (2001).

[31] S. Kuzmin and T. O'Neil, Numerical simulation of ultracold plasmas: How rapid intrinsic heating limits the development of correlation, Phys. Rev. Lett. **88**, 065003 (2002).

[32] D. Murphy, R. E. Scholten, and B. M. Sparkes, Increasing the Brightness of Cold Ion Beams by Suppressing Disorder-Induced Heating with Rydberg Blockade, Phys. Rev. Lett. **115**, 214802 (2015).

[33] M. Saffman, T. G. Walker, and K. Mølmer, Quantum information with Rydberg atoms, Rev. Mod. Phys. **82**, 2313 (2010).

[34] I. I. Beterov, D. B. Tretyakov, V. M. Entin, E. A. Yakshina, I. I. Ryabtsev, C. MacCormick, and S. Bergamini, Deterministic single-atom excitation via adiabatic passage and Rydberg blockade, Phys. Rev. A **84**, 023413 (2011).

[35] C. Ates, I. Lesanovsky, C. S. Adams, and K. J. Weatherill, Fast and Quasideterministic Single Ion Source from a Dipole-Blockaded Atomic Ensemble, Phys. Rev. Lett. **110**, 213003 (2013).

[36] L. Kime, A. Fioretti, Y. Bruneau, N. Porfido, F. Fuso, M. Viteau, G. Khalili, N. Šantić, A. Gloter, B. Rasser, P. Sudraud, P. Pillet, and D. Comparat, High-flux monochromatic ion and electron beams based on laser-cooled atoms, Phys. Rev. A **88**, 033424 (2013).

[37] B. Knuffman, A. V. Steele, and J. J. McClelland, Cold atomic beam ion source for focused ion beam applications, J. Appl. Phys. **114**, 044303 (2013).

[38] G. ten Haaf, S. H. W. Wouters, S. B. van der Geer, E. J. D. Vredenbregt, and P. H. A. Mutsaers, Performance predictions of a focused ion beam from a laser cooled and compressed atomic beam, J. Appl. Phys. **116**, 244301 (2014).

[39] S. H. W. Wouters, G. ten Haaf, R. P. M. J. W. Notermans, N. Debernardi, P. H. A. Mutsaers, O. J. Luiten, and E. J. D. Vredenbregt, Performance predictions for a laser-intensified thermal beam for use in high-resolution focused-ion-beam instruments, Phys. Rev. A **90**, 063817 (2014).

[40] M. Viteau, M. Reveillard, L. Kime, B. Rasser, P. Sudraud, Y. Bruneau, G. Khalili, P. Pillet, D. Comparat, I. Guerri, A. Fioretti, D. Ciampini, M. Allegrini, and F. Fuso, Ion microscopy based on laser-cooled cesium atoms, Ultramicroscopy **164**, 70 (2016).

[41] S. D. Saliba, C. T. Putkunz, D. V. Sheludko, A. J. Mcculloch, K. A. Nugent, and R. E. Scholten, Spatial coherence of electron bunches extracted from an arbitrarily shaped cold atom electron source, Opt. Express **20**, 3967 (2012).

[42] D. Murphy, R. W. Speirs, D. V. Sheludko, C. T. Putkunz, A. J. McCulloch, B. M. Sparkes, and R. E. Scholten, Detailed observation of spacecharge dynamics using ultracold ion bunches, Nature Comm. **5**, 4489 (2014).

[43] R. W. Speirs, C. T. Putkunz, A. J. McCulloch, K. A. Nugent, B. M. Sparkes, and R. E. Scholten, Single-shot electron diffraction using a cold atom electron source, J. Phys. B **48**, 214002 (2015).

[44] L. P. Yatsenko, B. W. Shore, and K. Bergmann, Detrimental consequences of small rapid laser fluctuations on stimulated Raman adiabatic passage, Phys. Rev. A **89**, 013831 (2014).

[45] T. Wang, S. F. Yelin, R. Côté, E. E. Eyler, S. M. Farooqi, P. L. Gould, M. Koštrun, D. Tong, and D. Vrinceanu, Superradiance in ultracold Rydberg gases, Phys. Rev. A **75**, 033802 (2007).

[46] N. Hoe, B. D'etat, and G. Coulaud, Electric field ionization rate of the hydrogen atom, Phys. Lett. A **85**, 327 (1981).

[47] R. J. Damburg and V. V. Kolosov, A hydrogen atom in a uniform electric field. III, J. Phys. B **12**, 2637 (1979).

[48] G. J. H. Brussaard and J. Hendriks, Photoconductive operation of a laser triggered spark gap, IEEE Trans. Dielectr. Electr. Insul. **14**, 976 (2007).

Microsc. Microanal. 20, 1008–1014, 2014
doi:10.1017/S1431927614000774

Microscopy AND Microanalysis

High-Coherence Electron and Ion Bunches From Laser-Cooled Atoms

Ben M. Sparkes, Daniel J. Thompson, Andrew J. McCulloch, Dene Murphy, Rory W. Speirs, Joshua S. J. Torrance, and Robert E. Scholten*

School of Physics, ARC Centre of Excellence for Coherent X-Ray Science, The University of Melbourne, Parkville, VIC 3010, Australia

Abstract: Cold atom electron and ion sources produce electron bunches and ion beams by photoionization of laser-cooled atoms. They offer high coherence and the potential for high brightness, with applications including ultra-fast electron-diffractive imaging of dynamic processes at the nanoscale. The effective brightness of electron sources has been limited by nonlinear divergence caused by repulsive interactions between the electrons, known as the Coulomb explosion. It has been shown that electron bunches with ellipsoidal shape and uniform density distribution have linear internal Coulomb fields, such that the Coulomb explosion can be reversed using conventional optics. Our source can create bunches shaped in three dimensions and hence in principle achieve the transverse spatial coherence and brightness needed for picosecond-diffractive imaging with nanometer resolution. Here we present results showing how the shaping capability can be used to measure the spatial coherence properties of the cold electron source. We also investigate space-charge effects with ions and generate electron bunches with durations of a few hundred picoseconds. Future development of the cold atom electron and ion source will increase the bunch charge and charge density, demonstrate reversal of Coulomb explosion, and ultimately, ultra-fast coherent electron-diffractive imaging.

Key words: ion beam, electron beam, electron diffraction, space charge, cold atom physics, coherence

Introduction

The ultimate goal of X-ray and electron imaging is the ability to create "molecular movies" of the dynamics of atomic-scale processes (Dwyer et al., 2006). Molecular movies, with atomic spatial and temporal resolution, will enable dramatic advances in our understanding of critical phenomena underlying biology, materials sciences, and technological applications. For instance, rational drug design relies on knowing the molecular structure and function of membrane proteins (Pinto et al., 1992), motivating development of many different technologies including billion-dollar X-ray-free electron lasers, which attempt to produce sufficient brightness in an X-ray beam for single-shot imaging of noncrystalline objects (Chapman et al., 2011).

Electrons offer an alternative to very bright X-ray sources, which, in any case, require a bright- and low-emittance electron source. The sample interaction is 10^4–10^6 times stronger for electrons compared to X-rays (Sciaini & Miller, 2011) but electron imaging is limited by the space-charge effect: that is, the Coulomb interaction within an electron bunch that dramatically reduces the source brightness and coherence. Coulomb-driven explosion of the electron bunch can be reversed if the electron bunch has a uniform ellipsoidal distribution (Luiten et al., 2004).

The ability to shape electron bunches into appropriate ellipsoidal distributions is one of the motivations behind the development of a cold atom electron/ion source (CAEIS) (Claessens et al., 2005). Other advantages of a CAEIS include high source coherence due to the low temperature of the electrons and ions, and the promise of high brightness, with up to 10^6 particles/bunch. Here we present an overview of our CAEIS, investigation of space-charge effects, and the creation of ultra-fast cold electron bunches.

Received November 14, 2013; accepted March 21, 2014
*Corresponding author. scholten@unimelb.edu.au

Materials and Methods

Cold Atom Source

In our experiments we laser-cool and trap rubidium-85 atoms. We use an effusive oven to produce hot rubidium, which is then cooled via a Zeeman slower before entering the trapping region. This provides a high-flux source of slow atoms, described in more detail in a study by Bell et al. (2010). The atoms are then confined in a magneto-optic trap (MOT) located between two accelerator plates separated by 50 mm. Using this method, up to 10^9 atoms at $\sim$70 μK can been trapped with a Gaussian width of <1 mm, leading to densities up to 10^{11} cm^{-3}, similar to or greater than other CAEIS experiments (Knuffman et al., 2011; Engelen et al., 2013). Densities of 10^{12} cm^{-3} have been achieved using a dark spot in a sodium MOT (Ketterle et al., 1993). The maximum density is important as it will ultimately limit the number of electrons or ions that can be produced for a region of a certain size. Recently, proposals have been made to use atom beams as opposed to trapped atoms to increase the flux (Kime et al., 2013; Knuffman et al., 2013).

Creating Shaped Bunches

To create electron and ion bunches, a two-stage ionization process is used (Fig. 1b). First, the trapping and cooling lasers, as well as the magnetic fields of the MOT, are turned off. A pulse of laser light resonant with the $F = 3 \rightarrow F' = 4$ transition (780 nm) and duration of order microseconds is then directed onto the atoms perpendicular to the accelerator plates. A 5 ns 480 nm pulsed laser beam is directed onto the excited atoms in a direction parallel to the accelerator plates. The wavelength of the pulsed blue laser can be changed over tens of nanometers to allow for either direct ionization of the already-excited atoms, or to excite them to a high-lying Rydberg state, where the static accelerator field induces field ionization.

The pulsed blue laser is focused into a ribbon of light at the MOT, with a full-width at half-maximum (FWHM) of approximately $\sigma_z = 150\,\mu$m. The size of the blue laser ribbon is important as it will determine the energy spread σ_u of the electrons and ions produced via $\sigma_u = e\sigma_z F$, where e is the fundamental electron charge and F the strength of the accelerating electric field. For a field of 40 kV/m, we obtain $\sigma_u = 6$ meV. The temporal length of the laser pulse determines the bunch length, 10 cm and 3 mm for pulse durations of 5 ns and 150 ps.

The 780 nm excitation laser profile is transformed into an arbitrary shape using a spatial light modulator (SLM). This combination of laser wavelengths and orientations creates the shaped electron and ion bunches, as shown in Figure 1a. Approximately 10^5 electrons were produced in each bunch. The repetition rate of the experiment is 10 Hz, limited by the repetition rate of the pulsed blue laser.

Detection

We select electrons or ions by appropriate choice of polarity for our accelerator front plates (e.g. electrons in Fig. 1a). After constant acceleration, the electrons or ions are propagated for 21.5 cm in a null field, then detected on a phosphor-coupled microchannel plate detector (MCP) and imaged with a CCD camera to provide two-dimensional spatial resolution of the bunch, as shown in Figure 1c. Temporal evolution of the bunch can be determined by monitoring the potential of the grounded component of the MCP.

Results

Temperature and Coherence Length Measurements of Cold Electron Bunches

The temperature of the electron source can be determined from the divergence of the bunches, calculated from the derivative of the edge of the image of the propagated bunch and the propagation distance. Using our ability to shape the excitation laser using a SLM, we produced a beam with sharply defined edges. The edge width before propagation was defined by the resolution of the excitation intensity profile, which in turn is defined by the optical resolution of the excitation laser imaging system, ~10 μm. The transverse thermal velocity of the electron cloud determines the angular spread after propagation (Sheludko et al., 2010):

$$\frac{dQ_e}{dr} = e\kappa \frac{d_1}{2d_1 + d_2} \sqrt{\frac{eF}{d1(k_B T_0 + \Delta E)}}, \qquad (1)$$

where Q_e is the detector signal proportional to charge, r the radial coordinate, e the electron charge, κ the linear magnification, d_1 and d_2 the distances through which the bunch is accelerated and freely propagated, F the accelerator field magnitude, k_B the Boltzmann constant, ΔE the excess energy of the electrons after ionization, and T_0 the minimum electron temperature (i.e., when $\Delta E = 0$). The excess electron energy can be varied by changing the wavelength of the blue laser (Fig. 2a), and the data fitted to equation 1 to determine κ and T_0. The minimum temperature of the electrons was found to be $T_0 < 10 \pm 5$ K (McCulloch et al., 2011) for a bunch containing 10^5 electrons (20 fC). The electron temperature is much higher than the cold atom temperature (70 μK) owing

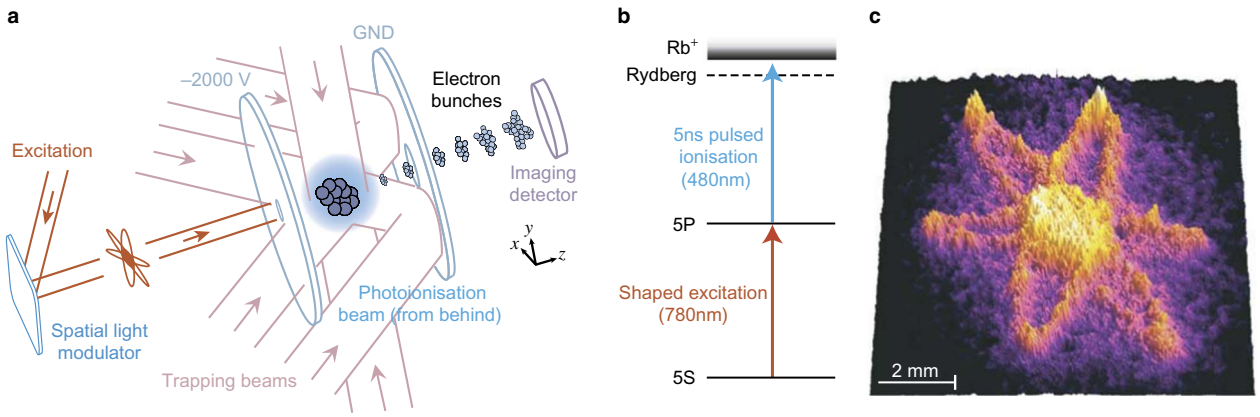

Figure 1. a: Experimental set-up of the cold atom electron/ion source. **b:** Energy-level diagram showing two-stage ionization process. **c:** False-color image of electron cloud detected on microchannel plate detector. From McCulloch et al. (2011).

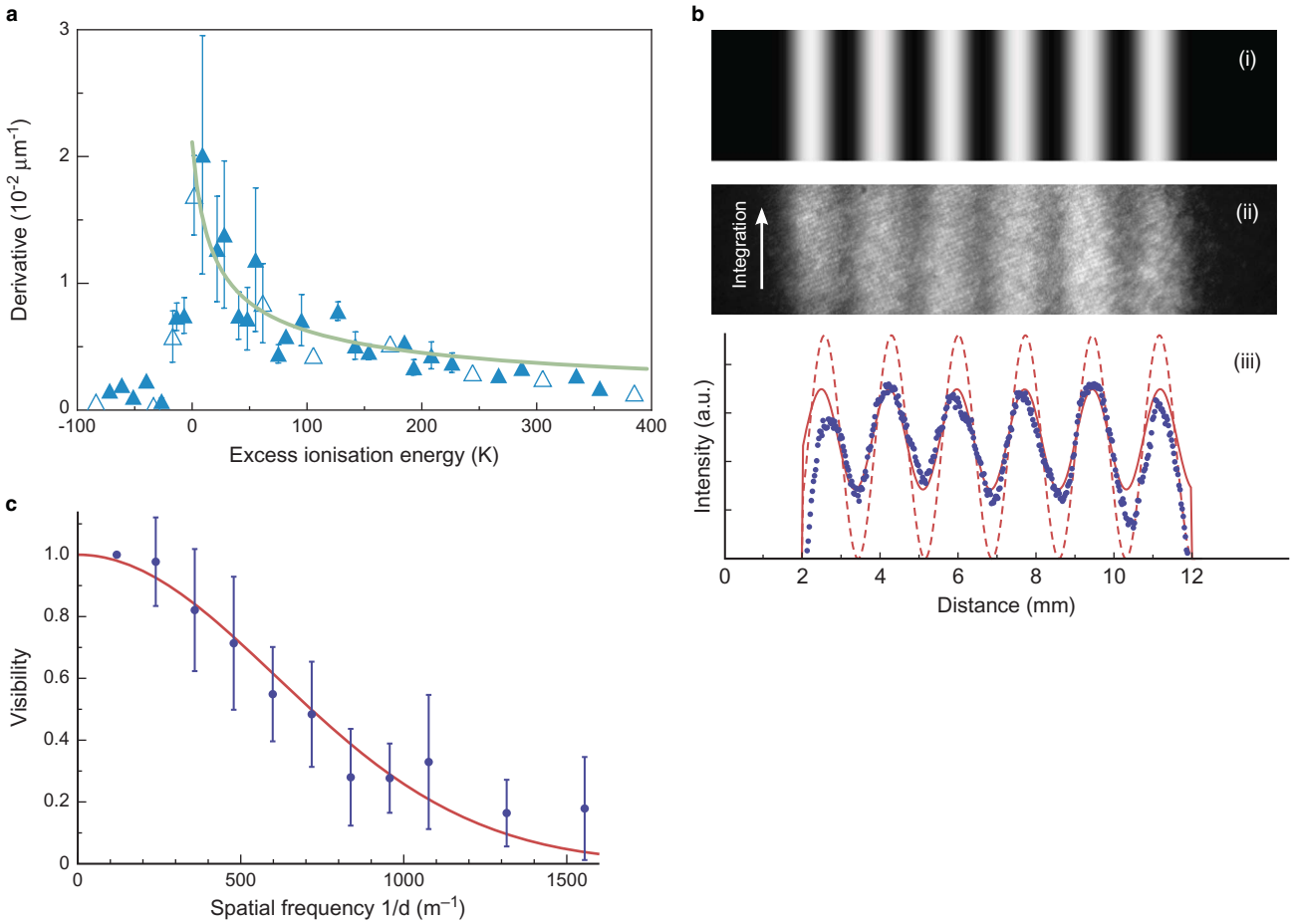

Figure 2. **a:** Measuring electron bunch divergence from edge acuity. Error bars indicate one standard deviation over 30 shots, including statistical and systematic uncertainties. An upper limit to source temperature of $T_0 = 10 \pm 5$ K is extracted for a bunch of 10^5 electrons by fitting equation 1 to the data (solid line) with excess ionization energy $\Delta E_c \geq 0$ K. From McCulloch et al. (2011). **b:** (i) Desired excitation laser beam intensity profile used to create the spatial light modulator phase mask. (ii) Image of resulting shaped electron bunch on microchannel plate detector. (iii) Integrated line profile of the calculated fully coherent electron distribution (red, dashed), the recorded electron image (blue points), and a fit to the recorded data (red, solid). **c:** Visibility of electron bunch pattern as a function of spatial frequency, with a Gaussian fit to the visibility function resulting in $L_c = 7.8 \pm 0.9$ nm. The systematic uncertainty in measuring d was 3%. From Saliba et al. (2012).

to the intrinsic heating processes encountered during ionization, such as disorder-induced heating.

From this minimum temperature we can determine the transverse coherence length of the electron bunch:

$$L_c = \hbar / \sqrt{m_e k_B T_0}, \quad (2)$$

where m_e is the mass of the electron. Using the value for T_0 obtained above gives $L_c > 10 \pm 3$ nm.

The arbitrary shaping ability of the CAEIS can also be used to directly measure the coherence length. This was achieved by using a sinusoidally shaped excitation laser and measuring the visibility of the electron pattern as a function of spatial frequency (Figs. 2b, 2c), resulting in a measurement of $L_c = 7.8 \pm 0.9$ nm following the procedure outlined in a study by Saliba et al. (2012). A coherence length of 10 nm at the source is already sufficient for imaging small biomolecules such as bacteriorhodopsin, where the unit cell length is of order 10 nm. In contrast, high-brightness conventional electron sources based on photoemission, with electron bunch temperatures of order 10^4 K, have an associated coherence length of just 0.3 nm.

Cold atom ion bunch temperatures are on the order of milliKelvins, limited by disorder-induced heating (Bannasch et al., 2013).

Ultra-Fast Cold Electrons

Ultra-fast electron diffraction enables the study of molecular structural dynamics with high resolution at sub-picosecond timescales. This is important for understanding biochemical dynamics such as protein folding and regulation, as well as the formation of cracks in novel materials (Schotte et al., 2003; Sciaini & Miller, 2011). Ultra-fast exposure times will also allow high-intensity imaging of radiation sensitive

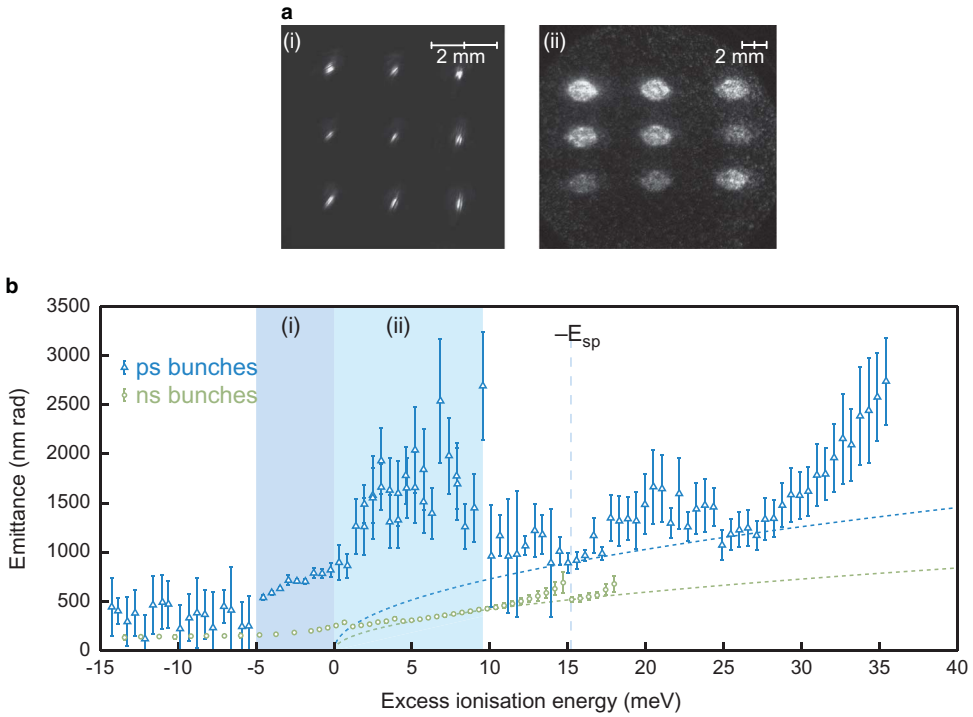

Figure 3. a: Typical pepperpot images used to extract the emittance of femtosecond-excited cold atom electron/ion source electron bunches with a charge of 100 fC. (i) A charge-coupled device image of the laser pulse used to excite the atoms. (ii) Detected electron signal on microchannel plate detector for an ionization wavelength of 478.00 nm. **b:** Measured radial emittance as a function of excess ionization energy. Each point represents 50 single-shot measurements with the error bars indicating one standard deviation combined from the statistical deviation and systematic uncertainties. The dashed lines are theoretical plots of the emittances using the experimentally determined temperature and beam radii [see equation (3)]. For more information see McCulloch et al. (2013).

samples, such as biologically active molecules, to obtain sufficient information about the molecule before it dissociates, known as "diffract-before-destroy" imaging.

To achieve this with our CAEIS, we replaced the continuous wave (CW) 780 nm excitation laser with a femtosecond laser, with a full-width-half-maximum (FWHM) of 40 nm. With femtosecond excitation, the initial electron pulse duration is limited by the spatial and temporal extent of the overlap between the new femtosecond pulses and the 5 ns pulses of 480 nm light. The overlap produces a shaped pulse of electrons or ions with a minimum duration of 150 ps (McCulloch et al., 2013). The charge of the electron bunches produced was 100 fC.

The high bandwidth inherent to short laser pulses might be expected to increase the excess energy spread of the electrons and thus destroy their transverse coherence. We performed an emittance measurement using the pepperpot method. Instead of using a physical pepperpot, we shaped the femtosecond excitation as shown in Figure 3ai and measured the spatial distribution of the electron bunches at the MCP detector. By knowing the initial and final electron beamlet distributions, the emittance ε_γ can be calculated (McCulloch et al., 2013). The pepperpot measurements were performed for a series of different blue laser wavelengths, similar to the temperature measurements discussed in Materials and Methods section, and compared to results with CW excitation.

From the results (Fig. 3b) it can be seen that in region i, just below the field-free ionization threshold, the emittance increases, coinciding with an increase in ionization efficiency and therefore an increase in space-charge effects. In this region the electron bunches that are produced are ultra fast and still highly coherent. Below region i the ionisation efficiency is poor, reflected in the large error bars. In region i the blue laser couples the $5P_{3/2}$ state to one or more field-ionizing Rydberg states, resulting in an electron bunch with minimal spread. Above threshold, in region ii, the emittance increases dramatically owing to the opening of an alternative ionization pathway: when the energy of the ionization laser is above threshold, the blue laser couples the $5P_{3/2}$ state directly to the continuum. In this case the large near-resonant bandwidth of the 780 nm femtosecond pulse substantially increases the energy spread.

As the excess ionization energy increases further, the emittance approaches the theoretical emittance growth function:

$$\varepsilon_r = \sigma_r \sqrt{\frac{k_B T}{m_e c^2}}, \tag{3}$$

where σ is the root mean square bunch width and T the electron temperature. As can be seen, the emittance will

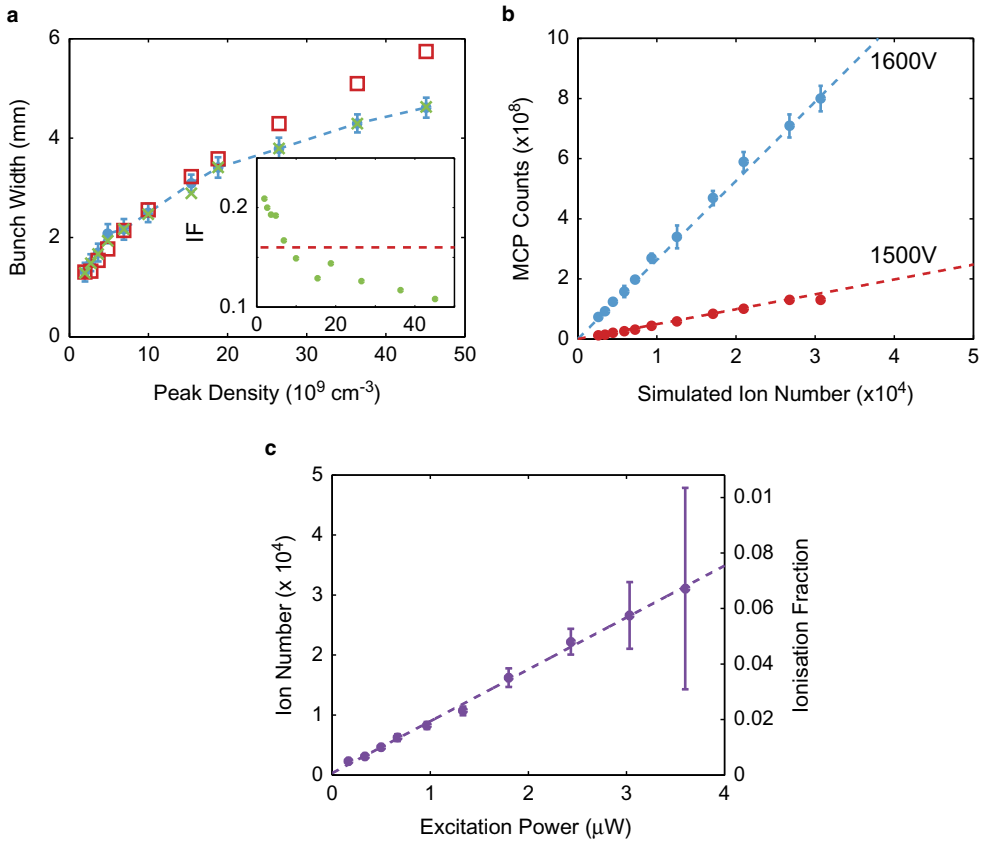

Figure 4. **a:** Gaussian bunch widths as a function of peak atom density. Blue circles indicate experimental data, with the error bars determined from the standard deviation of ~100 measurements; dashed blue line is to guide the eye; red squares indicate general particle tracer (GPT) simulations determined from the peak density and a 0.16 ionization fraction (IF) within the interaction region determined by the sizes of the excitation and ionization lasers; green crosses indicate GPT simulations with an ionization fraction chosen to match the experimental data. The inset shows the ionization fraction chosen for each density (green points) compared with the 0.16 constant value (red dashed line). **b:** Measured counts from the microchannel plate detector (MCP) as a function of the simulated ion number from the ionization fraction shown in inset of (**a**) for an MCP potential of 1,500 (red) and 1,600 V (blue). Points indicate experimental data, error bars from standard deviation of ~100 measurements and dashed lines indicate linear fit to data. **c:** Ion number, determined using the calibration from (**b**), as a function excitation pulse power for measured data. The right-hand axis shows the ionization fraction, determined from the atom density and ionization laser sizes. Each data point represents 100 single-shot measurements with the error bars indicating one standard deviation combined, the dashed line represents a linear fit to the data.

increase with the temperature of the electron produced, which, in turn, will depend on the excess ionization energy (see Fig. 2a). The difference from this theoretical line is most likely due to space-charge effects or other heating processes that occur during ionization and extraction, which equation 3 does not take into account. This shows that the bandwidth of the femtosecond laser is not contributing appreciably to the energy spread.

Below region i the emittance is approximately constant ($\varepsilon_r = 538 \pm 26$ nmrad), limited by heating during the extraction process. In the same region, the emittance with CW excitation was 141 ± 7 nmrad. Though the femtosecond emittance is larger, the corresponding coherence length is still relatively large for an electron source, at $L_c = 4.0 \pm 0.2$ nm (McCulloch et al., 2013). The difference in emittance and temperature (and therefore coherence length) between the nanosecond and picosecond bunches is because of the increased space-charge repulsion that will occur in a bunch with the same charge but density 30 times greater.

Observing Space-Charge Effects

Space-charge effects within clouds of electrons or ions cause bunch expansion. This is normally an irreversible process and leads to a loss in coherence and brightness. However, if the bunch shape is a uniform ellipsoid then the internal fields are linear, and though the bunch will still expand, the expansion can be reversed by refocusing with conventional linear-charged particle optical systems, preserving the initial coherence and brightness of the source. It has been theoretically shown that an initial bunch with a semi-circular transverse distribution and a very narrow

longitudinal distribution will evolve into a uniform ellipsoid (Luiten et al., 2004).

Creating such a distribution experimentally is challenging. The spatial distribution of the initial bunch depends not only on the excitation beam profile, but also on the initial density of the cold atom cloud, and the time-dependent behavior of the excitation process. We have simulated these effects using optical Bloch equations, and modeled the evolution of the bunch shape using general particle tracer (GPT) simulations (http://www.pulsar.nl/gpt).

We have investigated space-charge effects using ions rather than electrons because of their greater mass and lower velocity and consequently longer interaction times. The ion temperature is also orders of magnitude lower than for electrons, so the effects of thermal diffusion are minimal. In combination, the effects of Coulomb interactions within the bunch are much more clearly discernible.

By increasing the delay between the time when the MOT fields are turned off and the ionization beams are turned on, we are able to study the effect of atomic density on space-charge expansion of the ion bunches by making use of the thermal expansion of the atomic cloud, this is shown in Figure 4a, which shows the bunch size for varying initial density. As expected, as the atomic density increases the bunch width also increases, in good agreement with GPT simulations for a fixed ionization fraction of 0.16 (Fig. 4a), up to a density of around 3×10^{10} cm^{-3}. At higher density, we postulate that the reduced ionization fraction seen experimentally is because of absorption of some of the excitation beam by the atoms at the leading edge of the atom cloud, outside the interaction region, reducing the number of photons in the interaction region available to ionize the atoms and therefore reducing space-charge effects. The inset to Figure 4a shows the individual ionization fraction that best matched simulation and data for each initial atomic density.

By matching the simulations to the space-charge expansion data we have been able to calibrate the detection system to determine the ion number from the counts measured by the phosphor-coupled MCP and CCD imaging system. This was achieved by comparison of the integrated counts recorded on the CCD with the ion number used in GPT to obtain the correct bunch width shown in Figure 4a. The calibration is shown in Figure 4c for two different detector potentials. In both cases the R^2 coefficient was >0.99, indicating a strong linear relationship between the MCP counts and the simulated number of ions. We examined the effect between ion number and excitation power further at low power (well below the saturation limit of ~10 mW) to illustrate how absorption of the excitation laser outside the interaction laser could lead to a reduction in ion number. As can be seen from Figure 4c, the ion number (calculated with the calibration obtained from Fig. 4b) increases linearly with excitation power. We also calculated the ionization fraction using the sizes of the ionization beams and the peak atomic density of the MOT.

Our investigations have also led to the discovery of some interesting effects such as the formation of density waves around an initially uniform circular ion bunch. This can be explained by the formation of a diffuse halo of charges around the central core of the bunch. The halo is created by reabsorption of spontaneous emission from the directly excited atoms. The dense core then expands into the halo, due to space-charge repulsion, and creates a high-density ring. We have also investigated the space-charge interaction of parallel beamlets to see the influence of overlapping self-fields. Our studies show good agreement between simulations and experiments. The simulations reveal the sensitivity of the visibility of the high-density features to the initial ion temperature: the structure is lost at temperatures of a few tens of Kelvin, highlighting the advantages of the cold atom source in comparison with conventional sources, which operate at room temperature or above, for studying these effects.

Discussion

We have presented our CAEIS, including characterization of the temperature of the source and the corresponding transverse coherence lengths of the electron bunches. We have also investigated the effect of space charge on ion bunches as an analog to the much faster expansion of electron bunches, showing substantial space-charge effects. One of our main priorities is to overcome the space-charge expansion using the unique beam-shaping ability of cold atom sources to produce uniform ellipsoidal bunches. Our shaping ability is currently limited by speckle in the excitation beam image produced from the SLM owing to the hologram-production algorithm used. Overcoming this will involve implementing alternate algorithms and feedback control over the phase pattern on the SLM, by monitoring the excitation laser profile with an independent imaging detector.

Apart from space charge, another phenomenon limiting the minimum temperature of the ions produced from the CAEIS is disorder-induced heating. Nonuniform Coulomb interactions of the initially randomly distributed electrons and ions leads to an initial spread in the temperature of the bunch. For ions, this increases the temperature of the bunch by at least an order of magnitude (Bannasch et al., 2013). One way of overcoming disorder-induced heating is to use the phenomenon of Rydberg blockade, where the van der Waals' potential caused by an atom in a highly excited state prohibits nearby atoms from also being excited (Bannasch et al., 2013; Robert-de Saint-Vincent et al., 2013). We have recently developed an alternative blue laser system using a frequency locking scheme based on electromagnetically induced transparency (Abel et al., 2009). With this new laser we have produced preliminary results demonstrating blockade behavior with the 30S state and measurements of the temperature effects are in progress.

By overcoming both space-charge and disorder-induced heating effects we should be able to produce ion bunches capable of sub-nanometer resolution (van der Geer et al., 2007).

Conclusion

We have developed a CAEIS with the ultimate goal of producing single-shot electron diffraction of biological samples.

On the path to producing these we have developed a source with a coherence length of ~10 nm with electron temperature of 10 K. By using a femtosecond pulsed laser we have also produced ultra-fast bunches with a minimum duration of 150 ps, with a maximum coherence length of 4 nm. We have shown that space-charge effects are readily observable without the obfuscation of thermal diffusion, potentially providing a new approach to investigating subtle Coulomb interactions in high-current-charged particle sources. Finally, we have investigated the effects of space charge on the ion bunches produced with our system, and observed the formation of surprising structures. To improve the emittance and brightness of the source further, we are investigating reducing the temperature by using Rydberg blockade to overcome disorder-induced heating effects, and using our shaping ability to overcome space-charge effects. By implementing these advances, single-shot ultra-fast coherent-diffractive imaging with nanoscale resolution should become feasible, allowing for the creation of "molecular movies."

Acknowledgments

We thank D. V. Sheludko for his technical assistance. This work was supported by the Australian Research Council Discovery Project DP10960625.

References

Abel, R.P., Mohapatra, A.K., Bason, M.G., Pritchard, J.D., Weatherill, K.J., Raitzsch, U. & Adams, C.S. (2009). Laser frequency stabilization to excited state transitions using electromagnetically induced transparency in a cascade system. *Appl Phys Lett* **94**, 071107.

Bannasch, G., Killian, T.C. & Pohl, T. (2013). Strongly coupled plasmas via Rydberg blockade of cold atoms. *Phys Rev Lett* **110**, 253003.

Bell, S.C., Junker, M., Jasperse, M., Turner, L.D., Lin, Y.-J., Spielman, I.B. & Scholten, R.E. (2010). A slow atom source using a collimated effusive oven and a single-layer variable pitch coil Zeeman slower. *Rev Sci Instrum* **81**, 013105.

Chapman, H.N., Fromme, P., Barty, A., White, T.A., Kirian, R.A., Aquila, A., Hunter, M.S., Schulz, J., DePonte, D.P., Weierstall, U., Doak, R.B., Maia, F.R.N.C., Martin, A.V., Schlichting, I., Lomb, L., Coppola, N., Shoeman, R.L., Epp, S.W., Hartmann, R., Rolles, D., Rudenko, A., Foucar, L., Kimmel, N., Weidenspointner, G., Holl, P., Liang, M., Barthelmess, M., Caleman, C., Boutet, S., Bogan, M.J., Krzywinski, J., Bostedt, C., Bajt, S., Gumprecht, L., Rudek, B., Erk, B., Schmidt, C., Hömke, A., Reich, C., Pietschner, D., Strüder, L., Hauser, G., Gorke, H., Ullrich, J., Herrmann, S., Schaller, G., Schopper, F., Soltau, H., Kühnel, K.-U., Messerschmidt, M., Bozek, J.D., Hau-Riege, S.P., Frank, M., Hampton, C.Y., Sierra, R.G., Starodub, D., Williams, G.J., Hajdu, J., Timneanu, N., Seibert, M.M., Andreasson, J., Rocker, A., Jönsson, O., Svenda, M., Stern, S., Nass, K., Andritschke, R., Schröter, C.-D., Krasniqi, F., Bott, M., Schmidt, K.E., Wang, X., Grotjohann, I., Holton, J.M., Barends, T.R.M., Neutze, R., Marchesini, S., Fromme, R., Schorb, S., Rupp, D., Adolph, M., Gorkhover, T., Andersson, I., Hirsemann, H., Potdevin, G., Graafsma, H., Nilsson, B. & Spence, J.C. (2011). Femtosecond X-ray protein nanocrystallography. *Nature* **470**, 73–77.

Claessens, B., van der Geer, S., Taban, G., Vredenbregt, E. & Luiten, O. (2005). Ultracold electron source. *Phys Rev Lett* **95**, 164801.

Dwyer, J.R., Hebeisen, C.T., Ernstorfer, R., Harb, M., Deyirmenjian, V.B., Jordan, R.E. & Miller, R.J.D. (2006). Femtosecond electron diffraction: "Making the molecular movie". *Phil Trans R Soc A* **364**, 741–778.

Engelen, W.J., van der Heijden, M.A., Bakker, D.J., Vredenbregt, E.J.D. & Luiten, O.J. (2013). High-coherence electron bunches produced by femtosecond photoionization. *Nat Commun* **4**, 1693.

Ketterle, W., Davis, K.B., Joffe, M.A., Martin, A. & Pritchard, D.E. (1993). High densities of cold atoms in a dark spontaneous-force optical trap. *Phys Rev Lett* **70**, 2253–2256.

Kime, L., Fioretti, A., Bruneau, Y., Porfido, N., Fuso, F., Viteau, M., Khalili, G., Šantić, N., Gloter, A., Rasser, B., Sudraud, P., Pillet, P. & Comparat, D. (2013). High-flux monochromatic ion and electron beams based on laser-cooled atoms. *Phys Rev A* **88**, 033424.

Knuffman, B., Steele, A.V. & McClelland, J.J. (2013). Cold atomic beam ion source for focused ion beam applications. *J Appl Phys* **114**, 044303.

Knuffman, B., Steele, A.V., Orloff, J. & McClelland, J.J. (2011). Nanoscale focused ion beam from laser-cooled lithium atoms. *J Phys* **13**, 103035.

Luiten, O., van der Geer, S., de Loos, M., Kiewiet, F. & van der Wiel, M. (2004). How to realize uniform three-dimensional ellipsoidal electron bunches. *Phys Rev Lett* **93**, 94802.

McCulloch, A.J., Sheludko, D.V., Junker, M. & Scholten, R.E. (2013). High-coherence picosecond electron bunches from cold atoms. *Nat Commun* **4**, 1692.

McCulloch, A.J., Sheludko, D.V., Saliba, S.D., Bell, S.C., Junker, M., Nugent, K.A. & Scholten, R.E. (2011). Arbitrarily shaped high-coherence electron bunches from cold atoms. *Nat Phys* **7**, 785–788.

Pinto, L.H., Holsinger, L.J. & Lamb, R.A. (1992). Influenza virus M2 protein has ion channel activity. *Cell* **69**, 517–528.

Robert-de Saint-Vincent, M., Hofmann, C.S., Schempp, H., Günter, G., Whitlock, S. & Weidemüller, M. (2013). Spontaneous avalanche ionization of a strongly blockaded Rydberg gas. *Phys Rev Lett* **110**, 045004.

Saliba, S.D., Putkunz, C.T., Sheludko, D.V., Mcculloch, A.J., Nugent, K.A. & Scholten, R.E. (2012). Spatial coherence of electron bunches extracted from an arbitrarily shaped cold atom electron source. *Opt Exp* **20**, 3967–3974.

Schotte, F., Lim, M., Jackson, T.A., Smirnov, A.V., Soman, J., Olson, J.S., Phillips, G.N., Wulff, M. & Anfinrud, P.A. (2003). Watching a protein as it functions with 150-ps time-resolved X-ray crystallography. *Science* **300**, 1944–1947.

Sciaini, G. & Miller, R.J.D. (2011). Femtosecond electron diffraction: Heralding the era of atomically resolved dynamics. *Rep Prog Phys* **74**, 096101.

Sheludko, D.V., McCulloch, A.J., Jasperse, M., Quiney, H.M. & Scholten, R.E. (2010). Non-iterative imaging of inhomogeneous cold atom clouds using phase retrieval from a single diffraction measurement. *Opt Exp* **18**, 623–626.

van der Geer, S.B., Reijnders, M.P., de Loos, M.J., Vredenbregt, E.J.D., Mutsaers, P.H.A. & Luiten, O.J. (2007). Simulated performance of an ultracold ion source. *J Appl Phys* **102**, 094312.